PROCEEDINGS OF THE
MULTIDISCIPLINARY DOCTORAL SCHOOL
2007-2008 ACADEMIC YEAR
FACULTY OF INFORMATION TECHNOLOGY
PÁZMÁNY PÉTER CATHOLIC UNIVERSITY
BUDAPEST
2008

Faculty of Information Technology
Pázmány Péter Catholic University

Ph.D. PROCEEDINGS

PROCEEDINGS OF THE
MULTIDISCIPLINARY DOCTORAL SCHOOL
2007-2008 ACADEMIC YEAR
FACULTY OF INFORMATION TECHNOLOGY
PÁZMÁNY PÉTER CATHOLIC UNIVERSITY
BUDAPEST

July, 2008

Pázmány University ePress
Budapest, 2008

Contents

Introduction

Since September 2000, our multidisciplinary Doctoral School, originally established in 1993 as a joint program of four Universities, has been operating at our Faculty of Information Technology. We are now celebrating the 10th anniversary of the foundation of this Faculty.

During the last academic year 10 doctoral students got their Ph.D. degree. In addition, more than thirty doctoral students are presenting their annual reports.

It is our pleasure to publish this annual proceedings to demonstrate the genuine multidisciplinary research done at our Jedlik Laboratories. Thanks are also due to the supervisors and consultants, as well as to the five collaborating National Research Laboratories of the Hungarian Academy of Sciences and the Semmelweis Medical School. The collaborative works with foreign Universities are acknowledged at the special reports.

As a milestone of this special collaboration, we were able to jointly accredit and now start with the Semmelweis Medical School a new undergraduate curriculum on Molecular Bionics, the first of this kind in Europe.

We acknowledge the many sponsors of the research reported here. Namely,

- the Hungarian National Research Fund (OTKA),
- the Hungarian Academy of Sciences,
- the National Office of Research and Development (NKTH),
- the Gedeon Richter Co.,
- the Office of Naval Research (ONR) of the US,
- the National Science Foundation (NSF) of the US,
- IBM Hungary,
- Ericsson Hungary,
- Eutecus Inc., Berkeley, CA,
- Morphologic Ltd., Budapest,
- Analogic Computers Ltd., Budapest,
- AnaFocus Ltd., Seville, and
- the Pázmány Péter Catholic University.

Budapest, July 2008.

Tamás Roska

Head of the Doctoral School

Knowledge-based NP-Coreference Resolution in Hungarian

Márton Miháltz
(Supervisor: Dr. Gábor Prószéky)
mihaltz@digitus.itk.ppke.hu

Abstract—**In this paper we present experiments for automatically identifying relationships between entities in Hungarian texts. We identify coreference and possessor-possession relationships between noun phrases using a rule-based approach that relies on a deep parser, rules based on psycholinguistic research and knowledge from an ontology. We present evaluation of both tasks using a manually annotated corpus.**

Index Terms—**Coreference resolution, possessor identification**

I. INTRODUCTION

Identifying relationships between entities in text is a useful complement to NLP applications that can include, among others, information extraction, opinion mining, or machine translation.

In the experiments described below, we focus on the automatic resolution of coreference and possession relationships between distinct noun phrases in Hungarian texts. Both are implemented in the same system that utilizes rules that operate on the output of a deep parser and use knowledge from an ontology. We decided on this approach in favor of machine learning because of the current lack of hand-annotated Hungarian training material.

In the following sections, we describe each task, along with our methods and the evaluation methodology and results separately.

II. COREFERENCE RESOLUTION

In this task, the system has to identify coreference relationships between NPs, or the antecedents in a text that refer to the same entities in the real world as the anaphoric noun phrases.

In our experiment, we have dealt with the following 6 types of anaphoric phenomena (pairs of corefering noun phrases set in bold in the examples):

TABLE 1
EXAMPLES FOR THE TYPES OF COREFERENCE WE ATTEMPT TO RESOLVE

Type	Example (Hungarian, English)
Repetition	Tegnap találkoztam **egy ismerősömmel**. **Az ismerősöm** nagyon sietett. *I met **an acquaintance** today. **My acquaintance** was in a hurry.*
Proper Name Variant	**Kovács Jakab, az ABC Kft. igazgatója** tegnap sajtótájékoztatót tartott. Az eseményen **Kovács úr** bejelentette az új termékeket. ***Jakab Kovács, chairman of ABC Ltd.** held a press conference today. **Mr. Kovács** announced the new products.*
Synonym	Tamás kapott **egy biciklit**. Én is láttam **a kerékpárt**. *Tamás got **a new bicycle**. I saw **the bike**, too.*
Hypernym	Bejött **egy kutya**. **Az állat** fáradtnak tűnt. ***A dog** just came inside. **The animal** seemed tired.*
Pronoun	Beszéltem **Julival**. Megadtam **neki** a számodat. *I talked to **Juli**. I gave **her** your phone number.*
Zero Pronoun	**Viktor** ismeri **Ferit**, de (**ő**) nem kedveli (**őt**) túlságosan. ***Viktor**$_1$ knows **Feri**$_2$, but **he**$_1$ doesn't like **him**$_2$ very much.*

At present, we do not deal with cataphora, or the sub-parts of complex noun phrases, only simple, maximal NPs corresponding to the arguments of the main verb.

A. Methods

In recent work in the field of coreference resolution (CR), data-driven, machine learning-based approached have gained ground over traditional knowledge-based systems [9]. However, such an approach requires an extensive number of hand-labeled training examples, which is not available at present for Hungarian. For this reason, we had to commit ourselves to a rule-based approach in the design of our CR system.

Our system relies on several sources of knowledge: the morphological, syntactic and semantic information available from the output of the MetaMorpho MT system's deep parser [11]; rules based on Binding Theory in Hungarian syntax [3] and the results of psycholinguistic research on Hungarian sentence understanding [10]; rules based on semantic information available from the Hungarian WordNet [7]; and finally, we also employ character-based heuristics, similar to some of those described by [12].

The MetaMorpho parser identifies paragraph, sentence and token boundaries, clauses, maximal noun and verb phrases, and provides morphological, grammatical and semantic information for these. After this preprocessing, our system processes each anaphoric NP in the document from left to right and tries to identify the corefering antecedent that is closest to it. This means that pronouns and zero pronouns can be the antecedents of pronouns or zero pronouns as well.

Before coreference resolution, we try to identify as much as possible from the NPs that are formally anaphoric but are

likely to refer to entities outside the document. This is done in order to exclude NPs that would only introduce noise to the CR process [13].

Coreference resolution for a given NP in the input document is based on satisfying constraints, in order to eliminate as much as possible from the antecedent candidates and evaluating preferences in order the select the most likely candidate [8]. The algorithm for generating the list of antecedent candidates, filtering the list and finally selecting the winning candidate is specific to the type of the anaphoric NP (proper name, definite common noun, pronoun/zero pronoun) and is described in detail below.

1) Proper names

For proper names, the list of antecedent candidates consist of all the proper names prior to the anaphor in the entire document. At present, we do not apply any kind of filtering to these candidates. The most likely antecedent candidate is the one having smallest Minimum Edit Distance (MED) with the anaphor. Both antecedent and anaphor are normalized before the string matching: determiners are removed from the beginnings of the names, and the head word is lemmatized. The rule selects an antecedent only in case the MED for the closest candidate falls below a preset threshold. This way, the system is not forced to select one from the available candidates.

2) Common nouns

For common nouns with a definite article, we first try to exclude mentions that refer to unique objects inferable from common world knowledge (e.g. "the president of the United States"). At present, we do this by searching a predefined list of NPs. Antecedent candidates are the proper names and common nouns in the preceding part of the paragraph of the anaphor, up to the VP containing it (Binding Theory excludes candidates dominated by the main verb in the anaphor's VP.) Selecting the antecedent is done by identifying the closest candidate that has the same head, or the closest synonym or hypernym/hyponym. Synonymy is checked via Hungarian WordNet: if there is a synset that contains both anaphor and candidate they are considered synonyms. We use the Leacock-Chodorow similarity measure [4] in order to measure semantic relatedness via the hypernym/hyponym paths connecting the anaphor and the candidate (lexical forms of the heads are used.) The closest candidate that falls below a preset threshold is considered as the winning antecedent, but only if no identical or synonymous candidate was found. In the evaluation experiment described in section 3, the threshold was configured to accept candidates available in WN not further than 2 relation "steps" away.

3) Pronouns, zero pronouns

We only deal with personal pronouns, with the exception of *az* ("that") demonstrative pronoun in subject position and not referring to a subordinate relative clause (explanation follows). We exclude 1st and 2nd person pronouns (referring to discourse entities outside the text). The antecedent candidates are collected from the 2 sentences before the anaphor's sentence (if they exists) plus the clauses prior to the clause containing the anaphor in its sentence. All possible kinds of NPs in this scope are considered.

The antecedent candidates are filtered by checking person, number and 2 semantic features specified by the parser: *+/-animate* and *+/-human*. The latter two can have underspecified values (in case of zero pronouns and lexically ambiguous nouns), these are compatible with all other values. The filtering process also excludes candidates that have already been identified as antecedents of other NPs in the current clause (in accordance with Binding Theory.)

If there is more than one pronominal anaphor in the current clause, the system processes them in obliqueness order (subject, direct object, other valence arguments, modifiers.) This allows the simple identification of antecedents by ruling out already bound candidates (see above.) We also perform CR for common nouns and proper names before resolving pronouns within a sentence. This is done in order to further help resolution of pronouns, which are the most difficult, but also the most frequently occurring type of anaphor, according to our preliminary observations.

Identifying the antecedent of the pronoun or zero pronoun that is the subject in its VP follows research on Hungarian psycholinguistics [10]. The heuristic first assumes parallel grammatical functions across sentences, where the subject is preserved from the previous clause/sentence. This is overridden by the presence of the demonstrative pronoun *az* in subject position, which indicates change of subject. In case there are more than one non-subject NPs in the prior clause, the antecedent is selected using the obliqueness hierarchy and by checking distance from the anaphor (NPs closer to the end of the sentence are preferred). Resolution of pronouns and zero pronouns with grammatical roles other than subject are based on the obliqueness hierarchy and closeness to the anaphor.

B. Evaluation

We have compiled a small corpus (10 text segments, total 99 sentences, 1240 words) from excerpts from history textbooks. The texts in the corpus were processed with MetaMorpho to annotate structural and grammatical boundaries. The mentions identified by the parser were manually annotated by their closest antecedents in the texts. We used 16 different types of NP-coreference for the manual annotation, which had 132 occurrences in the corpus. 6 of these types are handled by our current CR system, which gives 81 annotated NPs for testing.

We performed coreference resolution for the texts in the corpus with our system and compared the results with the manual annotation. We calculated precision (the ratio of correctly resolved NPs to the number of NPs tagged by the system) and recall (the ratio of correctly resolved NPs to the number NPs manually annotated) for each type of coreference (Table 2.)

Looking at the results, we were able to confirm that the system performs fairly well (precision 71-80%, recall 61-83%) for the most frequent types of anaphora currently handled in the corpus (proper name variant matching, repeated forms of common nouns and pronouns, zero pronouns.) On the other hand, the performance of the synonym and hypernym heuristics was poor, but since the evaluation corpus contained only a small number of such instances, this figure might not reflect realistic evaluation.

We also conducted an examination of the various error types produced by the system. Each automatically assigned coreference link was examined, and assigned to one of four categories:

OK: coreference link produced by system is identical to manual annotation (correct).

OK_equ: coreference link produced by system is not identical to manual annotation, but refers to same entity (in the coreference chain), so it was regarded correct.

KO_parser: coreference link assigned by system is different from manual annotation (ie. erroneous); the error is due to erroneous syntactic parsing in the input (if the parser would have provided correct results, the automatic coreference assignment would have been correct.)

KO_cr: erroneous result; the antecedent was present in the text and the parsing was correct; the mistake was due to the CR algorithm.

As it can be seen from Table 3, about half of all the mistakes committed by the CR system are results of errors in parsing, such as incorrectly identified noun phrases, zero anaphors etc. Having perfectly parsed input would increase overall precision to 75%, pronoun/zero pronoun resolution precision to 91%.

Finding not exactly matching, but referentially equivalent antecedents is a phenomenon only observed in the case of pronouns/zero pronouns, as the pronominal CR algorithm mainly relies on tracking of the discourse. Tracing back to the beginning of coreference chains in order to label the first mention of each entity as antecedent would result in lower precision, due both to parsing errors and CR errors.

TABLE 3
CATEGORIZATION OF CR EVALUATION RESULTS

Coreference Type	OK	OK_equ	KO_parser	KO_cr
Pronoun	19	6	7	3
Repeated	13	0	4	1
Prop. name	12	0	0	3
Hypernym	0	0	0	2
Synonym	1	0	0	3
Hyponym	0	0	0	0
Total:	45	6	11	12

We have also experimented with a second round of evaluation in order to compare our results to a previous work on Hungarian anaphora resolution by [5], which uses an implementation of Centering Theory [1]. At the present stage, the coreference type covered by both [5] and our system is zero pronouns in subject positions. So far we have selected 3 news articles from the Szeged Treebank [2], which has accurate, manually created syntactic annotation. There were 15 anaphora occurrences in the selected articles, which were first manually labeled with their antecedents, then compared to the results of running [5] and our system. Both systems had very low coverage (4 and 3 anaphors attempted), of which 3 were correct (75% and 100% precision). We will continue to annotate coreference in selected texts from the Szeged Treebank in order to be able to compare our systems on the basis of more data that is not dependent on the output of a specific parser.

TABLE 2
EVALUATION OF COREFERENCE RE RESOLUTION

Coreference type	NPs manually annotated	NPs tagged Total	Correct	Precision	Recall	F-measure
Proper name	14	15	12	80.00%	85.71%	82.76%
Pronoun	46	35	25	71.43%	54.35%	61.73%
Repeated	15	18	13	72.22%	86.67%	78.79%
Synonym	2	4	1	25.00%	50.00%	33.33%
Hypernym	4	2	0	0.00%	0.00%	0.00%
Total/Average:	*81*	*74*	*45*	*68.92%*	*62.96%*	*65.81%*

I. POSSESSOR IDENTIFICATION

In this second task, the system has to identify the phrase in the text that is the possessor of another phrase in the text corresponding to a possession. We focus on the cases when the possessor noun phrases are detached from the possession noun phrases, which means that there are other words, phrases, or even sentence boundaries between them.

A. Method

In Hungarian, there are three basic possessive structures, when the possessor and the possession can be detached (related possessor and possession NPs in bold face):

a)   Special possession predicate:
   Jánosnak *van egy nagy, sárga* ***esőkabátja****.*
b)   Detached dative-case predicate (topicalisation, etc.)
   Jánosnak *ellopták a* ***könyvét****.*

c)   Detached nominative possessor:
   János *tegnap itt hagyta az* ***esernyőjét****.*

Type a) is a special predicate that expresses possession relationship between its arguments. Type b) is a complex NP, where other constituents can move between the possessor and the possession. Type c) is more of a discourse phenomena, where the hearer picks the possessor out of the entities introduced earlier in the discourse.

In our coreference resolution-possessor identification system, the MetaMorpho deep parser component is able to identify grammatical possessive phenomena such as type a) and b) (when the parse was complete enough), so we use the available possession relationships pointers in the parse. For type c), however, we use our own rule-based approach.

For type c) sentences, we rely on the assumptions that 1) the subject of the possession NP's dominating verbal phrase is the default possessor, 2) the possessor noun phrase matches in grammatical number and person to the

possession NP's owner number and person, carried by morphological information in Hungarian. The second assumption can override the 1st, so when the subject of the possession's VP does not match in number/person, the previous clause's subject can be the possessor, if it's still in the same discourse segment:

János *elutazott nyaralni. Én vigyázok a* **lakására***.*

Our possessor identification algorithm is therefore implemented as follows: for instances of type c), we identify the noun phrases up to the -2nd sentence before the clause of the possessor, up to but not further than the 1st sentence in the containing paragraph, that are subjects in their clause and match in number and person and number, and pick the one that is closest to the possessor (the "rightmost" one.) If no sentence-level parse, therefore no grammatical role information is available for the NPs in MetaMorpho's output, we select the rightmost NP before the possession with nominative case and matching number and person.

B. Evaluation

We used the same small corpus as for the coreference resolution task to create a manually annotated gold standard to serve as a reference for evaluation of our system's performance. Out of the 454 NPs in the 10 extracts, 38 were detached possessions. These were manually annotated with the ids of NPs corresponding to their possessors in the text. Comparing the system's output to the manual annotation, we counted the following cases: true positives (both manual and automatic possessor annotation is present for NP, and they are identical), misses (both manual and automatic possessor annotation is present for NP, but they are different), false positives (only automatic possessor annotation present for NP) and false negatives (only manual possessor annotation present for NP). From these, we calculated precision = |true positives| / (|true positives| + |misses| + |false positives|), and recall = |true positives| / (|true positives| + |misses| + |false negatives|, summarized in Table 4.

TABLE 4
EVALUATION OF POSSESSOR IDENTIFICATION

True positives (number of NPs)	26
Misses (number of NPs)	7
False positives (number of NPs)	1
False negatives (number of NPs)	5
Precision	76.47%
Recall	68.42%
F-measure	72.22%

We did a quick error analysis, and found that the majority of problems, again, as in coreference identification, originated from errors introduced by the parser.

However, there are cases when our heuristic method is insufficient, such as in the example below (from a history textbook paragraph describing the fighting tactics of 9th century A.C. Hungarian light cavalrimen):

(...) az első, ellenséggel való összecsapás után menekülést színlelve megfordultak, és futásnak eredtek. **Az ellenfél** *ekkor üldözőbe vette őket. Ez lett a* **vesztük***. A harcosok a vágtató ló hátán „kengyelbe állva", hátrafordulva lenyilazták üldözőiket.*

The possession relationship among the entities in question (set in boldface) can only be interpreted correctly after understanding the whole context. The grammatical number of the possessor (singular) and the possession's owner number (plural) do not match, we have to rely on our world knowledge: the singular NP corresponding to the possessor refers to the adversary in the battle, which usually is a group of people, thus it can also be referenced in plural form. Such frame-based knowledge could be coded into ontologies in order to aid processing of such problematic cases.

REFERENCES

[1] Brennan, Susan, Friedman, Marilyn W. and Pollard, Carl J.*: A centering approach to pronouns*. In *Proceedings of the 25th Meeting of the Association for Computational Linguistics* (ACL '87), (1987), pp.155-162.

[2] Csendes D., Csirik J., Gyimóthy T., Kocsor A.: The Szeged Treebank. In Proc. of *the Eighth International Conference on Text, Speech and Dialogue* (TSD 2005), Karlovy Vary, Czech Republic pp. 123-131 (2005).

[3] Kenesei, István: Az alárendelt mondatok szerkezete. (The Structure of Complex Sentences.) In: Kiefer Ferenc (ed.): *Strukturális Magyar Nyelvtan*, vol. I., Mondattan. Akadémiai Kiadó, Budapest (1992)

[4] Leacock, C., M. Chodorow: Combining Local Context and WordNet Similarity for Word Sense Identification. In C. Fellbaum (ed.): *WordNet: An Electronic Lexical Database*, MIT Press, Cambridge, MA (1998), pp. 265–285

[5] Lejtovicz, Katalin, Kardkovács, Zsolt: Anaphora Resolution in Hungarian Texts. In *Proceedings of The Fourth Conference on Hungarian Computational Linguistic*s (MSZNY 2006), Szeged (2006), pp. 362-363.

[6] Miháltz, Márton: Constructing a Hungarian Ontology using Automatically Acquired Semantic Information. In *Proceedings of the 5th International Workshop on Computational Semantics* (IWCS-5), Tilburg, The Netherlands (2003), pp. 475-478.

[7] Miháltz, M., Cs. Hatvani, J. Kuti, Gy. Szarvas, J. Csirik, G. Prószéky, T. Váradi: Methods and Results of the Hungarian Wordnet Project. In*: Proceedings of the Fourth Global WordNet Conference*, Szeged, Hungary, (2008), pp. 311–321.

[8] Mitkov, Ruslan: Anaphora Resolution: The State of The Art. Working Paper, University of Wolverhampton (1999)

[9] Ng, Vincent: Machine Learning for Coreference Resolution: From Local Classification to Global Ranking. *Proceedings of the 43rd Annual Meeting of the Associaction for Computational Linguistics* (2005)

[10] Pléh, Csaba*:"* Mondatközi viszonyok feldolgozása: az anafora megértése a magyarban." In: Pléh Csaba: *Mondatmegértés a magyar nyelvben*. Osiris Kiadó, Budapest (1998)

[11] Prószéky, Gábor; László Tihanyi; Gábor Ugray: Moose: a robust high-performance parser and generator. *Proceedings of the 9th Workshop of the European Association for Machine Translation, Foundation for International Studies*, La Valletta, Malta, pp. 138–142 (2004)

[12] Uryupina, Olga: Evaluating Name-Matching for Coreference Resolution. In *Proceedings of the 4th International Conference on Language Resources and Evaluation* (2004)

[13] Varasdi, Károly: Koreferenciák feloldása (Coreference resolution). Manuscript (2005)

A Random Method for Flexible Multiword Expression Extraction

Bálint Sass

(Supervisor: Dr. Gábor Prószéky)

sass.balint@itk.ppke.hu

Abstract—**We present a flexible general framework to handle verbal multiword expressions. A dependency grammar based language independent model is introduced which covers most of the different MWE types. A special extraction method based on cumulative frequency and random selection is described. This method can extract any types of MWEs which conforms the model, and is flexible in two ways: it detects automatically the number of elements in a MWV; and it detects automatically whether a content unit is relevant for a given MWE or just the relational units. The paper includes detailed evaluation for the Hungarian language on the Hungarian National Corpus.**

I. Introduction

Probably all languages contain multiword expressions (MWEs), which act as one unit in some sense. These units have non-compositional (in other words idiomatic) meaning. That means, we cannot figure out the meaning of the multiword unit, even if we know the meaning of its parts. But it is necessary to know these meanings if we want to process natural language intelligently in any field of natural language technology from information retrieval to machine translation [1].

The traditional (at most ten years old) approach of collecting/extracting multiword units apply the following scheme. Multiword units have an important property: their parts appear more frequently together than expected. Knowing this, particular statistical *association measures* are applied, which measure the strength of association between two units [2]. These measures are worked out to handle exactly two units, however there are several multiword units consisting three or more basic units as we will see. In the new approach presented here we put the following two requirements aiming to extend the traditional approach. The MWE extraction methods should be flexible in two ways.

- The number of units should not be restricted to two. The algorithm should detect the number of units within a multiword unit processed.
- The algorithm should detect if there are any inherent *content* unit in the MWE or just some *relational* units are relevant.

We can understand the notion of content and relational units by means of example (1). -*bA* and -*t* are relational units, the latter indicates the object function and also connects a relevant content unit (*orr*) to the verb in this case. This content unit is inherent part of the MWE, we cannot change it if we want to keep the non-compositional meaning of this expression. In this paper we will introduce a MWE extraction method fulfilling the above two flexibility requirements.

(1)   beleüt   orr-t   -bA
       knock·in nose-OBJ IN(-sg)
       ≈ 'meddle with sg'[1]

A good definition for *multiword expression (MWE)* can be the following [1], [3]: sequence of words with non-compositional meaning acting as a single semantic unit. MWEs have two typical properties: their meaning is non-compositional; their surface form is more or less rigid.

Classes of MWEs can be located along a scale from most idiomatic to most literal meaning [4]. Conventional classes [1], [3], [5] with examples are shown below.

1) fully rigid expressions – *ad hoc*;
2) idioms – *kick the bucket*;
3) verb particle constructions (VPCs) – *hand in*;
4) support verb constructions (SVCs) – *take a walk*;
5) institutionalized phrases – *turn off the light*;

Several MWEs are built up from a verb and one or more (noun phrase) arguments of it. The [verb + (noun phrase) argument(s)] – or *verb argument frame* – structure is very common among MWEs, we find MWEs of this general type in every classes mentioned above. *Multiword verbs (MWVs)* – MWEs with the above structure – cover substantial part of all MWEs, we will deal with this broad class aiming to have a comprehensive picture of MWEs in general.

II. Dependency model

For Hungarian[2] which is an agglutinative, free-word-order language the adequate method for language description can be dependency grammar (DG) [7]. In dependency grammar analysis we leave word order out of account, just record the functional relations – the so called *dependencies* or positions – between related units. In Hungarian the surface dependencies

---

[1] We provide Hungarian example MWEs with English glosses in this form. The first line contains the MWE, the verb is shown always first. The -*t* and -*bA* are casemarks. *orr-t* is not a real wordform but the lemma and the casemark separated by a dash for didactic purposes. Note: the upper case letter (e.g. in -*bA*) signs a vowel alternation point where the exact vowel is determined by Hungarian vowel harmony. The second line contains the word-by-word translation. The uppercase codes means functions/positions, witch can be SUBJ, OBJ or any preposition. The dot (·) separates two words, which has a one-word counterpart in the other language. The third line contains the overall English translation.

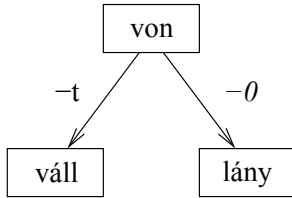[2] You can have a quick overview of grammar of Hungarian in [6].

Fig. 1. Dependency tree of sentence (2). Content unit *váll* 'sholuder' is in object position, and *lány* 'girl' is in subject position. Hungarian relational unit for subject is zero suffix depicted as *-0*.

Fig. 3. Dependency tree of SCF *hisz -bAn* 'believe IN'.

between the verb and its noun phrase arguments are expressed by relation markers at the end of noun phrases. Relation markers can be *casemarks* (e.g. *-bA* in example (1)) or *postpositions* (e.g. *mellett* 'beside'). Apart from the fact that the former are bound morphemes while the latter are separate words, their role is the same, thus, we will treat them the same way.

In DG the basic units are usually words. It is obviously good choice in isolative languages (like English), because it suitably separates relational and content units which are separate words. How can we do this separation in an agglutinative language, where relational units can be suffixes and words too? The idea is: choose the *morpheme* as basic unit. This allows to treat relational units in a uniform way, regardless of they are suffixes or separate words.

A suitable representation for sentences and also for dependency structures is the *dependency tree*: relational units become edges, content units become vertices. The dependency tree of example (2) can be seen in Fig. 1.

(2) A   lány váll-t   vont.
     the girl shoulder-OBJ shrug-PAST
     'The girl shrugged her shoulder.'

We call a position of a structure *fixed* if the content word is inherent part, that means, we cannot change it without changing the overall meaning. Similarly, we call a position *free* if just the relation is relevant, we can choose the content wordform a broad word class. Fig. 2 shows the dependency tree of example (1) exemplifying these notions.

The original MWE definition contains a language dependent criterion: MWEs must contain words. Accordingly, a relational unit can only be part of a MWE if and only if it is a word (e.g. the English preposition *in*). The idea is: to be able to process Hungarian we take all relations between the verb and
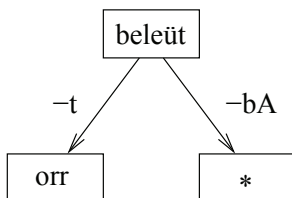

Fig. 2. Representation of example (1), a dependency structure with one fixed and one free position (depicted as *).
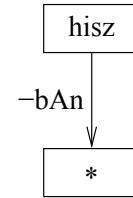
its argument as units regardless of how they expressed in a particular language. Thus, we include relational units which are bound morphemes also (e.g. the Hungarian casemark *-bAn*). Changing only one word in the original, we arrive at a new (more language-independent) definition of MWEs: sequence of *morphemes* with non-compositional meaning acting as a single semantic unit. (We could have called them *multimorpheme expressions*.) This is a general framework, it contains all mentioned MWVs regardless of language. Using this framework we can treat almost all MWVs in a uniform general way. This new definition allows one new type of MWVs: the *verb subcategorization frames (SCFs)*. They have only free positions, that is why they traditionally not treated as MWE-s, but our morpheme-based approach includes them also. An example is shown in Fig. 3.

III. METHOD

To test our MWV extraction method described below we need a corpus with verb-argument dependency annotation. We use the 187 million word Hungarian National Corpus, which is morphosyntactically tagged and disambiguated [8]. Reaching towards dependency annotation we do the following preprocessing steps using light tools:

- clause detection – to have one-verb units;
- partial syntactic parsing – to have noun phrases;
- verbstem detection and assignment of dependency relations – to approximate the dependency annotation.

This process and a corpus query tool on the top of the dependency annotated corpus are described in [9] in details. An experiment about generating Hungarian semantic verb classes based on syntactic patterns in this corpus is described in [10].

To the MWE extraction method which constitutes substantive part of this paper we get basic idea from a verb subcategorization frame extraction method [11]. We have to extend the method from SCFs to the whole class of one-level-deep dependency trees to be able to treat MWVs described above. The idea is: store not just relational units but the content units also. The algorithm consists of the following steps.

1) We extract the verb argument frames from corpus sentences.
2) We sort them according to *length*.
3) Starting with the longest one we discard frames with frequency less than 5, and add their frequency to a one-position-shorter frame chosen randomly.

4) MWV candidates are the final remaining verb frames, ranked by cumulative frequency.

As we see, we use cumulative frequency in a special way. Note: choosing at random was suggested by the original paper as the best performing possibility [11]. In case of SCFs the definition of length of verb argument frame is trivial: the number of (free) positions. Is case of MWVs this definition should be modified. It is desirable that the new definition fits the intuitive length of an MWE, namely how many units belong to it (beside the verb). To acieve this, we must count all relational and content units. In other words, we count fixed positions doubly. Accordingly, the *length* of a MWV is the following: number of free positions + number of fixed positions $*2$. (The length of the MWV shown in Fig. 2 is 3.) Taking this definition into account, a frame is "one-unit-shorter" if it has one less free positions *or* it has a free position instead of a fixed one.

To sum up, our method extracts dependency trees (with depth of one) with arbitrarily distributed fixed and free positions from dependency annotated corpora.

IV. EVALUATION

The traditional evaluation method in the MWE-extraction field is the n-best lists method [12], [2]. It consists of the following steps:

- the list of candidates is sorted by the extraction method;
- first n candidates is considered by human annotators;
- *precision* = the true positive MWEs from the first n candidates.

Using small n for long lists tend to provide unreliable results. We can improve reliability by applying several different n values annotating the first 5-10 percent of the list. We evaluate our method using n-best lists with one annotator. We take candidate list first as a whole to have a picture about overall performance, and then by type to map the strength and weaknesses ot the method. The *type* notation is just for convenience. Type of a MWV consists of three values in this order: the length (followed by a colon), the number of fixed positions and the number of free positions. For example type [4:20] means two fixed positions, and type of the MWV shown in Fig. 2 is [3:11].

Applying the method to the 8000 most frequent verbs in the Hungarian National Corpus, it provides a list of 47000 possible MWVs using a (very high) cutoff-threshold of 50. The distribution over types we obtained is shown in Table I. First line of Table I contains the verb subcategorization frames. Type [0:00] in the upper left corner are the non-transitive verbs without any relation (e.g. *villámlik* 'lighten'). These latter expressions are by no means multiword expressions, they are included in this investigation only for the sake of symmetry.

We evaluated types having at most two positions (gray section in Table I). We annotated true MWVs among the first $n = 500$; then per type among the first $n = 100$ (or $n = 200$). The annotation criterion was this: a candidate is a true positive MWV, if it has a non-compositional/idiomatic meaning.

TABLE I
DISTRIBUTION OF MWV CANDIDATE LIST OVER TYPES. MWVs CONTAINING AT MOST TWO POSITIONS ARE SHOWN IN GREY.

	szabad: 0	1	2	3	4	5
kötött: 0	5006	10790	8509	2140	256	9
1	10647	9077	44	-	-	-
2	1148	160	2	1	-	-
3	91	1	-	-	-	-
4	20	-	-	-	-	-
5	3	-	-	-	-	-
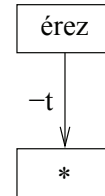
Fig. 4. Example MWV of type [1:01] − *érez -t* 'feel sg'.

Results obtained are summarized in Table II. Compared with the results found in literature these results are fairly good [12], [3]. We get better numbers for the simple types. We comment the best numbers (shown in grey in Table II) in the following discussion.

In type [1:01] we get best results in the case of simple transitive verbs (see e.g. Fig. 4), with precision values coming close to 100 percent. Results of type [1:01] MWVs having one non-object position (see e.g. Fig. 3) are around 80 percent. Concerning to MWVs having one fixed position (type [2:10]) if the fixed position is the subject position, the expression usually have compositional meaning (typically with verb *van* 'be' acting as a copula). Conversely, if the fixed position is non-subject (see e.g. Fig. 5) we obtain much better results. Type [3:11] structures are the *typical* multiword verbs. This type does not belong to SCFs nor to traditional MWEs, as it contains free and fixed positions both. Being such a borderline case, they usually get out of field of vision, however they are as important as other MWVs having idiomatic meaning (see our usual example in Fig. 2). The algorithm can extract more complicated structures also, an example is shown in (3), its dependecy tree is in Fig. 6.

(3)   hajt malom-A-rA   víz-t
        push sy's·mill-ONTO water-OBJ

Fig. 5. Example MWV of type [2:10] − *jön lét-rA* 'come into existence'.

15

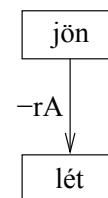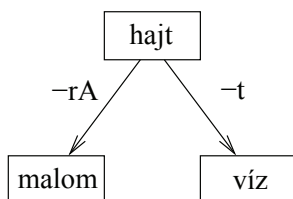| type	$n = 50$	100	150	200	500
[0:00]	88,0%	86,0%			
[1:01]	96,0%	93,0%	92,6%	92,5%	
object	100,0%	98,0%	98,6%	98,5%	
other	78,0%	79,0%	76,0%	78,0%	
[2:10]	52,0%	41,0%			
subject		13,1% (8/61)			
other		84,6% (33/39)			
[2:02]	70,0%	58,0%			
[3:11]	94,0%	85,0%			
[4:20]	44,0%	34,0%			
total	94,0%	95,0%	90,6%	91,0%	90,2%

Fig. 6. Example MWV of type [4:20] (see example (3)).

$\approx$ 'work for sy'[3]

V. CONCLUSION

This final example in Fig. 6 leads us to the conclusion. We state that significance of the method presented lies in its capability of extracting such more complicated, longer structures.

The method matches the two requirements of flexibility stated at the beginning of this paper.

- It adapts to the number of units in the expression – it extracts MWVs with two or more units alike.
- It adapts to the freeness/fixedness of positions – it extracts MWVs with (even mixed) free and fixed positions alike.

Type- and language independency is currently one of the important questions in the field of MWE-extraction. The method is type independent in the sense that it covers all types belonging to the dependency model outlined. Concerning language independency we expect that with agglutinative languages (like Estonian, Turkish etc.) it will provide almost the same results. It is also true that any language can be described with dependency grammar, accordingly, the method can be tested on them in the same way.

REFERENCES

[1] I. Sag, T. Baldwin, F. Bond, A. Copestake, and D. Flickinger, "Multi-word expressions: A pain in the neck for NLP," in *Proceedings of 3rd CICLING*, Mexico City, Mexico, 2002, pp. 1–15.

[2] S. Evert, *The Statistics of Word Cooccurrences: Word Pairs and Collocations*. Dissertation, Institut für maschinelle Sprachverarbeitung, University of Stuttgart, 2005.

[3] C. Oravecz, V. Nagy, and K. Varasdi, "Lexical idiosyncrasy in MWE extraction," in *Proceedings of the 3rd Corpus Linguistics conference*, Birmingham, 2005.

[4] D. McCarthy, B. Keller, and J. Carroll, "Detecting a continuum of compositionality in phrasal verbs," in *Proceedings of the ACL-SIGLEX Workshop on Multiword Expressions: Analysis, Acquisition and Treatment*, Sapporo, Japan, 2003, pp. 73–80.

[5] H.-J. Kaalep and K. Muischnek, "Multi-word verbs of Estonian: a database and a corpus," in *Proceedings of the LREC2008 workshop: Towards a Shared Task for Multiword Expressions*, Marrakech, Morocco, 2008, pp. 23–26.

[6] B. Megyesi, "The Hungarian language," 1998.

[7] G. Prószéky, I. Koutny, and B. Wacha, "Dependency syntax of Hungarian," in *Metataxis in Practice (Dependency Syntax for Multilingual Machine Translation)*, D. Maxwell and K. Schubert, Eds. Foris, Dordrecht, The Netherlands, 1989, pp. 151–181.

[8] T. Váradi, "The Hungarian National Corpus," in *Proceedings of the 3rd International Conference on Language Resources and Evaluation (LREC2002)*, Las Palmas, Spain, 2002, pp. 385–389.

[9] B. Sass, "The Verb Argument Browser," in *Proceedings of the 11th International Conference on Text, Speech and Dialogue*, Brno, Czech Republic (accepted for publication), 2008.

[10] ——, "First attempt to automatically generate Hungarian semantic verb classes," in *Proceedings of the 4th Corpus Linguistics conference*, Birmingham, 2007.

[11] D. Zeman and A. Sarkar, "Learning verb subcategorization from corpora: Counting frame subsets," in *Proceedings of the 2nd International Conference on Language Resources and Evaluation (LREC2000)*, Athens, Greece, 2000.

[12] S. Evert and B. Krenn, "Methods for the qualitative evaluation of lexical association measures," in *Proceedings of the 39th Meeting of the Association for Computational Linguistics*, Toulouse, France, 2001.

---

[3] Bound morpheme *-A* in *malom-A-rA* indicates the possessive suffix.

Developing an approach for Open-Domain, Interactive Question Answering

Lesi Zoltán
(Supervisor: Dr. Gábor Prószéky)
zoli@nix.hu

Abstract— **This paper contains plans and achievements considered during the investigation of question answering systems. Theoretical, technical issues, assumptions and constraints will be introduced, which were arosen during the investigation of our research field. We present a big picture about the planned and partly implemented Searcher system. The test enviroment was designed and partly implemented, but without these tests numeric results are missing.**

Index Terms—**Question-answering (QA), corpus, open-domain, Web**

I. INTRODUCTION

Finding the answer to a question by returning a small fragment of a text, where the answer lies, is different from the task of information retrieval or information extraction. Information retrieval is a wider category of the science of searching for documents, for information within documents and for metadata about documents, as well as that of searching relational databases and the World Wide Web. Information extraction is a type of information retrieval whose goal is to automatically extract structured information, i.e. categorized and contextually and semantically well-defined data from a certain domain, from unstructured machine-readable documents.

We would like to be pragmatic so we checked (in among the TREC papers [6]) what does a real-world user want from a Q&A system:

1) Timelines: The answer to a question must be provided in real-time, even when the Q&A system is accessed by thousands of users.
2) Accuracy: The precision of Q&A systems is extremely important – as incorrect answers are worse than no answers.
3) Usability: Often, knowledge in a Q&A system must be tailored to the specific needs of a user. Often, heterogeneous data sources are used – information may be available in texts, in databases, in video clips or other media.
4) Completeness: Complete answers to a user's question is desirable.
5) Relevance: The answer to a user's question must be relevant within a specific context. Often the case, interactive Q/A, in which a sequence of questions helps clarify an information need, may be necessary. Question complexity and the related taxonomy of questions cannot be studied without taking into account the representation of context, the common ground between the user and the Q&A system and without allowing for follow-up questions. The evaluation of Q&A system must be user-centered: humans are the ultimate judges of the usefulness and relevance of Q&A systems and of the ease with which they can be used.

Search engines on the Web and most existing question-answering (QA) systems provide the user with a set of hyperlinks or Web page extracts. It is then quite difficult for the user to know which answer is the correct one.

A. Issues in Question-Answering

QA research attempts to deal with a wide range of question types including: fact, list, definition, hypothetical, semantically-constrained (such as numerical), and cross-lingual questions [5]. Search collections vary from small local document collections, to internal organization documents to the World Wide Web.

Closed-domain question answering deals with questions under a specific domain (for example, medicine or automotive maintenance), and can be seen as an easier task because NLP systems can exploit domain-specific knowledge frequently formalized in ontologies.

Open-domain question answering deals with questions about nearly everything, and can only rely on general ontologies and world knowledge. On the other hand, these systems usually have much more data available from which to extract the answer.

The shallow methods of QA use keyword-based techniques to locate interesting passages and sentences from the retrieved documents and then filter based on the presence of the desired answer type within that candidate text. Ranking is then done based on syntactic features such as word order or location and similarity to query.

We call deep methods of QA where more sophisticated syntactic, semantic and contextual processing must be performed to extract or construct the answer. These techniques might include named-entity recognition, relation detection, coreference resolution, syntactic alternations, word sense disambiguation and so on. These systems will also very often utilize world knowledge that can be found in ontologies (such as WordNet, or SUMO) to augment the available reasoning resources through semantic connections and definitions.

Often happens that information need is not well captured by the Q&A system. In case if question processor missclassify, then false information will be used for

extracting and generating the answer. The questioner might want not only to reformulate the question, but (s)he might want to have a dialogue with the system. It is generally acknowledged that developing a successful computational model of interactive natural language, a dialogue component based on extensive analysis of sample dialogues needs to be implemented. Although the problem is complex, much analysis of human-human interactions has been done, most of the data employed was either human-human dialogues in relevant task domains or the Wizard-of-Oz dialogues in which a human (the Wizard) simulates the role of the computer as a way of testing the dialogue model.

Related subtasks:

1) Dialogue models for Q&A: follow-up questions, reference resolution, detection of intentions, common goals and plans.
2) Develop models that detect new developments – distinguish what is new from previous answers
3) Develop conversational models in which the system makes suggestions: e.g. "You mean …"

Answer extraction in itself implies the process of recognizing the answer of a question. In doing so at least three problems arise. The first one is related to the assessment of answer correctness, and implicitly to ways of justifying its correctness. The second problem relates to the method of knowing whether all the possible correct answers have been found throughout the data sources, and in a related way – whether no correct answer can be found to a given question. Thirdly, there is the problem of generating a coherent answer [3] when it's information is distributed across a document or throughout different documents. This problem can be extended to the case when an answer part is found in a given data source, whereas the other parts, with which it must be fused, are retrieved from different data sources, in different formats. Another extension is given by the case when special implicatures must be generated prior to the extraction of the answer – as the simple juxtaposition of the answer parts is not sufficient.

Currently the hotest part of researching is combining answering for complex question with using Web and closed corpora in the same time, deep methods, interactive elements, cross-linguistic answering and try to be open-domain until it is possible.

II. OVERVIEW OF THE SEARCHER SYSTEM

The basis of Searcher System is a dialog model, where the user send a question, the server tries to answer it with using a deep question-answer analysis and if the answer is ambiguous then ask back to the user. The communication between the user and QA server needs to be managed by a multi-threaded asynchron framework which has a question queue for the waiting requests. We present the architecture of the planned system, Figure 1. shows the sending back answers and questions will be plain and very quick.
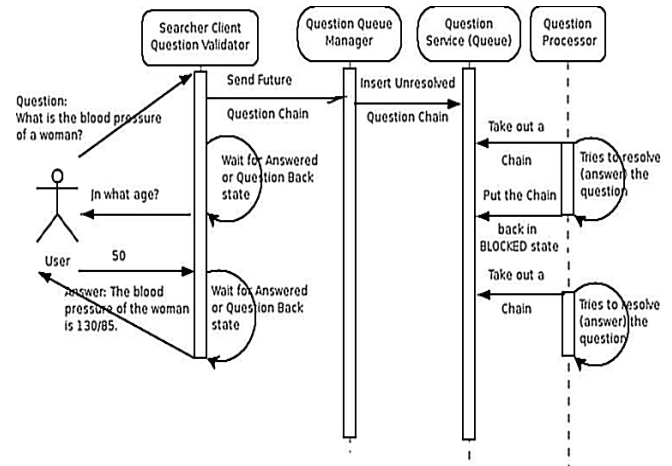
1. Figure Big picture about the planned Searcher System

The client inserts the question in a chain structure (Figure 2.) what hides our attempts, and contains the question and necessary information about the answer. Resolving linguistic ambiguations of the chain data gives the answer.
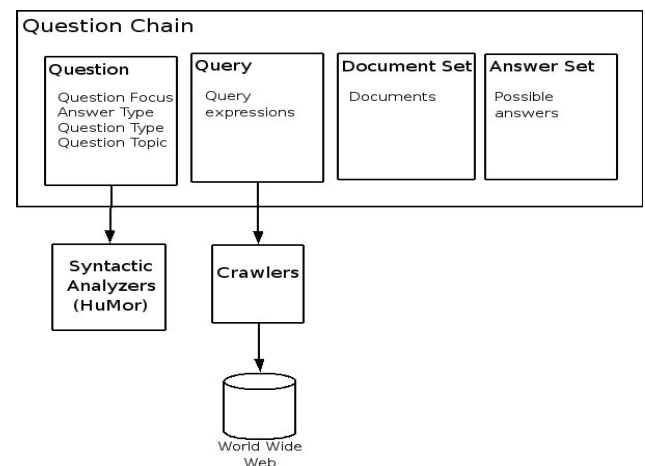
2. Figure Structure of the Question Chain

We use the deep methods of question answering models which relies on natural language processing. We perform the processing of the question by combining syntactic information to characterize the question (e.g. question type, answer type, question focus, question topic).

A. Question Processing

The role of the question processing module to determine the question type, the expected answer type, find out what is

question focus [1], and transform the question into queries for the search engine. Question type is an idiomatic categorization of questions for purposes of distinguishing between different processing strategies and/or answer formats. Answer type is the class of object (or rhetorical type of sentence) sought by the question. Question focus is the property or entity that is being sought by the question. Question topic is the object (person, place, …) or event that the question is about. The question might well be about a property of the topic, which will be the question focus. For example in next question:*"What is the height of Mt. Everest?"* where height is the focus and Mt. Everest is the topic.

High speed Unification Morphology [2] software was helped us to find focus and topic (the part of speech tagger of Morphologic Ltd.).

B. *Queries and Search engines*

Processing queries means sending queries to search engines (in our case it is Google), and collecting documents from ranking. The World Wide Web qualitatively different from a closed corpus, but we can use this virtual collaboration with it's tens of terrabytes size. This size gives rise to data redundancy sometimes with multiple formulations. The effects of poor quality (mispelling, wrong grammar, incorrect information) and heterogenity of the Web can be decreased with it's redundancy and combining with other closed corpora.

C. *Extracting Passages*

Documents that contain the keywords returned by the search engines gives too much unnecessary information. We need to filter some paragraph. Similar paragraph filtering was applied in Searcher that was introduced in the MULDER system [6]: we chose paragraphes where keywords occur more frequently than a treshold.

III. Corpus and Test enviroment

Different question-answering techniques can be used to find relevant information, and to compare these techniques, it is important to evaluate question answering systems. Most known measuring methods are Mean Reciprocal Rank (based on inverse of rank at which first correct answer was found) and Confidence-Weighted Score (Evaluates how well system know what they know).

$$CWS = \frac{\sum_{i=1}^{Q} i_c/i}{Q}$$

i_c = number of correct answers in first i questions
Q = total number of questions

The Cross-Language Evaluation Forum introduced an Answer Validation exercise in 2006, which aimed at automatically validating the correctness of the answers given by QA systems according to their supporting snippets. The goal is to improve the performance of QA systems and to make answer assessment semi-automatic. We can have more precise results [4] if validation of snippets would be extended with separate validation of the analyzed question (keywords, category, main verb), processed documents (named entity tagging, sentence selection and ranking) and answer extraction.

We have collected the question-answer corpus of former Text Retrieval Conference because we would like to measure the performance of our system.

IV. Achievements

During the last year the aim was to build up a framework for the question-answer system. We created a asynchron client-server framework with future request view model to ensure plain communication between the question chains and users.

Our investigation around question analysis were not finished yet. We did not have a syntax analyzer that is needed for precise determination of question focus and question topic, currently we use the HuMor part-of-speech tagger for this distinction.

The third goal was to collect a question-answer corpus and create a framework for testing the Searcher system. Continuous integration testing is very helpful, because we can see the changing end- and partial results during our investigation. The corpus was collected, but the testing framework was not finished yet, because of missing preliminary steps. Finally we have tried to run a test with a corpus with one hundred question, but without validation process only the absolutely punctual answers could be accepted, so we did not get meaningful results.

V. Further plans

There are further plans to implement the partly finished parts of the system. We will investigate the passage extraction methods to give fewer and more punctual set for answer extractor. There are concrete plans about answer validation, so this will be the next step in our investigation.

VI. References

[1] Dan Moldovan, Sanda Harabagiu, Marius Pasca, Rada Mihalcea, Roxana Girju, Richard Goodrum and Vasile Rus, "The Sructure and Performance of an Open-Domain Question Answering System"

[2] Prószéky, Gábor; Balázs Kis. "A Unification-Based Approach to Morpho-Syntactic Parsing of Agglutinative and Other (Highly) Inflectional Languages" Proceedings of the 37th Annual Meeting of the Association for Computational Linguistics (ACL), 261–268. College Park, Maryland, USA (1999)

[3] Véronique Moriceau. "Generating Intelligent Numerical Answers in a Question-Answering System" Proceedings of the Fourth International Natural Language Generation Conference.

[4] Anne-Laure Ligozat, Brigitte Grau, Anne Vilnat, Isabelle Robba, Arnaud Grappy. "Lexical validation of answers in Question Answering" Proceedings of International Conference on Web Intelligence. 2007.

[5] John M. Prager. „Question Answering Tutorial" Proceedings of RANLP 2003.

[6] Cody Kwok, Oren Etzioni, Daniel S. Weld. "Scaling question answering to the Web" In Proceedings of the Tenth International World Wide Web Conference

[7] John Burger, Claire Cardie, Vinay Chaudhri, Robert Gaizauskas, Sanda Harabagiu, David Israel, Christian Jacquemin, Chin-Yew Lin, Steve Maiorano, George Miller, Dan Moldovan, Bill Ogden, John Prager, Ellen Riloff, Amit Singhal, Rohini Shrihari, Tomek Strzalkowski, Ellen Voorhees, Ralph Weishedel. "Issues, Tasks and Program Structures to Roadmap Research in Question & Answering" Question & Answering (Q&A). NIST

Graph-based sense representation of written texts

Gyula Papp
(Supervisor: Dr. Gábor Prószéky)
gyupa@digitus.itk.ppke.hu

Abstract—**As a PHD student I started my work last September. This paper contains an introduction into my research topic and my achievements during the last two semesters. I examined the different possibilities of representing the sense of texts with graphs. I have re-implemented and modified HyperLex, a graph-based algorithm for unsupervised word sense disambiguation. Though some measurements have already been executed about the performance of the methods, their evaluation is still in progress.**

Index Terms—**word sense disambiguation, unsupervised WSD, HyperLex, natural language processing, co-occurrence graph**

I. INTRODUCTION

Semantic analysis of texts is one of the biggest challenges in natural language processing (NLP). The goal of semantic analysis is the computer-based representation of the text sense. A lot of NLP applications need an efficient and good quality solution of the problem. This could improve for example the quality of web searching applications and machine translation systems. One possible approach of the solution is to decide the word senses in the analyzed context. The name of this task is word sense disambiguation (WSD).

There are more types of WSD: supervised and unsupervised machine learning approaches and lexical resource-based systems.

Supervised WSD systems are the best performing in public evaluations, but they require a lot of hand-tagged data. Existing hand-annotated corpora provide not enough information about word senses, though supervised WSD systems surpass the most frequent sense heuristic. In theory, these systems would need larger amounts of training data to improve their performance significantly.

The other problem with supervised WSD is that the idea is based on the "fixed-list of senses" paradigm. This means that it considers senses as a closed list of discrete entities (for example dictionary entries of the target word). Lexicographers and semanticists have long warned about this approach. They prefer more complex representation, where, for instance, senses are dense regions of continuum [7].

Unsupervised WSD systems don't need any sense-tagged data. They try to retrieve information about word senses directly from the corpus. They use clustering techniques to discriminate the different senses. This is why unsupervised WSD task is called *word sense discrimination*. Since these systems don't retrieve real word senses the term *word use* is preferred to *word sense* in unsupervised WSD approaches.

Most of the unsupervised WSD systems are based on the vector space model ([9] and [10]). In 2004, Véronis published HyperLex, a graph-based algorithm for unsupervised WSD. HyperLex takes advantage of the small-world property of co-occurrence graphs.

This paper is structured as follows. At first HyperLex is briefly presented. Section IV describes the free parameters of the algorithm. After that my ideas about improving the performance of the algorithm are presented. Section V describes the general method for evaluating unsupervised WSD systems. In section VI my experiments and results are presented. Finally, I draw the conclusions and delineate my ideas for the future.

II. HYPERLEX ALGORITHM

The goal of HyperLex is to separate the uses of the target word. It builds a co-occurrence graph from a corpus. The corpus is a set of paragraphs which contain the target word. The co-occurrence graph is weighted and undirected. The vertices of the graph are the nouns and adjectives of the corpus (except the target word itself). Two nodes are connected if the two words occur at least once in the same paragraph. The weight of the connecting edge depends on the relative frequency of the co-occurrences of the two words. Specifically, let w_{ij} be the weight of the edge between nodes i and j, then

$$w_{ij} = 1 - \max[P(i|j), P(j|i)]$$

$$P(i|j) = \frac{freq_{ij}}{freq_j} \; and \; P(j|i) = \frac{freq_{ij}}{freq_i}$$

The weight of an edge measures how tightly connected the two words are. If two words occur always together the weight of the edge between them is 0. If they occur very rarely in the same paragraph they receive an edge weight close to 1.

Véronis showed that co-occurrence graphs are *small world graphs*. Small world graphs can be characterized by high *clustering coefficient* and low *characteristic path length*. This means that there are strongly connected components *(high-density components)* in the graph and among these components there are only loose connections.

Detecting the different uses of the target word amounts to isolating the high-density components in the co-occurrence graph. Unfortunately, the exact graph-partitioning methods are NP-hard. Since co-occurrence graphs contain several thousand nodes and edges, only heuristic-based techniques can be used.

The hub-detector method is a very simple iterative algorithm. At each step, the algorithm chooses the node with the highest relative frequency in the graph. If it meets some restrictions it is selected as a hub. Then the chosen node and its neighbors are removed from the list of hub candidates and the algorithm continues with the next iteration. If the chosen vertex candidate has a relative frequency below a certain threshold, the algorithm stops. Each root candidate has to have at least k neighbors to become a hub, where k is a free parameter of the algorithm. In addition, the average connection weight with the most frequent k neighbors of hubs has to be below a certain threshold.

At the next step, the target word is added to the vertices of the graph with connections to the detected hubs. The weight of these edges is 0. After that the *Minimal Spanning Tree* (MST) of the whole graph is calculated. Fig. 1 shows an example of the calculated MST.
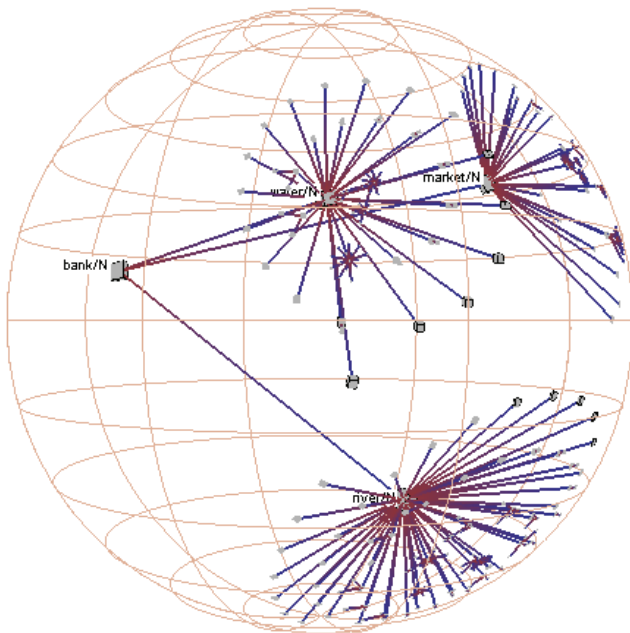

Fig. 1: Generated MST by HyperLex for target word *bank*. Three hubs were computed: *water*, *river* and *market*.

After the MST algorithm each word is placed under exactly one hub. Then a score vector is added to each word. Let **s** be the score vector of node v with as many dimensions as there are components in the MST:

$$s_i = \frac{1}{1+d(h_i,v)}, \text{ if } v \text{ belongs to component } i,$$

$$s_i =, \text{ otherwise,}$$

where $d(h_i,v)$ is the distance between hub h_i and node v in the tree.

During disambiguation the score vectors of words in the context of the target word are computed and summarized. The component with the highest value in the sum vector is the guessed word use.

III. FREE PARAMETERS OF HYPERLEX

There are 7 free parameters of the algorithm:
1) Minimum number of co-occurrences of two words. Other connections are removed from the co-occurrence graph.
2) Minimum frequency of vertices. Other vertices are

removed with the edges starting from them.
3) Maximum weight of edges. Edges with weight above this value are removed.
4) Minimum number of "useful" words in a context. Context containing fewer nouns and adjectives than this value are not processed.
5) Minimum number of adjacent vertices a hub must have.
6) Maximum mean weight of the connections between a hub and its most frequent k neighbors (where k is the previously mentioned parameter).
7) Minimum frequency of hubs.

The values of these parameters have a large effect on the structure of the generated MST. Parameters 5-7 are especially important for me because these values are used during hub filtering and this step plays a central role in my modifications of HyperLex, which is introduced in the next section.

IV. MODIFIED HYPERLEX ALGORITHM

A critical step of HyperLex algorithm is the hub selection. This is why I tried a couple of modifications with this step. It looked a promising idea to modify the selection order and the restrictions for hubs. Two solutions were examined:
1) Instead of the mean connection weight with *most frequent* neighbors the average edge weight with the *nearest* neighbors has to be under a threshold. With this modification lonely hubs in the MST can be avoided. Lonely hubs can appear if a node is selected as hub but the MST algorithm connects no or very few other nodes to it, as in Fig. 2. This problem can be avoided by the modifications of the free parameters, but it looks to be very difficult to compute parameter values optimal for all target words. With the above mentioned modification it seems easier to avoid the problem because it can be ensured that there are some very near neighbors of the hub, so these edges remain in the graph after the MST transformation.
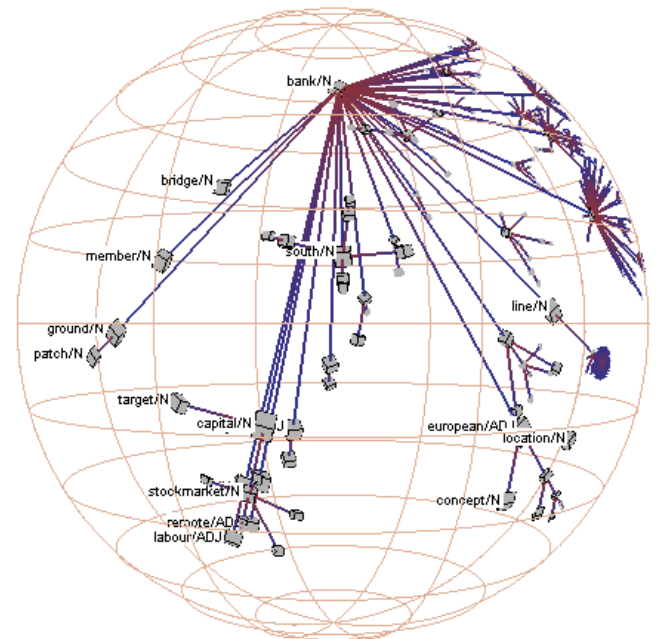

Fig. 2: Lonely hubs in the generated MST of word *bank*. There are more thousand vertices in the graph. However, some hubs (e.g. *bridge*, *member*, or *ground*) were incorrectly selected, because under them there are no or only a few nodes.

2) Another idea is to select those hubs which affect a sense of the target word. For example, choosing the word with the highest *mutual information* with the target word instead of the highest relative frequency looks a promising modification of hub selection. With this method too general words which are very frequent (e.g. *time* or *year*) won't appear as root hubs in the MST, even if the values of the free parameters allowed them to be hubs, as in Fig. 3.
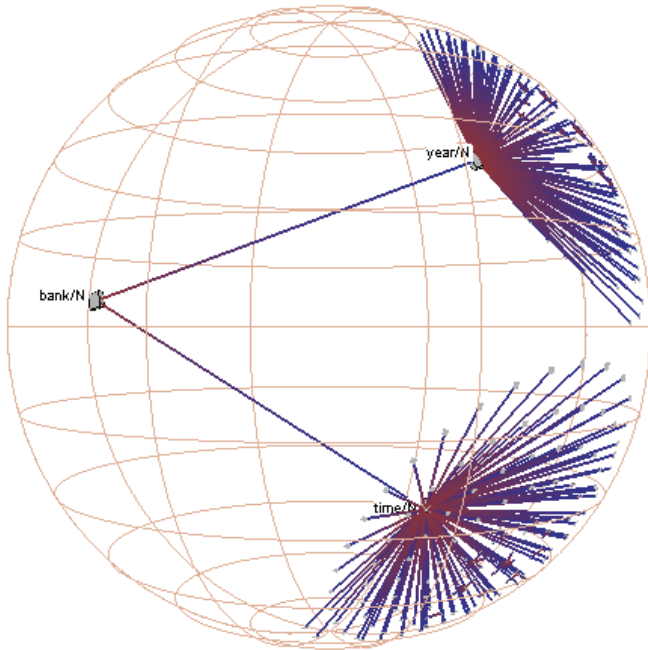

Fig. 3: Incorrectly selected hubs in the generated MST. The words *year* and *time* are very frequent words but they are not relevant for the sense of word *bank*.

These two modifications were tested and evaluated. This is described in section VI.

V. EVALUATING UNSUPERVISED WSD ALGORITHMS

It is more difficult to evaluate unsupervised WSD systems than supervised systems, because no test data can be found which is tagged with the hubs of the calculated MST for every word. So test corpus tagged with dictionary senses should be used. This causes another problem: before evaluation of the unsupervised WSD algorithm the calculated MST components have to be mapped to the dictionary senses of the target word.

So except the *base corpus* (used for creating the MST) a *mapping corpus* and a *testing corpus* are used, like in [3]. Mapping and test corpus should be tagged with senses of the target word. With the help of the mapping corpus word senses can be assigned to the MST components. A *mapping matrix* is calculated at this step. During evaluation hubs are selected for every test example of the test corpus by the disambiguation algorithm, and then these hubs are transformed to senses using the mapping matrix. The results can be compared to the sense tags of the test examples. The evaluation procedure can be seen in Fig. 4.
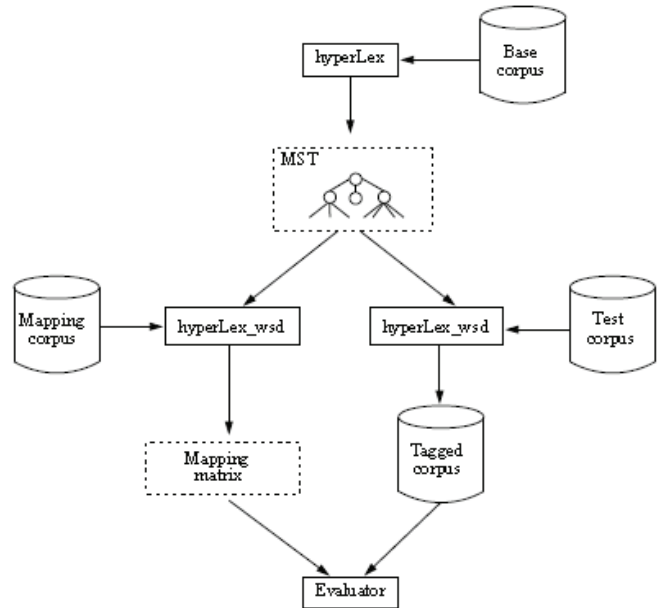

Fig. 4: Potential evaluation procedure for unsupervised word sense disambiguation systems. [3]

VI. MY EXPERIMENTS AND RESULTS

At first I implemented the HyperLex algorithm. After that I applied the two modification ideas described in section IV. I used the *British National Corpus* (BNC) as base corpus.

I measured the performance of the different versions on the nouns of the Senseval-3 English lexical sample task. The training and test examples of Senseval-3 are tagged with WordNet senses. I used the training examples of the Senseval-3 competition as mapping corpus. The mapping was done for each hub in the following way:

1. Those training examples were collected for which HyperLex gave the current hub as result.
2. For each word sense the number examples tagged with this sense were counted.
3. The most frequently used word sense was mapped to the current hub.

The test corpus contained the test examples of the Senseval-3 English lexical sample task. The evaluation happens in the following way: At first, for each test example HyperLex selects a hub. This hub is converted into a WordNet sense using the previously calculated mapping matrix. If the received WordNet sense result and the correct sense are the same, then the algorithm performed well.

The examined nouns are highly polysemous. For example the word *bank* has 10 different senses. There are very slight differences among some dictionary senses of the most words. Because of this the measured precision values are relatively low.

The evaluation of the different versions of the algorithm is in progress. The first obtained results can be seen on *Table 1* and *Table 2*. *Table 1* shows the fine grained, *Table 2* displays the coarse grained measurement results. Both table show precision scores because coverage is 100 percent for each target word. These are only temporary results, because the free parameters of the algorithm are empirical values. Further investigation is required whether these results really stand.

word	train	test	MFS	default	MI	NN
argument	221	111	**51.4**	**51.4.**	**51.4**	**51.4**
arm	266	133	82.0	82.0	82.0	**82.7**
atmosphere	161	81	66.7	**71.6**	**71.6**	70.4
audience	200	100	67.0	70.0	**72.0**	**72.0**
bank	262	132	67.4	**72.7**	**72.7**	**72.7**
degree	256	128	**60.9**	**60.9**	**60.9**	**60.9**
difference	226	114	40.4	41.2	41.2	**42.1**
difficulty	46	23	17.4	26.1	17.4	**34.8**
disc	200	100	38.0	45.0	46.0	**50.0**
image	146	74	36.5	43.2	**47.3**	43.2
interest	185	93	41.9	41.9	44.1	**46.2**
judgment	62	32	28.1	37.5	43.8	**46.9**
organization	112	56	73.2	**75.0**	**75.0**	**75.0**
paper	232	117	25.6	**36.8**	32.5	33.3
party	230	116	62.1	**64.7**	**64.7**	**64.7**
performance	172	87	32.2	42.5	**48.3**	39.1
plan	166	84	**82.1**	**82.1**	**82.1**	**82.1**
shelter	196	98	**44.9**	36.7	**44.9**	**44.9**
sort	190	96	**65.6**	**65.6**	**65.6**	**65.6**
source	64	32	**65.6**	**65.6**	**65.6**	**65.6**
		Average:	54.5	57.3	58.2	**58.3**

Table 1: Precision comparison among the different versions of the algorithm using fine grained evaluation. The second and third columns show the number of training and test examples for each target word. The MFS column corresponds to the most frequent sense. The last three columns show the evaluation results for the different versions of HyperLex: the original algorithm (default), the modification using mutual information (MI) and the modification using nearest neighbors (NN) for selecting hubs.

word	MFS	default	MI	NN
argument	**51.4**	**51.4**	**51.4**	**51.4**
arm	82.0	82.0	82.0	**82.7**
atmosphere	66.7	**71.6**	**71.6**	70.4
audience	93.0	93.0	**98.0**	**98.0**
bank	75.8	**81.1**	80.3	80.3
degree	69.5	69.5	**70.3**	69.5
difference	**62.3**	**62.3**	**62.3**	**62.3**
difficulty	**87.0**	**87.0**	**87.0**	**87.0**
disc	38.0	45.0	46.0	**50.0**
image	36.5	43.2	**47.3**	43.2
interest	44.1	44.1	46.2	**48.4**
judgment	28.1	43.8	43.8	**46.9**
organization	83.9	**85.7**	**85.7**	**85.7**
paper	37.6	**49.6**	44.4	47.0
party	62.1	**64.7**	**64.7**	**64.7**
performance	36.8	56.3	**64.4**	56.3
plan	**82.1**	**82.1**	**82.1**	**82.1**
shelter	**44.9**	36.7	**44.9**	**44.9**
sort	**77.1**	**77.1**	**77.1**	**77.1**
source	**65.6**	**65.6**	**65.6**	**65.6**
Average:	61.5	64.5	**65.6**	**65.6**

Table 2: Precision comparison among the different versions of the algorithm using coarse grained evaluation.

VII. PLANS FOR THE FUTURE

I plan to finish the measurement of the modified HyperLex algorithm in the near future and compare the results with the original algorithm.

After that I would like to continue my research with the extension of word sense representation. I'm going to try to represent the meaning of longer text units, e.g. sentences or paragraphs with graphs. The idea is to merge somehow the co-occurrence graphs of the different words in the analyzed text unit. This will be a completely corpus-driven approach because there is no fixed goal to reach with this attempt. The idea behind this experiment is that analyzing text units with this kind of graph could give us more information about the text unit than the words in it, because the graph can contain words which don't even occur in the analyzed text unit.

REFERENCES

[1] J. Véronis, "HyperLex: lexical cartography for information retrieval," *Computer Speech & Language*, 2004, 18(3), pp. 223-252.

[2] R. Mihalcea, T. Chklovski, and A. Kilgarriff, "The senseval-3 English lexical sample task," in *Senseval-3 proceedings*, 2004, pp. 25-28.

[3] E. Agirre, D. Martinez, O. Lopez de Lacalle, and A. Soroa, "Evaluating and optimizing the parameters of an unsupervised graph-based WSD algorithm," *Workshop on TextGraphs, at HLT-NAACL*, 2006, pp. 89-96.

[4] E. Agirre, D. Martinez, O. Lopez de Lacalle, and A. Soroa, "Two graph-based algorithms for state-of-the-art WSD," in *2006 Proc. EMNLP Conf.*, pp. 585-593.

[5] D. Jurafsky, J. H. Martin, *Speech and Language Processing; An Introduction to Natural Language Processing, Computational Linguistics, and Speech Recognition, Second Edition*, 2007, Chapter 20.

[6] C. Manning and H. Schütze, *Foundations of Statistical Natural Language Processing*, MIT Press. Cambridge, MA: May 1999, pp. 178-183.

[7] D. A. Cruse, *Polysemy: Theoretical and Computational Approaches*, chapter Aspects of the Microstructure of Word Meanings.

[8] D. J. Watts and S. H. Strogatz, "Collective dynamics of 'small-world' networks," *Nature*, June 1998, pp. 440-442.

[9] H. Schütze, "Automatic word sense discrimination," *Computational Linguistics*, 1998, 24(1):97-123.

[10] A. Purandare and T. Pedersen, "Word sense discrimination by clustering contexts in vector and similarity spaces," in *Proc. of CoNLL-2004*.

Direct Voice to Facial Animation Conversion

Gergely Feldhoffer

(Supervisor: Dr. György Takács)

flugi@digitus.itk.ppke.hu

I. INTRODUCTION

In the field of multimodal speech processing, one of the current topics is the conversion of audio speech to visual speech. This topic includes voice to facial animation for deaf and hearing impaired to lip-read, and also conversion for hearing people in animations (cartoons, movie SFX) or video games. These task have different demands. In the prevoius years I did research on conversion for deaf people.

II. THESIS DRAFTS

As a table of contents.

A. Animation

Direct voice to facial animation is capable of that quality which meets the demands of hearing people in animation.

B. Temporal structure

The visual coarticulation preceeds the audial coarticulation in time in normal and slow tempo.

C. Speaker dependency

I show a method to reduce the speaker dependency in direct voice to animation conversion systems. This method is based on iterative dynamic programming.

III. ANIMATION

As of 2008 the animation movie workflow includes the facial animation drawing by human designer and artists. For an example in the Moholy-Nagy University of Art and Design Budapest has a full semester training of facial animation for speech. This work has two parts, the design of the character's articulation properties, and the frame-by-frame animation drawing. In many cases these steps are done with computer aided designer systems, such as 3DStudio, Maya3D or Blender. These systems have possibilities to handle the animation of many vertices by only a few controller. This kind of animation can be described as series of animation controller values. Our voice to animation conversion system is able to learn any kind of audio and video representations if it contains enough information, and keep low degree of freedom. The task is to help the animator at the frame-by-frame drawing, while the artist can keep the control of the character articulation design.

A. Quality issues

The quality of audiovisual speech can be measured objective and subjective ways. The objective measurement can be numerical or recognition test with deaf or hearing impaired people. Numerical test is for example the synthetized animation control parameters compared to database values, using square error of the values. This is not suitable for hearing people's sense of quality since the control parameters have different importance, and the quare error is independent from the temporal structure. If there is very a small (2 pixel) deviation standard noise on one of the control parameters, the synthetized head will flicker which obviously not a human property of articulation, but it gives relatively good numerical result.

Recognition tests with deaf people is an objective measurement. Our system has a 48% recognition rate in animation sequences where the human lip-speaker's recognition rate is 98%. This difference is mainly because of the head model restrictions, the stored animation control parameters, which are used for traning, used as control of the head model gives the recognition rate of 55%. Comparing 55% to 48% would give the quality of the conversion since the database values of the animation control parameter is the best possible result of the trained system, but 55% instead of 98% as maximum value decreases the measurement accuracy. So for hearing people, the quality of the conversion tested by deaf people probably gives inaccurate results.

B. Opinion scores

A subjective measurement method is the opinion score based approach. There is an extensive use of opinion score in audiovisual quality measurements. I made a test, which partly follows the recommandation of ITU P.910, "Subjective Video Quality Assessment Methods for Multimedia Applications".

Opinion scores need to have a scale compared to. There is no widely accepted scale of quality of voice to animation conversion, so I tried to define a quality scale. The top quality is the reproduction of the database values. As the quality decreases, mistakes will occur. I used a heuristic quality decreaser, which distorts the parameter flow into a direction, and smoothed temporaly. The reason of this quality decreaser is that this seems to be natural (measurement needed) speech, if the signal is only this kind of distorsion. Other reason that the mistakes of a voice to animation system used to last an average duration of a phoneme, so the distorsion is smoothed to have this duration also.

The mistake is applied to the main principal components of the visual speech data. With this I can guarantee the naturalness of the result. I used the first N principal components where N is the index of the last symmetric principal component (symmetric in the meaning that change this dimension in the PC vector cause a symmetric change on the model's face)

Also an important issue is the energy dependent distorsion. In the measurement I used distorted videos where the distorsion was applied only when the speech energy was high enough to assume non-silent phase.

The first to do is to validate the scale with opinion scores. I made a test with 20 original videos and 20 distorted videos. The distorted videos were gradually distorted from 1 mistake/s to 20 mistake/s. There are 26 test subjects. The opinion scores are from 1 to 5, 5 is the best.
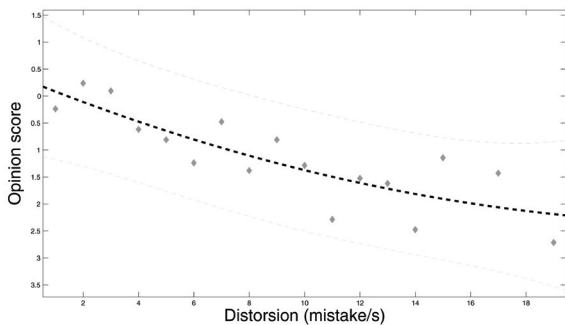

Fig. 1.   Average opinion scores and distorsion.

As it seems on Fig 1. the deviation is high. More measurements needed to validate the method with multiple instances of distortion rates. However the results hold out a promise as the correlation between the distorsion rate and the average opinion scores are relatively high, even while the relation between them is not linear.

TABLE I
ABSOLUTE OPINION SCORE AND DISTORTION CORRELATION

	all subjects	selected subjects
all videos	0.805	0.852
only distorted	0.649	0.788
selected videos	0.862	0.892

I examined the effectiveness of the test subjects. I found that 4 of the 26 subjects can not make difference between the original videos and the most distorted ones. They gave the same average score of original videos and average score of distorted more than 15 mistake/s. The "selected subjects" in Table 1 and Table 2 mean those 22 test subjects who gave at least 0.5 point (on 1-5 scale) more for original videos than the most distorted ones.

Also I found that there are videos which receive much better scores than expected. As I examined these videos it turned out

that the distorsions push the signal frequently towards the right direction. This cause some kind of strange behavior since the values can go out of the valid intervals causing the mouth to shut more than it used to be, or open greater. In the opinion scores these vigorous motions appeared as "better than reality" at some of the test subjects. The "selected videos" mean in Table 1 and Table 2 those videos which have no motion like this.

TABLE II
CORRELATION OF DISTORTION AND OPINION SCORE DIFFERENCE
BETWEEN ORIGINAL AND DISTORTED

	all subjects	selected subjects
all videos	0.635	0.692
selected videos	0.717	0.752

C. Animation Conclusion

More measurement needed to prove that this mistake/s approach is valid for scale of audio to visual conversion quality. The problem seems to concern the deviation of opinion scores, the approach generally is promising. It is also needed to examine the dependency between the distorsion and the opinion scores. On Fig 1. only a polynomial fit is shown, which is just to show that the human perception makes greater difference at low distortions than high distortions.

IV. TEMPORAL STRUCTURE

The synchrony of the audio and video data is checked by word papapa in the beginning and the end of the recording. The first opening of the mouth by this bilabial can be synchronized with the burst in the audio data. This synchronization guaranties that the pairs of audio and video windows were recorded in the same time, which gives an input and an output for a back-propagation neural network.

For the best result the neural network has to be trained on larger temporal scope of audio information. The mutual information between audio and video data was measured for different time shifts. 200 ms delay is advised. This can be explained as the speech process is a predicting mental process which moves the mouth according to not only the actual but the next approximately 200 ms of voice since the facial muscles are slower than the muscles in the tongue.

The PCA representation of the data is not the best choice since mutual information can be estimated most easily between one dimensional data sequences, and PCA vectors are not independent. Still it a good demonstration tool because it represents physically interpretable values as in the audio data the energy or in the video data the motion of the jaw-bone. Figure 2 show how the energy of the voice determine the video information shifted in time. For example the motion of the jaw-bone and the energy 200ms later has around 0.55 bit mutual information.

Better way to determine the global mutual information is to choose a representation where the inter-channel mutual information is minimal. This is the independent component
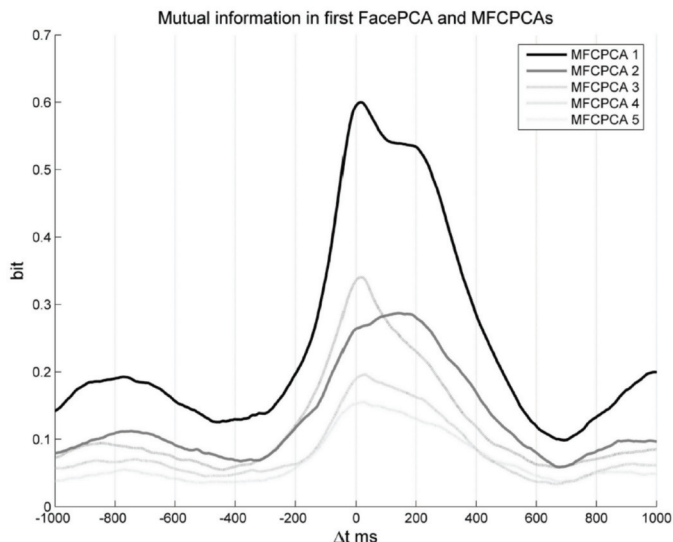
Fig. 2. Sum of the mutual information curves of the principle components the video and the first principle component of the audio. The asymmetry is clearly visible.

analysis (ICA). If both the audio and the video information is coded into ICA components the interchannel mutual information can be treated as zero, so it gain sense to add the mutual information curves. The sum of all audio channel - video channel mutual information can be seen on Fig 3
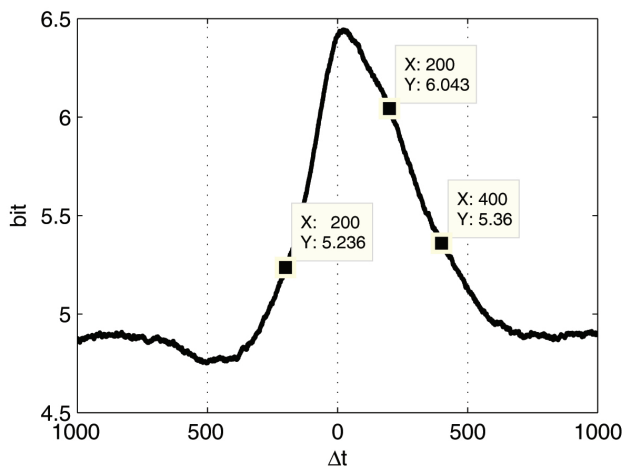

Fig. 3. Sum of the mutual information curves of the independent components. This independent components were taken from the audio and the video information with ICA.

Therefore we are using a 5 element sized queue of audio feature vectors as the input of the neural network, and the corresponding PCA vector from the video data.

A. Theoretical significance of the temporal asymmetry

As the figures show the temporal asymmetry in the multimodal speech is a natural phenomena. To build the best possible VACS the system has to consider this phenomena. A possible solution of this situation is to use a 200 ms delay in

this case, but it needs to be noted that this 200 ms value comes from our special database which was recorded for deaf people with a slower tempo of 4-6 phonem/sec. This coincidence obviously show some deeper connections but we do not know more yet. This topic has emphasized attention in our future work.

V. SPEAKER DEPENDENCY

The described system works on well defined pairs of audio and video data. This is evident if the database is a single person database. If the video data belongs to a different person, the task is to fit the audio and the video data together.

The text of the database was the same for each person. This allows the aligning of audio data between speakers. We used the Dynamic Time Warping technique for this, which is a widely used method in speech recognition on small dictionaries. Usually for speech recognition purposes this is a distance estimation method using cumulative distance sums. We used it to extract the best match of the windows between the two audio data.

This matching is represented by index arrays which tell that speaker A in the i moment says the same as speaker B in the j moment. As long as the audio and video data of the speakers are synchronized, this gives the information of how speaker B holds his mouth when he says the same as speaker A speaks in the moment i.

With this training data we can have only one person's video information which is from a professional lip-speaker and in the same time the voice characteristics can be covered with multiple speakers' voices.

A. Iterative DTW

There are problems with pure DTW because of the limit of the gradient. This allows only twice as fast or twice as slow warped signal on every location. There are situations where this limit is overrun, for example longer or shorter pause in between parts of sentences.

For this problem a possible solution is the iterative application of the DTW based on the MFC data. With this we can avoid the problem of the limited gradient since the second phase can double or halve the speed difference compared to the previous phase so with enough phases every possible gradients can be reached.

B. Subjective validation

The DTW given indices were used to create test videos. For audio signals of speaker A, B and C we created video clips from the FP coordinates of speaker A. The videos of A-A cases were the original frames of the recording, and in the case of B and C the MPEG-4 FP coordinates of speaker A were mapped by DTW on the voice. Since the DTW mapped video clips contains frame doubling which feels erratic, all of the clips was smoothed with a window of the neighboring 1-1 frames. We asked 21 people to tell whether the clips are original recordings or dubbed. They had to give scores, 5 for the original, 1 for the dubbed, 3 in the case of uncertainty.
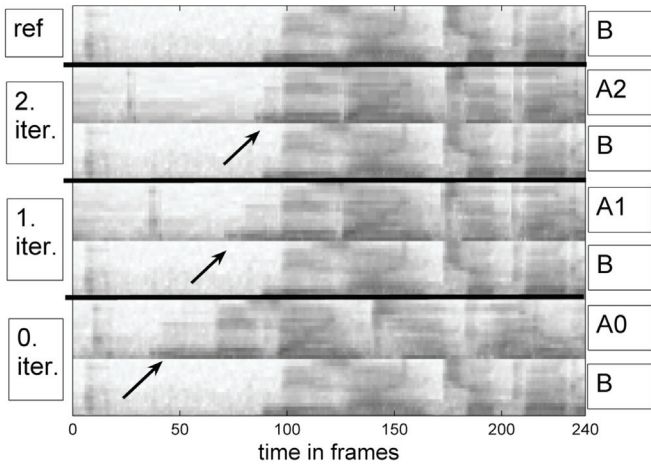
Fig. 4. Iterative DTW work phases. On phase 1 the most of the data is aligned but there are still some problematic areas noted by arrows. This secondary errors can be eliminated by repeated DTW alignments of the previous result.

As it can be seen on Fig. 3. the deviations are overlapping each other, there are better scored modified clips than original. The average score of original videos is 4.2, the modified is 3.2. We treat this as a good result since the average score of the modified videos are above the uncertain score.

C. Objective validation

A measurement of speaker independency is testing the system with data which is not in the training set of the neural network. The unit of the measurement error is in pixel. The reason of this is the video analysis, where the error of the contour detection is about 1 pixel. This is the upper limit of the practical precision.

40 sentences of 5 speakers were used for this experiment. We used the video information of speaker A as output for each speaker, so in the case of speaker B, C, D and E the video information is warped onto the voice. We used speaker E as test reference.

Fig. 5. Training with speaker A, A and B, and so on, and always test by speaker E which is not involved in the training set

First, we tested the original voice and video combination, where the difference of the training was moderate, the average error was 1.5 pixels. When we involved more speakers's data in the training set, the testing error decreased to about 1 pixel, which is our precision limit in the database. See Fig. 5.

VI. CONCLUSION

A speaker independent VACS is presented. Subjective and objective tests confirm the sufficient suitability of the DTW on training data preparing. It is possible to train the system with only voice to broaden the cover of voice characteristics. Most of the calculations are cheap enough to implement the system on mobile devices. The speaker independency induces no plus expense on the client side. The most problematic part is the implementation of the head model. A very basic head model as John still consumes more CPU than it would be affordable on an average open system 2nd generation mobile devices as Nokia Series 60 family for example. However on 3rd generation IP based video communication gives the possibility to implement this application in server-client architecture, which is already accomplished on PC. It is advised using a 2D head model instead, or implementing on 3rd generation client to accept any voice calls.

Speaker independency is an important feature of a VACS, and it is possible to change only the training phase.

REFERENCES

[1] B. Granström, I. Karlsson, K-E Spens *SYNFACE - a project presentation*, Proc of Fonetik 2002, TMH-QPSR, 44: 93-96. 2002.
[2] M. Johansson, M. Blomberg, K. Elenius, L.E.Hoffsten, A. Torberger *Phoneme recognition for the hearing im-paired*, TMH-QPSR. vol 44 Fonetik pp. 109-112, 2002.
[3] E. Sifakis, A. Selle, A. Robinson-Mosher and R. Fedkiw *imulating Speech with a Physics-Based Facial Muscle Model*, ACM SIG-GRAPH/Eurographics Symposium on Computer Animation (SCA), pp. 261-270, 2006.
[4] Gy. Takács , A. Tihanyi, T. Bárdi, G. Feldhoffer, B. Srancsik *Speech to Facial Animation Conversion for Deaf Customers*, Proceedings of EUSIPCO Florence Italy, 2006.
[5] M. Cohen and D. Massaro *Modeling coarticulation in synthetic visual speech*, Computer Animation 93. Springer-Verlag, 1993.
[6] P. Kakumanu and R. Gutierrez-Osuna and A. Esposito and R. Bryll and A. Goshtasby and O. Garcia *Speech Driven Facial Animation*, Proc. of the Workshops on Perceptual/Perceptive User Interfaces (PUI), Orlando, FL, PUI 2001.
[7] P. Kakumanu,A. Esposito, O. N. Garcia, R. Gutierrez-Osuna *A comparison of acoustic coding models for speech-driven facial animation*, Speech Communication 48 pp 598-615, 2006.
[8] P. Scanlon, G. Potamianos, V. Libal, and S. M. Chu *Mutual Information Based Visual Feature Selection for Lipreading*, in Proc. of ICSLP 2004, South Korea, 2004.

The Implementation of Throwing Motion on a 6-DOF Robot Manipulator

Ferenc Lombai

(Supervisors: Dr. Tamás Roska and Dr. Gábor Szederkényi)

lombai.ferenc@itk.ppke.hu

Abstract—**A 6-degree-of-freedom rigid robot arm and its throwing motion generation is described in this paper. The trajectories for the joint variables are generated as a cubic spline obtained using general constrained nonlinear optimization, taking into consideration limitations (position, speed, acceleration and jerk) of the joint actuators, and the current limit of the whole structure. The obtained trajectories are previously checked to avoid collisions using oriented bounding boxes and their separating axis theorem tests. The trajectory tracking of the individual joint is done using a discrete-time constrained optimal control technique.**

I. INTRODUCTION

The capability of throwing was a great step in the human evolution and the reproduction of such a motion is also a great challenge in the field of robotics. Not only the design of a precise and long range capable machine is demanding but targeting a point outside the reachable workspace with an existing, general purpose robot arm as well. Plenty of implementations focused on the topic of throwing but few of them dealt with the implementation on higher degree-of-freedom (DOF) robotic arms.

In this paper we give a possible solution for this motion planning task by the use of general constrained nonlinear optimization as many other practical robotic solutions do [1], [2], [3]. We present a revised implementation of the algorithm [4] for planning time-jerk optimal trajectories on a 6-DOF robot arm. The original method has been greatly reworked to fulfill the needs of the problem. Beyond the modified optimization space and objective function, additional constraints involve the nonlinear optimization related to joint variable limits and to the instantaneous power consumption of the actuating motors.

II. DESCRIPTION OF THE PROBLEM

The most of the motivation behind this work is to generate possible motions and by the results investigate the capabilities of the robot arm. This process can be considered as an optimization process in a high dimensional nonlinear space fragmented by strict nonlinear constraints.

So it is necessary to define the space in which each point characterize one throwing motion, construct the objective function which gives the measure of the quality of a given motion, and build constraint function which measures implementability. Both of these functions can be treated as guidelines during optimization thus it is necessary to produce acceptable solution for any inputs.

If the goal is to aim at a given target position we have to find such a trajectory which crosses the robot's work space and on the cross section we have to find a point that the robot is capable to reach in a valid configuration and able to drive its end effector (EF) according to the first derivative of the parabolic path. We assume that after the release time instant no interaction occurs between the load and the robot. Furthermore the robot have to be able to stop inside the joint position limits with the given maximal acceleration-, jerk- and current consumption restrictions. The robot also has to avoid collision with itself or with other parts of the environment. The motion have to be formulated in such a way that is easy to compute for arbitrary time slice, thus appropriate splines are searched for each actuator that describe the joint motions from an initial zero velocity to another motionless state.

Then the control algorithm have to actuate the robot through the found joint space trajectory. During the last control part, all the disturbances from real word have to be compensated specially, but not limited to the full electric and dynamic behavior of the actuators, the robot dynamics, spring like cable forces and mechanical self oscillations.

III. SYSTEM DESCRIPTION

The robotic arm detailed description can be found in [5]. The whole construction and its model used for collision detection can be seen in figure 1.
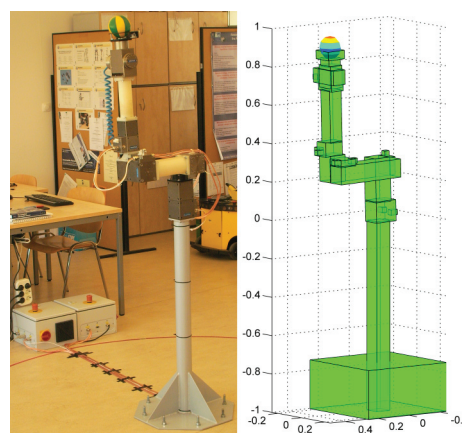

Figure 1. The robot arm and its collision detecting model.

From control point of view, each joint can be actuated and measured as a discrete-time system through one 1 Mbit/sec CAN bus. However, there are no built in functions to produce controlled torque or even acceleration. With the provided C++ dynamic link library (DLL) the discrete-time acceleration commands were generated using the so called ramp velocity profile motion which is a sequence of acceleration, constant speed and deceleration phases. The whole robot is powered by two DC 24V 30A power-supplies.

IV. DESCRIPTION OF THE ALGORITHM

The algorithm works as follows. Given the target position $\mathbf{p}_{tr}$, the robot description (mDH parameters, joint limits ($\mathbf{Pc}_{min}$ and $\mathbf{Pc}_{max}$), velocity limits ($\mathbf{Vc}$), acceleration limits ($\mathbf{Ac}$), maximum allowable jerks ($\mathbf{Jc}$), the maximum output currents of the power supplies $\mathbf{Cc}$), the maximum allowed current consumption of each module $\mathbf{C}_{max}$ and a 4x4 homogeneous transformation $\mathbf{T}_{RF}$ that represents the position and release capable orientation of the load with respect to the EE frame (EEF) in such a way, that the thrown body fall out along the z axis of the resulted coordination system. This coordinate system will be further referenced as the release frame (RF). Then the optimization input is constructed as a vector

$$\mathbf{h} = [\theta, \phi, r, \gamma, \omega, t_f, t_t, t_b],$$

where $[\theta, \phi, r]$ gives the spherical coordinates of the release position in world frame (further referred as $\mathbf{p}_0$), γ and ω defines orientation and angular velocity measured around the z axis of the RF frame at the release time, t_f is the flight time of the thrown object between $\mathbf{p}_0$ and $\mathbf{p}_{tr}$, t_t defines the duration of motion spent to achieve release position and velocity, and t_b is the time needed to decelerate till a static configuration. Further, $\mathbf{h}_{min}$ and $\mathbf{h}_{max}$ bounds the search space which values were manually set to comprehend all possible solutions but to exclude infeasible ones. The optimization can be started from different initial conditions chosen randomly along all dimensions of $\mathbf{h}$ between $\mathbf{h}_{min}$ and $\mathbf{h}_{max}$ using a general constrained nonlinear optimization method such as the `fmincon` function in the Matlab Optimization Toolbox.

The solution for the joint motions is searched in the form of a two-segment cubic spline. Let $\mathbf{Q}_t(t) : \mathbb{R} \rightarrow \mathbb{R}^6$, $\mathbf{Q}_t(t) = \mathbf{a}_t t^3 + \mathbf{b}_t t^2 + \mathbf{c}_t t + \mathbf{d}_t$ denote such a multidimensional cubic polynomial (over the interval $[0, t_t]$) that starts from a moveless state and have the desired position and velocity at time t_t, and similarly $\mathbf{Q}_b(t) : \mathbb{R} \rightarrow \mathbb{R}^6$, $\mathbf{Q}_b(t) = \mathbf{a}_b t^3 + \mathbf{b}_b t^2 + \mathbf{c}_b t + \mathbf{d}_b$ defined on the interval $[t_t + t_b, t_b]$ that gives the same position and first two derivatives as $\mathbf{Q}_t$ at time t_t and zero velocity at time $t_t + t_b$. If we further assume that the throwing velocity must be the maximum velocity during the motion both of the polynomial's second derivative have to be zero at t_t.

Based on $\mathbf{p}_{tr}$, $\mathbf{p}_0$ and t_f the initial velocity vector for the body is searched as follows::

$$\mathbf{v}_0 = \frac{\mathbf{g}}{2} t_f + \frac{\mathbf{p}_{tr} - \mathbf{p}_0}{t_f},$$

where $\mathbf{g}$ is the gravity vector. Using $\mathbf{p}_0$, the orientation information of $\mathbf{v}_0$ and $\mathbf{T}_{RF}^{-1}$, we can compute the position vector of joint angles ($\mathbf{q}_t$) according to the inverse kinematics

relationship. For the given kinematic structure eight different solution is symbolically given, thus for each valid $\mathbf{q}_t$ there is a $\dot{\mathbf{q}}_t$ that can be assigned using the inverse jacobian of the robot. To compute $\dot{\mathbf{q}}_t$ most of the previously given values have to be considered, namely $\mathbf{q}_t$, $\mathbf{p}_0$, $\mathbf{v}_0$, $\mathbf{T}_{RF}^{-1}$ and ω. If multiple solutions exist the pair of $[\mathbf{q}_t, \dot{\mathbf{q}}_t]$ that consumes less current can be chosen using the current consumption model described later. Then the two cubic polynomials can be found by solving the following system of equations:

$$
\begin{aligned}
\mathbf{Q}_t(t_t) &= \mathbf{q}_t = \mathbf{Q}_b(t_t), \\
\dot{\mathbf{Q}}_t(t_t) &= \dot{\mathbf{q}}_t = \dot{\mathbf{Q}}_b(t_t), \\
\dot{\mathbf{Q}}_t(0) &= \mathbf{0} = \dot{\mathbf{Q}}_b(t_t + t_b), \\
\ddot{\mathbf{Q}}_t(t_t) &= \mathbf{0} = \ddot{\mathbf{Q}}_b(t_t).,
\end{aligned}
$$

and the solution is given by

$$
\begin{array}{ll}
\mathbf{a}_t = -\dfrac{\dot{\mathbf{q}}_t}{3 t_t^2}, & \mathbf{a}_b = -\dfrac{\dot{\mathbf{q}}_t}{3 t_b^2} \\[2ex]
\mathbf{b}_t = \dfrac{\dot{\mathbf{q}}_t}{t_t}, & \mathbf{b}_b = \dfrac{\dot{\mathbf{q}}_t t_t}{t_b^2} \\[2ex]
\mathbf{c}_t = \mathbf{0}, & \mathbf{c}_b = \dot{\mathbf{q}}_t - \dfrac{\dot{\mathbf{q}}_t t_t^2}{t_b^2} \\[2ex]
\mathbf{d}_t = \mathbf{q}_t - \dot{\mathbf{q}}_t \dfrac{2 t_t}{3}, & \mathbf{d}_b = \mathbf{q}_t + \dot{\mathbf{q}}_t (-t_t + \dfrac{t_t^3}{3 t_b^2}).
\end{array}
$$

The collision avoidance is solved using a model which covers the rigid volume of the arm with oriented bounding boxes (see fig. 1). The base and each link contains 3-5 boxes whose position and orientation updated through forward kinematics. None of these boxes allowed to have any overlapping and this property is checked by separating axis theorem tests [6]. This process only takes place in a trial end error manner with zero tolerance restriction on a fine set of equally spaced time instances through the optimized motion.

A. Objective function

The objective function computes the weighted sum of terms that describe the behavior of the throwing motion, namely

$$J(\mathbf{h}) = k_V |\mathbf{v}_0| + k_F t_f + k_T t_t + k_B t_b + k_O \omega^2 \qquad (1)$$

where k_V, k_F, k_T, k_B, and k_O are weighting parameters and their sign indicates the minimization or maximization of the corresponding quantity. It is possible that for a particular value of h the result can not be computed because no configuration is capable to reach the given release position and orientation. In this case a high predefined value is returned. Unfortunately this solution degrading optimization performance with the loss of continuity in the output. The term $k_V |\mathbf{v}_0|$ is built in the objective function to guide releas position to the direction of the target position. t_f is given as optimization parameter to force upward initial velocity to avoid spilling of the object before t_t, that is necessary if the robot is not equipped with active gripping mechanism. Parameters k_T and k_B help to achieve slowly accelerating but fast decelerating motion to fulfill the assumption that the robot loses contact with the thrown object after t_t.

B. Constraint function

To find only implementable solutions all the given constraints have to be fulfilled, namely

$$
\begin{align}
q_j(t) &\leq Pc_{j\,max}, \quad j = 1, \ldots, N \tag{2} \\
q_j(t) &\geq Pc_{j\,min}, \quad j = 1, \ldots, N \tag{3} \\
|\dot{q}_j(t)| &\leq Vc_j, \quad j = 1, \ldots, N \tag{4} \\
|\ddot{q}_j(t)| &\leq Ac_j, \quad j = 1, \ldots, N \tag{5} \\
|\dddot{q}_j(t)| &\leq Jc_j, \quad j = 1, \ldots, N, \tag{6}
\end{align}
$$

where N is the number of actuators, $Pc_{j\,min}$ and $Pc_{j\,max}$ indicates minimum and maximum joint positions, furthermore Vc_j, Ac_j and Jc_j are given velocity, acceleration and jerk bounds, respectively for each joint j. Other necessary but more difficult constraints are applied, regarding the power consumption of the robot arm, namely

$$
\max_{t \in [0, t_t + t_b]} I_j(t) \leq C_{max\,j}, \quad j = 1, \ldots, N \tag{7}
$$

$$
\max_{t \in [0, t_t + t_b]} \sum_{j \in \mathbf{list}_k} I_j(t) \leq Cc_k, \quad k = 1, 2, \tag{8}
$$

where $\mathbf{list}_k$ lists the index of motors connected to the kth power supply, and $I_j(t)$ is the current consumed by the jth motor at time t, more precisely

$$
I_j(t) = I_{gap_j} + K_{Bj} |\dot{q}_j(t)| + K_{Mj} \tau_j(\mathbf{q}(t), \dot{\mathbf{q}}(t), \ddot{\mathbf{q}}(t)), \tag{9}
$$

where I_{gap_j} represents maximal current that still not moves the unloaded motor j, K_{Mj} is the slope of the linear correspondence between armature current and output torque for the jth motor and $\tau_j(\mathbf{q}(t), \dot{\mathbf{q}}(t), \ddot{\mathbf{q}}(t))$ is the computed torque acting on joint j in the actual robot state, regarding desired position, velocity and acceleration of the joints.

For the current consumption limits we used the simplifying assumption that motor dynamics is dominant over load torques, which means that currents mainly depend on motor velocities. Thus only $\tau(\mathbf{Q}_t(t_t), \dot{\mathbf{Q}}_t(t_t), \mathbf{0})$ have to be computed to determine the $I_j(t_t)$'s.

C. Initial conditions and parameters

In every iterative methods, specially in gradient based methods the initial condition has a great role both in the overall running time and the convergence properties. Thus some kind of exploration was used to store information from those optimizations that did not yield valid solution. Every time the constraint function is called if there exists the inverse kinematic solution, the computed output is checked whether it is completely different subsets of the $6N + 2$ constraints defined in (2)-(8) and the input is stored in a database according to which of the inequalities are fulfilled. Next time the optimization is started the initial condition can be set near one from the found partially most valid solutions. Practically the most complete solution is preferred, and this iteration is done till the optimization finds optimal solution.

V. THE CONTROLLER

Based on the facts that the actuating motors have enough power and they have built-in PID controllers, a decentralized control scheme was used based on the individual trajectory tracking control of the joints. Let us denote the position and velocity of joint i by $z_{1,i}$ and $z_{2,i}$, respectively. Furthermore, let us assume that the manipulable input variable is the joint acceleration command (v_i). If we denote the reference for $z_{1,i}$ and $z_{2,i}$ by $z_{1ref,i}$ and $z_{2ref,i}$, respectively, then the tracking error system can be written as

$$
\begin{align}
\dot{e}_{1,i} &= e_{2,i} \\
\dot{e}_{2,i} &= u_i \tag{10}
\end{align}
$$

where $e_{1,i} = z_{1,i} - z_{1ref,i}$, $e_{2,i} = z_{2,i} - z_{2ref,i}$ and $u_i = v_i - \dot{z}_{2ref,i}$. Thus, by the asymptotic stabilization of the dynamics (10) the asymptotic tracking of the reference trajectory is assured.

The known physical constraints for the acceleration inputs v_i must be satisfied during operation. The minimum-maximum values for v in the case of the different joints can be given in the following vector form

$$
v_{min/max} = -/ + [10.4\ 10.4\ 10.4\ 10.4\ 16.6\ 22.3]\,rad/sec^2 \tag{11}
$$

Denote the minimum and maximum acceleration values of the designed joint trajectories by a_{min} and a_{max}, respectively. From this, it is clear that the physical constraints (11) will be fulfilled, if the following inequalities hold for the transformed input v in (10):

$$
v_{min,i} - a_{min,i} \leq u_i \leq v_{max,i} - a_{max,i}, \text{ for } i = 1, \ldots, 6 \tag{12}
$$

A possible and easily computable discrete-time solution for this problem is the *constrained linear control technique* (see, e.g. [7], [8]) that considers the following discrete time LTI system class:

$$
\begin{align}
x(k+1) &= Ax(k) + Bu(k) \\
y(k) &= Cx(k) + Du(k) \tag{13}
\end{align}
$$

where $x(k) \in \mathbb{R}^n$ is the state vector, $u(k) \in \mathbb{R}$ and $y(k) \in \mathbb{R}$ are the input and output respectively. A, B, C and D are real matrices of appropriate dimensions.

The so-called Constrained Finite Time Optimal Control Problem is using matrices $H \in \mathbb{R}^{l \times n}$ and $K \in \mathbb{R}^l$ to define a prescribed polytopic region of the state space inside which the state variables have to evolve subject to the constraints

$$
\begin{align}
u_{min} &\leq u(k) \leq u_{max} \\
y_{min} &\leq y(k) \leq y_{max} \tag{14} \\
Hx(k) &\leq K.
\end{align}
$$

The result of this controller design problem is a polytopic decomposition of the appropriate part of the state space, with a feedback structure of the form

$$
u(k) = F_j x(k) + G_j \tag{15}
$$

where j is the number of the polytopic region of the state space into which the actual measured state vector belongs.

For the numerical solution of the constrained linear optimal control problem, the Multi-Parametric Toolbox (MPT) [9] of

the Matlab computational environment had been used. The controller constructed for the discretized version of the error dynamics (10) of the individual joints and implemented in a sequential manner using time stamping for all incoming and outgoing data.

VI. Simulation and measurement results

A. Optimization results

In figure 2, valid and optimized trajectories can be seen for $\mathbf{P}_{tr} = [0.8, 0.8, -1]$ m. On the bottom of the figure, the computed overall current consumption is drawn. The dashed lines show the current consumption for the two power supplies. The optimization was done with parameter values $k_O = 1$, $k_T = -10$, $k_B = 20$, $k_F = -10$, and $k_V = 0.1$, furthermore the search space was limited by

$$\mathbf{h}_{min} = [-\frac{\pi}{2}, -\frac{\pi}{2.5}, 0.6, -\pi, -\frac{\pi}{2}, 0.2, 0.2, 0.1]$$
$$\mathbf{h}_{max} = [\frac{\pi}{2}, \frac{\pi}{2}, 0.95, \pi, \frac{\pi}{2}, 2.0, 2.0, 1.0],$$

and the optimized output was

$$\mathbf{h} = [0.238, 0.341, 0.808, -0.958, -0.563, 0.561, 0.547, 0.431].$$
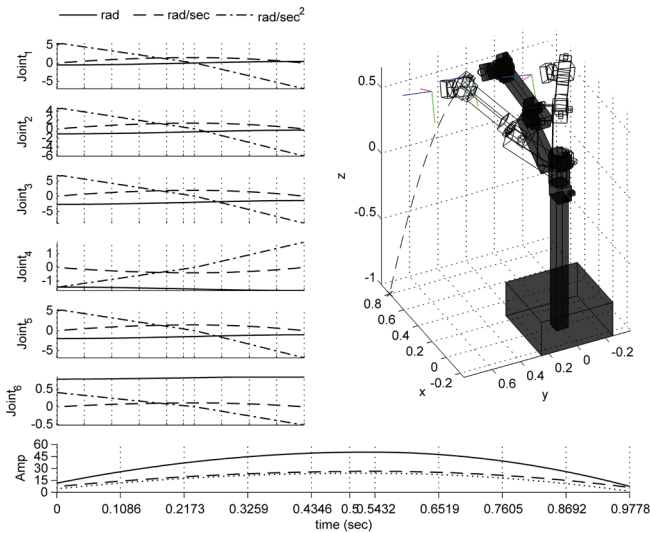

Figure 2. Optimized trajectory within maximum current constraints.

During the development of the algorithm it turned out, that even for a short range throwing motion the DC motors consume a lot of current due to the high joint velocities at release time. It also became clear, that more over current limits, the joint position limitations and the collision avoidance restriction badly reduce the set of feasible solutions and necessitate the collection of partially feasible solutions.

B. The implemented motion

The robot arm was driven through the optimized throwing trajectory to check tracking error and overall current consumption in practice. Figure 3 shows position (line) and velocity (dashed line) tracking errors for each joint. The time scale and time lags can be shown on the bottom of the picture.

The measured current consumption is plotted on the upper axis. It can be seen, that there is a small varying difference between measured and model-computed currents that is due to the unmodeled effects like the frictional terms and mechanical resonances.
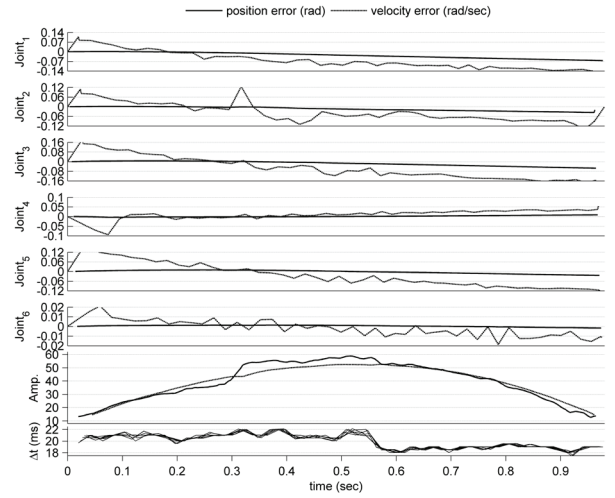

Figure 3. Reference tracking measurements

VII. CONCLUSIONS AND FUTURE WORKS

The throwing motion generation and implementation on a 6-DOF rigid robot arm was shown in this paper. The trajectory tracking of the joints is performed using a discrete-time linear controller. Later on the whole control should be adopted to a real-time computation environment and a gripper with tactile sensors should extend the capabilities of the system. The proposed linear approximation gave usable results, even in the presence of unpredictable time lags but additional work on the actuation model is needed.

REFERENCES

[1] S.M. LaValle. *Planning Algorithms*. Cambridge University Press, 2006.
[2] J. E. Bobrow. Optimal robot plant planning using the minimum-time criterion. *IEEE Journal of [see also IEEE Transactions on Robotics and Automation] Robotics and Automation*, 4(4):443–450, August 1988.
[3] L. C. T. Wang and C. C. Chen. A combined optimization method for solving the inverse kinematicsproblems of mechanical manipulators. *IEEE Transactions on Robotics and Automation*, 7(4):489–499, August 1991.
[4] A. Gasparetto and V. Zanotto. A technique for time-jerk optimal planning of robot trajectories. *Robotics and Computer-Integrated Manufacturing*, in press:doi:10.1016/j.rcim.2007.04.001, 2007.
[5] F. Lombai and G. Szederkényi. Trajectory tracking control of a 6-degree-of-freedom robot arm using nonlinear optimization. In *The 10th International Workshop on Advanced Motion Control – AMC'08*, pages 655–660, 2008.
[6] S. Gottschalk, M. C. Lin, and D. Manocha. OBBTree: A hierarchical structure for rapid interference detection. *Computer Graphics*, 30(Annual Conference Series):171–180, 1996.
[7] A. Bemporad, F. Borrelli, and M. Morari. Explicit solution of LP-based model predictive control. In *Proc. 39th IEEE Conf. on Decision and Control, Sydney, Australia*, pages 823–828, 2000.
[8] A. Bemporad, M. Morari, V. Dua, and E.N. Pistikopulous. The explicit linear quadratic regulator for constrained systems. *Automatica*, 38:3–20, 2002.
[9] M. Kvasnica, P Grieder, M. Baotic, and F.J. Christophersen. *Multi-Parametric Toolbox (MPT)*. Automatic Control Laboratory, Swiss Federal Institute of Technology, Zurich, 2006.

GPU powered CNN simulator (SIMCNN) with graphical flow based programmability [18]

József Veres (Supervisors: Tamás Roska, György Cserey and Gábor Szederkényi)

verjo@digitus.itk.ppke.hu

Abstract— In this paper, we introduce an innovative CNN algorithm development environment that significantly assists algorithmic design. The introduced graphical user interface uses Matlab Simulink with UMF-like program description, where direct functionality accompanies better accessability. The new generation of graphical cards incorporate many general purpose Graphics Processing Units, giving the power of parallel computing to a simple PC environment cheaply. Therefore, analysis of CNN dynamics become more feasible with a common hardware setup. Our measurements demonstrate the efficiency of the realized system. In the case of simpler algorithms, real-time execution is also possible.

I. INTRODUCTION

CNN-UM has numerous analogue and digital hardware implementations [8], [9], [10], [11], [12], [13], [14] that are ideal tools for processing two dimensional topological flows (especially for visual ones). They have specific development environment for programming; however, a high-level UMF (Universal Machine on Flows) model and the dependent UMF charts exist for describing these algorithms.

We developed a simulator system for running these graphically represented algorithms directly. More precisely, one can draw UMF-like diagrams with simple drag&drop technique and test them before optimizing them to a specific hardware. We are using SIMULINK from the MathWorks Inc. because it is able to simulate almost any dynamic system constructed from simple blocks. A block-set had been created containing necessary high level blocks for the CNN-UM structure including simple access for the one-layer, linear type subset of the template library. Using SIMULINK's built-in solver, it is ideal for educational purposes. If we exchange the most computational expensive part, namely if we are running the CNN dynamics on a faster external hardware or software component, we get a powerful development environment that combines the advantages of UMF modelling with affordable simulation speed. The most common hardware accelerators for a desktop PC are the multi-cored CPUs and the Graphical Processing Units (GPUs). We have chosen the GPU for our purpose. As we know another group is also working on GPU acceleration of the template running. [17]

II. GPU AS A HARDWARE ACCELERATOR

A. CPU vs. GPU comparison

By the end of 2007, more than a billion transistors [4] could be found on a single digital chip. This means a huge opportunity for creating not only single but dual, quad or many cores on a single die. But this way of getting more
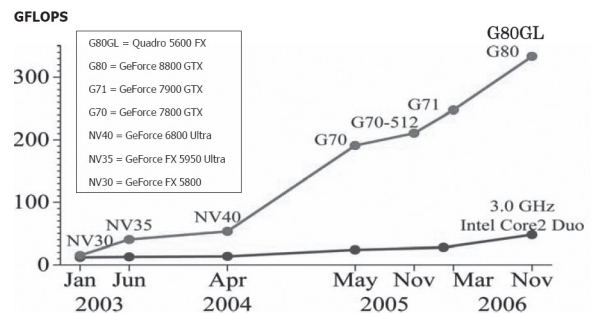

Fig. 1. Comparison in giga floating point operations per second between the last few years' computational capabilities of CPUs and GPUs, where we can realize a huge increase in the PC's video card areas. [5]

and more computational power for a desktop PC influenced not the Central but the Graphics Processing Units first. This could be proved by the fact that at this time anybody can buy a GPU with 128 processors, but only dual or quad cores are common on nowadays CPU's market. In Fig. 1. the rise of the two typical processor types can be followed.

The diagram shows actually a more than five times greater computational capability in desktop GPUs that we can achieve compared to nowadays' worldwide used personal computer's CPU. This is the result of the multiple cores driven by a higher memory bandwidth. Furthermore, the main significant difference is the transistor count that is dedicated to the data processing elements. The high percentage of the transistors in CPUs is responsible for the flow control and for the caching.

If we are not only analysing the desktop models from the CPU side, there are many competitors that could come up. One could be the well known Cell processor from the STI alliance (Sony, Toshiba and IBM). This is a very powerful digital processor but for some applications, the most advanced NVIDIA card, GF8800GTX overperforms it. While the Cell Broadband Engine Architecture with 8 Synergistic Processing Elements (SPE) clocked at 3.2Ghz is capable of 208.4 Gflops [6], the 8800GTX with 128 stream processors clocked at 1.35Ghz reaches roughly 520 Gflops [7] for nearly the same price.

So we can state that today's GPUs with their high level of parallelism are cost-efficient processors for performing the CNN simulator's power resource extensive task, namely the template running.

B. CUDA: NVIDIA's newest architecture

In order to realize a non-graphic operation like template running, on the graphics card there must be a software and hardware solution to access the high computational power of the GPU. This need is fulfilled by NVIDIA's newest development, the Compute Unified Device Architecture (CUDA). This is a totally new approach where we can build our code in C-like language without any knowledge about graphical programming like DirectX or OpenGL. Fortunately, it is not only available on the high-end category but also on the whole NVIDIA's 8 series cards. This means that it could get very common soon, and anybody will be able to benefit from its advantages for a low price. Before the technical implementation, we highlight the major hardware parts of the GPUs architecture.
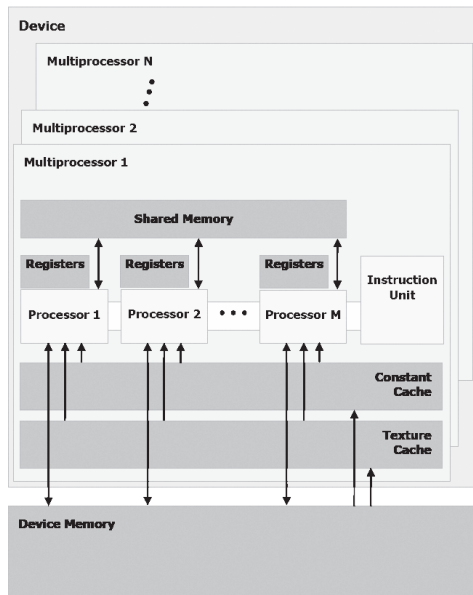

Fig. 2. Hardware model of the GeForce 8 series cards. There are no separate vertex and pixel shaders. It is a new unified hardware architecture where we can find multiprocessors (MPs) that have a shared memory and a few scalar-based processors. [5]

In Fig. 2. we can see the hardware model of this architecture. We can realize that there are no pixel and vertex shaders we were used to on the previous series of the video cards. Instead of that, unified, scalar-based processors were introduced. Eight of these processors are grouped with an Instruction Unit to form a single-instruction-multiple-data (SIMD) multiprocessor (MP). The number of MPs are varying from 1 to 16, which means 8 to 128 parallel processors. Global memories are much faster than those we are using in our main boards, but these would be slow for supplying the data for all processors. Therefore we have three ways for caching. A 16 KB per MP high-speed universal purpose shared memory is available beside the constant and texture caching memory.

III. SIMCNN AND ITS GRAPHICAL FLOW BASED PROGRAMMABILITY

A. The software framework

The simulator is based on SIMULINK from The Math-Works Inc. It is a worldwide used software that has support nearly for any operating systems. Graphical flow based programmability has many advantages compared to the standard imperative command based ways. The perspicuity of the algorithm is much higher because there are just a few well declared blocks we have to work with. In the SIMCNN blockset, we defined necessary extensions for accessing the video card and to run templates on it (Fig. 3). SIMULINK has built in blocks for realizing specific data flow structures, like parallel or conditional execution and signal routing. Once an image is uploaded to the device, we can refer to it using a real value as ID-like pointer in C. For the first execution time, the code is only initializing using the surrounding block's IDs to determine its real dimensions. After the initialization phase, template running will be performed. SIMULINK calls event handler functions of each block one by one in a good serialized order. Our blocks are implemented using the s-function interface of SIMULINK to produce interface for the CUDA based binaries. We also created a small user interface for browsing the linear one-layered subset of the template library. The user can also have custom templates.

B. UMF description

UMF stands for Universal Machines on Flows [2]. The UMF library [3] contains the basic image processing algorithms and numerous powerful ones like the CenterPointDetector or the GlobalConnectivityDetection. This library can give idea for developers for creating their own programs.

CNN template running and special flow control marks are the basic operations of the UMF.

1) With the additional blocks: The "Elementary instruction" is the basic template that is implemented by the block that can be seen on Fig. 3. The parameters can be set using the user interface. Template values can be supplied by external matrices also. "Parametric templates" can be realized this way. Some of the possible "Operators" like the Global White or Black is also implemented with the blocks named GBW and GBB respectively.

2) With the built-in blocks: For creating the data path, basic SIMULINK knowledge is needed. Fortunately MATLAB help is quite detailed and has good tutorials for learning. The video processing blockset gives the ability to handle two dimensional input and output data like images and video streams. For implementing "variables" built in Memory blocks can be used. To realize "Triggers" Unit Delay Enabled blocks can be applied. We can specify the starting value. The input flow is blocked if the condition is not satisfied. Complex flow sequences like conditional loops can be joined together using conditions that can be realized using "multiplexer" blocks. We can create "subsystems" using built-in mechanism to align algorithmic parts. "Enabled subsystems" combined with If or Switch blocks can be used for branching.
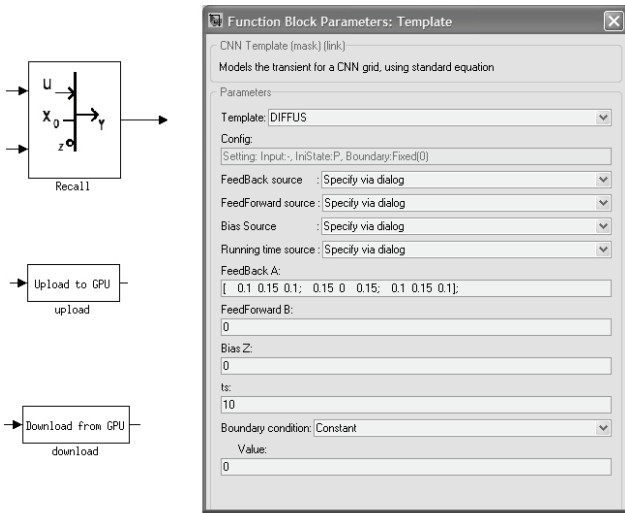
Fig. 3. In this figure, the blocks for communication with the GPU and template running are presented. They are implemented using C language S-functions. Using a mask (Simulink GUI) for the template runner block, the user can load an item from the template library or specify a custom operation.

IV. EXPERIMENTAL RESULTS

For our test results, we used an NVIDIA GeForce 8800 GT GPU connected via PCI Express 16x to an Intel Xeon 3.4 GHz CPU. Our applications ran atop Linux with NVIDIA driver version 169.07 (64bit) and CUDA Tool kit 1.1. The used MATLAB version was 2007b and SIMULINK was 7.0.

First we have made experiments with a 512x512 sized image. The simulation included an image loading from hard-drive, uploading to GPU, a template operation on GPU, a downloading from GPU and a frame rate estimation. SIMULINK's built-in profiler has about 10 ms resolution, so for fast running blocks it is quite unreliable, but the total time measurement can be used as reference. If we have a large iteration number for template running, the average iteration time can be estimated more precisely. Furthermore, we found in our specific case that it converges to a given value. This number is the execution time of one iteration which equals to 0.242 ms. This would allow us to do 4132 iterations per second (IPS), but the influence of the additional blocks give an overhead. We recorded the update speed measured in frames per second (FPS) for this mini-algorithm with the Frame Rate Display block in the function of iteration numbers. (Fig. 4.) It is an overall speed indicator that also includes the overhead. For comparison, we depicted the theoretical speed limit deduced from the estimated pure template running time. This overhead is about 20 ms and could be reduced if the result is not downloaded to the host computer but displayed using direct rendering on the video card.

We can compare this results to other simulators. For educational purposes, one of the most common tools is CANDY from Analogic Computers Inc. It also offers an algorithmic framework with template iteration time of 21 ms for an 512x512 sized image running on a 1.8 Ghz Pentium 4 computer. Considering this, a slightly more than 80x speed-up was reached. A comprehensive comparison can be found
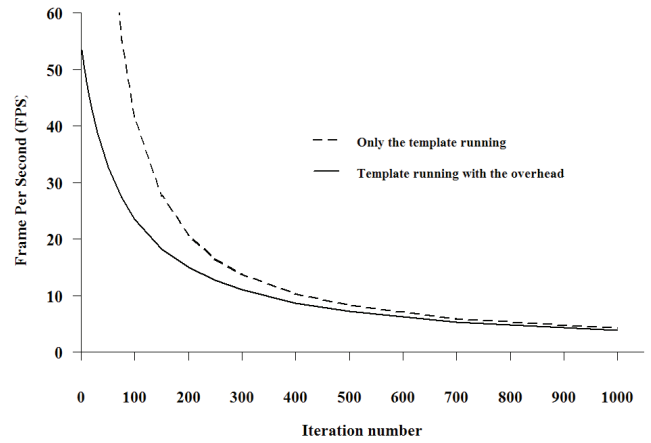

Fig. 4. Execution speed in FPS of a single template running for N iteration is displayed - measured value influenced by all necessary interface blocks with strait line and theoretical maximum without any overhead with stripped.

in [15] for the actual CNN simulators and emulators. We extended the measured data with our results. (Table I.) The first two columns show results from Intel Core Duo and Quad respectively using Intel Performance Library [16]. The next one is the Cell Broadband Engine. It's clear that the Cell is the best but integration into our desktop system is not yet supported. We have also placed an FPGA implementation in the last column. We can state that our solution is five times faster then the cutting-edge PC's CPU.

TABLE I
COMPARISON OF TEST RESULTS WITH OTHER IMPLEMENTATIONS

	T7200	Q6800	CELL	**8800GT**	Candy	XC3S5000
Frequency (MHz)	2000	2933	3200	**1350**	1800	150
# of Processors	2	4	8	**120**	1	34
M cell iteration	48	100	3627	**524**	12	1700
Power (W)	34	130	86	**160**	60	10

If our system is powered by a 8800GT to realize a real-time algorithm with 25 fps, we can include different templates consuming 80 iterations. For demonstration purposes, we show a feature extractor algorithm running on a video flow on Fig 5. It takes 50 iterations altogether allowing us to display the intermediate results as well. The input is a noisy and slightly off-focused video flow captured via a microscope. The goal is to distinguish between the elongated worms and the other blood components. First, we create two thresholded maps with different bias values. The first contains most of the worms with additional disturbance. The second one is more aggressively thresholded containing less information about the worms, but noise is also strongly suppressed. Than we apply the Small
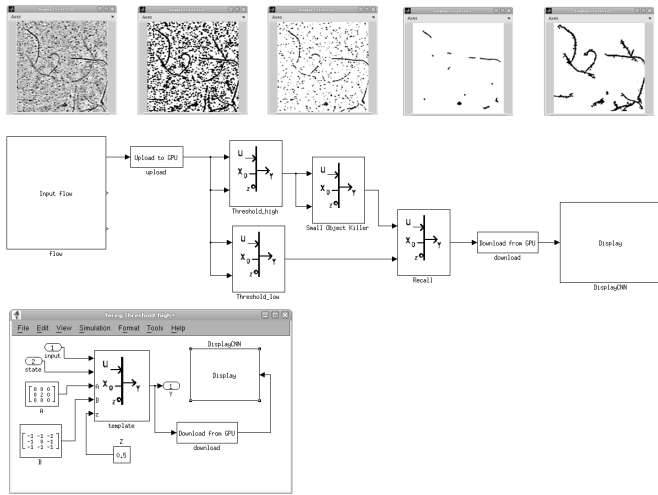
Fig. 5. This figure shows a screenshot of the SIMCNN framework. It contains the UMF diagram-like flow chart of a simple algorithm that can be run video real-time. The upper left display shows the input image and is followed by the two thresholded intermediates, the one after running the Small Object Killer and finally the reconstructed one that is the result of the algorithm. In the middle, the uploading and the downloading blocks are placed, all blocks among them representing templates running on the GPU. Finally, in the bottom, the template block subsystem is displayed.

Object Killer template to remove most of the noisy pixels. Finally ,this mask will be used with the other thresholded one to recall the deleted worm parts.

V. CONCLUSION

We have presented an algorithmic development framework for designing and testing CNN algorithms using UMF diagram-like notations. SIMULINK gives an environment for handling various data streams and to create complex flow structures to build algorithms. With the additional blocks for accessing GPU and running templates on it, we can get an efficient CNN simulator for an affordable price. We have introduced our design consideration for optimal mapping between the CNN and the GPU architecture, resulting in a competitive speed that is five time faster than the cutting-edge CPU implementation using high-level optimization. To apply for this **SIMCNN software package** visit [19].

REFERENCES

[1] Roska, T.; Chua, L.O., "The CNN universal machine: an analogic array computer," Circuits and Systems II: Analog and Digital Signal Processing, IEEE Transactions on [see also Circuits and Systems II: Express Briefs, IEEE Transactions on] , vol.40, no.3, pp.163-173, Mar 1993

[2] Roska, T., "Computational and computer complexity of analogic cellular wave computers," Cellular Neural Networks and Their Applications, 2002. (CNNA 2002). Proceedings of the 2002 7th IEEE International Workshop on ,vol., no., pp. 323-338, 22-24 Jul 2002

[3] T. Roska, L. Kék, L. Nemes, A. Zarándy, M. Brendel, and P. Szolgay, "CNN software library (templates and algorithms), version 7.2.," Tech. Rep. DNS-CADET-15, Analogical and Neural Computing Laboratory, Computer and Automation Research Institute, Hungarian Academy of Sciences (MTA SzTAKI), 1998.

[4] "World's First 2-Billion Transistor Microprocessor - Tukwila", Intel Corporation, http:/www.intel.com/technology/ architecture-silicon/2billion.htm?iid=homepage+ news_itanium_platform; accessed February 24, 2008

[5] "NVIDIA CUDA Programming Guide 1.1", NVIDIA Corporation, http://developer.download.nvidia.com/compute/ cuda/1_1/NVIDIA_CUDA_Programming_Guide_1.1.pdf; accessed February 24, 2008

[6] H. Peter Hofstee, IBM Corporation, "Introduction to the Cell Broadband Engine" http://www.nvidia.com/attach/941771?type= support&primitive=0; accessed February 24, 2008

[7] Technical Brief: "NVIDIA GeForce 8800 GPU Architecture Overview" Santa Clara, California,November 2006. http://www.nvidia.com/ attach/941771?type=support&primitive=0; accessed February 24, 2008

[8] P. Dudek and P. Hicks, "A general-purpose processor-per-pixel analog simd vision chip," IEEE Transactions on Circuits and Systems - I: Analog and Digital Signal Processing, vol. 520, no. 1, pp. 13-20, 2005.

[9] P. Foldesy, A. Zarandy, C. Rekeczky, and T. Roska, "Digital implementation of cellular sensor-computers," International Journal of Circuit Theory and Applications, vol. 34, no. 4, pp. 409-428, 2006.

[10] A. Zarandy, P. Foldesy, P. Szolgay, S. Tokes, C. Rekeczky, and T. Roska, "Various implementations of topographic, sensory, cellular wave computers," in Proceedings of the IEEE International Symposium on Circuits and Systems, ISCAS 2005, (Kobe, Japan), pp. 5802-5805, May 2005.

[11] G. Linan, S. Espejo, R. Dominguez-Castro, and Rodriguez-Vazquez, "ACE4k: an analog I/O 64 x 64 visual microprocessor chip with 7-bit analog accuracy," International Journal of Circuit Theory and Applications, vol. 30, no. 2-3, pp. 89-116, 2002.

[12] A. Rodriguez-Vazquez, G. Linan-Cembrano, L. Carranza, E. Roca-Moreno, R. Carmona-Galan, F. Jimenez-Garrido, R. Dominguez-Castro, and S. Meana, "ACE16k: the third generation of mixed-signal SIMD-CNN ACE chips toward VSoCs," IEEE Transactions on Circuits and Systems Part I: Regular Papers, vol. 51, no. 5, pp. 851-863, 2004.

[13] R. Galan, F. Garrido, R. Castro, S. Meana, and A. Vazquez, "CACE1K User's Guide, A Complex Analog and Logic Computing Engine with 1024 Processing Cells," Inst. de Microel. de Sevilla CNM CSIC, Jan, vol. 23, 2002.

[14] A. Zarandy and C. Rekeczky, "Bi-i: a standalone ultra high speed cellular vision system," IEEE Circuits and Systems Magazine, vol. 5, no. 2, pp. 36-45,2005.

[15] Z. Nagy, "Implementation of emulated digital CNN-UM architecture on programale logic devices and its applications," PhD Thesis, Department of Image Processing and Neurocomputing University of Pannonia Veszprém, Hungary ,2007.

[16] Intel Performance Libraries Homepage, http://www.intel.com/ software/products/perflib; accessed February 24, 2008

[17] A. Fernandez, R. San Martin, E.Farguell and G.Egidio Pazienza, "Cellular Neural Networks Implementation on a Parallel Graphics Processor Unit," Proceedings of the 11th International Workshop on Cellular Neural Networks and their Applications, 2008

[18] S. Gergely Balazs, V. Jozsef, R. Adam and Gy. Cserey, "GPU powered CNN simulator (SIMCNN) with graphical flow based programmability," in Proceedings of 11th International Workshop on Cellular Neural Networks and their Applications, CNNA 2008 (Santiago de Compostela, Spain) July 2008; accepted

[19] Our SIMCNN software package, http://robotlab.itk.ppke. hu/simcnn; accessed February 24, 2008

3D Modular CNN Architecture using Chua's Circuits

Ákos Tar

(Supervisors: Tamás Roska, György Cserey and Gábor Szederkényi)
tarak@digitus.itk.ppke.hu

Abstract— **This paper introduces the design and architecture of an easy to use hardware platform that is able to connect different type of oscillators in a 3D Cellular Nonlinear Network (CNN) like topology using four neighbor connectivity. We made an effort to ensure maximal flexibility in the design of the topologies and the joining of the elements. Topologies are not strictly bound. The architecture allows the possibility to disconnect the coupling between cells thereby providing the flexibility to explore several architectures of interconnected oscillators. We also present a standalone robust Chua's chaotic circuit kit which is used as a cell for the CNN grid. The first aim was to study synchronization phenomena in oscillatory and chaotic networks along with several test cases of connecting Chua's circuit in different topologies are provided.**

I. INTRODUCTION

Synchronization of oscillator systems is an extensively studied research field [1], [2], [3], [4]. One reason could be the potential usage in many engineering areas such as electronics, communication [5], or information processing. Another reason can be attributed to the fact that it is very prevalent phenomenon in nature [6]. Chaos theory and control of chaotic systems is seen as an emerging field in the research community. Chaotic systems are well known for strange patterns in their phase space, which has always attracted attention of the research community [7], [8]. More interesting behavior can be observed when (two or more) chaotic systems are connected together in different topology [9], [10], [11].

In this paper, we present a new hardware architecture that is able to connect any kind of oscillators in different kind of topology, coupled by any two ports passive component. The core architecture is based on a 6 neighborhood CNN connection with each cell being an autonomous system coupled to neighbors by a passive coupling. In the presented experiments chaotic oscillator as the cell of the structure and resistive coupling were used. This system could be utilised for hardware simulations in oscillatory networks in two ways: either by using general or custom connection topology. We hope many simulation results can be proved by using our hardware and experimental results will inspire new research.

This paper is aimed at studying synchronization phenomena in coupled systems and have developed a hardware test bed which can have oscillators easily plugged into. Note that the paper is aimed at understanding the coupling phenomenon of chaotic and oscillatory networks in real time.

This paper is divided as follows: Section II and Section III discusses the design of a robust plug and play Chua's

circuit that can be used as a cell of the CNN structure. The core architecture of 3D-CNN is discussed in Section IV which explains the general architecture as well as how we intend to use Chua's circuit as one of the cells of this system. Section V shows the experimental results obtained by using the proposed hardware architecture.

II. CHUA'S CHAOTIC CIRCUIT

As a CNN cell we used a simple electronic circuit developed by Leon Chua [12], [13]. The reason for this is in the easy experimental implementation and the highly robust quality of the circuit. Since it only consists of four linear elements (two grounded capacitors, one grounded inductor and one linear resistor), and one non-linear resistor it makes the electronic realization very simple. The system is described by the following set of differential equations:

$$C_1 \frac{dv_1}{dt} = G(v_2 - v_1) - f(v_1) \tag{1}$$

$$C_2 \frac{dv_2}{dt} = G(v_1 - v_2) + i_3 \tag{2}$$

$$L \frac{di_3}{dt} = -v_2 \tag{3}$$

Where v_1, v_2 and i_3 denote the voltage across capacitor C_1, voltage across C_2, and current across inductor L.

$$i_R = f(v_R) = G_b v_R + 0.5(G_a - G_b) \\ \cdot (|v_R + B_p| - |v_R - B_p|) \tag{4}$$

4 denotes to the voltage current characteristic of a non-linear resistor, also called as *Chua's diode*. Here G_a and G_b are the slopes of the segments, and B_p denotes the breakpoint as shown in Fig. 1.
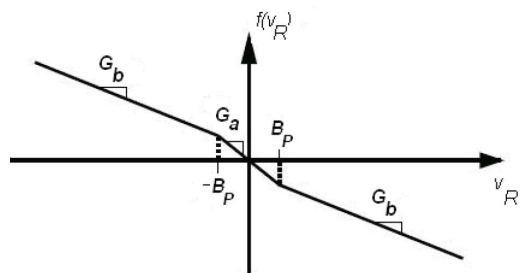

Fig. 1. Current vs. voltage characteristics of the Chua's Diode

By substituting

$$x = \frac{v_1}{B_p}, y = \frac{v_2}{B_p}, z = i_3\left(\frac{R}{B_p}\right) \qquad (5)$$

$$\alpha = \frac{C_2}{C_1}, \beta = \frac{R^2 C_2}{L}, k = sgn(RC_2) \qquad (6)$$

$$a = RG_a, b = RG_b, \tau = \frac{t}{|RC_2|} \qquad (7)$$

$$G_k = \frac{1}{R_k} \qquad (8)$$

the equations in dimensionless form can be written as

$$\frac{dx}{d\tau} = k\alpha(y - x - f(x)) \qquad (9)$$

$$\frac{dy}{d\tau} = k(x - y + z) \qquad (10)$$

$$\frac{dz}{d\tau} = -k\beta y \qquad (11)$$

$$f(x) = bx + 0.5(a - b) \cdot (|x + 1| - |x - 1|) \qquad (12)$$

Here $sgn(x)$ is a standard sign function [14]. Parameter k, that equals 1 or -1, specifies the direction of *Chua's circuit* dynamics.

These equations are the so called *Chua's equations*. They have been used in many simulations [15] and electronic implementation have been also proven [16].

III. Chuas's Circuit implementation

As a realization of the Chua's chaotic circuit we built a compact, easy to use kit. This kit also can help amateurs in building Chua's circuit in a few minutes and can observe chaotic behavior on their personal computer through the sound card' line-in port.
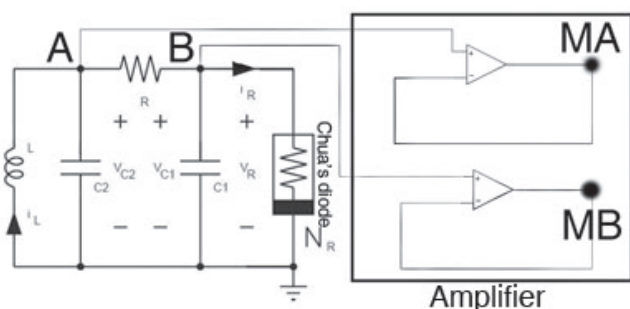

Fig. 2. Schematic of the used Chua's circuit and a simple signal amplifier. The circuit provides four outputs. The two nodes of the capacitors is named A and B, and the corresponding buffered signals are named MA and MB.

The kit provides four different outputs: A, B, MA, and MB. A and B donate the two non-grounded nodes of the capacitors, while MA, MB are the corresponding buffered signals. The programmable logic board (discussed later) selects one of the four possible outputs that can be used as the node for connecting the Chua's circuit as a cell of the CNN

structure.

The circuit schematic diagram can be seen on Fig. 2 and a snapshot of the real kit on Fig. 3.
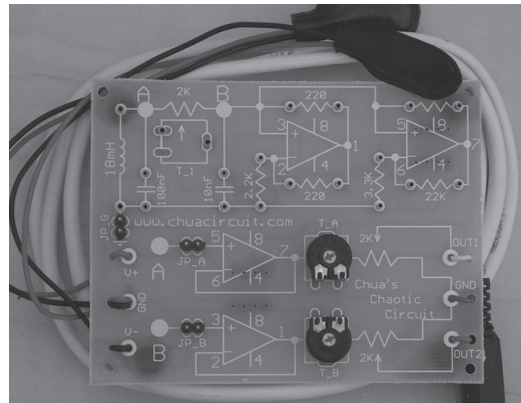

Fig. 3. Snapshot of the designed kit board without the passive component placed. The kit runs on two 9V battery. It can be connected to the sound card' line-in port. By using a software oscilloscope the kit phase portrait can be observed on the screen.

IV. Hardware Architecture

The designed architecture is aimed for experimental purposes, so we made an effort to ensure maximal flexibility in the design of the topologies and in the joining of the elements. Topologies are not strictly bound, in a given $n \times n \times n$ 3D matrix, the elements can be coupled to each other by the rule of six neighborhood (i.e. North, South, East and West, Up, Down). The hardware architecture contains 3 electronic sections that can be separately well defined:

- Interconnecting Interface

- Programmable Logic

- Coupling Grid

A programmable logic along with a coupling grid constitute a single layer of autonomous CNN. Each coupling grid can manage the coupling of 4x4 cells and also the coupling through the next layer. Allowed to a cell to have maximum six neighbors connection. By connecting more layer together 4x4xn architecture can be realized. The architecture allows the possibility to disconnect the coupling between cells, thereby providing the flexibility to explore several architectures of interconnected chaotic Chua's circuits. The design can be treated as a six neighborhood anisotropic CNN with autonomous cells. The currently designed system supports a $4 \times 4 \times n$ size 3D matrix. We have used variable resistors in our experiments as the coupling between the neighboring cells. Note that since it is a generalized architecture, the hardware is prepared to plug in easily any capacitive or inductive or their combinations or any two-port passive components.

V. Experimental results

A number of experiments with different architectural topologies were performed and several interesting phenomena were observed. In the first experiment we only connected two Chua's circuit together with one coupling resistor. Both of them were in double scroll. By modifying the coupling resistor from $10K\Omega$ to 0Ω the system moved from de-synchronization to synchronization. The two stages can be observed in Fig. 4.
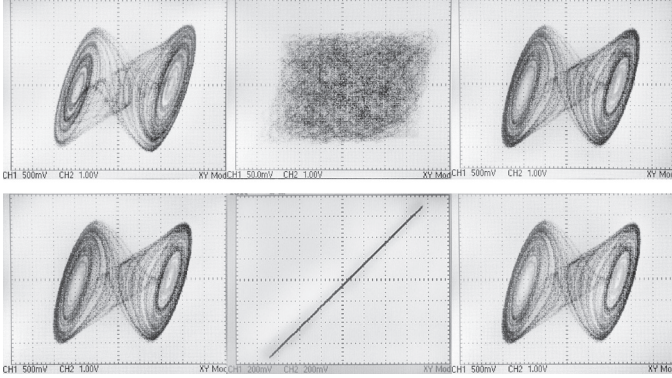

Fig. 4. Two connected Chua's circuits can be seen here. On the top the coupling value is $10K\Omega$, meaning not synchronized, on the bottom at 0 Ω and the system is synchronized. On the figure left and right oscilloscope trace shows the two circuits state (A vs. B channel). In the middle their correlation can be observed.

An interesting observation was also made. As we decreased the coupling value and the system moves from de-synchronization to synchronization, it was found that, there is a specific coupling value where the two oscillators synchronize and they are in phase lag with each other. During this time neither of the chaotic circuits showed chaotic behavior. The oscilloscope' tracing of such phenomenon is shown on Fig. 5. At a lower coupling value they de-synchronized again and did not show this phenomenon until 0 Ω where they showed linear correlation.
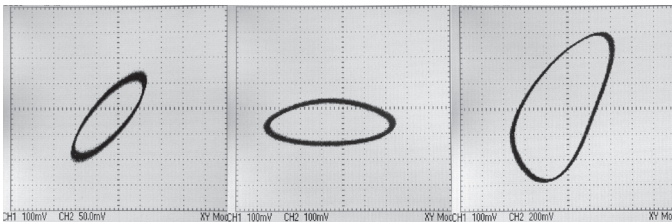

Fig. 5. Two connected Chua's circuits can be seen here. The left and right oscilloscopes show the states of the Chua's circuits, in the middle the coupling behavior can be observed. There is a value of coupling coefficient where the two Chua's circuits are in phase lag with each other. During this time neither of the chaotic circuits remains chaotic.

A. Common point connection

This experiment was further extended by using more Chua's circuits. Due to the connection flexibility of the designed hardware architecture we could make a connection type where every new added Chua's circuits connected to a common point by its coupling weight. The system contains as many coupling values as connected circuits. The connection topology can be seen in Fig. 6 / A.
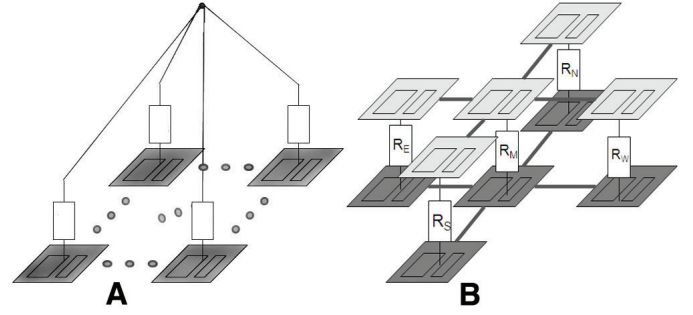

Fig. 6. On this figure during in the experiment used connection topologis can be bee seen. On the left each Chua's circuit is connected to a virtual point through it's coupling weight. On the right ten circuits are connected in a plus form creating 3D architecture. On each layer the coupling resistors were 0 Ω. And only the coupling values between layers were set.

Each circuit was in double scroll showing chaotic oscillation and were connected by the A terminal. We decreased all of the coupling values together from $10K\Omega$ to 0Ω. During the tests while increasing the number of connected Chua's circuits up to 9 in every case we could observe the same phenomena. The coupling values for the test cases are shown in Table I.

TABLE I
DIFFERENT NUMBER OF CHUA'S CIRCUITS ARE CONNECTED TOGETHER. EACH CIRCUIT WAS IN DOUBLE SCROLL SHOWING CHAOTIC OSCILLATION. THEY WERE CONNECTED BY THE A TERMINALS TO A VIRTUAL POINT EACH THROUGH IT' COUPLING WEIGHT. THE RANGE OF THE COUPLING VALUES CAN BE SEEN HERE WHERE WE OBSERVED THE SIMILAR PHENOMENA.

Chua Circuts are connected								
Num. of Chua Circuits	2	3	4	5	6	7	8	9
Initial value $(K\Omega)$	3	2.6	2.5	2.7	3.2	3.3	2.7	2.7
Final value $(K\Omega)$	2.5	1.2	1.5	1.6	1.6	1.6	1.5	1.7

Taking the mean of the values it could be pointed out that this phenomena can be observed around $2.7K\Omega$ coupling value to around $1.5K\Omega$ so it is in a range of around $1K\Omega$. One of the reasons for the different values could be due to difference of each Chua's circuits. While one circuit is at a specific bifurcation potmater value is on the edge of the double scroll than the other is more stable. In the first case the circuits much more likely synchronize to other cells then in the second case. As a result we can conclude that the system in every case around $3K\Omega$ down to $2K\Omega$ showed similar phenomena. In this test case we modified all the coupling values together. In the next step we modified them separately to observe how each coupling value effects the others.

By connecting two circuits together and applied the coupling at $3K\Omega$ the similar phenomena appeared and then we added one more Chua's circuit to the system with a $10K\Omega$ weighting. The whole system moved back to chaotic

oscillation. By decreasing the coupling of the third (just con-nected) circuit at around $2.6K\Omega$ the system showed the similar phenomena. It means that the third oscillator is synchronized to the other oscillators only at a specific coupling value.

For the same 3 circuits connected we set the first and second weights to 3.8-3.8$K\Omega$ and the last at $0.9K\Omega$. The mean weighting is around $3K\Omega$ and the system showed a similar behavior. Proving that the whole system coupling weights matters not just the independents cells weights.
To confirm this theory we tested it on different numbers of connected Chua's circuit and we can conclude that:

The appearance of this phenomena in this current topology proves that the independent cell coupling weights are not important as the determining factor is the mean of the used coupling values. This phenomena can be observed in the mean coupling values of $3K\Omega$ and $2K\Omega$ in range. The correct values could depend on the bifurcation potmeter value used.

B. 3D connection

Due to the limited number of Chua's circuits available to us the number of possible connections of connecting them in 3D were restricted. We decided to connect them in a cross formation. Each layer contained five-five circuits so the middle cells had 5 while the side cells had 2 neighboring connections. The connection topology can be seen in Fig. 6/ B.

All of the Chua's circuits were in double scroll showing chaotic oscillation.

On each layer we set the coupling resistance to 0Ω so on a layer level they were synchronized. We only modified the coupling between layers moving from $10K\Omega$ to 0Ω. In this case we could also observe the similar phenomena that we found in the previous experiments. It started at $7.2K\Omega$ and at $4.2K\Omega$ the system turned back to chaotic oscillation. The oscilloscope trace of the middle cells and the in correlation phase portrait were very similar as illustrated in Fig. 5.

VI. CONCLUSION

In this paper, we present a new hardware implemented system that is able to connect different kind of oscillators in a 3D Cellular Nonlinear Network (CNN) like topology using six neighbor connectivity. We used Chua's chaotic circuit as the cell element of the CNN structure. Several architectures of resistively coupled CNN were studied and laboratory re-sults were found to yield several interesting phenomena. By connecting two Chua's circuits together we found that at a specific coupling value the entire chaotic system loses its chaotic behavior and comes in phase lag with each other. This experiment was further extended by connecting more Chua's circuits in different topologies coupled by resistors and the same phenomena was observed in each case. The explanation of this kind of phenomena could be the aim of an other paper. We hope that in the future this hardware can be a useful tool to study different kind of phenomena in oscillatory and chaotic networks.

REFERENCES

[1] L. Pecora and T. Carroll, "Synchronization in chaotic systems," *Physical Review Letters*, vol. 64, no. 8, pp. 821–824, 1990.
[2] L. Pecora and T. Carroll, "Driving systems with chaotic signals," *Physical Review A*, vol. 44, no. 4, pp. 2374–2383, 1991.
[3] G. Chen and X. Dong, *From Chaos to Order: Methodologies, Perspectives, and Applications*. World Scientific, 1998.
[4] T. OHIRO, Y. SETOU, Y. NISHIO, and A. USHIDA, "Circuit Real-ization of a Coupled Chaotic Circuits Network and Irregular Pattern Switching Phenomenon," *IEICE TRANSACTIONS on Fundamentals of Electronics, Communications and Computer Sciences*, vol. 81, no. 9, pp. 1785–1790, 1998.
[5] G. VanWiggeren and R. Roy, "Communication with Chaotic Lasers," *Science*, vol. 279, no. 5354, pp. 1198–1200, 1998.
[6] M. Barahona and L. M. Pecora, "Synchronization in small-world sys-tems," *Phys. Rev. Lett.*, vol. 89, p. 054101, Jul 2002.
[7] L. Chen and K. Aihara, "Strange attractors in chaotic neural networks," *Circuits and Systems I: Fundamental Theory and Applications, IEEE Transactions on [see also Circuits and Systems I: Regular Papers, IEEE Transactions on]*, vol. 47, pp. 1455–1468, Oct. 2000.
[8] E. Bilotta, P. Pantano, and F. Stranges, "A gallery of chua attractors: Part II," *International Journal of Bifurcation and Chaos*, vol. 17, pp. 293–380, Feb. 2007.
[9] T. L. Carroll and L. M. Pecora, "Synchronizing chaotic circuits," *IEEE Transactions on Circuits and Systems*, vol. 38, pp. 453–456, Apr. 1991.
[10] A. Dabrowski, W. Dabrowski, and M. Ogorzalek, "Dynamic phenomena in chain interconnections of Chua's circuits," *Circuits and Systems I: Fundamental Theory and Applications, IEEE Transactions on [see also Circuits and Systems I: Regular Papers, IEEE Transactions on]*, vol. 40, no. 11, pp. 868–871, 1993.
[11] D. Hillier, S. Gunel, J. Suykens, and J. Vandewalle, "Partial synchro-nization in oscillator arrays with asymmetric coupling," *International Journal of Bifurcation and Chaos*, vol. 17, no. 11, pp. 4177–4185, 2007.
[12] L. Chua, M. Komuro, and T. Matsumoto, "The double scroll family," *Circuits and Systems, IEEE Transactions on*, vol. 33, no. 11, pp. 1072–1118, 1986.
[13] K. Murali, M. Lakshmanan, and L. Chua, "The simplest dissipative nonautonomous chaotic circuit," *Circuits and Systems I: Fundamental Theory and Applications, IEEE Transactions on [see also Circuits and Systems I: Regular Papers, IEEE Transactions on]*, vol. 41, no. 6, pp. 462–463, 1994.
[14] S. Wolfram, *A new kind of science*. Champaign, Ilinois, US, United States: Wolfram Media Inc., 2002.
[15] T. Matsumoto, "A chaotic attractor from chua's circuit," *IEEE Transac-tions on Circuits and Systems*, vol. 31, no. 12, pp. 1055–1058, 2000.
[16] M. P. Kennedy, "Robust OP amp realization of chua's circuit," *Frequenz*, vol. 46, pp. 66–80, 1992.

Self-Similar Property of Brain Electrical Activities in Different Types of Human Epilepsy

Béla Weiss

(Supervisors: Dr. Tamás Roska, Dr. György Karmos and Dr. Zsuzsanna Vágó)

weiss@itk.ppke.hu

Abstract—**Self-similarity of brain electrical activities in different types of human epilepsy has been analyzed by estimation of the Hurst exponent. Long-term intracranial electroencephalogram (*IEEG*) recordings of twenty-four patients suffering from different types of epilepsy have been evaluated. It has been found that the Hurst exponent (*H*) changes drastically during the seizures regardless of the type of epilepsy. In preictal states epilepsy type dependent gradual changes of *H* have been detected.**

Index Terms—**Electroencephalogram, epileptic seizure, Hurst exponent, R/S statistics, self-similarity.**

I. INTRODUCTION

Epilepsy affects 1% of the world's population hereby it is the second most common neurological disorder after stroke. Two-thirds of patients can be cured sufficiently by oral drug administration. Additionally, 25% of drug resistant patients (i.e. 8% of all) can benefit from resective surgery. For the remaining 25%, no sufficient treatment is currently available. The quality of life of these patients could be improved by new diagnostic and therapeutic approaches based on the detection and prediction of epileptic seizures. In the last twenty years different measures have been tested for detection and prediction of seizures. Nevertheless, sufficient algorithms considering sensitivity and specificity measures are not developed yet [1].

Self-similarity of brain electrical activities at different levels has been revealed in animals and humans [2]-[5]. The aim of this study was to compare the self-similar property of long-term *IEEGs* in different types of epilepsy, to analyze whether this measure could be used to develop seizure detection and prediction algorithms.

II. DATA AND METHODS

A. Database

Drug resistant patients suffering from focal epilepsy can be proposed for a resection surgery. In the presurgical monitoring procedure video and scalp *EEG* recordings should be sometimes supplemented by invasive *IEEG* with higher signal to noise ratio for precise localization of the seizure generating foci. Such long-term *IEEG* recordings were provided by the following four institutes: Epilepsy Center, University Hospital Freiburg, Germany (*FEC*); Department of Epileptology, University of Bonn, Germany (*BEC*), National Institute of Neurosurgery, Budapest, Hungary (*NIN*); National Institute of Psychiatry and Neurology, Budapest, Hungary (*NIPN*).

Database from *FEC* [6] contained 21 patients. Recordings were acquired by depth, grid, and strip electrodes at f_s=256 Hz sampling rate. Each recording contained *IEEG* of 6 contacts (3 focal, 3 extra-focal). Separate seizure recordings containing at least 50 minutes of preictal period, and 24 hour long continuous (in some cases concatenated from more than one segment) periods without seizures were available for all patients. To assess continuous data containing seizures as well we used recordings from *BEC*, *NIN*, and *NIPN*. Recording from *BEC* contained 10 clinical seizures of a patient suffering from temporal lobe epilepsy (*TLE)*. The 5d 17h 41m long data were sampled at f_s=200 Hz using depth (two 1x10) and strip (four 1x4, and two 1x6) electrodes. *NIN* provided a 22h 33m long recording that contained four seizures from a patient suffering from frontal lobe epilepsy (*FLE)*. These data were recorded by grid (right frontal convexity, 6x8 contacts; interhemispherial double sided with 2x2x5 contacts) and strip (two interhemispherial, 1x8 contacts; one cortical above the right central and parietal convexities with 1x8 contacts) electrodes at f_s=500 Hz. The 2d 19h 51m long recording from *NIPN* contained 3 seizures of a patient suffering from *TLE*. The sampling rate was f_s=256 Hz. Only signals recorded by bilateral depth foramen ovale (*FO*) electrodes with four contacts were analyzed.

Additional information about the database can be found in Table I.

B. Methods

The stochastic process *X(t)* with continuous parameter *t* is self-similar with the self-similarity parameter *H* if the distribution of the rescaled process $c^{-H}X(ct)$ is the same as the distribution of *X(t)*, where *c>0* is arbitrary. *H* is called the Hurst parameter or the Hurst exponent. Increments *Y(t)=X(t)-X(t-1)* of the self-similar process *X(t)* are stationary. In case of discrete time processes one would get the increment sequence *Y(i)=X(i)-X(i-1), (i=1,2,3, …)*. The *ρ(k)* autocorrelation function of the process *Y(i)* is equivalent to $H(2H-1)k^{2H-2}$ when $k \rightarrow \infty$. Thus, if *H*=0.5, observations of the *Y(i)* process are uncorrelated. When 0<*H*<0.5, an increase in the process is more probably followed by a decrease and vice-versa, the

41

Patient	Institute	Sex	Age	Electrodes	Origin	Lobe	Seizure type	Seizures analyzed	Ictal drop of H	Preictal changes of H
1	FEC	F	15	g, s	nc	FR	SP, CP	4	3	4 ↑
2	FEC	M	38	d	h	T	SP, CP, GTC	3	3	1 ↑, 2 ↓
3	FEC	M	14	g, s	nc	FR	SP, CP	5	5	4 ↑, 1 ↓
4	FEC	F	26	d, g, s	h	T	SP, CP, GTC	5	5	3 ↑, 2 ↓
5	FEC	M	16	g, s	nc	FR	SP, CP, GTC	5	5	2 ↑, 3 x
6	FEC	F	31	d, g, s	h	TO	CP, GTC	3	3	3 ↓
7	FEC	F	42	d	h	T	SP, CP, GTC	3	3	2 ↓, 1 x
8	FEC	F	32	g, s	nc	FR	SP, CP	2	2	2 ↑
9	FEC	M	44	g, s	nc	TO	CP, GTC	5	5	2 ↑, 3 ↓
10	FEC	M	47	d	h	T	SP, CP, GTC	5	5	3 ↓, 2 x
11	FEC	F	10	g, s	nc	P	SP, CP, GTC	4	4	4 ↑
12	FEC	F	42	d, g, s	h	T	SP, CP, GTC	4	4	1 ↑, 1 ↓, 2 x
13	FEC	F	22	d, s	h	TO	SP, CP, GTC	2	2	2 ↓
14	FEC	F	47	d, s	h/nc	FT	CP, GTC	4	4	4 ↑
15	FEC	M	31	d, s	h/nc	T	SP, CP, GTC	4	4	3 ↑, 1 ↓
16	FEC	F	50	d, g, s	h	T	SP, CP, GTC	5	5	5 ↓
17	FEC	M	28	g, s	nc	T	SP, CP, GTC	5	5	5 ↑
18	FEC	F	25	g, s	nc	FR	SP, CP	5	4	4 ↑, 1 x
19	FEC	F	28	g	nc	FR	SP, CP, GTC	4	4	2 ↑, 2 ↓
20	FEC	M	33	d, g, s	nc	TP	SP, CP, GTC	5	5	3 ↑, 2 ↓
21	FEC	M	13	g, s	nc	T	SP, CP	5	4	3 ↑, 2 x
22	BEC	M	19	s	h	T	SP, CP	10	10	2 ↑, 8 ↓
23	NIN	F	34	g, s	nc	FR	SP, CP, GTC	4	4	4 ↑
24	NIPN	F	36	FO	h	T	SP, CP	3	3	3 ↓

FEC = Epilepsy Center, University Hospital Freiburg; BEC = Department of Epileptology, University of Bonn; NIN = National Institute of Neurosurgery, Budapest; NIPN = National Institute of Psychiatry and Neurology, Budapest; M = male, F = female, T = temporal, FR = frontal, P = parietal, TP = temporo/parietal, TO = temporo/occipital, FT = fronto/temporal, d = depth, g = grid, s = strip, FO = foramen ovale, h = hippocampal, nc = neocortical, SP = simple partial, CP = complex partial, GTC = generalized tonic clonic, ↑ = preictal increase of H, ↓ = preictal decrease of H, x = visually no observable changes of H in the preictal state.

process has short-range dependence. When $1 > H > 0.5$, an increase in the process is more probably followed by an increase and a decrease is more probably followed by a decrease, the process has long-range dependence [7].

I have implemented the rescaled adjusted range or R/S statistics based method for estimation of H [8]. Before the estimation no preprocessing was applied, raw data were used to minimize the computational cost and to reveal the sensitivity to artifacts. It was found that some artifacts can be rejected using a bipolar montage of electrode contacts and/or by averaging the estimated H values of several channels. Different techniques will be presented in the next heading. The R/S statistics based approach is valid only for stationary data. Due to the non-stationarity of *IEEG* signals 3s long non-overlapping data segments were used to estimate H. These were considered stationary. Moving average using sliding windows of different lengths (*maw*) was applied on the estimated values to emphasize slower dynamics.

III. RESULTS

The observed phenomena will be presented based on results of three patients with seizures of different origin. Results of all patients will be summarized afterwards.

A. Frontal lobe epilepsy

The black curve in Fig. 1 shows the average H of eight bipolar channels placed near to the seizure onset zone. Four drops can be observed during the 22h 33m long recording of patient 23. Before each drop there is a gradual increase. Jumps of H appear as a rebound effect after the drops. Jumps are followed by gradual decrease in all four instances. Drops of H occurred immediately after the onsets of the seizures which are denoted by the vertical lines. Applying a detection threshold ($H_{dt} = 0.6$) to this curve all seizures can be detected with a mean detection delay of 24.75s (standard deviation *SD = 0.9574s*) without false positive alarms. Slower dynamics are emphasized by the green curve which stands for the average H of the same eight bipolar channels but using a 1 hour long
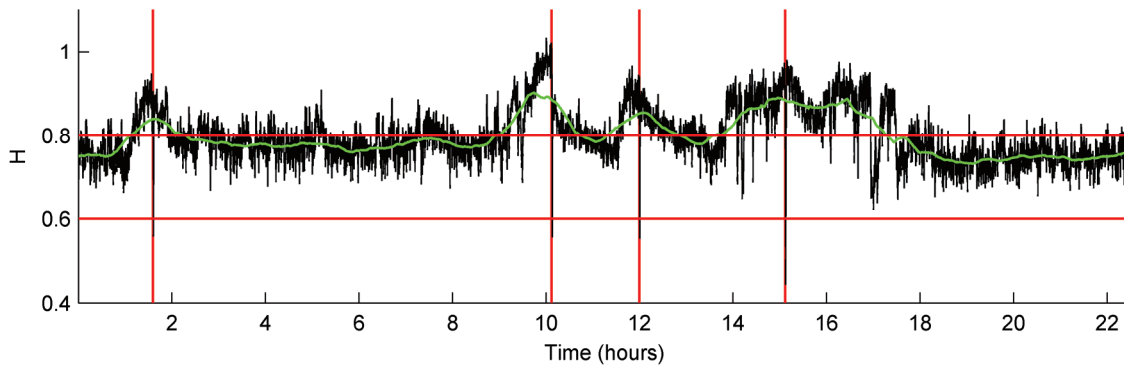
Fig. 1. Patient 23, 22h 33m long recording, 4 seizures. Black curve – average H of 8 bipolar channels ($maw = $ 1m); green curve – average H of 8 bipolar channels with same estimation parameters as for the black curve, but $maw = $ 1h; vertical lines – onset times of seizures provided by *NIN*; horizontal lines – applied detection ($H_{dt} = 0.6$) and prediction ($H_{pt} = 0.8$) thresholds.

moving average window. This curve exceeds the applied prediction threshold $H_{pt} = 0.8$ before each seizure. Thus, all seizures could be anticipated with a mean prediction interval of 59 m 28 s (*SD = 28m 53s*) without false positive alarms.

B. *Temporal lobe epilepsy*

Fig. 2 depicts the estimated H values of the electrode contact *TL5* placed into the seizure generating left hippocampus. Four seizures occurred during the 13 hours long recording of patient 22 suffering from *TLE*. The four seizures are indicated by the drops of H. While in *FLE* we observed gradual increase of H before seizures, in this case the opposite phenomenon i.e. a gradual decrease is noticeable in the preictal state of all the four seizures.

Fig. 3 shows the average H of 3 focal and 3 extrafocal contacts for four 1 hour long recordings, each containing one seizure. Patient 17 showed an increase of H in the preictal states of all the seizures similarly to patient 23. After the seizure onset times a drop of H can be observed during the ictal states.

C. *Other types of epilepsy*

The database also contains a patient suffering from parietal lobe epilepsy along with five patients with seizures of multilobal origin (patients 6, 9, 13, 14, and 20). Ictal drops and preictal changes (increase or decrease) of H were found for all these seizures, but for a statistical validation a larger database is needed. Nevertheless, these results were also used

when classification of seizures by hippocampal and neocortical origin was applied (see the next heading).

D. *Summary*

Table I contains detailed results for all patients separately. A drop of H could be observed for 27 of 29 seizures (93.1%) in *FLE*, for 51 of 52 seizures (98.1%) in *TLE*, and for 101 of all 104 seizures (97.1%). In case of the other three seizures no visually noticeable changes could be found. A comparison of the preictal changes of H in *FLE* and *TLE* is shown in Fig. 8 (a). In the preictal period of the *FLE* seizures a gradual increase of H occurred in 75.9% of the cases. For the remaining seizures a decrease (10.3%) or no visually observable changes of H (13.8%) were found. The decrease of H in *TLE* (51.9%) was not as notable as the increase in *FLE*. A gradual increase was also observed in 34.6% of the seizures. This was also shown in part *B* of this section using the results of patients 17 and 22. Duality of H in the preictal state of *TLE* seizures could be due to the different origin of these seizures. Namely, in mesial temporal lobe epilepsy, seizures originate from the archicortex, mostly from the hippocampus, while in lateral temporal lobe epilepsy from the neocortex. If we classify the available pure temporal lobe seizures by hippocampal and neocortical origin we get that in case of the seizures of hippocampal origin the gradual decrease of H (68.4%) predominates over the increase (18.4%). It is also presented in Fig. 8 (b) that for patients 17 and 21 with seizures of neocortical origin, a preictal gradual
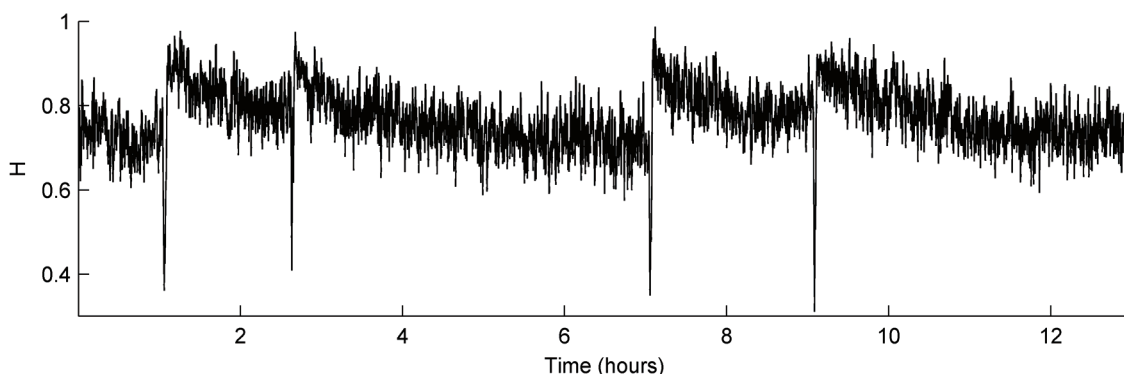

Fig. 2. Patient from *BEC*, 13h long recording, 4 seizures, H of the TL5 contact placed into seizure generating left hippocampus, $maw = $ 30s.
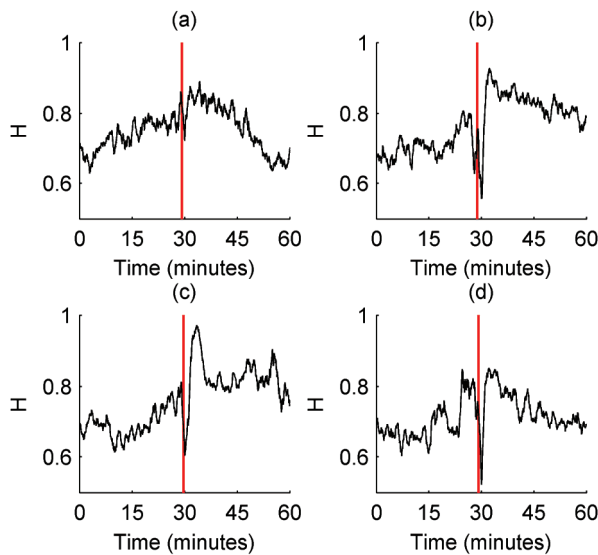
Fig. 3. Patient 17, 4 seizures, 1h long recordings. Black curves – the average H of 3 focal and 3 extrafocal electrode contacts, the peak of the drop during the seizures is in the middle; vertical lines – onset time of seizures provided by *FEC*.

increase of H occurred in 80% of the cases, while decrease could not be observed. Statistics considering seizures with pure and partial temporal lobe origin are also shown in Fig. 8 (c). Similar results can be seen as in Fig. 8 (b), except a less remarkable percent of increases of H for neocortical seizures. Results for all the seizures are also summarized using hippocampal and neocortical classification in Fig. 8 (d). For hippocampal seizures it was found that a gradual decrease of H occurred for 72.1% of the seizures, gradual increase in 16.3%, while for 11.6% of seizures no changes could be found in the preictal period. Neocortical seizures show the opposite phenomenon. Namely, a gradual increase of H was present in 73.6% of the seizures, while a decrease occurred in only 15.1%. Seizures of patients 14 and 15 were categorized as seizures with mixed, hippocampal and neocortical origin.
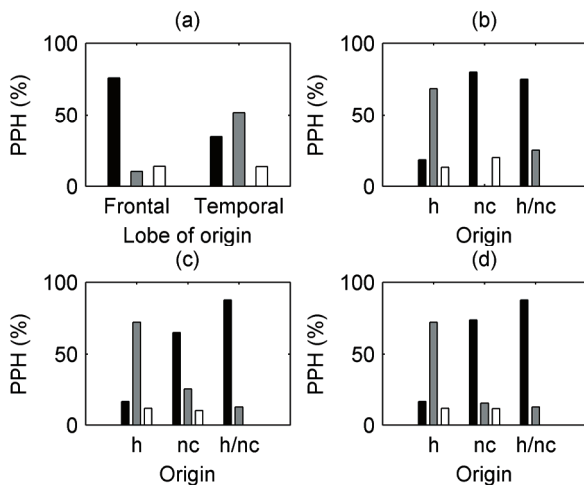

Fig. 4. PPH – preictal profile of H, h – hippocampal, nc - neocortical. Black bar – preictal increase of H, gray bar – preictal decrease of H, white bar – no preictal changes of H. (a) Comparison of preictal changes of H in *FLE* and pure *TLE*. (b) Preictal profiles of H of pure *TLE* seizures classified by origin. (c) Preictal profiles of H of seizures with pure and partial temporal lobe origin. (d) Preictal changes of H of all seizures classified by origin.

Based on the results we could presuppose neocortical origin of these.

IV. CONCLUSION

Self-similar property of long-term *IEEG* recordings could provide useful information about the dynamics of epileptic seizures. Development of seizures could follow different routes in *FLE* and *TLE* considering gradual changes of the Hurst exponent estimate before seizures. The observed difference was more remarkable when classification of seizures by hippocampal and neocortical origin was applied. Brain electrical activity before neocortical seizures tends to have a longer memory, whereas in preictal state of hippocampal seizures the opposite trend is observed. This finding could imply different seizure generation mechanisms and propose different models and prediction approaches for seizures with hippocampal and neocortical origin. A drop of H was observed during 97.1% of the seizures. Based on these findings a detection/prediction algorithm has been introduced using different moving average windows and thresholds for a patient suffering from *FLE*. The proposed method could be used with slight modification for 62.5% of the patients showing only one type of gradual changes in the preictal states.

REFERENCES

[1] F. Mormann, C. E. Elger, K. Lehnertz, "Seizure anticipation: from algorithms to clinical practice," *Current Opinion in Neurology*, vol. 19, pp. 187-193, 2006.
[2] S. B. Lowen, L. S. Liebowitch, J. A. White, "Fractal ion-channel behaviour generates fractal firing patterns in neuronal models," *Phys. Rev. E. Stat. Phys. Plasmas Fluids Relat. Interdiscip. Topics*, vol. 59, no. 5, pp. 5970-5980, 1999.
[3] C. D. Lewis, G. K. Gebber, P. D. Larsen, S. M. Barman, "Long-Term Correlation in the Spike Trains of Medullary Sympathetic Neurons," *The Journal of Neurophysiology*, vol. 85, no. 4, pp. 1614-1622, April 2001.
[4] S. Spasic, A. Kalauzi, G. Grbic, L. Martac, M. Culic," Fractal analysis of rat brain activity after injury," *Med. Biol. Eng. Comput.*, 43, pp. 345-348., 2005.
[5] N. Kannathal, U. Rajendra Acharya, C. M. Lim, P. K. Sadasivan, „Charactization of EEG – A comparative study," *Computer Methods and Programs in Biomedicine*, 80, pp. 17-23, 2005.
[6] EEG database of the Epilepsy Center, University Hospital Freiburg, Germany [Online]. Available: https://epilepsy.uni-freiburg.de/freiburg-seizure-prediction-project/eeg-database
[7] J. Beran, *Statistics for Long-Memory Processes*. Boca Raton, London, New York, Washington, DC., Chapman & Hall, 1994.
[8] Murrad S. Taqqu. R/S Method [Online]. Available: http://math.bu.edu/people/murad/methods/rs/rs.web.ps

Relation of Muscle Activities and Joint Rotations in Reaching Arm Movements

Robert Tibold

Supervisors: Jozsef Laczko,Gyorgy Karmos

Abstract—**Our purpose is to develop a movement model in MATLAB environment which simulates reaching arm movements - by means of angular changes, kinematic parameters, inertial parameters of the whole arm and biomechanical characteristics, like muscle force-muscle length relation - in the three-dimensional space. By solving the inverse kinematic problem as a result of the simulation we get muscle forces, and muscle activities that acted during the experimentally measured reaching-arm movement. In order to do that, first of all we need to know the relation between flexors and extensors, between muscle activities and joint rotations. Furthermore, we have to obtain muscle origins and insertion areas in the three- dimensional space as well. This one is pretty difficult, because the lack of anatomical information and anthropometric parameters. An experimental method and the relation between four arm-muscles and joint rotations (biceps, [BI] triceps, [TR] deltoid anterior, [DA] deltoid posterior [DP]) are presented and investigated in this paper. This work contains moreover an experimental method as an idea to solve the 3D muscle origins-insertion area problem by means of the fundamentals of [1]**

I. INTRODUCTION

Our goal, namely to develop a 3D movement model which simulates reaching-arm movements is very important. On one hand while investigating the literature it turned out that many studies have been conducted to develop and present kinematic models that are able to solve the inverse kinematic problem in 2D. However, only few studies have focused on the upper extremity. They have only focused on biomechanical models of the human upper limb [2] and they have not reported three-dimensional results. 3D kinematics and a clinical measurement of the whole arm during functional tasks were presented two years ago for standardizing clinical applications. [3] However, this one was concentrated on data collection and not on model development and simulation tasks. On the other hand the simulation results of the model will be applied for developing a functional electrical stimulation (FES) method which will help the patient to move his arms by stimulating the above mentioned four arm-muscles. During my thesis we investigated kinematic parameters, namely the variance of angular changes and of the end point. It turned out that there was significant difference between the movements without external load and with external load. The calculated variances were decreasing with respect to the increase of the mass of the load. This means that the increase of the mass made the movement more stable and more reproducible. These statements were proved by using a statistical method called T-probe. [4] In the present study a method for determining the angular changes of the shoulder in the three-dimensional space is presented as well,

as one part of our model which is under development and is based on the measurements done in 2006. For more details about the experiment see *THE EXPERIMENTAL METHOD*.

II. THE EXPERIMENTAL METHOD

We have investigated a usual arm movement under experimental conditions. However, during the whole movement there was a restraint. Namely, every subject had to hold his arm during the movement in an unusual pronated position. This was necessary because our main goal is to use the simulation results of the 3D model for stimulating proper arm muscles (BI,TR,DA,DP) with the help of FES so that hemiplegic or stroke patients would be able to move their limbs. There was no learning phase. After the markers and the EMG electrodes had been placed on the subject, the experiment was immediately started and no training phase was allowed.

A. Subjects

Twenty-four healthy subjects (aged 21-27), 10 man and 14 woman with no extremity complaints, voluntarily participated in the study were measured by the cooperation of the OORI. (Natonal Institute for Medical Rehabilitation). All subjects except one was right handed. In his case both arms were measured under same condition. All subjects signed an informed consent after being informed on the aims and procedures of the experiment.

B. Instrumentation

Movements have been investigated by the use of an ultrasonic-movement analyzer (MA) called ZEBRIS CMS 20S (ZEBRIS GMBH, Germany). 8 ultrasonic markers and 4 bipolar EMG electrodes were placed on the subject. See Table(I), Figure(1). All data were sampled at 200 Hz respect to the MA. If we consider the sampling rate of the MA marker from marker we get 200/8 = 25 Hz. In contrast with the sampling rate of the MA the EMG has higher sampling frequency, namely 1000 Hz. The syncronization of the MA and the EMG was solved by the manufacturer.

C. The measured movement

Each subject sat in front of a 2-level-computer desk. The distance between the chair and the desk was predefined. The maximum stretch of the elbow was defined in degree. The external angle of the elbow required to be about 10-15 degrees depending on the height of the subject. The external angle
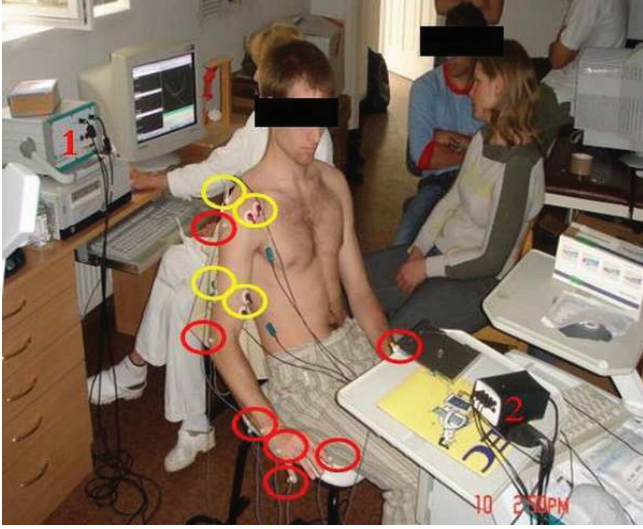
Fig. 1. Configuration of the experiment before putting down phase. Yellow circles present the four EMG channels and red circles show the 8 ultrasonic markers. The MA can be seen in the top-left of the figure signaled by 1 and the EMG of the system can be seen in the bottom-right of the figure signaled by 2. In the case of EMG electrodes the peak of the elbow was used as the reference point. Markers of the MA were used as transceivers. The Y shape receiver of the ZEBRIS system cannot be seen in the picture. During the experiment it was connected to the MA signaled by 1. Ultrasonic information of the 8 markers were received and transmitted to the MA that generated the real-time moving rod figure on the screen of the PC.

MEASURED DATA CHANNELS

	CHANNELS	
	EMG	MARKER
1	BI	SHOULDER
2	TR	ELBOW
3	DA	WRIST
4	DP	LITTLE FINGER BASE
5		LITTLE FINGERTIP
6		INDEX FINGERTIP
7		MASS MARKER
8		REFERENCE MARKER ON THE CHAIR

TABLE I
8 ULTRASONIC MARKERS AND 4 EMG BIPOLAR ELECTRODES WERE USED
DURING THE EXPERIMENT.

of the elbow was obtained by measuring the angle of the forearm respect to the elongation of the upper arm segment. Each maximum angular stretch had been measured directly by means of a protractor, before the experiment was started. The difference between the two levels in the sense of the computer desk was 20cm.

Three different conditions were defined corresponding to three loads with different mass (CD case, 1kg mass, 2kg mass). The actual load was placed on the lower level of the desk. The movement had three different phases. In the starting position the subjects arm was hanging along the body. First, from the starting position the subject had to lift his arm to reach and grasp the mass on the lower level of the desk and had to uplift it to the upper level and then the subject had to put his arm back to the starting position. This was the uplifting phase. In the second phase, the arm is in the starting position while taking a short pause. Finally, in the third phase, the subject had to reach the mass on the upper level, put it back to the

lower level and after releasing the mass the arm is placed to the starting position. This was the putting down phase. The important phases were the first and the last ones because during this time the mass was moved upward or downward. In the second phase there wasn't any action to measure. However, if we take into account the time needed for the first and third phase together than, we would get very long output files. If we consider data processing this would have made our situation more difficult. In order to collect enough data for variance calculation, each movement phase was repeated ten times under every load condition. The movement might have been influenced on by the effect of fatigue although this effect wasn't investigated at the present study.

D. Data processing

Two types of data were collected during the experiment. From this point of view data processing was divided into two parts as well. One part was the processing of kinematics and the another one was the processing of EMG's.

1) Kinematics: Angular changes of the upper extremity were obtained from three-dimensional data acquired by the MA. Angular changes of the elbow and the wrist were calculated and analyzed by using the methods according to [5]. During this stage of data processing simple cosine theorem was applied to obtain angles of the elbow and wrist. Angular changes in the shoulder complex were more difficult because of its complexity in the three-dimensional space. The issue is to obtain three-dimensional angular changes from marker coordinates acquired by the measurement system.

We managed to implement a mathematical method as the part of the 3D model mentioned in the abstract in MAT-LAB environment which calculates three-dimensional angular changes of the shoulder from marker coordinates and muscle insertion-origin points. These points were determined from anatomical description, which gave us a hard approximation of muscle attachment sites respect to the length of the bones in which the muscle attaches. For example if we are looking for γ the angle of the shoulder in the three-dimensional space we need two origin-insertion points of DA and the coordinates of one ultrasonic marker. In this case the marker that is placed above the shoulder. The scheme of the algorithm can be seen in Figure(2) in the case of shoulder angle.

T_1ST_2 triangle is given by three-dimensional coordinates.T_1 and T_2 was calculated by means of an anatomical description which gave us an approximation of the selected muscle attachment. The sides of the triangle can easily be calculated as follows:

$$a = \overline{ST_1} = \sqrt{(S_x - T_{1_x})^2 + (S_y - T_{1_y})^2 + (S_z - T_{1_z})^2}$$
$$b = \overline{ST_2} = \sqrt{(S_x - T_{2_x})^2 + (S_y - T_{2_y})^2 + (S_z - T_{2_z})^2}$$
$$c = \overline{T_1T_2} = \sqrt{(T_{1_x} - T_{2_x})^2 + (T_{1_y} - T_{2_y})^2 + (T_{1_z} - T_{2_z})^2}$$
$$(1)$$

Now, because we know all the sides of the triangle, applying the cosine theorem we get the following form:
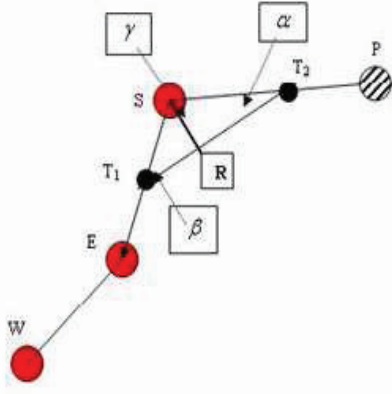
Fig. 2.   The sketch diagram of the three-dimensional angular changes calculator algorithm. Red transparent circles illustrate markers placed on the W-wrist; E-elbow; S-shoulder. Black circles represent muscle attachment sites of the DA. $(T_1 T_2)$ Stripped white circle illustrates the end point of the clavicula although it wasn't marked. As a result of the algorithm we get γ that can be calculated geometrically as follows.

$$Cos\gamma = (a^2 + b^2 - c^2)/2ab \qquad (2)$$

If we take the arc cosine of (2) we get the angular changes of the shoulder complex. Considering the area of the triangle we can write two equations:

$$T = (ab * Sin\gamma)/2 \qquad (3)$$

$$T = (m_c * c)/2 \qquad (4)$$

From equation (3) and (4) we get:

$$m_c = (ab * Sin\gamma)/c \qquad (5)$$

Hence, the moment arm of the muscle R, is equal to m_c (5). Although this paper is focused on the relation of muscle activities and joint rotations, the moment arm of muscles is going to play a very important role in the sense of three-dimensional modeling in order to determine muscle-forces that were generated during the movement.

2) EMG: EMG data processing was solved in two steps:

- Filtered by means of a 4th order Butterworth filter [5],[6]
- Smoothed by means of RMS where RMS is as follows:

$$RMS(n) = \sqrt{\frac{\sum_{k=n-a}^{n+a} EMG(k)^2}{2a+1}} \qquad (6)$$

First, EMG data was filtered by means of a 4th order Butterworth band-pass filter. Frequencies less than 50 Hz and more than 450 Hz were cut off by the help of the MATLAB built-in Butterworth filter [5]. After filtering all data, root mean square (RMS) algorithm was applied [5] in order to smooth EMG signals according to (6), where *a* signs the sampling window and *n* assigns the length of the measured muscle activities separately. The size of the sampling window was

40 ms. The length of the separate muscle activities (number of samples) is the same as the time elapsed from the uplifting phase to the putting down phase. Both types of the collected data were normalized in time according to [5] so that many comparisons could be taken.
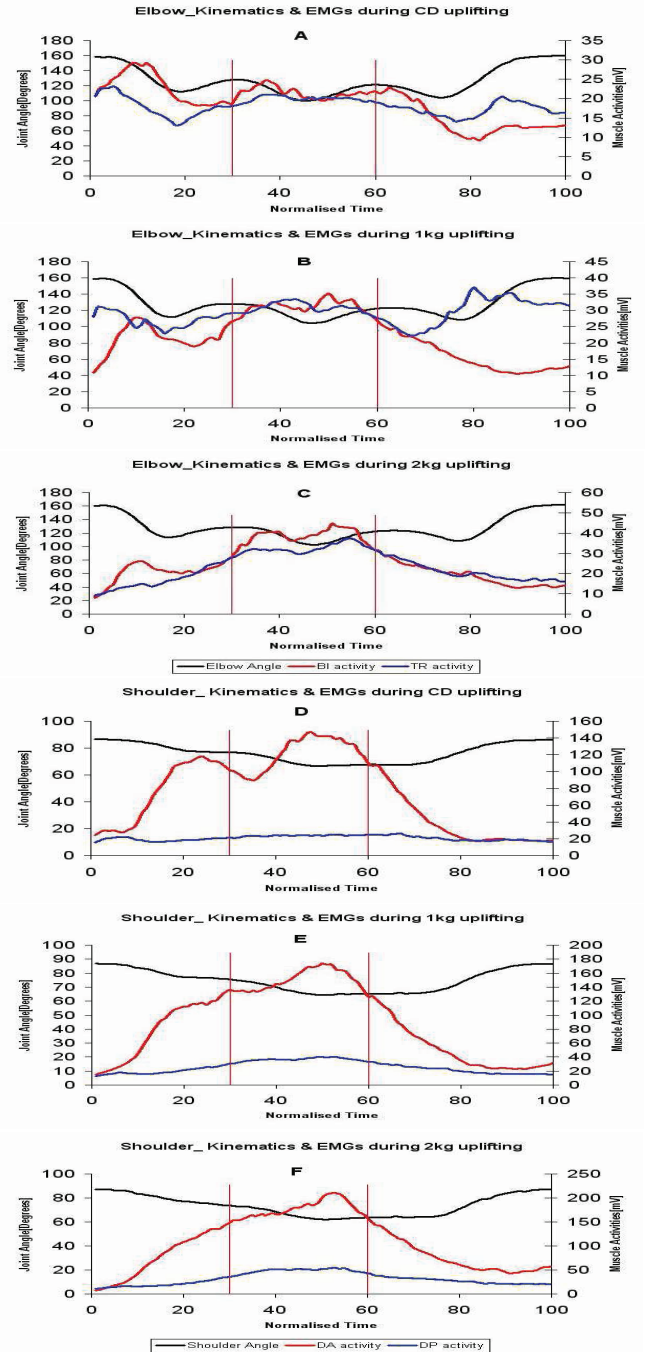
III. RESULTS

Fig. 3.   Averaged reaching arm movements of 18 subjects. In A-C elbow kinematics and activities of BI, TR are presented in each load condition. In D-F shoulder kinematics and DA, DP activities are presented under each load condition. Vertical lines are showing the interval when the load was hold by the subject.

IV. DISCUSSION

In the movement without load three local maxima can be observed in the BI activity. These 3 local maxima correspond to the the elbow flexion phases mentioned in *The measured movement part*. During movement with 1 kg, similarly to the movement without load, the first local maximum of BI assigns the first flexion of the elbow when the arm started to reach towards the target. The second and third local maxima of the activity align with each other, and remain high while the load is hold in the hand. Similar activity pattern occurs during the movement with 2 kg but with higher amplitude.

In the case of CD case and 1 kg load TR activities have three local maxima staying close to the BI activities. However, in the third condition there are no evident first and third local maxima and between the vertical lines steadily increasing amplitudes can be detected. This means that in A-B TR has had only controlling role while during C it must have been in cooperation with BI. In the case of the shoulder the situation is very similar to the elbow, although in D considering DA activity only 2 local maxima is observed. The first one is the starting flexion of the shoulder while the second one is the uplifting itself when the load was in hand. In E-F only one evident local maxima can be seen, however in both cases it occurs at the same time. Considering DP only one local maximum can be observed mostly in E-F, although with very low amplitudes. This means that during the movement in the sense of the shoulder the generated force was mostly due to DA and DP had only controlling role as well as TR. These statements are acceptable because if we consider that the arm is maximally stretched and the mass is in hand then the gravitational force has powerful effect on the upper limb and the gravitational torque remains high. In that case each muscle of the arm must generate greater torque and muscle-force in order to overcome the gravitational effect.

Our findings show, that the measured kinematic and muscle activity patterns obey physical and biomechanical laws that will be investigated after the simulation of the 3D movement model.

V. FURTHER PLANS

There are further measurements planned to obtain muscle 3D origin-insertion areas of the four arm-muscles. They are based on [1]. The method of the experiment is very similar to the measurements mentioned in *THE EXPERIMENTAL METHOD* part. The only difference is the placement of ultrasonic markers. The effect of fatigue wont influence on data acquisition because of a random order execution of the trials in varying conditions corresponding to CD case, 1k-2kg mass. The marker configuration of the measurement can be seen in Figure(4). A mathematical algorithm based on [1] will be applied on the collected data. As a result of the algorithm the 3D muscle origin-insertion area problem will be solved subject by subject depending on body parameters. Using the results of this paper and the 3D muscle attachment parameters the realistic movement model is going to be simulated and evaluated. Results of the simulations will be used for generating generic movement patterns and stimulating strategies for reaching arm movements.
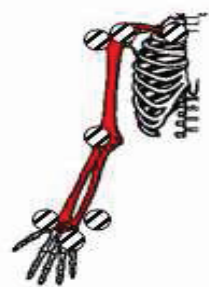

Fig. 4. Stripped circles present ultrasonic markers of the MA. They'll be placed on in the following sequence: 1.: the proximal side of the clavicula, 2.: AC-joint, 3-4.: upper arm markers, 5-6.: distal and proximal side of the wrist, 7.: base of the little finger.

VI. ACKNOWLEDGMENT

REFERENCES

[1] K. N. A. H.E.J Veeger, Bing Yu, "Parameters for modeling the upper extremity," *Journal of Biomechanics*, vol. 30, pp. 647–652, 1997.
[2] S. A. Yamagushi G.T., "A survey of human musculotendon actuator parameters," *Multiple Muscle Systems: Biomechanics and Movement Organization*, pp. 717–773, 1990.
[3] van Andel CJ et al, "Complete 3d kinematics of upper extremity functional tasks," *Gait Posture*, 2007.
[4] A. Poka, "Karmozgasok 3d elemzese es varianciajanak vizsgalata," Master's thesis, Semmelweis University of Medicine, June 2008.
[5] R. Tibold, "Neuromorf mozgasszabalyozasi elvek vizsgalata celt elero karmozgasok kinematikai es elektromiografiai jellemzoinek merese alapjan," Master's thesis, Peter Pazmany University Department of Information Technology, June 2007.
[6] K.Erer, "Adaptive usage of the butterworth digital filter," *Journal of Biomechanics*, vol. 40, pp. 2934–2943.

Electrophysiological Study of the Cortico-hippocampal Interaction

Balázs Dombovári

(Supervisors: Dr. György Karmos and Dr. István Ulbert)

dombovari@cogpsyphy.hu

Abstract—**The relationship between the oscillatory families in the cortex and hippocampus is not well understood. We suggest that the cortical slow oscillation temporally coordinates the oscillations in the hippocampus. Our research goals were to analyse the interactions between intracortical and hippocampal spontaneous activity derived from chronically implanted cat brain. To understand how information is transferred from cortex to hippocampus, one needs to know how the pattern of information is represented in the cortex, how this pattern is transferred to the hippocampus and, finally, how it is represented and stored in the hippocampus. One of my previous study we examined this relation with frequency- power analysis of different waves of the responses derived from the auditory cortex and hippocampus, as well as with time- frequency analysis. We found that prominent cortical down-up transitions induced increased power in the hippocampus with temporal shift. In this actual paper I investigated the properties and changes of the neural activity with other mathematical methods which provide us more exact information and helps to understand how different neuronal generators work.**

Index Terms - **EEG, neocortex, hippocampus, memory consolidation, sleep**

I. INTRODUCTION

Cortico-hippocampal interaction, especially during quiet wakefulness and sleep, is thought to be important for the formation of long-term memories by a process of consolidation. During these behavioral states and under anaesthesia, neocortical neurons are spontaneously active, and their activity is modulated by slow, 0.1- to 2-Hz oscillations called up-down states characteristic of slow wave sleep (SWS) oscillations. Both the local field potential (LFP) and the membrane potential show that up-down states are synchronized across large areas of the cortex. Although neocortex is the major source of input to the hippocampal formation, the hippocampal LFP shows large, irregular activity during SWS that seems uncorrelated with the neocortical activity. This is indicative of minimal cortico-hippocampal interaction during up-down states. However, recent studies have shown cortico-hippocampal interaction during various behavioral states including SWS. The mechanisms underlying this interaction and the contribution of different parts of the hippocampal circuit to this interaction remain to be understood [1], [2], [3].

A. Neocortical up-down oscillation

Slow oscillations are reflected in fluctuations in the membrane potential of neocortical neurons at the single-cell level. The membrane potential of virtually all neocortical neurons undergoes relatively abrupt transitions from a hyperpolarized down state to a substantially more depolarized up state. The down state is associated with a positive polarity LFP in infragranular layers (Figure 1). Rhythmical shifts between down and up states have also been described in striatal and thalamic neurons.
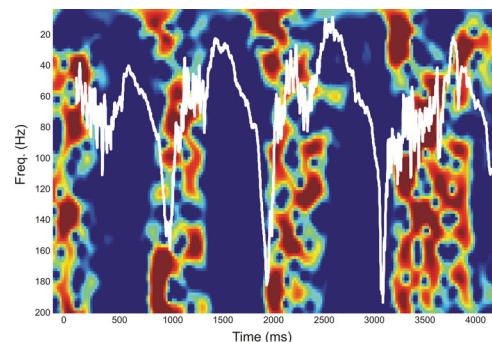

Figure 1. Wavelet plot of cortical up an down oscillation in anaesthesia. Original cortical signal is superimposed with white color.Under up states the wavelet power was increased in separated stripes.

B. Hippocampal oscillations under deep sleep and anaesthesia

State-dependent EEG in the hippocampus has traditionally been divided into two activity patterns: theta, a large-amplitude, regular oscillation with a bandwidth of 4-8 Hz, and large-amplitude irregular activity, a less regular signal with broadband characteristics. Both of these activity patterns have been linked to the memory functions subserved by the hippocampus. Wolansky and his colleagues described a novel hippocampal state in rats during deactivated stages of sleep and anaesthesia that is characterized by a prominent large-amplitude and slow frequency (< 1 Hz) rhythm [4]. In cats, under ketamine- xylazine anaesthesia we found the same hippocampal slow oscillation but with higher frequency (2 Hz) and only under prominent cortical down-up transition.

II. MATERIALS AND METHODS

A. Animals,Surgery

The experiments were carried out on three adult cats (three males weighing 2.9-3.4 kg). All procedures were approved by
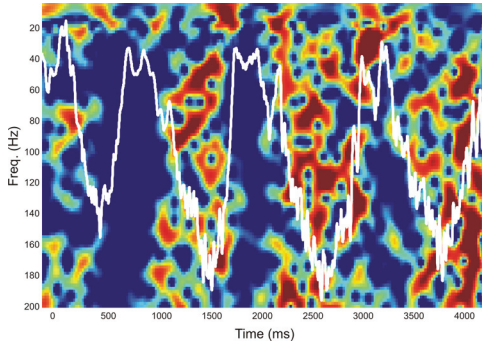
Figure 2. Wavelet plot of hippocampal delta oscillation. Original hippocampal signal is superimposed with white color.

to give indications on the feedback that exists between the analyzed systems. Previously we developed a software which is based on time-frequency analysis. From wavelet transforms of two time series we constructed the Cross Wavelet Transform (CWT), which exposes their common power and relative phase in time-frequency space. Other methods, such as perievent time histogram (PETH) and cross correlation had been Since the measures mentioned above are linear, we extend our investigations by considering also nonlinear measures. An alternative measure for synchronization which can be applied in our data is the S-estimator.

C. Cross Correlation

In signal processing, the cross-correlation is a measure of similarity of two signals, commonly used to find features in an unknown signal by comparing it to a known one. It is a function of the relative time between the signals.The true cross-correlation sequence is:

$$R_{xy}(m) = E\left\{x_{n+m}y_n^*\right\} = E\left\{x_n y_{n-m}^*\right\}$$

where x_n and y_n are jointly stationary random processes, $-\infty < n < \infty$, and $E\left\{\cdot\right\}$ is the expected value operator. Cross Correlation must estimate the sequence because, in practice, only a finite segment of one realization of the infinite-length random process is available.

D. Cross Wavelet Transform

The cross wavelet transform of two time series x_n and y_n is defined as $W^{XY} = W^X W^{Y^*}$, where * denotes complex conjugation [5] . We further define the cross wavelet power as $\left|W^{XY}\right|$. The complex argument $arg\left(W^{xy}\right)$ can be interpreted as the local relative phase between x_n and y_n in time frequency space. The theoretical distribution of the cross wavelet power of two time series with background power spectra P_k^X and P_k^Y is given as:

$$D\left(\frac{\left|W_n^X(s)W_n^{Y^*}(s)\right|}{\sigma X \sigma Y} < p\right) = \frac{Z_\nu(p)}{\nu}\sqrt{P_k^X P_k^Y}$$

where $Z_\nu(p)$ is the confidence level associated with the probability p for a pdf defined by the square root of the product of two χ^2 distributions.

E. S-estimator

An alternative measure for synchronization which can be applied in both bivariate and multivariate data is the S-estimator [6]. First we perform PCA meaning that we eigendecompose the covariance matrix of the data:

$$R_{FF} = E\left\{F \times F^T\right\} = L\Lambda L^T$$

where Λ is a diagonal eigenvalue matrix and L is the corresponding eigenvector matrix. From the diagonal elements λ_i of the eigenvalue matrix Λ we compute the normalized

the Institutional Ethical Committee. Brain electrical activity was recorded by chronically implanted epidural electrodes made of 0.23 mm diameter enamel insulated stainless steel wire and a laminar multielectode with 24 contacts made of polyimide insulated platinum-iridium wires. They were implanted under pentobarbital anesthesia (40 mg/kg i.p.) using aseptic techniques. Before implantation, small holes (1 mm in diameter) were drilled in the skull overlying the auditory cortical areas, and intraoperative ERP recordings were carried out to map area AI. After mapping, a 5x5 tube matrix was placed on the surface of the cortex. The tube matrix covered both the primary and surrounding auditory fields and between tubes it contained 8 cortical surface wire electrodes to localize the strongest primary auditory signals. Two twisted pair stainless steel electrode were implanted into the two hippocampi. Further electrodes were implanted under surgery to verify sleep states, e.g. EoG, muscle electrodes. Stainless steel screws were inserted into the bone of the frontal sinus and the occipital protuberantia, to serve as the reference and ground respectively. The leads were connected to a miniature connector and the whole implant was fixed to the skull by dental acrylic. An impression was formed for a bone conductor in the frontal part of the acrylic implant. After convalescence, a laminar multielectrode was implanted intracortically through the tube matrix. EEG data was recorded from each animal for an average of six months. After finishing the experiments, the animals were given a lethal dose of barbiturate, and the placement of the electrodes was anatomically verified. Reconstruction of the approximate placement of the electrode matrix was achieved by histological images of the laminar multielectrode location.

B. Data analysis

The brain electrical activity was amplified, filtered (bandpass: 0.1 Hz-0.5 kHz) and digitized at 2000 Hz sampling rate. Off-line analysis was carried out on a PC using the NeuroScan data processing software and custom-made MATLAB softwares.
The traditionally formulated but still the most common way of analysing the functional coupling of cortical and hippocampal assemblies is the correlation. However correlation is not able

eigenvalues λ_i' as follows:

$$\lambda_i' = \frac{\lambda'}{tr\,(\Lambda)}$$

From the K normalized eigenvalues we compute the S-estimator:

$$S = 1 + \frac{\sum_{i=1}^{K} \lambda_i' \log(\lambda_i')}{\log(K)}$$

We can see from the above equation that when all eigenvalues are equal to $1/K$ then S become zero, whereas if only one strong eigenvalue exist then S becomes maximum and equal to 1. The number of eigenvalues indicates the number of uncorrelated signals within data matrix F. In brief, when the EEG channels are combinations of many uncorrelated signals no synchronization exists. On the contrary when we have small number of uncorrelated signals all brain sources are synchronized according to these signals.

III. Results

After EEG recording the next step was to select all of the prominent down-up transitions in a cortical channel and peaks of delta waves in a hippocampal channel with Matlab based nsview software. These events were saved in .*ev2* file format. With NeuroScan I epoched the original continuous files in order to place the above down-up transitions in zero point of time. I used these epoched files (.*eeg* format) for further data processing.

A. Peri Event Time Histogram

Previously I prepared the cortical and hippocampal .*ev2* files, which contain temporal information about prominent down-up transitions and hippocampal delta peaks. Figure 3 shows that how often an event happened in the hippocampus compared to the cortex. Distinctly visible that all hippocampal events grouped around the cortical down-up transitions.
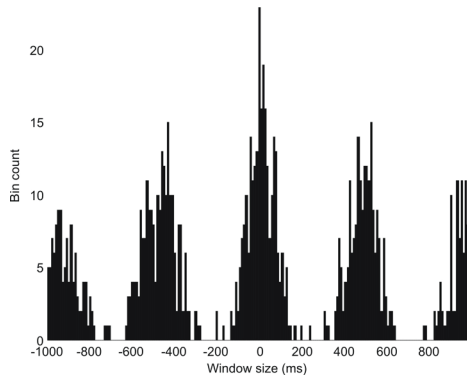

Figure 3.   Perievent Time Histogram.

B. Cross Correlation

Cross correlation is a conventional measure between to time series. I used the built-in Matlab function to get how strong the relation between two brain areas is. Figure 4 shows the cross correlation between an auditory cortical and a hippocampal channel.
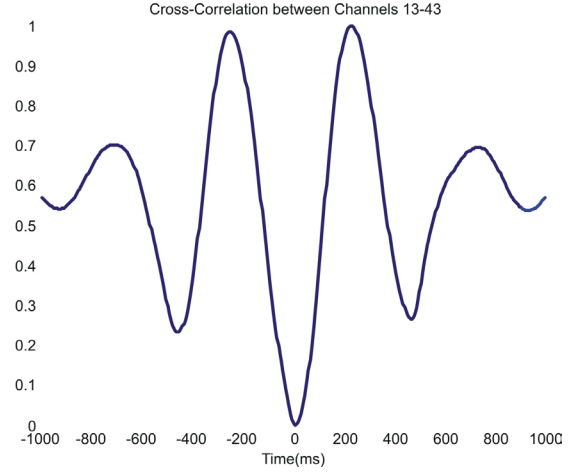

Figure 4.   Cross Correlation of a cortical and a hippocampal channel.

C. S-estimator

We can see on Figure 5 the S-estimation of an auditory cortical and a hippocampal channel. This picture shows an average of 0.42 S-value which means that a notable part of the connections are synchronized, in other words these channels are partly correlated with each other.
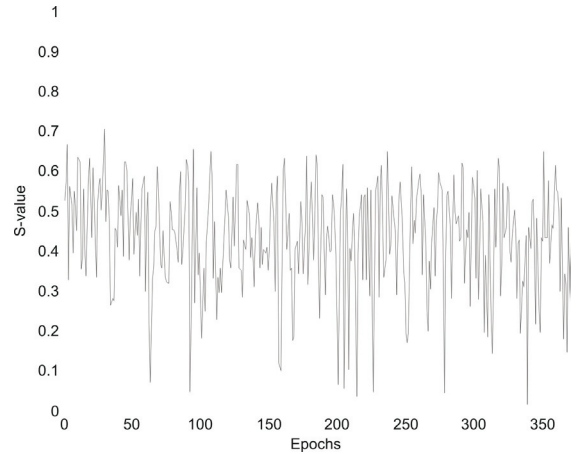

Figure 5.   S-estimation of a cortical and a hippocampal channel.

D. Cross Wavelet

In contrast with previous studies we can see on Figure 6 that there is a strong relationship between cortex and hippocampus under the end of down state and at higher frequencies.
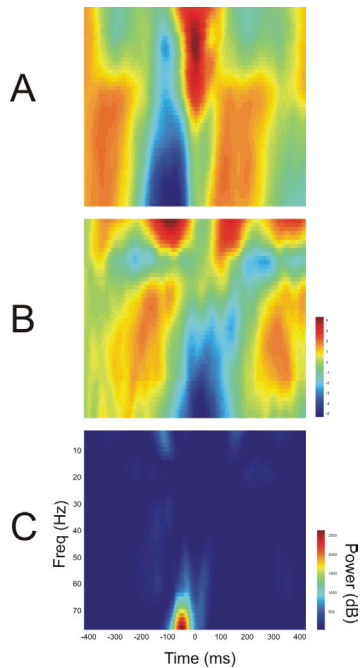
Figure 6. Cross Wavelet of a cortical and a hippocampal channel. A: Wavelet transform of a cortical channel, B: Wavelet transform of a hippocampal channel, C: Cross-Wavelet transform of A and B.

IV. CONCLUSION

Under natural deep sleep and anaesthesia cortical neurons oscillate between two states, depolarized 'up'- and hyper-polarized 'down'- states, while hippocampal field potential shows delta waves and irregular fast activities. In order to get stable recording, we anaesthetized the animals with ketamine-xylazine mixture. From all of my experimental results the following hypothesis can be drawn, that under ketamine anaesthesia the transition of down-up states with higher power and larger amplitude induce a transfer function between cortex and hippocampus. This is supported by several mathematical algorithms, such as the classical cross correlation function, S-estimator and cross wavelet transform. This cortico- hippocampal connection might be also very important in memory consolidation.

REFERENCES

[1] A. Sirota and G. Buzsáki, "Interaction between neocortical and hippocampal networks via slow oscillations."

[2] G. Buzsáki, Ed., *Rhythms of the Brain*, 1st ed. New York, USA: Oxford University Press, 2006.

[3] Y. I. et al., "Integration and segregation of activity in entorhinal-hippocampal subregions by neocortical slow oscillations," *Neuron*, vol. 52.

[4] T. W. et al., "Hippocampal slow oscillation: A novel eeg state and its coordination with ongoing neocortical activity," *The Journal of Neuroscience*, vol. 26, no. 23.

[5] A. G. et al., "Application of the cross wavelet transform and wavelet coherence to geophysical time series," *Nonlinear Processes in Geophysics*, vol. 11.

[6] V. S. et al., "Assessment of linear and non-linear eeg synchronization measures for evaluating mild epileptic signal patterns," *IEEE TRANSACTIONS ON INFORMATION TECHNOLOGY IN BIOMEDICINE*.

Proving the positive effects of regular FES-cycling by physiological parameters

Tamás Pilissy

(Supervisor: József Laczkó)

piltom@ieee.org

Abstract — **Functional Electrical Stimulation (FES) was discovered in the 60's and its positive effects have been proved since then. Despite this fact most rehabilitation centers still do not use it for improving their patients' state of health. In the last year we have followed up not only the improvement in performance but also in some physiological parameters. Hence we are now able to prove the advantageous physiological effects of regular FES-cycling by quantitative measurements. In my previous studies I built up a big database of kinematic and myoelectric parameters what I collected from healthy cycling subjects. Presently I use this data for defining adequate muscle stimulation patterns for generating natural, neuromorph kinematic patterns for cycling movements in spinal cord injured patients.**

Index Terms — **FES-cycling, muscle stimulation, state of health**

I. INTRODUCTION

In this short report I would like to give an overview about the multidisciplinary area of Functional Electrical Stimulation (FES), focusing on FES assisted cycling movements of spinal cord injured (SCI) patients.

There are over 2.5 million people in the world who suffered such serious spinal cord injury whereupon the ability of moving the lower limb has been lost [1]. Since this state is mostly irreversible, the lost motor-functions should be recovered artificially. Functional Electrical Stimulation of the muscles by surface electrodes is an accepted and non-invasive technology for this task [2-5].

It is well-known that moving is an important requirement of well-being. In the case of spinal cord injury the body still needs motor activities for maintaining proper respiratory and cardiovascular functions.

Over the last one-half year several spinal cord injured people had the opportunity to train their muscles by FES-driven cycling in the National Institute for Medical Rehabilitation. In this way some of them have already had more than fifty trainings. The regular muscle stimulation not only prevents the atrophy of the muscles but also improves the state of the health which is especially important after spinal cord injury.

II. PRELIMINARY MEASUREMENTS

In 2006 we measured biomechanical parameters of lower-limb cycling by recording this movement task at 42 healthy subjects using an ultrasound based Zebris CMS70P motion-analyzer system [6].

Ultrasound emitting markers were placed above anatomical landmarks of the hip, knee and ankle joints and one marker was mounted on the pedal to gain information about the cadence of cycling (Fig. 1). The subjects were asked to drive the pedal of the recumbent bike with two different speeds – about 45 and 60 rounds per second (rpm), besides the level of load was also changed from light to heavy in three steps. It means that we recorded six phases of cycling at each subject. The measurement system was capable to measure only one lower limb during a session therefore only the left lower limb was measured.
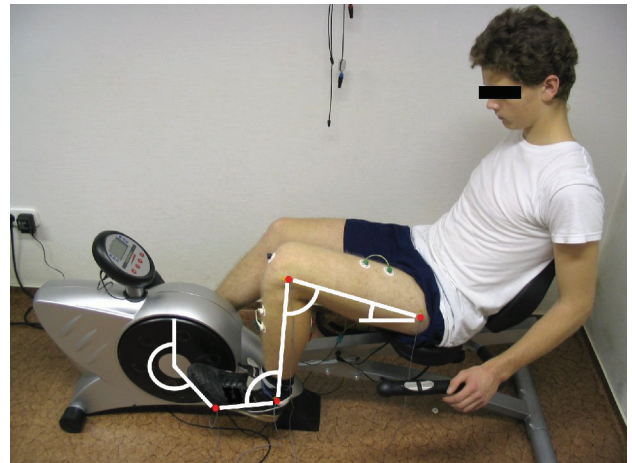

Fig. 1. The measurement setup as it was "seen" by the ultrasound-sensors of the motion-analyzer system. The vectors and angles that were defined from the marker positions are also shown.

After the measurements the joint and pedal angles were computed from the recorded marker-positions by VisualBasic programs while the EMGs were filtered in MATLAB with Butterworth filter.

After the processing we had got a huge database containing all of the important data that would be essential for further investigations related to cycling movement. A possible utilization may be the verification of neuromechanical models, but first we used it to define new stimulation pattern for FES-cycling. In this way, after several months of fine-tuning, our patients had got a stimulation pattern that differed fundamentally from the earlier patterns. The new muscle stimulation pattern for paraplegics was defined by imitating measured muscle activity patterns of healthy subjects (e.g. the sample what is presented at Fig. 2).
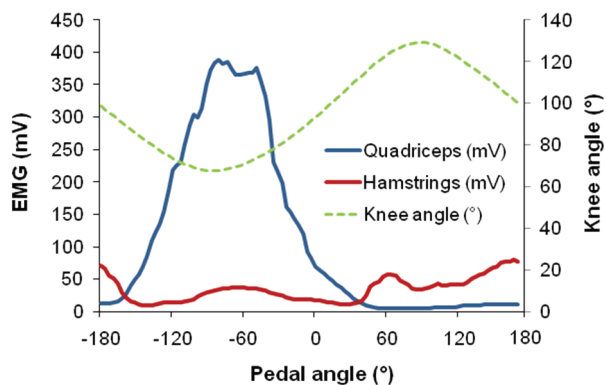
Fig. 2. Thigh muscle activities and knee joint angle changes as functions of pedal angle. The means of 10 consecutive cycles of one subject are presented.

III. CURRENT FES-CYCLING PROJECT

Practical application of FES has been in progress since Richter Gedeon Corporation had bought a stimulator for us. The method what we used at the beginning of the project was derived from studies of the Ludwig Maximilians University in Munich, Germany [3-5]. It must be mentioned here that I spent ten days in Munich lately and it seems that we will be able to compare and publish our patients' results soon.

Fig. 3. FES-cycling system. The legs are fastened to the pedals of the ergometer with straps to prevent accidents. The stimulator and some surface electrodes on a SCI patient's muscles are also shown.

The Motionstim8 stimulator that we have been using since 2007 is a product of Krauth+Timmermann Ltd. It contains a Hitachi microcontroller that is responsible for controlling the output channels. These 8 stimulation channels are programmable with manufacturer's own program (MotionSoft) via serial port. The biphasic, rectangular stimulation impulses are produced in the frequency range of 1 to 99Hz while the pulse length can be set between 10 and 500 µs [7].

As for the stimulation intensity it is optional to set maximum current but the actual values had to be set manually on the stimulator. The stimulator had got a FES-cycling program that required information about the position of the lower limb (Fig. 3). This information was delivered in the form of pedal angle which is a usual method among FES-cycling systems.

A. Stimulation pattern

We have also acquired the programming software (MotionSoft) for the stimulator. In this program we could generate custom stimulation patterns as functions of the pedal angle. The MotionSoft considers the zero degree as the uppermost position of the left pedal. The pedal angle is measured relative to this position; positive angles presented clockwise (Fig. 4). In this respect the default cycling program stimulated the left quadriceps from -70 to 100 degrees with biphasic square-impulses, while the frequency and pulse-width was 20 Hz and 300 µs respectively. As for the amplitudes, it had to be adjusted manually on the device every time we used it. This was a bit uncomfortable but also useful since the necessary amplitudes varied among the measurements and the subjects.

In the beginning we applied this built-in stimulation program and in the course of some measurements the proper impulse-amplitudes were determined for each patient. We found that at most of them the two legs developed different performances for equal stimulation; therefore an asymmetric stimulation (e.g. 80 vs. 60 mA) was applied for generating a symmetric occupation of the muscles. Due to this adjustment a slightly smoother motion could be generated compared to the symmetrical stimulation.

Later we realized that the default stimulation program was not proper in the timing of the muscle-activations, which was reflected in rugged leg movements. Thus we wished to improve the stimulation pattern. Using our empirical observations we improved the built-in stimulation pattern by changing the timing of the muscle activations. After some attempts we could generate somewhat smoother motion, but at last we introduced a quite different stimulation pattern that resulted in a much better performance and smoothness.

Observing the cycling of the healthy people we found that the maximal quadriceps activity was measured when the pushing of the pedal began, but the activity started to increase much earlier. We also noticed that the quadriceps activity decreased in the same rate as it had increased, hence at the top position of the pedal the quadriceps activity on the same side approached zero.

These findings helped us to define a new stimulation pattern (Fig. 4/b) in which the activations were applied earlier (in the means of pedal angle) compared to the default cycling program (Fig. 4/a). The quadriceps activation was shifted backward with 50 degrees and lasted for a shorter range of pedal angle (shorter with 50 degrees), while the hamstrings got almost the opposing activation range as in the old program [8].
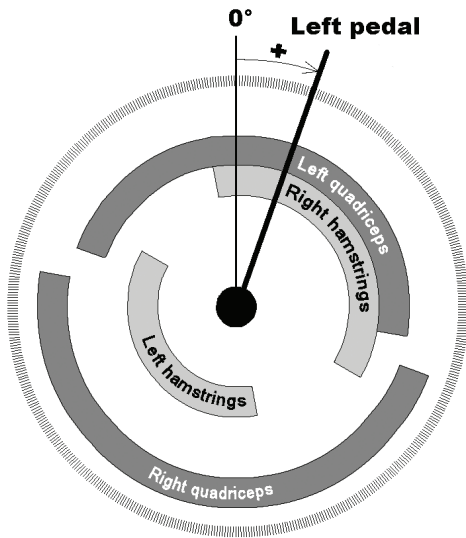
a) Motionstim8 default
cycling program
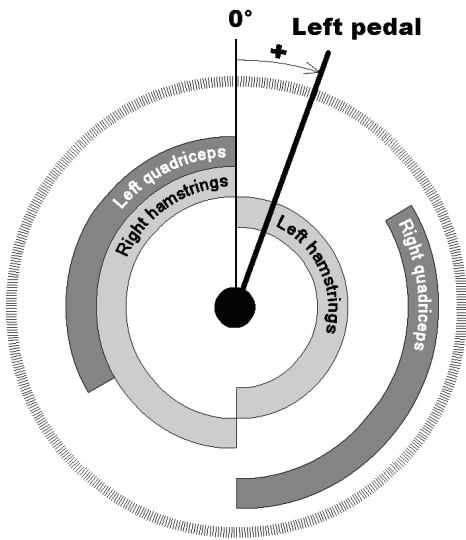
b) Stimulation based
on healthy EMG

Fig. 4. The relation of muscle activations and pedal angle ranges.

B. Procedure of FES-cycling

A FES-cycling training lasted about 20-30 minutes (exclusive the several minutes of passive warm-in and warm-out by the ergometer). During this time the pedal-resistance of the ergometer was set in the hardest level in which the patient was able to keep a cadence of 40-50 rpm. The actual level of load, the corresponding time-interval and average velocity were registered. Later these values were used to compute average performance by the formula that Dr. Szécsi also used in his similar measurements [4-5].

$$P = 0.105 \cdot v \cdot (r+1) \cdot 0.7 \qquad (1)$$

where v is velocity in rpm, and r is the resistance of the pedal. Since the latter is not an exact torque value (has 20 levels on the ergometer), the computed performance is also not an exact wattage but perfect for comparison.

Based on this formula we computed average performance for each training session.

As for physiological parameters, heart rate (HR) and blood pressure (BP) were registered during the trainings at least in every 10 minutes. Besides blood-gas, spiroergometry and breath-function measurements were also performed in every two months.

IV. RESULTS

The muscle-activations in the new stimulation pattern differed basically from the ones that were used previously but the improved performance of the patients proved the advantage of our new sequence of stimulation. Due to this new program our patients' performance increased by 66% in average (Table I); meanwhile the smoothness of their motions also became more natural.

TABLE I
PERFORMANCE INCREASE DUE TO OUR NEW STIMULATION PATTERN

Patient No.	Average performance [W]		
	Before	After	Increase
1	7.75	12.78	64.90%
2	5.81	9.60	65.23%
3	4.51	7.60	68.51%

The improved performance at the three patients who were using both (the old and our new) stimulation pattern for FES-cycling. The "before" and "after" values are the averages of three trainings before and after the change.

From the physiological point of view, it is important that neither the new stimulation pattern nor the intrinsic performance improvement evoked higher HR and BP values (Fig. 5). Due to this we can claim that neither source of the improved performance caused overload for the cardiovascular system.
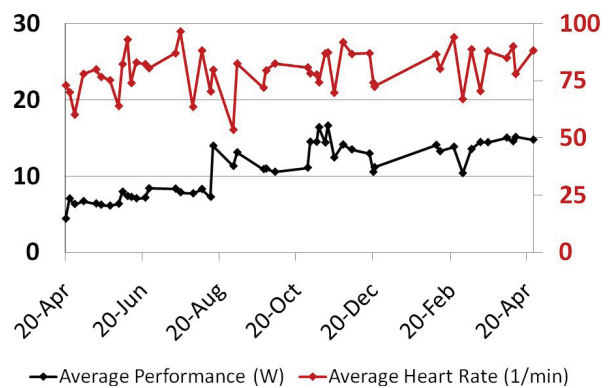

Fig. 5. The increased performance did not cause overload for the cardiovascular system, as the heart rate remained in the same range in the course of the trainings.

Another interesting point that at our strongest subject (with over 60 FES trainings), we measured 6.7mmol/l lactate after 25 minutes of FES-cycling. At the beginning this concentration was 2.0mmol/l which is a normal value

at rest. The increases of concentration above the resting values are presented in Fig. 6.

Since the lactate is an indicator of anaerobic metabolic pathway we can conclude that the muscles do significant amount of work during the stimulation.

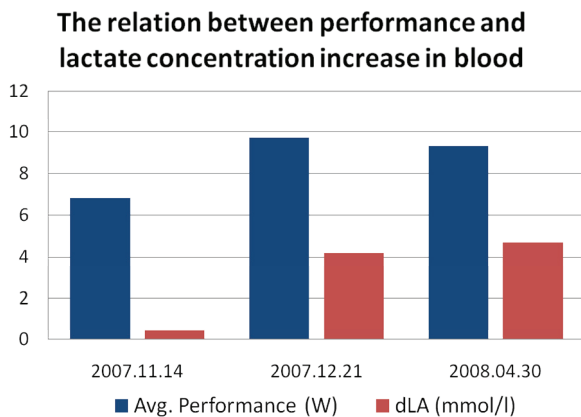**The relation between performance and lactate concentration increase in blood**

Fig. 6. At high performance the lactate concentration of the blood increased significantly during the training. These three measurements prove the increased endurance of our strongest SCI patient.

This high concentration of lactate proves that spinal cord injured patients can successfully train their paralyzed muscles through FES. For comparison this concentration is as approximately high as it would be in a healthy person after 10 minutes of run.

V. CONCLUSION

I defined enhanced muscle stimulation patterns for the quadriceps and hamstring muscle groups, using the experience and observations what I gained in experiments studying of healthy cycling movements.

At the present we apply FES for a flexor-extensor muscle pair of the knee. Although, the results of our measurements of healthy subjects suggest that the ankle plays an important role in natural movement [9].

It must be mentioned that some of the patients were in very bad state in the first trainings, because they were just getting acclimatized with sitting after months of lay. In the first time the patients whose injury was higher (at cervical vertebrae) were also very weak in physiological sense. In their cases the respirator and cardio-vascular system was usually unable to keep pace with the muscles. In this way they cycled with good performance for a short period of time and became tired quickly. Despite these facts they were able to reach reasonable improvement with FES.

The results also showed that it is possible to generate useful muscle-force with the non-invasive method of surface electrodes.

Finally we can conclude that at most patients the active muscle training cause significant improvement not only in the condition of the stimulated muscles but in the overall state of health as well.

VI. FURTHER PLANS

As it was mentioned above the abilities of our current stimulator are limited. For instance the stimulation intensity is adjustable only by current intensity and there are a lot of parameters that has to be fixed for the whole stimulation time. In the future we would also like to take the velocity into account, because there is significant difference between slow and fast cadence of cycling from the viewpoint of stimulation.

For this reasons we would like to develop our own stimulator based on the imperfections of the current stimulator and other observations. Preparing for the development of this new stimulator we have already defined the required functions, so the specification is almost ready.

Another exciting plan is to use a tricycle beside the erogmeter. Toward this goal, the development of a required component, the pedal angle encoder, has begun.

REFERENCES

[1] http://www.spinalcordsociety.org/2007/whatissci/whatissci.php
[2] Hunt K J et al.: A Pilot Study of Lower-limb FES Cycling in Paraplegia, 7th Annual Conference of the International Functional Electrical Stimulation Society (IFESS 2002) http://ifess.org/ifess02/therapeutic_stimulation/HuntKJ.pdf
[3] Szécsi J,Fiegel M, Krafczyk S, Straube A(2004) Smooth pedaling of the paraplegic cyclist – a natural optimality principle for adaptation of tricycle and stimulation to the rider, J.Rehabil. Res. Dev.,41 Supp.2: 30
[4] Szécsi J, Fincziczki Á, Laczkó J, Straube A. (2005): Elektrostimuláció segítségével meghajtott (háromkerekű) kerékpár: Neuroprotézis harántsérült páciensek mindennapos használatára. Rehabilitáció, 15. Évfolyam pp.9-14
[5] Szécsi J, Fincziczki A, Laczkó J, Klauber A (2006): Functional electrical stimulation for cycling of paraplegics: individual adaptation of the clinical environment in Hungary. 11th Annual Congress of the European College of Sport and Science, Book of abstracts, p.406.
[6] Pilissy T, Lábmozgások kinematikai és bioelektromos jellemzőinek modellezése gerincsérültek és egészségesek kerékpározó mozgásánál, Diploma work, 2007
[7] N Negard et al.: Application Programming Interface and PC control for the 8 channel stimulator MOTIONSTIM8, 10th Annual Conference of the International FES Society July 2005 – Montreal, Canada
[8] Pilissy T, Klauber A, Fazekas G, Laczkó J, Szécsi J: Improving functional electrical stimulation driven cycling by proper synchronization of the muscles, Ideggyogy Sz 2008;61(5–6)
[9] Pilissy T, Pad K, Fazekas G, Horváth M, Stefanik Gy, Laczkó J: The role of ankle-joint during cycling movement task. Proceedings of the 9th Congress of European Federation for Research in Rehabilitation, Budapest, Aug 26-29. 2007. Int J Rehabil Res 2007;30 (Suppl 1):58-59.

Amblyopia – New Options in Examination

Patrícia Domsa
(Supervisors: Dr. Zoltán Vidnyánszky, Dr. Viktor Gál)
domsa.patricia@itk.ppke.hu

Abstract

MOT experiments

The goal of our base study was to investigate the efficacy of visual attentional selection in amblyopia using the multiple object tracking (MOT) task. The results provide evidence that in amblyopic patients attentional tracking is less efficient in the case of visual information conveyed by the amblyopic eye as compared to that originating from the fellow eye.

In our first control experiment we tested healthy patients with artificially deteriorated vision, to explore the effect of impaired vision on MOT task performance. Artificially deteriorated vision control implies that vision deterioration can affect MOT performance but the mechanism differs from underlying amblyopia. We suggest, that randomization affected eye dominancy in MOT task.

Orientation integration tests:
Integration of orientation information across space is impaired in amblyopia. We plan to use a method developed by Ilona Kovács et al for quantifying orientation-domain processing. The test format is suitable for clinical application. The test comprises a graded series of cards where each card includes a closed path (contour) of high contrast Gabor signals embedded in a random background of Gabor signals. Contour visibility in both normals and patients with histories of abnormal binocular vision depends jointly on the spacing of elements on the contour as well as background element density. Firstly we plan to test healthy controls to investigate the learning effect of this kind of orientation integration test if used several times. Secondly we would like to test 4-5 years old children diagnosed with amblyopia just before occlusion, 6 weeks after the start point and the end of the therapy. The goal of our tests would be to find out, if occlusion can help to develop orientation integration in amblyops.

Digital visual acuity testing in kindergarten:
We developed a new software for visual acuity testing for children in kindergarten. The software is platform free, small, easy to use, not only for experts, but for nurses as well.
Vision and heterophory screening:
We started an amblyopia and heterophory screening program. We developed an amblyopia questioner for adults. We screened 24 patients and 5(21%) of whom were amblyopic. .After our successful first day we plan to continue our screening program.

Index Terms—**amblyopia, multiple object tracking, eye dominancy, orientation integration, visual acuity, test digital, children**

I. PATIENTS AND METHODS

The goal of our base study was to investigate the efficacy of visual attentional selection in amblyopia using the multiple obj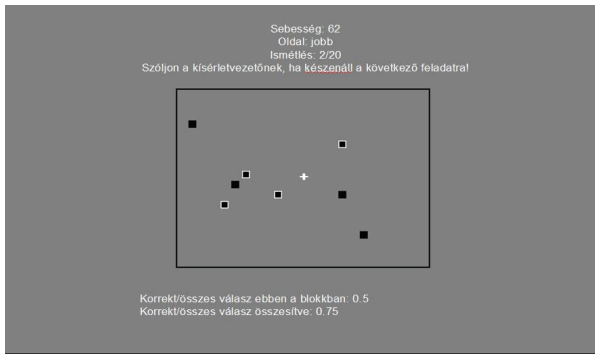ect tracking task, which require selection and tracking of a subset of visual objects in a visual display containing moving identical objects.

Participants
We assessed 15 adult patients with unilateral amblyopia and 15 controls on the multiple object tracking task. Both the amblyopic and the control group were tested monocularly and data were analyzed separately for the amblyopic and the fellow eye of the amblyops as well as the dominant and non-dominant eye of the controls. There were three testing conditions which differed in the speed of the moving objects.

Method
The display was a 16 • 12 deg dark-gray rectangle in which eight identical black squares (0.5 deg) moved in random fashion. At the beginning of the block bright white frame was flashing around four of the squares for 3 sec. After this all squares started to move in random fashion. The block duration was 12 sec. The discs ''bounced'' off the edge of the square and each other. Thus, the squares never occluded or collided with each other. We used three different velocity levels (2,8 deg/sec; 4,2 deg/sec; 6,2 deg/sec).

Figure 1. MOT task

II. RESULTS

ANOVA revealed a significant main effect of eye (F=11,806; p<0,0018) and speed (F=103,879; p<0,0001). It was found that patients with amblyopia performed significantly better with their fellow eyes than with their amblyopic eyes at all three speed levels tested (p<0,0282 at 2,8 deg/sec; p<0,0037 at 4,2 deg/sec; p<0,0457 at 6,2 deg/sec).

In the patients with amblyopia, there was a significant positive correlation between the Amblyopia Index (AI – the visual acuity of the amblyopic eye divided by the visual acuity of the dominant eye – Va/Vd) and the MOT performance (performance of the amblyopic eye divided by the performance of the dominant eye in the MOT task – Pa/Pd) at the low (p<0,04) and intermediate (p<0,01), but not at the highest speed tested (p>0,347).

III. CONCLUSION

Our results provide evidence that amblyopia affects attentional functions. In amblyopic patients attentional selection is less efficient in the case of visual information conveyed by the amblyopic eye as compared to that originating from the fellow eye.

IV. CONTROL STUDY WITH ARTIFICIALLY DETERIORATED VISION

The goal of the study was to investigate the effect of artificial vision deterioration of healthy patients on MOT task performance.

V. PATIENTS AND METHODS

Participants

We tested 15 healthy adult patients. We implemented artificial vision deterioration with glasses.

VI. RESULTS

ANOVA revealed a significant main effect artificial vision deterioration (F=17,495; p<0,000921) and speed (F=200,427; p<0,0001).

Patients performed MOT task worse with artificially deteriorated vision at all of the three speed levels. At the highest speed, with artificially deteriorated vision, the performance of the non-dominant eye was better. Performance on the MOT task was worse with artificially deteriorated, than with normal vision, but in the healthy patients, there was no correlation between the Amblyopia Index and the MOT performance at none of the three speeds tested.
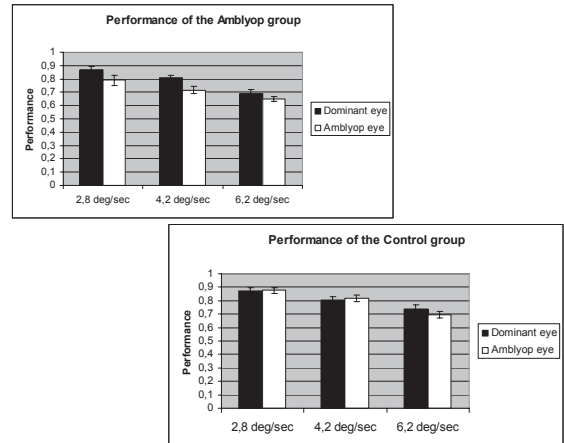

Figure 2. Performance of Amblyops and Control Group

CONCLUSION

Artificially deteriorated vision control implies, that vision deterioration can affect MOT performance but the mechanism differs from underlying amblyopia.

The effect of randomization on eye dominancy:

We suggest, that randomization affected eye dominancy in MOT task. Dominancy is not a wired status in healthy controls, but adjustment is contiguous in the visual system. If visual conditions necessitate eye dominancy can shift.

VII. TESTING ORIENTATION INTEGRATION IN AMBLYOPIA

Several studies have reported that the integration of orientation information across space is degraded in amblyopia. The initial studies in this area utilized a lateral masking paradigm.

We plan to use a card format that was developed by Ilona Kovács et al. and it is suitable for clinical staircase procedures, such as those used for Preferential Looking tests of grating acuity. Each card consisted of a smoothly aligned, closed

path of Gabor elements embedded in a random array of Gabor elements of the same spatial frequency and contrast. (Figure 1.) The average spacing between adjacent elements in the background relative to the spacing between neighboring elements along the contour defines a parameter which we refer to as Δ. The parameter Δ is the ratio of background spacing over contour spacing. Our test battery consists 15 cards. The cards differ in the location and the Δ ratio of the closed contour.
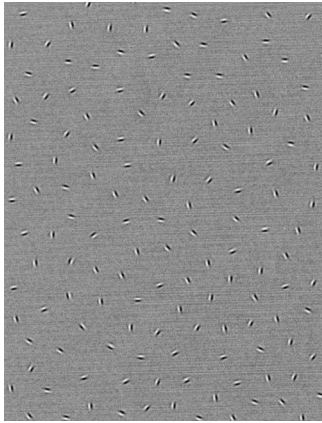
Figure 3. Example of the test cards used to assess the strength of spatial interactions in amblyopia. A closed path of Gabor signals is embedded in noise. The observer is asked to indicate the location of the contour.

Firstly we plan to test healthy controls to investigate the learning effect of this kind of orientation integration test if used several times in the same year. Secondly we would like to test 4-5 years old children diagnosed with amblyopia at three times: just before occlusion, 6 weeks after the start point and the end of the therapy. The goal of our tests would be to find out, if occlusion can help to develop orientation integration in amblyops.

VIII.   DIGITAL VISION TESTING IN KINDERGARTEN

We developed iLAB, a new software, suitable for vision testing in kindergarten. The first modul ready to use is the visual acuity test (VAT). The software is platform free, small, easy to use not only for experts, but for nurses as well.

Figure 4. iLAB start site

iLAB can save the personal datas by kindergarten groups. We specify our patients with name, birth date and health insurance number.
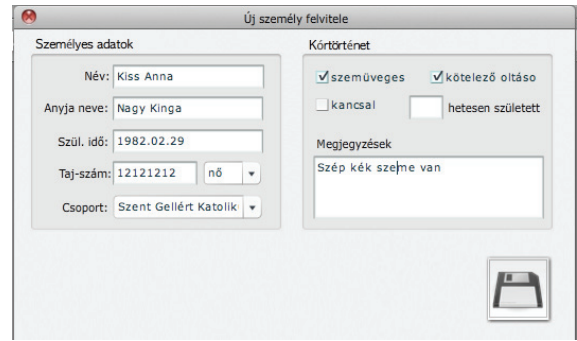

Figure 5. Personal data and notes

Our test battery consists 10 optotypes designed for 3-6 years old children. The original optotypes are 10x10cm size plastic cards, available in four picture sizes for 0.1, 0.3, 0.6 and 1.0 visual acuity.

Figure 6. Original optotypes

iLAB VAT starts with calibration of optotype view on the monitor in use. For the calibration process the user needs only a small ruler. User has to adjust the virtual scale on the monitor to the centimeter scale of the ruler.

Figure 7. Calibration

VAT starts with a pretest phase to make certain if the child to be tested can identify the objects on the optotypes.
We test VA monocularly. For the algorithm of optotype iteration we took into account the method of vision testing in the Amblyopia Treatment Study.
We would like to test our new software as soon as possible to find the accidental 'bugs' and to compare iLAB VAT to the original card test.
The next examination type we would like to digitalize and place to iLAB environment is stereo vision test.

IX. ADULT AMBLYOPIA SCREENING PROGRAM

We started an amblyopia and heterophory screening program. The idea came from our experiences with collecting subjects for our MOT experiments.

The amblyopia 'self diagnosis' of volunteers who came for the preliminary eye examination – students, friends, people reading our invitation on the internet – was wrong in many cases. It seems that the concept of amblyopia is missing from the common medical knowledge.

We developed an amblyopia questioner for adults.

Kérjük karikázza be az Ön által helyesnek ítélt választ!

Ön szerint mi az a tompalátás?
1. *Féloldali vagy kétoldali látásvesztés, vakság*
2. *Szemfenék meszesedésből adódó látásromlás*
3. *A megfelelő rövidlátó vagy távollátó szemüveg hiánya*
4. *Gyenge látás zavart látásfejlődés következtében*
5. *Szem szöveteinek homálya, csökkent átlátszósága*

Ön szerint mi a szemtengelyferdülés?
1. *Rejtett kancsalság*
2. *Látható kancsalság*
3. *Cilinderes szemüvegigény*
4. *Féloldali gyengénlátás*

Van-e Önnek kancsalsága?
1. *Nem*
2. *Igen, kívülről is látható*
3. *Igen, rejtett*
4. *Volt, de megoperálták*
5. *Nem tudom*

Ön tompalátó-e?
1. *Igen, véletlenül derült ki*
2. *Igen, gyermekkoromban kezeltek miatta*
3. *Nem*
4. *Nem tudom*

Visel szemüveget?
1. *Nem*
2. *Nem, pedig kellene*
3. *Igen, közelre*
4. *Igen, távolra*
5. *Igen közelre és távolra is*

Van-e Önnek dioptriakülönbség a két szeme között?
1. *Igen, nem tudom mennyi*
2. *Igen, több mint 3 dioptria*
3. *Igen, kevesebb, mint 3 dioptria*
4. *Nem*
5. *Nem tudom*

Figure 8. Amblyopia questioner

We decided to invent our screening program in a mall using the office of an optometrist friend. Designed throwaways and tagged T-shirts as marketing. Two ophthalmologists, an optometrist and three medical students participated on the first screening day.

We screened 24 patients and 5(21%) of whom were amblyopic. It seems that our 'marketing work' directed involved patients to us. After our successful first day we plan to continue our screening program.

REFERENCES

[1] Buckingham, T., Watkins, R., Bansal, P., & Bamford, K. (1991). Hyperacuity thresholds for oscillatory movement are abnormal in strabismic and anisometropic amblyopes. Optometry and Vision Science, 68, 351–356.

[2] Hess, R. F., Demanins, R., & Bex, P. J. (1997). A reduced motion aftereffect in strabismic amblyopia. Vision Research, 37, 1303–1311.

[3] Ho, C. S. & Giaschi, D. E. (2006). Deficient low-level and high-level maximum motion displacement in amblyopic children. Vision Research, submitted, under revision.

[4] Ho, C. S., Giaschi, D. E., Boden, C., Dougherty, R., Cline, R., & Lyons, C. (2005). Deficient motion perception in the fellow eye of amblyopic children. Vision Research, 45, 1615–1627.

[5] Levi, D. M. (1991). Spatial vision in amblyopia. In D. Regan (Ed.), Spatial Vision (pp. 212–238). London: MacMillan.S. Magnussen, "Low-level memory processes in vision," *Trends Neurosci.*, vol. 23, pp. 247-251, 2000.

[6] Ilona Kovács (2000). Human development of perceptual organization. Vision Research 40 (2000) 1301–1310

[7] Ilona Kovács, Uri Polat, Philippa M. Pennefather, Arvind Chandna, Anthony M. Norcia (2000). A new test of contour integration deficit sin patients with a history of disrupted experience during visual development. Vision Research 40 (2000) 1775–1783

Flawless Visual Short-term Memory for Facial Emotional Expressions

Éva M. Bankó

(Supervisor: Dr. Zoltán Vidnyánszky)

banko.eva@itk.ppke.hu

Abstract — **Facial emotional expressions are important cues of human social interactions. In contrast to facial identity, one's emotions are continuously changing and thus should be monitored, memorized and compared from time to time during social intercourse. However, it is not known how efficiently emotional expressions can be stored in short-term memory. Previously we have shown that facial emotion discrimination is just as good for novel as for familiar faces and it is not impaired when the faces to be compared are separated by several seconds. Here we prove that this flawless short-term memory for emotional expressions is indeed based on the storage of fine-grained emotion-related information in short-term memory: it requires the activation of posterior superior temporal sulcus and inferior frontal cortex, both considered as markers for processing of emotion-related facial information.**

Index Terms—**visual short term memory, changeable facial features, facial emotion, posterior superior temporal sulcus**

I. INTRODUCTION

FACIAL emotional expressions are crucial components of human social interactions. Among many of its important functions, emotional expressions are used to express our general emotional state (e.g. happy or sad); to show liking or dislike in everyday life situations; or to signal a possible source of danger. Therefore, it is not surprising that humans possess the ability to efficiently monitor emotional expressions and can effortlessly detect even subtle changes in emotional state. For this it is inevitable that we continuously attend to, memorize and compare emotional expressions of the persons we interact with. Despite that it is of paramount importance, to date there has been no study that was aimed at investigating how efficiently humans can store facial emotional information in visual short term memory.

In contrast to emotions, which are changeable facial attributes, there are facial attributes that on the short and intermediate timescale are invariant (such as identity or gender)[1,2]. While changeable cues require constant online monitoring during social interaction, the same does not hold true for facial identity. Moreover, it was shown that the processing of changeable and invariant facial attributes takes place on specialized, to a considerable extent independent functional processing routes [1,2]. Functional neuroimaging results suggest that facial identity might be processed primarily in the inferior occipito-temporal regions, including the fusiform face area [3,4], whereas processing of the information related to emotional expressions involves the superior temporal cortical regions [5,6,7,8,9,10].

In a previous study we investigated how efficiently humans can store facial emotional expressions and identity in visual short term memory and proposed a facial attribute discrimination task to measure it. The results provided behavioral evidence that the ability to compare facial emotional expressions and identity is not impaired when the emotion-related information has to be stored for a few seconds in short term memory; i.e. when the faces to be compared became separated by up to 10 seconds. However, it is crucial to show that performance in our facial attribute discrimination tasks is indeed based on high-level, face-specific attributes or attribute configurations as opposed to some intermediate or low level feature properties of the face images (e.g. local contour information, luminance intensity).

Previous studies have shown that increased fMRI responses in the posterior superior temporal sulcus (pSTS) during tasks requiring perceptual responses to facial emotions compared to those to facial identity can be considered as a marker for processing of emotion-related facial information. Therefore, we conducted an fMRI experiment to verify that the delayed emotion discrimination task proposed earlier and also used in the present study – requiring discrimination of very subtle differences in facial emotional expression – involved emotional processing and activated pSTS. fMRI responses were measured during delayed emotion (happiness) and identity discrimination with interstimulus intervals (ISI) of varying length: 5-8 s. Importantly, the same physical face stimuli were used in the emotion and in the identity tasks, thus the two conditions differed only in task instructions.

II. RESULTS

Subjects' accuracy during scanning was slightly better in the identity than in the emotion discrimination task (mean±SEM: 79.7±1.4% and 83.0±2.0% for emotion and identity tasks, respectively; $t_{(9)}$= -2.72, p=0.024). Reaction times did not differ significantly across task conditions (mean±SEM: 831±66 ms and 869±71 ms for emotion and identity, respectively; $t_{(9)}$=-1.49, p=0.168).

To asses the difference between the neural processing of the same face stimuli in the emotion and identity discrimination tasks, we contrasted fMRI responses in the emotion discrimination trials with those in the identity trials. We found significantly higher activations for the sample stimuli in the case of emotion compared to identity discrimination in the right posterior superior temporal sulcus (Br. 37, peak at x,y,z = 43, -55, 7; t=6.18, $p<0.01_{FDR}$, Figure 1B). This cluster of activation extended ventrally and rostrally along the superior temporal sulcus and dorsally and

rostrally into the supramarginal gyrus (Br. 22, x,y,z = 42, -28, 0; t=4.43; Br. 40, x,y,z = 45, -42, 25; t=4.87, $p<0.01_{FDR}$, centers of activation for mid-STS and supramarginal gyrus, respectively). Furthermore, we found five additional clusters with significantly larger activations in: left superior temporal gyrus (Br. 37, x,y,z = -51, -65, 7; t=4.91, $p<0.01_{FDR}$), left superior temporal pole (Br. 38, x,y,z = -45, 18, -14; t=4.70, $p<0.01_{FDR}$), bilateral prefrontal cortex: specifically in right inferior frontal gyrus (triangularis) (Br. 45, x,y,z = 51, 26, 7; t=4.73, $p<0.01_{FDR}$) and in left inferior frontal gyrus (opercularis) (Br. 44, x,y,z = -51, 14, 8; t=4.53 $p<0.01_{FDR}$) and finally, in left insula (Br. 13, x,y,z = -36, 8, 13; t=4.65 $p<0.01_{FDR}$). This network of cortical areas showing higher fMRI responses in the emotion than in the identity task is in close correspondence with the results of earlier studies investigating processing of facial emotions. Interestingly, in the case of fMRI responses to the test face stimuli, even though many of these cortical regions, including pSTS, showed higher activations in the emotion compared to the identity task, these activation differences did not reach significance. This is in agreement with recent findings [10], where the authors also failed to find significant difference between these conditions during the retrieval phase.

Since subjects' performance during scanning was slightly better in the identity discrimination condition than in the emotion discrimination we performed a further analysis to exclude the possibility that the observed differences in fMRI responses between the two conditions are due to a difference in task difficulty. For this, we selected three runs from each subject in which accuracy for the two tasks was similar and reanalyzed the fMRI data collected from these runs. Even though there was no significant difference between subjects' accuracy in the emotion and identity tasks in these runs (mean±SEM: 82.2±1.7% and 81.9±2.0% for emotion and identity tasks, respectively; $t_{(9)}$=0.145, p=0.889), the emotion vs. identity contrast revealed the same clusters of increased fMRI responses as when all runs were analyzed; including a significantly higher activation during the emotion discrimination task in the right posterior STS (peak at x,y,z = 45, -52, 4; t=5.08, $p<0.03_{FDR}$). Thus, our fMRI results provide evidence that discrimination of fine-grained emotional information required in our experimental condition led to the activation of a cortical network that is known to be involved in processing of facial emotional expression.

Although we did not track eye position during scanning, it appears highly unlikely that the difference between the fMRI responses in the emotion and identity discrimination task could
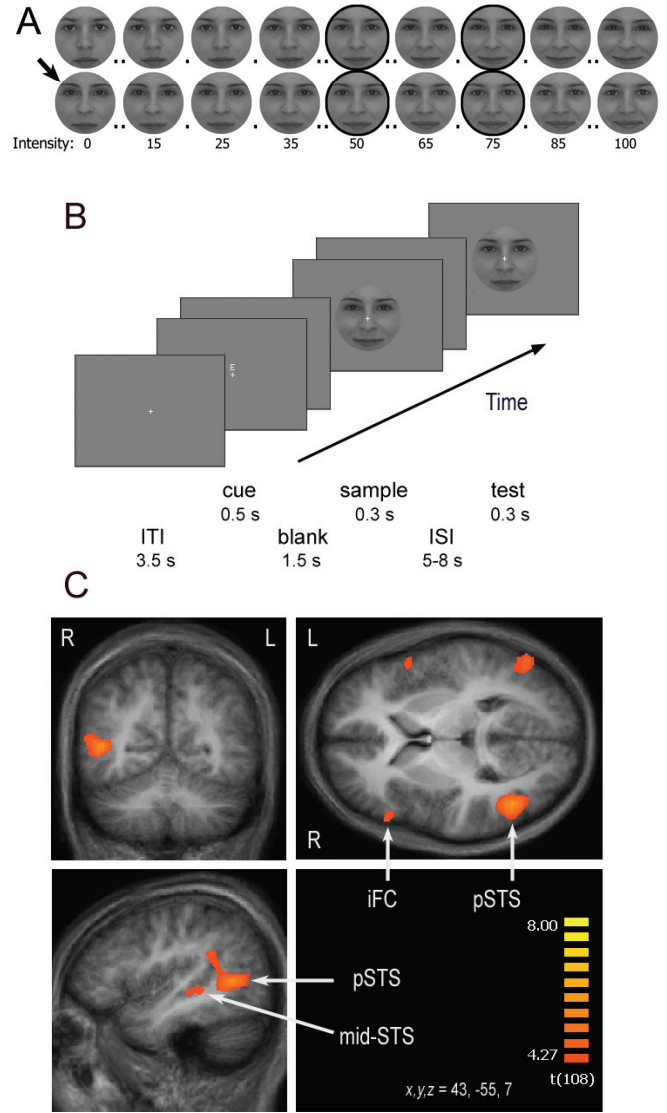

Fig. 1. Composite morphed face set, experimental design and fMRI responses for sample faces. (A) One of the two composite face set created in Winmorph. Black circles indicate a typical face pair used, yielding 75% performance. The reference face for the identity discrimination is denoted by an arrow. (B) Stimulus sequence showing the happy emotion discrimination task. (C) Emotion vs. identity contrast revealed significantly stronger fMRI responses during emotion than identity discrimination within right superior temporal sulcus (STS), (two clusters: posterior and mid), and right inferior frontal cortex (iFC). Coordinates are given in Talairach space; regional labels were derived using the Talairach Daemon [11] and the AAL atlas provided with MRIcro [12]

be explained by a difference in fixation patterns between the two tasks. Firstly, we recorded eye movements during the practice sessions prior to scanning and the data revealed no significant differences between the facial attributes (emotion vs. identity, $F_{(1,4)}$=1.15, p=0.343) or the task phases (sample vs. test, $F_{(1,4)}$=0.452, p=0.538) and there was no interaction between these variables ($F_{(1,4)}$=0.040, p=0.852). These indicate that there was no systematic bias in eye-gaze direction induced by the different task demands (attend to emotion or identity). Secondly, in the whole-brain analysis

of the fMRI data we found no significant differences in activations of the cortical areas known to be involved in programming and execution of eye movements (i.e. in the frontal or supplementary eye field, [11]) in response to emotion and identity discrimination tasks.

III. DISCUSSION

Bruce and Young has proposed a model of face recognition [12] in which it was assumed that recognition of facial identity and facial emotions takes place in separate functional processing routes. Since that, both behavioral as well as neurobiological results provided strong support that indeed, these two facial attributes are coded to a considerable extent separately in the brain. Based on the results of the extensive functional neuroimaging investigations of face processing in humans, Haxby and colleagues developed the notion of the separate processing of facial identity and facial emotions into a detailed neurobiological model of the processing of different facial attributes [1]. The central statement of this model is that invariant (e.g. identity, sex) and changeable (e.g. emotions, eye gaze) facial attributes are coded by functionally and neurologically different visual pathways: involving the inferior occipital gyrus and lateral fusiform gyrus in the former and the inferior occipital gyrus and superior temporal sulcus in the later case. Interestingly, while the anatomical dissociation of the neural representation of changeable and invariant facial attributes has been extensively investigated the question how neural and perceptual processing is specialized to suit the specific input properties and task demands characterizing these different attributes received little attention. The neural mechanisms underlying the superior capacity of visual short term memory for facial expressions remains to be uncovered. Interestingly, a recent fMRI study [10] found that, although initial processing of emotion and identity is accomplished in anatomically segregated temporal and occipital regions, sustained, delay related activations in case of these two features overlapped in the orbitofrontal cortex, amygdala and hippocampus.

To conclude, the findings of the present study show that the previously shown perfect resolution visual short-term memory for facial emotional expressions is based on processing and retaining of emotional expressions. Such flawless short term memory is inevitable for the ability to efficiently monitor emotional expressions and it is tempting to propose that impairment of such high-precision short term memory storage of emotional information might be one of the possible causes of the deficits of emotional processing found in psychiatric disorders including autism and schizophrenia [13].

IV. EXPERIMENTAL PROCEDURES

A. Subjects

Thirteen subjects participated in this experiment. However, fMRI and concurrent psychophysical data of three participants were excluded due to excessive head movement in the scanner, leaving a total of ten right-handed subjects (6 females, mean age: 24 years). None of them had any history of neurological or ophthalmologic diseases and all had normal or corrected-to-normal visual acuity.

B. Stimuli and Procedure

Stimuli were derived from front view pictures of two females and two males with neutral and happy facial expressions. Faces were cropped and covered with a circular mask. For test stimuli face sets were generated with a morphing algorithm where both facial expression and identity changed gradually by morphing a neutral face of one facial identity with the happy face of another identity and visa versa: the happy face of the first identity with the neutral face of the second to minimize correlation between the two attributes. Stimuli (8 deg) were presented centrally (viewing distance of 60 cm) on a uniform grey background. Emotion and identity discrimination was measured by a two-interval forced choice procedure using the method of constant stimuli. Subjects were required to report which of two successively presented faces, termed sample and test, had the more happy facial expression or resembled more to the reference identity. We used the same composite face sets for both tasks to ensure that the physical properties of the stimuli were the same (there were no stimulus confounds) and the conditions only differed in which face attribute subjects had to attend to make the discrimination.

In the main experiment, six (3+3) face pairs yielding 75% performance were used from each composite face set, selected based on the performance in a practice session prior to the experiment. Trials of emotion and identity discrimination tasks were presented within a block in an optimized pseudorandomized order to maximize separability of the different tasks. For each subject the same trial sequence was used.

Visual stimuli were projected onto a translucent screen located at the back of the scanner bore using a Panasonic PT-D3500E DLP projector (Matsushita Electric Industrial Co., Osaka, Japan) at a refresh rate of 75 Hz. Stimuli were viewed through a mirror attached to the head coil with a viewing distance of 58 cm. Head motion was minimized using foam padding.

A trial began with a task cue (0.5 deg) appearing just above fixation for 500 ms being either 'E' for emotion and 'I' for identity discrimination. Following a blank fixation of 1530 ms the faces appeared successively for 300 ms separated by a long ISI of varied length. The ITI was fixed in 3.5 s, which also served as the response window. The ISI varied between 5 and 8 seconds in steps of 1 s to provide a temporal jitter. Subjects performed 24 trials for each of the seven functional runs (12 trials of emotion and 12 trials of identity discrimination), for a total of 168 trials.

Before scanning, subjects were given a separate practice session where they familiarized themselves with the task and the image pairs with approximately 75% correct performance were determined. Eye movements of five randomly chosen subjects were recorded in this session by an iView XTM HI-Speed eye tracker (Sensomotoric Instruments, Berlin, Germany) at a sampling rate of 240Hz. In all experiments the stimulus presentation was controlled by MATLAB 7.1. (The MathWorks, Inc., Natick, MA) using the Psychtoolbox 2.54 [14]

C. Data Analysis

1) Behavioral data analysis

Responses and reaction times were collected for each trial during the practice and scanning sessions to ensure subjects were performing the task as instructed. Accuracy and mean RTs were analyzed with paired t-tests.

2) Analysis of eye-tracking data

Eye-gaze direction was assessed using a summary statistic approach. Trials were binned based on facial attribute (emotion vs. identity) and task phase (sample vs. test) and mean eye position (x and y values) was calculated for periods when the face stimulus was present on each trial. From each of the four eye-gaze direction dataset, spatial maps of eye-gaze density were constructed and then averaged to get a mean map for comparison. Subsequently, each of these maps was compared with the mean map and difference images were computed. The root mean squares of the density difference values for these latter maps were entered into a 2×2 ANOVA [9].

3) fMRI imaging and analysis

Data acquisition. Data were collected at the MR Research Center of Szentágothai Knowledge Center, (Semmelweis University, Budapest, Hungary) on a 3.0 Tesla Philips (Best, The Netherlands) Achieva scanner equipped with an eight-channel SENSE head coil. High resolution anatomical images were acquired for each subject using a T1 weighted 3D TFE sequence yielding images with a $1\times1\times1$ mm resolution. Functional images were collected using 31 transversal slices (4 mm slice thickness with 3.5×3.5 mm in-plane resolution) with a non-interleaved acquisition order covering the whole brain with a BOLD-sensitive T2*-weighted echo-planar imaging sequence (TR=2 s, TE=30 ms, FA=75°, FOV=220 mm, 64×64 image matrix, 7 runs, duration of each run=516 s).

Data analysis. Preprocessing and analysis of the imaging data was performed using BrainVoyager QX (v 1.910; Brain Innovation, Maastricht, The Netherlands). Anatomicals were coregistered to BOLD images and then transformed into standard Talairach space. BOLD images were corrected for differences in slice timing, realigned to the first image within a session for motion correction and low-frequency drifts were eliminated with a temporal high-pass filter (3 cycles per run). The images were then normalized into standard Talairach space and spatially smoothed using a 6 mm full-width half-maximum Gaussian filter. Based on the results of the motion correction algorithm runs with excessive head movements were excluded from further analysis leaving 10 subjects with 4-7 runs each.

Functional data analysis was done by applying a mass univariate general linear model (GLM) for an event-related design. First, delta functions were constructed corresponding to the onset of each event type (emotion vs. identity discrimination × sample vs. test face). Then these delta functions were convolved with a canonical hemodynamic response function (HRF) to create predictors for the subsequent GLM. Temporal derivatives of the HRFs were also added to the model to accommodate different delays of the BOLD response in the individual subjects. Analysis was based on a two-level GLM. For the first-level anaysis, individual data was modeled with two (face attribute: emotion vs. identity) × two (type of face: sample vs. test) × two (temporal derivatives of each predictor) predictors. Next, the resulting β weights of each current predictor served as input for the second-level whole-brain random-effects analysis, treating subjects as random factors. Linear contrasts pertaining to the main effects were calculated and the significance level to identify cluster activations was set at p<0.01 with false discovery rate (FDR) correction.

REFERENCES

This is paper is an excerpt of an article of the same title submitted to Journal of Vision.

[1] J. V. Haxby, E. A. Hoffman and M. I. Gobbini, "The distributed human neural system for face perception," *Trends Cogn. Sci.*, vol. 4, pp. 223-233, 2000.

[2] A. J. Calder and A.W. Young, "Understanding the recognition of facial identity and facial expression," *Nat. Rev. Neurosci.*, vol. 6, pp. 641-651, 2005.

[3] N. Kanwisher, J. McDermott, and M.M. Chun, "The fusiform face area: a module in human extrastriate cortex specialized for face perception," *J. Neurosci.*, vol. 17, pp. 4302-4311, 1997.

[4] J.V. Haxby et al., "Distributed and Overlapping Representations of Faces and Objects in Ventral Temporal Cortex," *Science*, vol. 293, pp. 2425-2430, 2001.

[5] M.E. Hasselmo, E.T. Rolls, and G.C. Baylis, "The role of expression and identity in the face-selective responses of neurons in the temporal visual cortex of the monkey," *Behav. Brain Res.*, vol. 32, pp. 203-218, 1989.

[6] J. Narumoto et al., "Attention to emotion modulates fMRI activity in human right superior temporal sulcus," *Brain Res. Cogn. Brain Res.*, vol. 12, pp. 225-231, 2001.

[7] P. Vuilleumier et al., "Effects of Attention and Emotion on Face Processing in the Human Brain - An Event-Related fMRI Study," *Neuron*, vol. 30, pp. 829-841, 2001.

[8] T.J. Andrews and M.P. Ewbank, "Distinct representations for facial identity and changeable aspects of faces in the human temporal lobe," *NeuroImage*, vol. 23, pp. 905-913, 2004.

[9] J.S. Winston et al., "fMRI-adaptation reveals dissociable neural representations of identity and expression in face perception," *J. Neurophysiol.*, vol. 92, pp. 1830-1839, 2004.

[10] M.L. LoPresti et al., "Working memory for social cues recruits orbitofrontal cortex and amygdala: a functional magnetic resonance imaging study of delayed matching to sample for emotional expressions," *J. Neurosci.*, vol. 28, pp. 3718-3728, 2008.

[11] K.A. Dyckman et al., "An effect of context on saccade-related behavior and brain activity," *NeuroImage*, vol. 36, pp. 774-784, 2007.

[12] V. Bruce and A. Young, "Understanding face recognition," *Br. J. Psychol.*, vol. 77, pp. 305-327, 1986.

[13] N. Sasson et al., "Orienting to social stimuli differentiates social cognitive impairment in autism and schizophrenia," *Neuropsychologia*, vol. 45, pp. 2580-2588, 2007.

[14] D.H. Brainard, "The Psychophysics Toolbox," *Spatial vision*, vol. 10, pp. 433-436, 1997.

Neural Dynamics of Shape-specific Visual Information Processing in Amblyopia

Judit Körtvélyes
(Supervisor: Dr. Zoltán Vidnyánszky)
kortvelyes.judit@itk.ppke.hu

Abstract— **Amblyopia is a visual disorder starting at early childhood. It has been shown recently that in amblyopia - in addition to the well known deficits in contour integration, encoding of visual position and motion perception – there is also an impairment of high-level shape processing. It was also suggested that the impairment of shape perception is primarily confined to the fovea and that it might be specific for the processing of visual faces. We used event related potentials (ERP) to investigate the dynamics of shape processing in amblyopia in case of foveal as well as perifoveal presentation of the visual stimuli. We also aimed at uncovering the category specificity of the possible impairment of the shape processing in amblyopia by using human faces as well as human hands as stimuli. Our preliminary results - in accordance with previous findings – revealed that deficits in shape processing are indeed confined to the central, foveal vision in amplyops. Furthermore, our findings also suggest that the deficit in amblyopia is not restricted to processing of visual faces but it extends to other categories, including processing of human hands.**

Index Terms— **amblyopia, object processing, perception of visual faces and hands**

I. Introduction

Amblyopia commonly known as lazy eye, is a developmental visual disorder, (affecting about 2% of the population) which starts at an early age. A key issue in its treatment is an early diagnosis. For best results correction should happen no later then 3-5 years. It can caused by strabismus, deprivation and anisometropia [6].

In amblyopia there is a decline in (specific for different types):

- Visus (Snellen, Landolt C)
- Contour integration [5]
- Encoding of visual position
- Motion perception [4]

However, visual loss in amblyopia is not restricted to reduced visual acuity and deficits in spatial vision. Recently, it was suggested that *attentional functions* and *object perception* might also be impaired in amblyops.

Malach et al. found that face-related cortical areas show a severe disconnection from the amblyopic eye, while the connection of building-related regions remain essentially normal using fMRI [1].

There is a special region in extrastriate cortex, fusiform face area (FFA), which response correlates with and hence probably involved in, both the detection and identification of faces [2].

In another experiment of Malach et al. the visual stimuli were used to map the size-related activation. Stimuli were colored in red and green to separate stimulation to the amblyopic and the dominant eye; red–green glasses were used to view the images. The large stimuli had a hole placed on the fixation spot for better isolation of the foveal activation. They found drastic reduction in the cortical reactivity to small images when they were presented to the amblyopic eye. Moreover, there was a greatly reduced activation by small images in low-level retinotopic as well as center-related high-order regions both for individual subjects and for the groups. In contrast, there was no deficit in these cortical activations when the large-object stimuli were used. It suggests selective fovea-related deprived activation in retinotopic and high-order visual cortex of human amblyops [3].

II. Goal

The goal of the experiment was to investigate the *category specificity* of impairment of object processing in amblyopia and find differences between *foveal and perifoveal vision*. Our aim was also to investigate the *dinamics* of information processing in amblyopia using ERP.

III. Experimental Procedures

A. Subjects

Nineteen naive, healthy control subjects (eight females, mean age was 25 years) gave their informed and written consent to participate in the study. None of them had any history of neurological diseases or ophthalmologic diseases and were not under medication. All of them had normal or corrected-to-normal visual acuity.

Twenty naive, amblyop patients (ten females, mean age was 27,2 years) gave their informed and written consent to participate in the study. None of them had any history of neurological diseases or other ophthalmologic diseases than

strabismus or/and anisometropia and all had best corrected visual acuity (Table 1.). None of them were under medication.

Patient	BCVA d F	BCVA s F	BCVA d N	BCVA s N	Etiology of amblyopia
Zeda	1,0	0,8	1,0	1,0	hypermetropia
Szvi	0,25	1,0	0,8	1,0	anisometropia
Mecs	1,0	0,25	1,0	0,67	anisometropia
Decs	0,4	1,0	1,0	1,0	strabismus, anisometropia
Hoba	1,0	0,5	1,0	1,0	anisometropia
Toka	1,0	0,6	1,0	0,9	anisometropia
Recs	1,0	1,0	0,1	0,2	strabismus, anisometropia
Szba	1,0	0,25	1,0	0,67	anisometropia
Kova	1,0	0,1	1,0	0,3	strabismus, anisometropia
Acad	1,0	0,7	1,0	0,8	strabismus
Csdo	1,0	0,7	1,0	0,8	anisometropia
Soev	0,3	1,0	0,4	1,0	anisometropia
Veat	1,0	0,3	1,0	0,6	anisometropia, hypermetropia
Kofa	1,0	0,2	1,0	0,25	anisometropia
Neba	1,0	0,7	1,0	1,0	strabismus
Hokl	1,0	1,0	0,15	0,4	anisometropia
Kozs	1,0	0,1	1,0	0,1	strabismus, anisometropia
Veor	1,0	0,6	1,0	1,0	strabismus
Baar	1,0	0,15	1,0	0,3	microstrabismus, hypermetropia
Csat	1,0	0,1	1,0	0,2	strabismus

Table 1.: Patients data, BCVA (best corrected visual acuity; d: right eye, s: left eye, F: for far, N: for near) and etiology of amblyopia

B. Eye dominance

We determined the eye dominance of the subjects by the Dolman method also known as the "hole-in-the-card test". According to the Dolman method the subject is given a card with a small hole in the middle, instructed to hold it with both hands, then instructed to view a distant object through the hole with both eyes open. The subject then alternates closing the eyes or slowly draws the hole close to the head to determine which eye is viewing the object (i.e. the dominant eye) [7]. We used a cd instead of the card and the subject had to fixate our nose as a distant object to make the test more objective. We repeated it 10 times.

The dominant eye of the amblyop patients correspond with their non amblyopic eye.

During the experiment every subject was tested with both eyes separately. The other eye was patched.

C. Stimuli and Procedure

Psychophysics:

Stimuli were front view pictures of faces and hands on different noise levels. Stimuli were covered with a circular mask eliminating the outer contours (screen refresh rate was 85 Hz). The different noise levels were generated with Fourier phase randomization.

Subjects were tested in a dimly lit room. They were instructed to fixate a blue spot in the center of the monitor and to perform a two-alternative forced choice face hand discrimination task by pressing either the left or right mouse button when they perceived a face or a hand, respectively. Stimuli were presented using the method of constant stimuli. Trials were initiated by the subjects by pressing either of the response buttons.

We used 4 different faces and 4 different hands (Fig. 1.) on different noise levels (Fig. 2.) and in different sizes: perifoveal (visual angle was 15 degree) with 1,5 degree hole placed on the fixation spot for better isolation of the foveal activation and foveal (visual angle was 2 degree) stimuli (Fig. 2.). They were presented centrally (viewing distance of 50cm) on a uniform black background. Stimuli were displayed for 250 ms, and appeared in a random order. Between two stimuli only the fixation point was present. The interval delay was 0,7sec with 0,2sec jitter.

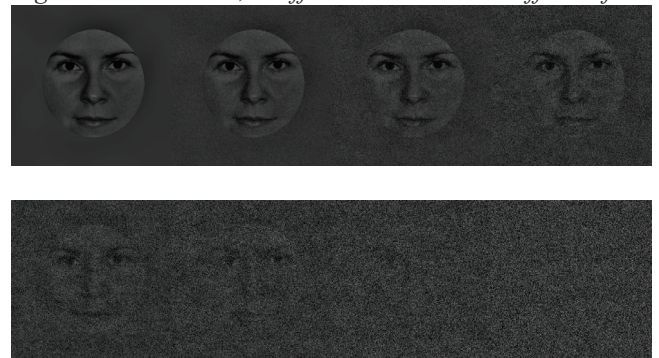*Fig 1.: Visual stimuli, 4 different hands and 4 different faces*

Fig. 2.: Visual stimuli on different noise levels

Each block contained 288 trials (six different noise levels for four different hands and for four different faces, repeated six times). The six levels of noise were determined upon performance. Four different blocks were presented monocular to the participants (perifoveal and foveal images used the dominant and the non dominant eye separately), each being repeated two times. Block order was randomized across subjects.

All software was written in MATLAB 7.0.4. (Mathworks Inc.) using Psychtoolbox 2.45 for Windows.
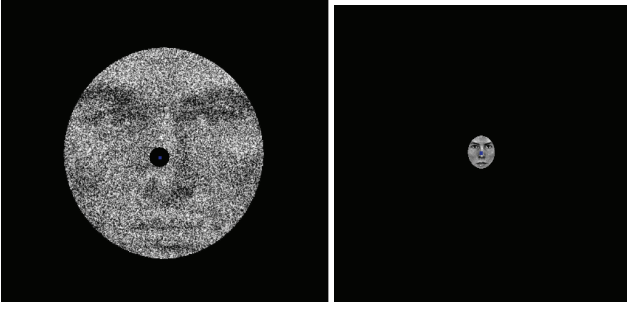
Fig. 3.: Visual stimuli, perifoveal (visual angle 15 degree) and foveal (visual angle 2 degree) stimuli

EEG:

To identify the components related to perceptual decision making, we measured the psychophysical performance of subjects while simultaneously recording neuronal activity using a high-density EEG electrode array (64 channels). EEG data were acquired using a BrainAmp (Brain Products GmbH). EEG was recorded with 60 Ag-AgCl scalp electrodes (BrainCap) plus four periocular electrodes placed above and below the right eye and at the left and the right outher canthi. All channels were referenced to the earlobes while the ground was placed on the nasion. Electrode impedance was kept below 5kΩ.

Altogether ERPs were recorded for 70-80 min. During the experiment subjects were asked to refrain from movements and blinking.

Eye Tracker:

We used eye tracking (iView X System) to control the fixation of the participants. iView X uses infrared cameras to capture the eye movements. Images of the eye are analysed in real-time with video field rate, resulting in a 280Hz sampling rate.

The eye tracker uses contrast to locate the center of the pupil and uses infrared light to create a corneal reflexion (CR). The vector between these two features can be used to compute gaze intersection with a surface after a simple calibration for an individual.

D. Data Analysis

Psychophysics:

Psychophysical data obtained with perifoveal and foveal images viewed with dominant and non dominant eye were analyzed separately. Data were modeled by Weibull psychometric function.

EEG:

EEG data analysis was performed with BrainVision Analyser (Brain Products GmbH).

Data were sampled at 1000Hz with an analog pass band of 0,016-250Hz using 12dB/octave high-pass filter. Subsequently, a software-based 0,5Hz 12dB/octave high-pass filter was used to remove DCdrifts, 30Hz 24dB/octave high-pass filter, and a 50Hz notch filter was applied to minimize line-noise artifacts. All filters were fourth-order zero phase Butterworth filters.

EEG was segmented into 800ms long trials, using a 200ms prestimulus interval for baseline correction. Trials containing movements, EEG baseline drift were rejected by automatic artifact detection. All trials with activity exceeding ±50μV measured on the four periocular electrodes were rejected as blink artifacts.

ERPs were averaged separately for each subject, condition and channel.

IV. RESULTS

Psychophysics:

There was no difference in performace of the control group between the dominant and non dominant eye in neither of the tested conditions (Fig. 5.).

However, the amblyops performed worse with their amblyopic eye as compared to the fellow eye when the stimuli were presented foveal. Whereas in the case of perifoveal stimuli there was no difference between the amblyop and fellow eyes of the amblyops and their performance was similar to the performance of the control group (Fig. 6.).

The impairment in case of foveal stimuli – both for hands and faces - was especially pronounced in amblyop subjects with very low visual acuity. Importantly, however, even in the strong amblyops there was no difference between the amblopic and fellow eye in case of perifoveal stmuli.
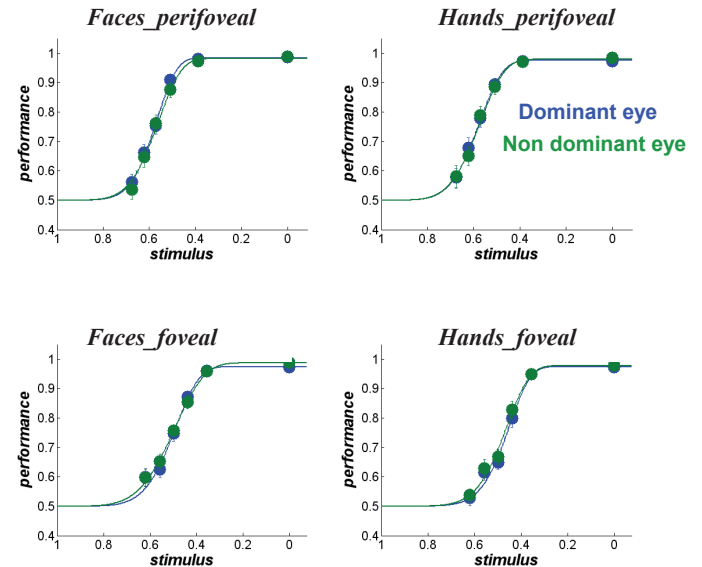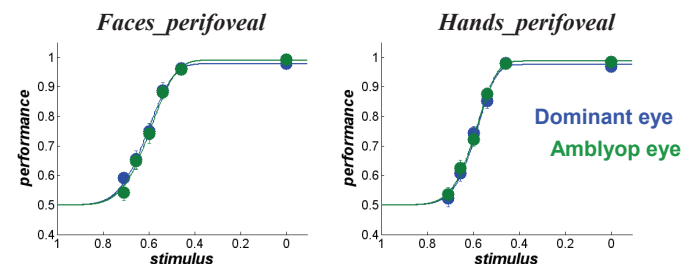

Fig. 5.: Average performance of the control group in the face vs. hand discrimination task on different noise levels
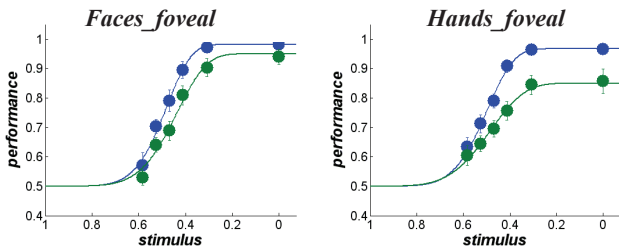
Fig. 6.: Average performance of the amblyop group in the face vs. hand discrimination task on different noise levels

EEG:

ERPs were averaged separately for each condition and channel. One of the most representative channel is O2 localised over the visual cortex selected for presentation.

Our preliminary analysis of the ERP results obtained so far revealed that there is a noise-level dependent modulation of the late ERP components starting from 200ms both in the patient and the control group (Fig. 7.). In all of the conditions except the case of foveal stimuli viewed with the non dominant eye ERPs look similar between the amblyops and control group. However there is a drastic decrease in the amplitude of ERP component evoked by the foveal stimuli in the amblyopic compared to the control group which supports the theory of foveal impairment of the amblyops (Fig. 8.).

Fig 7.: Decrease in the amplitude of ERP components evoked by the foveal stimuli in the amblyopic eye

REFERENCES

[1] Y. Lerner, P. Pianka, B. Azmon, H. Leiba, C. Stolovitch, A. Loewenstein, M. Harel, T. Hendler, and R. Malach, "Area-Specific Amblyopic Effects in Human Occipitotemporal Object Representations," *Neuron*, vol. 40, pp. 1023–1029, 2003.

[2] K. Grill-Spector, N. Knouf & N. Kanwisher, "The fusiform face area subserves face perception, not generic within-category identification," *Nature Neuroscience,* vol, pp. 2004.

[3] Y. Lerner, T. Hendler, R. Malach, M. Harel, H. Leiba, C. Stolovitch, and P. Pianka, "Selective fovea-related deprived activation in retinotopic and high-order visual cortex of human amblyopes," *NeuroImage*, vol. 33, pp. 169–179, 2006.

[4] C. S. Ho, D. E. Giaschi, C. Boden, R. Dougherty, R. Cline, C. Lyons, „Deficient motion perception in the fellow eye of amblyopic children," *Vision Research,* 2005.

[5] S. P. McKee, D. M. Levi, J. A. Movshon, "The pattern of visual deficits in amblyopia," *Journal of Vision*, vol. 3, pp. 380-405, 2003.

[6] J. M. Holmes, M. P. Clarke, "Amblyopia," *Lancet* vol. 367. pp. 1343-51, 2006.

[7] Cheng CY, Yen MY, Lin HY, Hsia WW, Hsu WM. "Association of ocular dominance and anisometropic myopia." *Invest Ophthalmol Vis Sci.* 2004 Aug;45(8):2856-60.
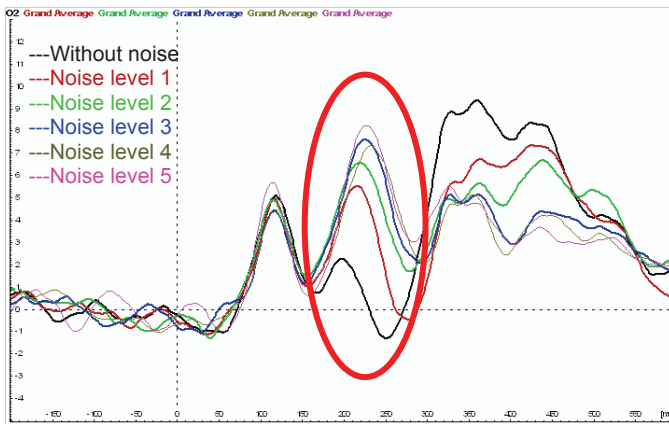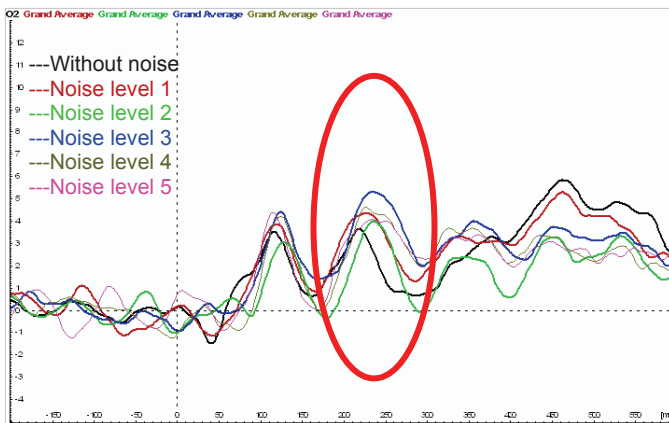
Fig 7.: Noise-level dependent modulation of the late ERP components in the case of foveal hands in the amblyop group viewed with the dominant eye

Extraction of Moving Persons in Video with Strong Motion and Noise

Dániel Szolgay

(Supervisors: Dr. Jenny Benois-Pineau, Dr. Tamás Szirányi and Dr. Tamás Roska)
szoda@digitus.itk.ppke.hu

Abstract—**Human silhouette detection is an important task in the field of image processing. In this paper a method is presented for silhouette detection for moving cameras, based on ego motion. Objects with ego motion are detected through the estimation of the camera motion and by building a probabilistic background model. This background model helps to eliminate the noise coming from quantization and the change of the perspective.**

Index Terms—Human Silhouette Detection, Motion Compensation, Ego Motion

I. INTRODUCTION

The video surveillance for the purposes of healthcare and home assistance to elderly people is getting more and more into the focus of research. With the ageing of population in the world, the care of dementia diseases becomes one of the medical priorities. Impairment in Instrumental Activities of Daily Living (IADL) related to cognitive decline is a major diagnostic criterion for Dementia [1]. However a valid evaluation of this criteria is often difficult to obtain because of deny or anosognosia by the patient, or by his caregiver [2]. Thus, an objective and operational tool designed to evaluate IADL functions could be of major interest in clinical or epidemiological studies on Dementia.

A project is going on under the name of "Wearable video monitoring", which aims to help the detection of aged dementia. The basic idea is to monitor the patients in their natural environment to give the medical practitioners a better overview about the state of the patient.

The patient wears a light recording set (a low cost camera, microphone and a radio transmitter). The recorded picture and sound is transmitted to a PC in 100 meter range.

Four laboratories are participating in this project from the University of Bordeaux 1 and 2 and the University Paul Sabatier. This paper concentrates mainly on the work done in LaBRI (Laboratoire Bordelais de Recherche en Informatique) in the field of human silhouette detection. For a global overview on the project, please see [3].

The paper is organized as follows: in Section 2 we give a brief overview about the existing human detection methods, in Section 3 the general scheme of the proposed method is introduced. The detailed description is in Section 4, while the conclusion and future plans can be found in Section 5.

II. HUMAN DETECTION METHODS

Human detection is an active research area with many different approaches, some of them can detect humans directly with a detector, trained on the features of human appearance, others indirectly, through foreground modelling

A. Direct Methods

The direct methods use trained human classifier and scan the image with a detection window. The main difference between these methods is the feature the classifier uses. Haar-like features were a popular choice [5] because it can be calculated fast, using integral image, however later researches show that histogram of oriented gradients [6] are outperform them in sense of precision and with certain restrictions the integral image technique can also be used [7].

The main drawbacks of these methods are the computational complexity, and the difficulty of handling the wide range of the appearance and pose of a human body.

B. Foreground Detection

Other methods are based on the assumption that the human is moving and with a background model ([8] [9], [10]) it can be distinguished from the other parts of the image. These methods do not require any a priori information about the moving object, but for this reason they detect not only the object of interest, but also other moving objects and noise (e.g. the shadow cast by the object).

One of the most popular approaches is the Mixture of Gaussians model which estimates each image pixel probability density function with not just one, but multiple Gaussian functions. The number of Gaussians can be fix [8] or varying [9].

Foreground detection is more complex task when the camera is moving. In this case to find objects with ego motion, the camera motion has to be compensated first [3], [4]. Then with the compensated frames the same background building techniques can be applied, however the result might be much noisier depending on the magnitude of the camera motion and the changing in the perspective. Another possibility is, after compensating the camera motion, simply calculate the difference of two consecutive frames and the result error image will give back those regions that are moving independently from the camera.

C. Used Methods

In this work we use the difference of consecutive frames after motion compensation and try to eliminate the noise through building the background on the error image. The building of this background model is similar to the one discussed in [10], however we are working with moving camera and calculating the model on the error image to

exclude constantly appearing false positive foreground parts.

We are using the foreground image not only for human detection, although for privacy reasons it is a very important. All the humans on the picture have to be detected, otherwise the records cannot be given to the doctors. To achieve this task we need a detector trained on human appearance model. Assuming that the humans are moving, they are part of the foreground, which means the detector has to scan only the foreground areas. At the present state of the work the direct human detector is not part of the system.

III. GENERAL SCHEME OF THE PROPOSED HUMAN DETECTION METHOD

To detect silhouettes on the records, first the camera motion has to be compensated between two consecutive frames. After the compensation the two frames have the same coordinate system and the error image can be calculated as the difference of the frames. This error image should contain only the foreground regions. However, due to quantization error, changes in the perspective, and other sources of noise (transmission noise, strong motion blur, etc.), the foreground contains a lot of false positives. To eliminate this noise we use a background model, built on a modified error image which contains not only luminance but colour information also. We filter the error image based on the information of the background model and use a density based classifier on the remaining foreground points to build foreground objects. By estimating the camera angle, the objects transformed to upright position.

In the future we will add an appearance based human detector to decide whether the object is a human or not.

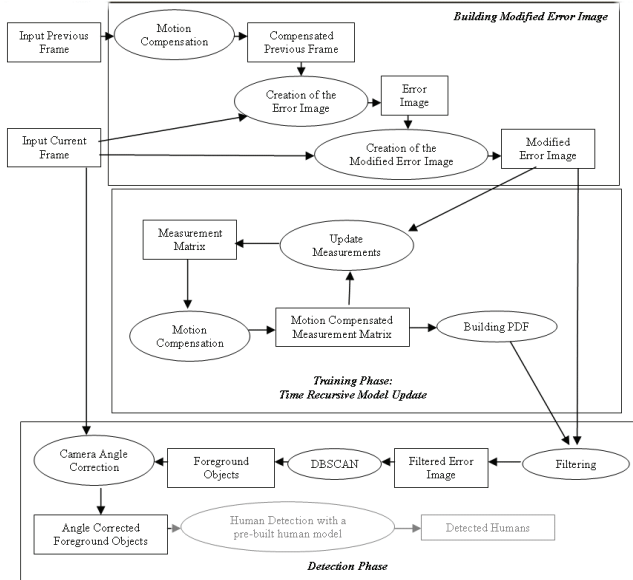The diagram shows the main steps of the algorithm.

Fig. 3. Diagram of the Silhouette Extraction Method

IV. DETAILED DESCRIPTION OF THE PROPOSED HUMAN DETECTION METHOD

A. Building of the Modified Foreground Image

Let $I(k-1)$, $I(k)$ be two consecutive frames. Based on the camera motion, using the method introduced in [4] we transform $I(k-1)$ according to the camera motion between

the two frames $I(k-1)$, $I(k)$. We use this transformed image, $\tilde{I}(k-1)$ to calculate an error image $E(k)$, which shows only those objects that are moving independently from the camera:

$$E(k) = \left| \tilde{I}(k-1) - I(k) \right| \qquad (4)$$

Fig. 4. The current frame (left) and the error image (right).

The modified error image at time t, is containing the colour information of the original frame on those (x,y) points, where, the value of the error image, $E(x,y,t)$ is significant. More formally, the modified error image, E^m is built as follows:

$$E^m(x,y,t) = \begin{cases} I(x,y,t) & if \quad E(x,y,t) > threshold \\ 0 & if \quad E(x,y,t) \le threshold \end{cases} \qquad (5)$$

where I is a 3 channel frame taken by the camera at time t, E is the grey scale error image at time t. The threshold value is currently set to 10. The resulted error image contains colour information, which will be useful at the decision making step.
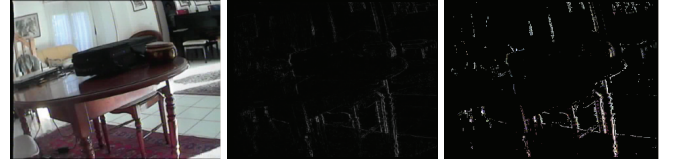

Fig. 5. The original frame (left), grey scale error image (middle) and the modified error image (right)

B. Foreground Detection

During the training phase a *measurement matrix*, M is built. This matrix contains the information of modified error images, in N consecutive time instances.

The updating of the measurement matrix at time t means, that we add the information of the modified error image of time t, to the previous measurement matrix at time $t-1$. To do this the camera motion between time instance $t-1$ and t has to be compensated first.

$$M(x,y,t) = \Theta_t M(x,y,t-1) \cup E^m(x,y,t)$$
$$M(x,y,1) = E^m(x,y,1) \qquad (6)$$

Here the operator $\cup$ means adding new "plane" of measurements to the measurement matrix, while the "oldest plane" is being removed, thus the number of planes in the matrix remains always the same.

The operator Θ_t stands for the affine transformation with the estimated parameters of camera motion between time instance $t-1$ and t.

Based on the values of the measurement matrix, probability density functions (PDF) are built for all the non zero (x,y) pixels of the new modified error image:

$$f_{x,y}(v) = \frac{1}{n \cdot \sqrt{2\pi}} \cdot \sum_{i=1}^{n} \frac{1}{\sigma_i} e^{\frac{-(v-v_i)}{2\sigma_i^2}} \tag{7}$$

where v_i is the a previously measured value of the *(x,y)* point, stored in the *M* matrix, *n* is the number of measurements and σ is a parameter, which determines the width of the Gaussians. The value *v* is a vector, which contains the YUV colour components, thus the *f* function has to be calculated for each channel independently with different σ values.

The σ_i parameter is calculated as the variance of the k nearest neighbour around v_i measurement:

$$\sigma_i^2 = \frac{1}{k} \sum_{j=1}^{k} (v_i - v_j)^2 \tag{8}$$

where v_j is the *j*th nearest value to v_i in the measurement matrix. We use k=n/2, where n is the number of available measurements.

This calculation of probability density functions is similar to the method used in [10], although there, the model was built on isotopic features, based on RGB colour component, while we are working with the non isotopic YUV colour components and 3 marginal distributions.

The $f_{x,y}$ function is a probability function that shows how likely that the pixel *(x,y)* takes a *v* value. But the probability of a value alone is not enough to decide whether it fits well to the PDF or not. The threshold has to be adapted to the "shape" of the PDF function. We used the *f* function's values at the measured points:

$$th = q \cdot \frac{\sum_{i=1}^{n} f(v_i)}{n} \tag{9}$$

where q is a constant, n is the number of the available measurements and $v_i \in M(x,y)$.

C. Detection Phase

During the detection phase, for each new frame, we have to decide what is the foreground and what is the background. The error image, *E* shows us the parts that are moving independently from the camera. But this error image contains returning false positives around the edges due to quantization and perspective changes. To eliminate these false positive parts a filter is used based on the error background model.

Each time instance we build the modified error image, and use the measurements in *M* to build the *f* PDF and the *th* threshold for each pixel and for each channel. The filtering is a simple decision making; if the new value has a high probability at the given (x,y) position than we consider it as part of the background and eliminate it from the error image:

$$E_f^m(x,y) = \begin{cases} E^m(x,y) & if \quad f_{x,y}(v) < th \\ 0 & if \quad f_{x,y}(v) > th \end{cases} \tag{10}$$

The resulted $E_f^m(x,y)$ is the filtered error image, which contains the points of the foreground.

To find moving object silhouettes and eliminate noise, a clustering algorithm, called DBSCAN [11], was used on the foreground points. Each foreground point is described with a 7 dimensional feature vector, which contains the x, y coordinates, the Y, U and V values and the dx, dy motion parameters of the point: $X = (x,y,C_1,C_2,C_3,dx,dy)$.
DBSCAN (Density-Based Spatial Clustering of Applications with Noise) is a density-based clustering algorithm that can separate arbitrary shaped clusters. The main advantages of DBSCAN are: it dose not require knowing a priori the number of clusters, does not have a bias towards a particular cluster shape or size and resistant to noise. On the other hand, it dose not work well on high dimensional data or a dataset with varying density. Detailed description of the algorithm can be found in [11].
There are 3 questions about the DBSCAN. What is the appropriate *epsilon* (minimum distance between neighbour points) and *minimum points* (minimum number of points in a cluster) values, and what is the best distance metric?
For distance measure we used normalized Euclidean distance (or Mahalanobis distance with diagonal covariance matrix):

$$d(X,Y) = \sqrt{\sum_{i=1}^{l} \frac{(X_i - Y_i)^2}{\sigma_i^2}} \tag{11}$$

where *X* and *Y* are *l* dimensional vectors and σ_i is the variance of the *i*th coordinate over the dataset. The main advantage of this measure is the scale-invariance property, which allows us to handle different type of descriptors with different dynamic range.
The *minimum points* parameter was determined based on the size of the biggest connected components on E_f^m:

$$P_{\min} = k \cdot CC_{\max} \tag{12}$$

where P_{min} is the minimum points parameter, CC_{max} is the size of the greatest connected foreground object and *k* is a constant.
The epsilon parameter is based on the number of the descriptors:

$$\varepsilon = c \cdot \sqrt{l} \tag{13}$$

where *l* is the dimension of the feature vector (in our case *l*=7) and *c* is a constant, which means that *epsilon* is proportional to the diagonal of the unitary hypercube in the feature space. The results of the clustering can be seen on figure 6.
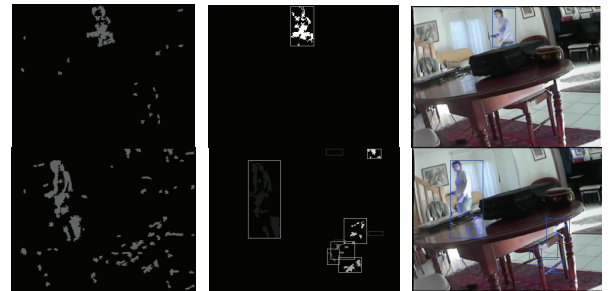

Fig. 6. The result of the DBSCAN algorithm: the input image with the foreground points (left column), the resulted clusters (in the middle) and the clusters drawn on the original image (right)

The clusters correspond to foreground objects. The human detection has to be made for only these objects. But before the using the detector we have to solve a problem that negatively affects most object detector's result.

Most detectors are sensitive to the camera orientation. Usually it is not a serious problem because the camera positioned uprightly, but in case of wearable cameras, the camera can tilt. Usually this results approximately ±30° deflection from the vertical/horizontal direction at worst case.

To determine the orientation of the camera a simple idea was used. We calculated the edge orientation histogram $H(k)$ of each frame $I(k)$. In this work we used 32 bin histograms for the angle range 0-180°. Generally a picture showing an ordinary living environment (house, garden) contains mainly horizontal and vertical edges. This means that we will have one or two peaks in the histogram, and these peaks will determine the horizontal or vertical direction.
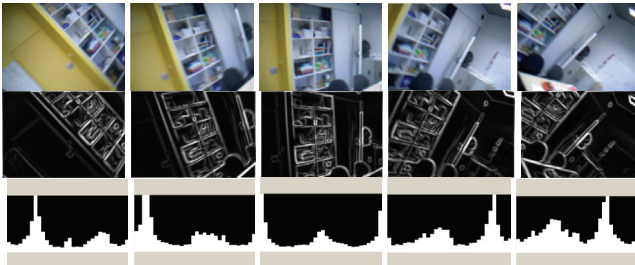

Fig. 6. This image sequence shows how the edge orientation histogram changes along with the camera orientation.

Assuming that the real vertical/horizontal direction is closer to the camera's vertical/horizontal direction, the result of the algorithm is unambiguous. However it can only handle α angular offsets, that are smaller then 45°.

Knowing the angular offset of the camera, the image can be transformed to upright position with a simple affine transformation.

V. CONCLUSION AND PERSPECTIVE

The method described in this paper is extracts silhouette of moving objects from video frames, recorded with a wearable moving camera. In the future we would like to use direct human detector on these silhouettes. The quality of the frames is sometimes very poor due to the strong camera motion and the transmission noise.
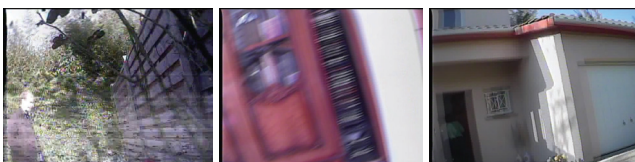

Fig. 7. Transmission noise (left) and motion blurring (middle, right) on the frames.

On these frames the detection of the moving silhouettes is not always possible. In the future we would like to track the detected objects to help processing the noisy frames.

Another problem at present state is the narrow filed of view of the camera. To solve this we are planning to use fish-eye cameras.

At present state the algorithm is not real time. It would be interesting to see if it is possible to achieve real time performance with an up-to-date hardware configuration.

REFERENCES

[1] American Psychiatric Association. "*Diagnostic and statistical manual of Mental Disorders."* DSM III-R. Washington DC: Amer Psychiatr Ass; 1987.

[2] J.-F. Dartigues, *"Methodological problems in clinical and epidemiological research on ageing,"* Revue d'épidemiologie et de sante publique, 2005, 53(3):243-9.

[3] R. Megret, **D. Szolgay**, J.Benois-Pineau, Ph. Joly, J. Pinquier, J.-F. Dartigues, C. Helmer, *"Wearable Video Monitoring of People With Age Dementia: Video Indexing at the Service of Healthcare."* International Workshop on Content-Based Multimedia Indexing (CBMI), London, 2008.

[4] M. Durik, J. Benois-Pineau, *"Robust motion characte-risation for video indexing based on MPEG2 opticalflow,"* Proceedings of the International Workshop on Content-Based Multimedia Indexing, CBMI'01, pp. 57–64, 2001.

[5] P. Viola and M. J. Jones. *"Rapid Object Detection using a Boosted Cascade of Simple Features"* In Proceedings 2001 IEEE Computer Society Conference on Computer Vision and Pattern Recognition (CVPR), 2001.

[6] N. Dalal and B. Triggs. *„Histograms of oriented gradients for human detection.*" In Proceedings of the 2005 IEEE Computer Society Conference on Computer Vision and Pattern Recognition (CVPR), 2005.

[7] Zhu, Q., Yeh, M., Cheng, K., and Avidan, S. *"Fast Human Detection Using a Cascade of Histograms of Oriented Gradients."* In Proceedings of the 2006 IEEE Computer Society Conference on Computer Vision and Pattern Recognition (CVPR), 2006

[8] C. Stauffer and W. Grimson. *"Adaptive background mixture models for real-time tracking".* Computer Vision and Pattern Recognition, 2:246–252, 1999.

[9] Shimada, A., Arita, D., and Taniguchi, R. *"Dynamic Control of Adaptive Mixture-of-Gaussians Background Model."* In Proceedings of the 2006 IEEE international Conference on Video and Signal Based Surveillance (AVSS), 2006

[10] A. Mittal, N. Paragios, *„Motion-Based Background Subtraction Using Adaptive Kernel Density Estimation",* In Proceedings of the 2004 IEEE Computer Society Conference on Computer Vision and Pattern Recognition (CVPR), 2004

[11] M. Ester, H.-P. Kriegel, J. Sander, X. Xu, *"A density-based algorithm for discovering clusters in large spatial databases with noise,"* In: Proc. of Second Int. Conf. on Knowledge Discovery and Data Mining, Portland, OR, 1996, pp. 226-231.

High Field Characteristics of 2D Graphene FETs

Kristóf Tahy

(Supervisor: Dr. Árpád I. Csurgay)

kristof@tahy.hu

Abstract—**The single layer graphene (nano)ribbon based field-effect-transistors (GNRFETs) have been explored and proposed to be the promising candidates for the next generation integrated-circuit (IC) devices. Large area graphene ribbon (1.5 μm wide) and graphene nanoribbon (GNR, 10 nm wide) devices were fabricated with channel lengths ranging from 250 nm to 8 μm. The Dirac-point shift of the back gated devices had been investigated both at room temperature and at 77 K. Saturation like behavior is presented at high bias.**

Index Terms—**graphene, nanoribbon, FET**

I. INTRODUCTION

The recent discovery of graphene [1], a single atomic sheet of graphite, has ignited intense research activities to explore the electronic properties of this novel two-dimensional (2D) electronic system. Charge transport in graphene is substantially different from that of conventional 2D electronic systems as a consequence of the linear energy dispersion relation near the charge neutrality point (Dirac point) in the electronic band structure [2].

If graphene is patterned into a narrow ribbon, and the carriers are confined to a quasi one-dimensional (1D) system, the opening of an energy gap is expected. Similar to CNTs, this energy gap is inversely proportional to the width and depends on the crystallographic orientation of the graphene nanoribbon [3].

Both materials have remarkable electronic properties such as high current drive with high mobility, but to engineer the band-gap of CNTs is not too easy or even impossible – the same for graphene is possible. In addition depositing graphene with an exact width (and thus with exact band-gap) can be carried out lithographically.

II. FABRICATION AND MEASUREMENT

Fabrication of the bottom-gate device with symmetric source and drain was processed by standard silicon field-effect device processes. P-type silicon wafers with 300 nm thick thermal oxide were used with exfoliated graphene flakes provided by Graphene Industries [4]. Back sides of the wafers were metalized first to improve back-gate contacts. Drain and source (top)contacts were defined by e-beam lithography. After developing it has been annealed on 350 °C to remove photoresist residues. E-beam evaporated Cr/Au was used as contact material. Next the graphene area was tailored by reactive ion etching in oxygen. First graphene channel devices were fabricated with 1.5 μm width for high current measurements. Then the graphene area was further thinned with the same process to 10 nm.
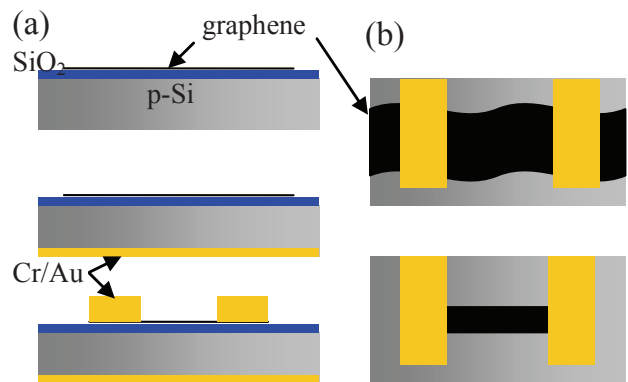

Fig. 1. Process flow of the fabrication of the bottom-gate device structure with a symmetric source/drain. (a) Side view of the formation of the structure starting with 300 nm oxide on silicon with graphene flakes on the top and followed by metallization of the back-side, and contact formation. (b) Top view of the patterning the originally formless graphene flake.

An optical and SEM micrograph of the device can be seen on Figure 2. (a) and (b) respectively. The device was measured using Keithley 4200 semiconductor parameter analyzer in ambient environment as well as in a vacuum ($5 \cdot 10^{-5}$ Torr), at room temperature and at low temperatures (77 K).

III. RESULTS AND DISCUSSION

Ohmic source and drain contacts has been verified in all devices, which can be attributed without doubt for the zero (or very small, for GNR) bandgap of graphene. TLM measurements showed contact resistances of about 200 Ω/cm^2 and graphene sheet resistivity in the order of a few kΩ.

Leakage through the oxide is measured to be ~100 pA, which is many magnitudes lower than the source-drain current, thus negligible.

A. 1.5 μm wide graphene FET characteristics

The gate dependence was measured at 20 mV drain-source voltage using the backgate, and 4X-8X modulation was observed. At first on ambient atmosphere the Dirac point was about 80 V for long channel devices, and increased for shorter channels. This can be explained by the screening of the drain-source electrodes. As the pressure was decreased to $5 \cdot 10^{-5}$ Torr the Dirac point shifted to 5 V – 25 V for long and short channel devices respectively. The pumping down took a long time (overnight) so there was enough time for outgasing. The mobility was calculated to be 2300 cm^2/Vs and wasn't affected by the change of the pressure. By sweeping the gate field back and forth
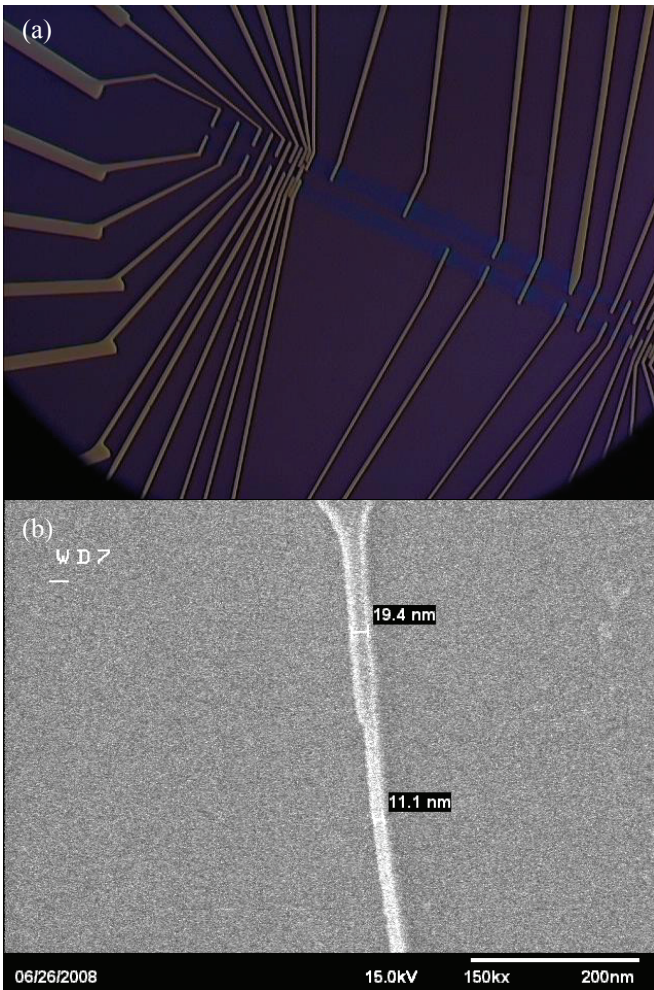
Fig. 2. (a) Optical image of wide graphene devices. (b) SEM image of a 10-20 nm GNR heterojunction device

current which definitely degrades the gate modulation and the corollary the source-drain current at a given gate bias. The underlying physical process is yet unclear but possibly not because of the velocity saturation of the carriers.

B. GNR electrical characteristics

Channel width of less than 15 nm achieved. This leads to band gap opening in the nanoribbon as mentioned. While it is inversely proportional to its width lateral heterojunctions can be formed using different widths of the same material (Fig. 2.(b)).

While the band-gap opening is definitely useful in lowering the off-current on the other hand it significantly decreases the current drive capabilities. It can be partially restored by using GNRs parallel. These kinds of devices were fabricated with 5 or 10 parallel ribbons and behaved as expected by driving higher current.

At the Dirac-point much lower off-currents were measured which is a clear indication of gap-opening and on the other hand it increased the achievable modulation by one order of magnitude at room temperature and by one more at 77 K (Fig. 3.(b)). The exact determination of the bandgap needs further investigation, because as reported in [2] the planned and patterned device width can be very different than the real fabricated device. Also by low
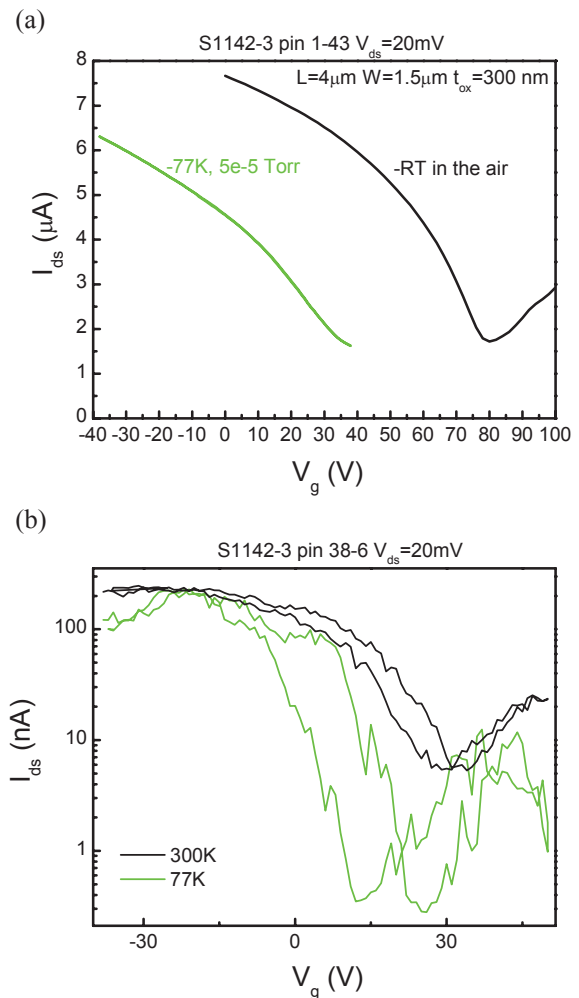

Fig. 3. Gate voltage dependence and modulation of (a) wide (1.5 μm) channel (b) and GNR (10 nm) FETs.

hysteresis was observed as can be seen on Fig. 3.

Measurements on 77 K have been carried out, which didn't affect significantly the Dirac voltage or the mobility. On the other hand it completely eliminated the hysteresis (Fig. 3.(a)).

Source-drain current saturation had been predicted [5] but has not been experimentally verified yet. High drain-source bias was applied on the devices to study breakdown behavior and to achieve current saturation (Fig. 4.(a)). Current saturation like characteristics was observed indeed, but it cannot be addressed to approaching carrier density or velocity limits but rather to changing gate effect. As can be seen on Fig. 4.(b), both the Dirac point and the gate modulation significantly changed due to the high current drive. Actually the gate modulation almost broke off, and the position of the Dirac point became unclear, while there are more minima was observed.

Occasionally we had a graphene flake which consists of a few parallel ribbons with a width of a few micrometers (Fig 5(a)). The device was carrying milliamps of currents while it had been driven to breakdown. Before breakdown clear saturation can be observed as well as the consecutive breakdown of the ribbons is obvious (Fig. 5.(b)). The saturation in other devices which were biased with less voltage is not so evident. As one can see on Fig. 4.(a) some nonlinear saturating characteristic can be observed generally in the first measurements, while later it's more like linear. This can be addressed to the effect of the high passing

temperature measurement it can be characterized, by it

wasn't determinable so 4 K measurements are required.

In addition the hysteresis was very strong in those devices and did not eliminate on low temperatures. This indicates that the reason of hysteresis is perhaps not the oxide charges as anyone would expect but rather some feature of the graphene ribbons. The fact that it's stronger in thinner ribbons point towards that it can be because of surface roughness scattering.

Heterojunction devices have been characterized as well. Difference in the gate dependence is not definite, but weak rectification was observed.

C. Optical response

Optical measurements have been carried out on both device types. The current is so high on the wide devices that the light induced carrier generation cannot be observed. Incidentally the contact of some device was not perfect due to fabrication issues. The devices in these cases have shown rectification and much lower current drive due to Schottky contact formation with the Ti/Au fingers. In those cases photocurrent measurement became possible. We have tried to determine the frequency dependence of the photocurrent or at least to find a cut-off frequency but it happened to be more-or less constant in a wide range. While the wide devices have only very little confinement, and so bandgap,
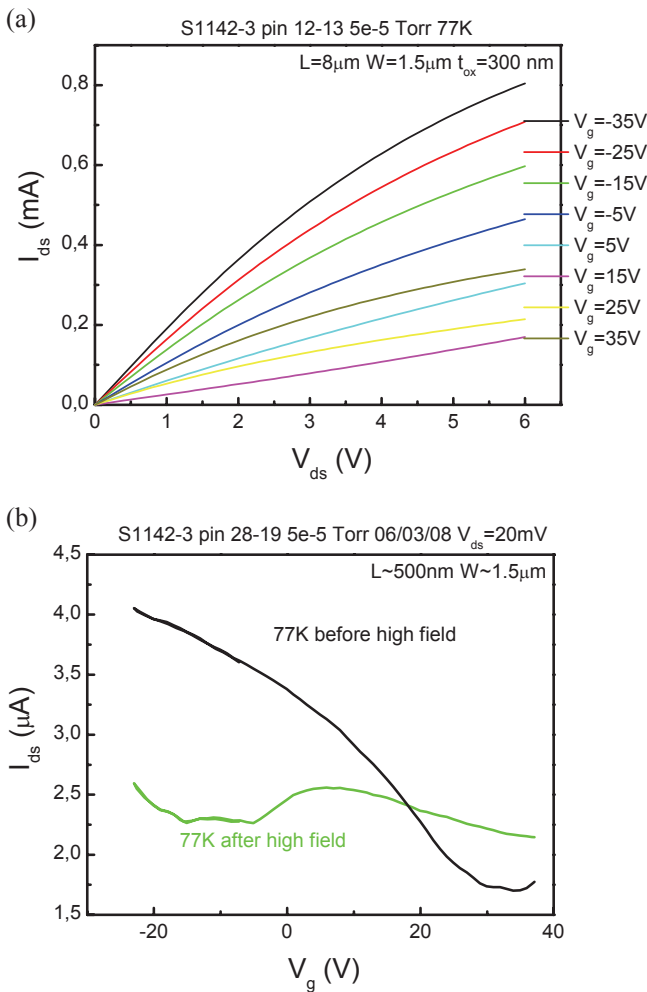
(a)

Fig. 4. (a) Current saturation in graphene FET at high drain-source field. (b) Elimination of gate modulation by high current drive.

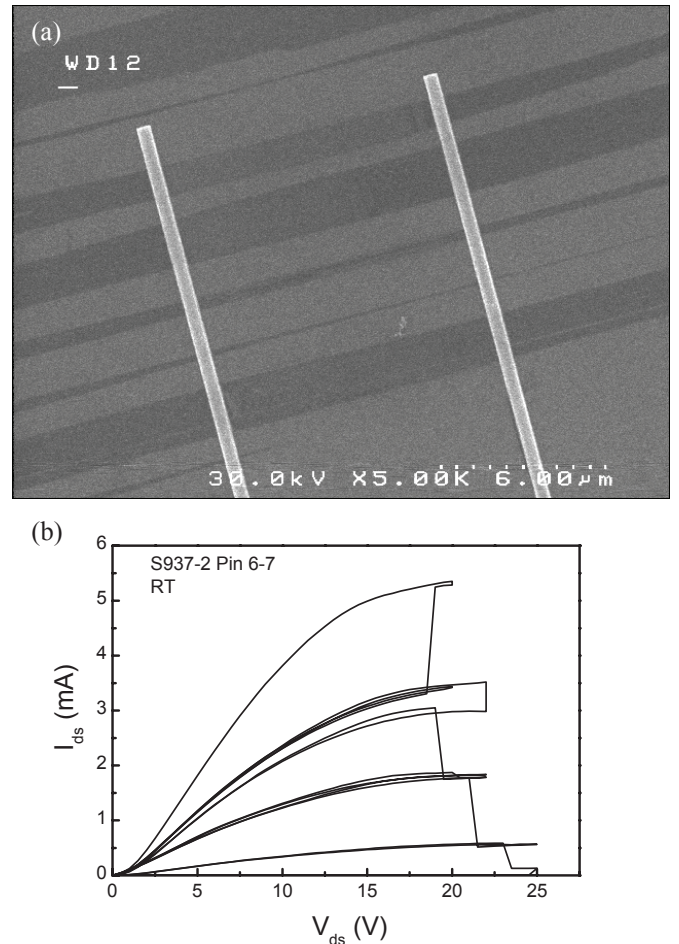it is not surprising that the cut-off has not been reached.

Fig. 5. (a) SEM image and (b) consecutive breakdown of naturally multi-channel graphene FET.

Ohmicly contacted 10/20 nm wide heterostructure devices have been excited by white microscope lamp. Strong photocurrent has been measured, which might validate that the two part of the device have different and relatively large band-gaps. The calculated bandgaps are 100 meV and 50 meV[6], which could enable far-infrared detection even till the 30 THz range [7,8]. Sensor application of this new material is more attractive than using it as channel in FETs because the high mobility and the large current drive is not so promising in epitaxial devices, which could be made wafer-scale [9].

IV. CONCLUSION

A tendency towards current saturation is observed at high drain biases (~2.0 – 3.0 V). At low biases (20 mV) 6X-8X gate modulation can be observed, which is decreased to 2X-4X or even lower if the device had been driven to saturation before.

The decrease in the pressure significantly moves the Dirac point toward s zero, while the decreasing temperature moves it away from it. At 77 K the previously addressed hysteresis in the gate dependence ceased.

GNR devices were fabricated and characterized with on/off current ratios of 500. High current annealing had been tried, which increases the current carrying capacity of the device indeed but significantly decreases the gate modulation. The hysteresis in GNR devices did not eliminated at low temperatures which implies surface roughness scattering as the reason of it instead of trapped

charges in the oxide.

REFERENCES

[1] K. S. Novoselov, A. K. Geim, S. V. Morozov, D. Jiang, Y. Zhang, S. V. Dubonos, I. V. Grigorieva and A. A. Firsov, "Electric Field Effect in Atomically Thin Carbon Films," Science, vol. 306, pp. 666, Oct. 2004

[2] Y. Zhang, Y.-W. Tan, H. L. Stormer and P. Kim, "Experimental observation of the quantum Hall effect and Berry's phase in graphene," Nature, vol. 438, pp. 201-204, Nov. 2005

[3] M. Y. Han, B. Özyilmaz, Y. Zhang and P. Kim, "Energy Band-Gap Engineering of Graphene Nanoribbons," Phys. Rev. Lett., vol. 98, pp. 206805, May. 2007

[4] K. S. Novoselov, D. Jiang, F. Schedin, T. J. Booth, V. V. Khotkevich, S. V. Morozov, and A. K. Geim, "Two-dimensional atomic crystals," PNAS, vol. 102, pp. 10451-10453, July 2005

[5] V. Ryzhii, M. Ryzhii, and A. Satou, "Current-voltage characteristics of a graphene nanoribbon field-effect transistor," Applied Physics Express, vol. 1, pp. 013001, Jan. 2008

[6] Y-W. Son, M. L. Cohen, S. G. Louie, "Energy Gaps in Graphene Nanoribbons," Physical Review Letters, vol. 97, Issue 21, id. 216803, Nov. 2006

[7] F.T. Vasko and V. Ryzhii, "Photoconductivity of an intrinsic graphene," Phys. Rev. B, vol. 77 (19), p.195433, Febr. 2008

[8] V. Ryzhii1, V. Mitin, M. Ryzhii, N. Ryabova1, and T. Otsuji, "Device Model for Graphene Nanoribbon Phototransistor," eprint arXiv:0804.1833, Apr. 2008

[9] A. Rogalski, "Infrared detectors: status and trends", in: Progress in Quantum Electronics, vol. 27, pp. 59-210, 2003.

Multi-Fovea Algorithms for Real-Time Object-Motion Detection in Airborne Video Flow

Balázs Gergely Soós
(Supervisor: Dr. Csaba Rekeczky)
soos@digitus.itk.ppke.hu

Abstract—**The visual navigation system of an unmanned aerial vehicle (UAV) is a complex embedded device that should modify the path of the motion depending on objects or events detected on the ground. Processing all pixels captured by the on-board camera(s) in real time with high frame rate needs huge computational effort that is often unnecessary. An adequate computational strategy would focus only on interesting parts similarly as it is done in retinas of various spices. In this article an automatic focusing mechanism is proposed based on multi-fovea processing for detecting moving objects on the ground and compared to a state of the art method.**

I. INTRODUCTION

Changes in the environment arise the need for animals to accommodate or even to react. Large percent of events can be detected in the visual field therefore it is the main perceptual modality in mammals and humans as well. Artificial vision systems are ideal central elements of navigating robots or UAV-s.

A. Unmanned Aerial Vehicles

Unmanned aerial vehicles offer economic solutions for vegetation classification, flood and fire defense, and large area surveillance. Today unmanned planes are capable to fly over the operation zone on a predefined path using intelligent navigation system based on GPS and motion sensors. During the flight they can collect information or even send it to a ground station using radio connections. Recorded videos can be analyzed after the landing in offline mode, so deep analysis is feasible either by human experts or using machine intelligence. The aim of our recent project ALFA [1] was to develop a long term visual navigation system using a commercial autopilot for surveillance tasks. The path of flight can be modified when interesting event is detected in order to collect more detailed information.

B. Motion Detection

Some recent project highlight the need for video surveillance from small airplanes [2],[3]. Important class of events incorporate motions on the ground e.g. flooding water, or traversing vehicles. A good review for tracking can be found in [4]. For medium altitude video flows (100-300m) main streams in detection are optical flow [5] based and registration based methods [6],[7]. For low altitude videos real 3D analysis of the scene is needed [8]. In surveillance tasks medium altitude is more common. In this article state-of-the-art Lucas-Kanade-Tracker [9] based method is compared with algorithms designed using multi-fovea concept.

In section II. model of video capturing and the scene in consideration is given. In section III. a general algorithmic framework is defined for object detection. This framework will be used to compare different algorithms briefed in section IV. and V. Performance of algorithms are compared in section VI. and VII.

II. SCENE MODEL

A. Images and Video Frames

Our airplane is flying over the inspection area, facing the ground. The camera is capturing *frames* on regular time instances. Frames I_k ($k = 0, 1, ...$) are sampled light intensities projected to the *image plane* (sensor) represented by a series of vector scalar function.

Using homogenous representation points on image plane are column vectors $\mathbf{x}(x_1, x_2, x_3)^T, x_1, x_2, x_3 \in \mathbb{R}, x_3 \neq 0$, where the corresponding point in descartes coordinates is $(x_1/x_3, x_2/x_3)^T$. Scene points (points in 3D world) are represented by descartes coordinates $\mathbf{X}(X_1, X_2, X_3)^T, X_1, X_2, X_3 \in \mathbb{R}$. Image points and scene points will be referred with bold and capital bold letters respectively.

In practice video sensors has finite resolution for sampling therefore intensity values in frames are measured for integer valued coordinates only. Later on images meant to be theoretical infinite resolution representations, and frames are sampled versions with integer coordinates.

The camera is projecting scene points to image points:

$$\mathbf{x} = P(\mathbf{X}). \tag{1}$$

P is defined more precisely in the next subsection. It assigns a ray of 3D points to an image point. In a simplified world model we have light sources and reflecting surfaces. Pixel value in a frame is the total intensity coming from the specific ray, therefore we are interested in the point $\mathbf{X}$, where the ray is intersecting a surface element of the scene. We consider surfaces with diffuse reflection. Intensity for an image point depends on the incoming intensity and emission at the corresponding 3D location but not on the relative orientation of the surface element and the camera.

$$I_k(\mathbf{x}) = I(\mathbf{X}) \tag{2}$$

Detailed description of epipolar geometry can be found in [10].

B. Background and Objects

In this article we consider middle altitude flying planes (100-300m). The scenes under consideration, namely large open field areas, or highway regions with region of interest constraints can be regarded as flat surfaces since the variation in height of the ground is small compared to the distance to the camera. Thus we can model ground as a plane π with texture $Bg(\mathbf{X}), \mathbf{X} \in \pi$. This texture is the *background* image, the description of the static empty screen. In some cases small part of the sky is also visible on the frames. We will use region of interest to get rid of this problem.

Bounded volumes of the 3D scene having non negligible height or changing position are *objects*. Objects on frames or images can be described by their *shapes* and *appearances*. Shape of an object is the region where it covers the background, the appearance is the way it alters the background. Both properties are time dependent because of the camera motion. By definition areas where shadow is casted also belongs to the specific object. In this article detection of independent object motion is interpreted as locating shapes on frames belonging to non static scene object.

C. Global Image Motion Model

Using homogenous vector representation for both image coordinates $\mathbf{x}$ and world points $\mathbf{X}$, the camera mapping (1) can be directly described with a 3 by 4 linear transformation.

$$\mathbf{x}_i = P(\mathbf{X}) = H_{3*4}^k \begin{pmatrix} X \\ Y \\ Z \\ 1 \end{pmatrix} \qquad (3)$$

This representation can be used both for pinhole or ortographic camera models holding camera pose dependent external parameters and internal parameters as well.

World coordinate system can be defined as the ground plane lying in the "$X - Y$" plane. The camera at time instant k is located at C and has a specific orientation. During the frame by frame time camera center is moved and the orientation is changed. Points from the surface are projected to Image planes, forming video frames I_k and I_{k+1}.

Since for all background points Z coordinate component is zero, we can simplify the mapping. The plane to plane transformation for the actual image can be described by an invertible 3 by 3 linear assignment.

$$\mathbf{x}_k = H_{3*3}^k \begin{pmatrix} X \\ Y \\ 1 \end{pmatrix} \qquad (4)$$

$$\mathbf{x}_{k+1} = H_{3*3}^{k+1} \begin{pmatrix} X \\ Y \\ 1 \end{pmatrix} \qquad (5)$$

Or we can express direct relation between points on image k and $k + 1$:

$$\begin{aligned} \mathbf{x}_{k+1} &= H_{3*3}^{k+1}\mathbf{X} = H_{3*3}^{k+1} \left[(H_{3*3}^k)^{-1}\mathbf{x}_k \right] \\ &= \left[H_{3*3}^{k+1}(H_{3*3}^k)^{-1} \right] \mathbf{x}_k \\ &= H_{3*3}^{k,k+1}\mathbf{x}_k \\ \mathbf{x}_k &= H_{3*3}^{k+1,k}\mathbf{x}_k \end{aligned} \qquad (6)$$

$H_{3*3}^{k+1,k}$ maps coordinates from the coordinate system of k-th frame to the coordinate system of $k + 1$. The geometrical relationship implies description for video frames as well. Applying 6 and 2 we derive

$$\begin{aligned} I_{k+1}(H_{3*3}^{k,k+1}\mathbf{x}) &\leftrightarrow I_k(\mathbf{x}) \\ I_{k+1}(\mathbf{x}) &\leftrightarrow I_k(H_{3*3}^{k+1,k}\mathbf{x}) \end{aligned}$$

This means frames containing common parts from the background can be aligned by a linear transformation matrix. In most general case this can be a projective transformation. This is our global model for *image motion*. Since for frames we use integer coordinate values the image transformation should be interpolated.

III. OBJECT DETECTION ALGORITHM

A. Frame Registration

If proper transformation from one image to the next can be discovered, it is possible to calculate it for all known image points (all pixels) and it can be interpolated. This process called *registration* [11]. For a basic framework we can sum up necessary steps:

1) On frames locate robust feature point locations
   $\longrightarrow$ **BasePoints** on I_k

2) Match feature pairs
   Find corresponding **InputPoints** on I_{k+1}

3) Estimate transformation on point correspondences
   $\longrightarrow H_{3*3}^{k+1,k}$

4) Registration
   a. Calculate transformation and interpolate
   $\longrightarrow J_k(\mathbf{x}) = I_k(H_{3*3}^{k,k+1}\mathbf{x})$

Error measure can be defined on the intersecting frame regions (W) *e.g.* E_1 or E_2.

$$\begin{aligned} E_2 &= \sum_{\mathbf{x} \in W} \left[I_{k+1}(\mathbf{x}) - J_k(\mathbf{x}) \right]^2 \qquad (7) \\ E_1 &= \sum_{\mathbf{x} \in W} \left| I_{k+1}(\mathbf{x}) - J_k(\mathbf{x}) \right| \qquad (8) \end{aligned}$$

4) b. Calculate error map
   $\longrightarrow$ **DiffMap(AlignMap)**

After extracting point features and forming pairs, based on (6) transformation matrix can be linearly estimated using four correspondences. Since points are located with moderate precision on frames, some error arises. If the matrix is used to register the full image afterwards, it is better to use

more correspondences with some robust fitting technique like RANSAC or Least Median Square.

The result of the first part of the algorithm is DiffMap, a greyscale description, with high pixels vales for suspected object regions. The global registration based methods calculate the error measure AlignMap, and gives it as DiffMap.

When a frame is sampled from an image with fine features - textures and region boundaries are mapped to a pixel or a neighbouring one depending on interpolation strategy. Due to this one pixel unambiguity this regions can rise high registration error. Other reason for high error is the presence of an object not covered perfectly by the flat world model. When an object is changing its location between frames large regions can raise high error values. Analysis of the error map can highlight object, and especially moving ones. This method can detect object boundaries and non overlapping object parts but not exact object shape. Thus *extraction of the objects* is partially solved. Step 5 is the *object detection* part of the algorithmic framework. The result of it is a binary mask marking interesting regions.

5) Object detection: error map analysis
⟶ **DetectionMask(AlignMask)**

If an object is detected on more frames a tracker can be initialized to describe the motion of the object, and to build up better object extraction, later on the track can be classified as moving object or static object.

6) Object tracking: independent motion detection

If the detection rate of the algorithm is high, extracted regions can be further analyzed. They can be used for initializing and maintaining a tracking mechanism. For this reason, this framework is considered to give a focusing mechanism, filtering regions with possible object parts.

B. Local Motion Model

Step 1 and 2 can be done simultaneously. Frame regions around point pairs can be matched, using similar considerations as for the whole frame. There exists a transformation mapping one region to its corresponding pair in the consecutive frame regarding some error measure. For small time intervals even pure displacement can be used as *local motion model*.

In next two sections three different method will be briefed. All of them using the basic algorithmic concept but focusing different amount of computational effort on a specific step.

IV. Lucas Kanade Tracker

This algorithm is a well known solution for tracking feature points in a video flow. Basic concept of Lucas-Kanade optical flow calculation were presented in 1981,[12], later on it was extended to track feature points robustly [9]. Based on resulting point correspondences registration and object detection can be done.

Point features are extracted exploiting the properties of matching model. In the basic realization pure displacement
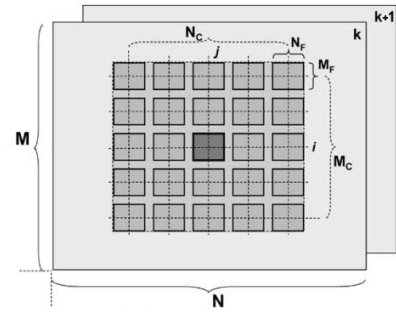

Figure 1. For each (M x N) sized frame (M_c x N_c) windows ($W_{i,j,k}$) are defined each with (M_F x N_F) resolution at a regular grid. Main part of the processing is done in the windows.

model is used for consecutive frames, although affine extension also exists.

We have two images $F(\mathbf{x})$ and $G(\mathbf{x})$. G representing a region from the actual frame, with windowing region W, and F is the next image in the flow. We try to align them: search for the ideal displacement rising the minimal registration error:

$$E = \sum_{\mathbf{x}\in W} \left[F(\mathbf{x}+\mathbf{h}) - G(\mathbf{x})\right]^2 \tag{9}$$

After linearization with first order Taylor polynom explicit local optimum can be found for the displacement vector:

$$Z = \sum_{\mathbf{x}\in W} \left(\frac{\partial F}{\partial \mathbf{x}}\right)^T \left(\frac{\partial F}{\partial \mathbf{x}}\right) \tag{10}$$

$$\mathbf{h} = Z^{-1}\left[\sum [G(\mathbf{x}) - F(\mathbf{x})]\left(\frac{\partial F}{\partial \mathbf{x}}\right)^T\right] \tag{11}$$

$$\tag{12}$$

In (12) the gradient vector is a row vector, Z is a 2 by 2 matrix. Z must be invertible to calculate $\mathbf{h}$. This stands if both eigenvalues are large positive numbers. This property is used for selecting good features to track. This feature selection is analogue to the Harris corner extraction [13]. Since G and H must be similar for successful match, features can be located on G.

The linearization error is moderate only for small displacements, so an image pyramid is used with coarse to fine processing, and iterative search in all levels for airborn sequences.

V. Multi-fovea Processing

A. Concept

In a video flow frames have fix resolution (M row ,N column). To process the entire data at full resolution is computationally expensive and in most cases unnecessary. If in early stage of the algorithm decision can be made to locate interesting regions to focus effort to critical areas efficient processing scheme can be formulated. Hardware realization can be designed to solve parallel tasks in each window, or existing vision processors can be utilized. Processed regions are called foveas analog to fovea of mammal retina.

In this proposed framework processing regions are rectangular windows with M_p by N_p resolution. Rectangular regions of the original frame are mapped after optional scaling. More detailed description can be found in [14].

Regular sparse grid can be defined for these processing windows arranged equidistantly. They are arranged into rows and columns and are referred as $W_{i,j,k}$, where i,j are row and column indexes, respectively. Sparse grid has M_c by N_c resolution (Fig. 1). Algorithmic properties for actual time instant and results are described for each window using matrices, like

$X_{i,j}, Y_{i,j}$ - coordinates of the center of $W_{i,j,k}$
$S_{i,j}$ - scale factor of $W_{i,j,k}$

The position and scale can be dynamic in order to adapt to actual video data.

B. Multi-fovea Independent Motion Analysis

1-st and 2-nd step of the algorithm - feature detection, and association - can be interpreted in multi-fovea concept, as extracting central region of a window on the actual frame - *template*, and finding best correspondence inside the window on successive frame using E_1 error measure. Basic algorithm can apply exhaustive search for template at all possible location. This is analogue to find displacement with integer shifts. Since all data is available at integer positions no interpolation is needed. Adaptive search methods can find good matches with smaller number of template check although they can stuck in local minima.

For robust calculation on global image motion model it is important that the point pairs are distributed along the whole image. The sparse grid configuration is good for this reason. In EG-IMA spatial adaptation for foveas is not used.

C. Elastic Grid

The global model for image motion is projective or affine. Even projective transformation conserves collinearity: if a point lie on a line defined by to others, after the transformation it will be still on the line. This property can be used to define an adaptive iterative search mechanism.
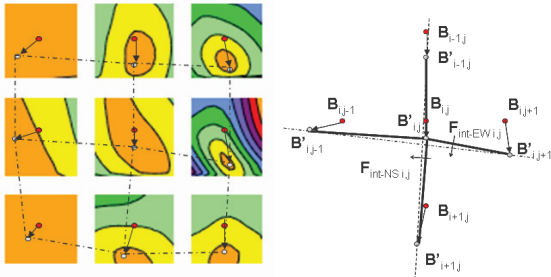

Figure 2. Left: Displacement vectors are originated at the centers of the windows $\mathbf{B}_{i,j}$. End points $\mathbf{B}'_{i,j}$ are the control points of the elastic grid. Edges are connections between closest 4-neighbors. Right: $F_{i,j}^{int-NS}$ and $F_{i,j}^{int-EW}$ are the two components of the internal force affecting $\mathbf{B}'_{i,j}$.

$\mathbf{B}_{i,j}(X_{i,j}, Y_{i,j})^T$ vector is the center of $W_{i,j}$ window on frame k. The template $T_{i,j}$ is extracted around $\mathbf{B}$, and matched on the next frame. The displacement vector is $\mathbf{h}_{i,j}(DX_{i,j}, DY_{i,j})^T$, pointing to the center of matching region $B'_{i,j}$. The corresponding error value is $E(\mathbf{h})$, and corresponding confidence measure $\eta_{i,j}$. This is the complement of normalized value of E respect to template size in [0,1] interval.

Elastic contours are popular tool for e.g. segmenting noisy images. The contour is built up from segments defined by control points. These points are iteratively moved on the image by a task specific external force for exact segmentation result while internal force is balancing this effect to keep contours nice (e.g. with low curvature).

Elastic contour concept can be extended to *elastic grid* (ELG). Since $B_{i,j}$ form collinear points by construction with its neighbour e.g. $B_{i,j-1}$ and $B_{i,j+1}$, the same must stand for corresponding pairs after translation. An elastic grid can be defined on $B'_{i,j}$ points with 4-neighbours connectivity. The collinearity constraints means grid is nice, if connecting line segments are almost parallel (Fig. 2).

E is computed on integer coordinates forming a potential map. Searching is started with $(0,0)^T$ displacement. During the search values of the map are calculated, overwriting initial values. In all iteration steps 3 by 3 part of the potential map is considered. Missing values are computed, and smallest among them is selected. Using these $\mathbf{h}_{i,j}^{ext}$ values internal force is computed using neighboring displacement components are weighted with their confidence values:

$$\mathbf{F}_{i,j}^{int} = \begin{pmatrix} \frac{\eta_{i,j-1}DX_{i,j-1}+\eta_{i,j+1}DX_{i,j+1}+\eta_{i,j}DX_{i,j}}{\eta_{i,j-1}+\eta_{i,j+1}+\eta_{i,j}} - DX_{i,j} \\ \frac{\eta_{i-1,j}DY_{i-1,j}+\eta_{i+1,j}DY_{i+1,j}-\eta_{i,j}DY_{i,j}}{\eta_{i-1,j}+\eta_{i-1,j}+\eta_{i,j}} - DY_{i,j} \end{pmatrix} \tag{13}$$

Depending on the orientation of the internal force vector, new candidate is selected $\mathbf{h}_{i,j}^{int}$ from the 9-neighbourhood of $\mathbf{h}_{i,j}^{ext}$.

$$|\mathbf{F}_{i,j}^{ext}| = |E(\mathbf{h}_{i,j}^{int}) - E(\mathbf{h}_{i,j}^{ext})| \tag{14}$$

If $\mathbf{h}_{i,j}^{int}$ has smaller potential value, or $\lambda|\mathbf{F}_{i,j}^{int}| > |\mathbf{F}_{i,j}^{ext}|$, $\mathbf{h}_{i,j}^{int}$ is used for next iteration, otherwise $\mathbf{h}_{i,j}^{ext}$ is kept. This mechanism means the search is moving towards smaller error values, but if the distortion of the grid is growing it is lowered by climbing to slightly worst locations. This joint optimization method can find good solution for untextured windows with flat error surfaces, and can find global optimums without the need of exhaustive search.

In Elastic Grid algorithm global model is not estimated, and no global image alignment is done, instead the calculated displacements are applied for all template region. This multiple displacement model gives alignment used for DiffMap calculation. After adaptive thresholding DetectionMask is created. This mask highlights possible object parts. The processing windows of the Elastic Grid algorithm can be used directly for tracking. Regions with large remaining force after iterations contain regions with reliable displacement estimation that is not consistent with the surroundings are supposed to contain

some object part. More details on the algorithm is given in [15].

VI. Performance of Methods

The output of the algorithms after step four is the DiffMap, in basic implementation of step five this is thresholded and filtered to get DetectionMask. For Elastic Grid method, estimation of the transformation matrix and calculation of the AlignMap is not needed, but for testing the coupled search performance and to compare performance of all the three algorithms it is calculated.

The quality of the methods were compared for registration and detection. The registration is successful if the AlignMap is zero for almost all pixels - or mean value is small, and large percent of region boundaries are also covered. For edge statistics canny edge detector was used on actual and next frame, and actual was aligned with the same transformation as the video frame.

The detection capability was measured using hand-made ground truth reference. True positive intersection with the reference were recorded and scored. False positive detections can be filtered using tracking.

Main steps of the algorithms are compared in Table I. The object tracking is not yet tested.

Table I
MAIN STEPS FOR THE ALGORITHMS

	Video: 320x240 Search Range: 8	KLT	MF-IMA	MF-ELG
1	Feature Extracion	Finging Corners	Fixed	Fixed
2	Feature Matching	Solving linear equation	Exhaustive search	Joint search
3	Model Estimation	LMS	LMS	○
4	Interpolation	Bilinear	Bilinear	○
5	Object Detection thresholding	Adaptive thresholding	Adaptive thresholding	Adaptive thresholding
6	Object tracking	...	...	...

Some estimation on image processing complexity for critical steps is given in Table II considering involved pixel count. KLT uses real coordinates in searching and needs interpolation. Bilinear interpolation was used and represented with a factor of four. Since IMA and ELG does not search for good features but uses predefined windows they need larger support area containing some feature. IMA needs more correspondences than KLT to have enough inliers for supporting LMS. In case of ELG almost the whole image is covered with templates.

ELG is directly comparable with IMA it has considerable smaller complexity. It is hard to compare with KLT. Computation effort of arithmetics on floats and integers are highly platform dependent. In systems with no floating point support ELG can be a reasonable choice.

VII. Experimental Results

For testing the algorithms both synthetic and recorded field video flows were used. In the following diagrams results for a 75 frame field video is given. In the sequence airplane is flying over a car moving in opposite direction on the ground.

Table II
COMPLEXITY OF MAIN STEPS FOR THE ALGORITHMS

	Video: 320x240 Search Range: 8	KLT	MF-IMA	MF-ElasticGrid
1	Preprocessing	Image gradients (2x320x240)	○	○
1	Number of features	30	64	14x12
2	Template size	7x7	16x16	16x16
2	Search step	Weighted Imdiff (2x7x7+4x7x7) Z matrix (2x7x7)	Absdiff (2x16x16)	Absdiff (2x16x16)
2	Number of steps	10-15	17x17	10-15
4	DiffMap	(320x240+ 4x320x240)	(320x240+ 4x320x240)	(2x320x240) 10-15

If the mean value of the AlignMap (or DiffMap) is large, the registration is unsuccessful. Checking edge coverage statistic heuristic limit was set for good alignment with mean AlignMap value of 3.0. The number of outstanding gray values are displayed on (Fig. 3). After adaptive thresholding they will represent possible objects on the DetectionMask. Frame pairs with unsuccessful registration may contain large number of false negative detections, thus they are filtered out (Fig 4). Elastic grid method has similar feature pair detection capability, since the number of remaining frame pairs after filtering is similar. The detection rate is around 60%. This can be used to initialize and maintain tracks reliably.

VIII. Conclusion

Two multi-fovea algorithms were proposed and compared to a state of the art method for registration based motion detection. These algorithms do not need floating point arithmetic for feature point detection and assignment. They have similar power for registration. Elastic Grid method uses joined search strategy, to dramatically reduce template matching effort compared to brute force search. It was also shown that multiple displacement model can be used for medium altitude airborne videos for detection purpose.

References

[1] "Alfa project webpage." http://lab.analogic.sztaki.hu/alfa/en/indexx.php.
[2] "Comets project web site." http://www.comets-uavs.org/.
[3] "Mlb company." http://www.spyplanes.com/.
[4] A. Yilmaz, O. Javed, and M. Shah, "Object tracking: A survey," *ACM Comput. Surv.*, vol. 38, p. 13, 2006.
[5] J. Barron, D. Fleet, S. Beauchemin, and T. Burkitt, "Performance of optical flow techniques," in *Proceedings of the IEEE Computer Society Conference on Computer Vision and Pattern Recognition,CVPR '92.*, pp. 236–242, 1992.
[6] R. Kumar, H. Sawhney, S. Samarasekera, S. Hsu, H. Tao, Y. Guo, K. Hanna, A. Pope, R. Wildes, D. A. H. Hirvonen, M. A. H. Hansen, and P. A. B. Burt, "Aerial video surveillance and exploitation," *Proceedings of the IEEE*, vol. 89, pp. 1518–1539, 2001.
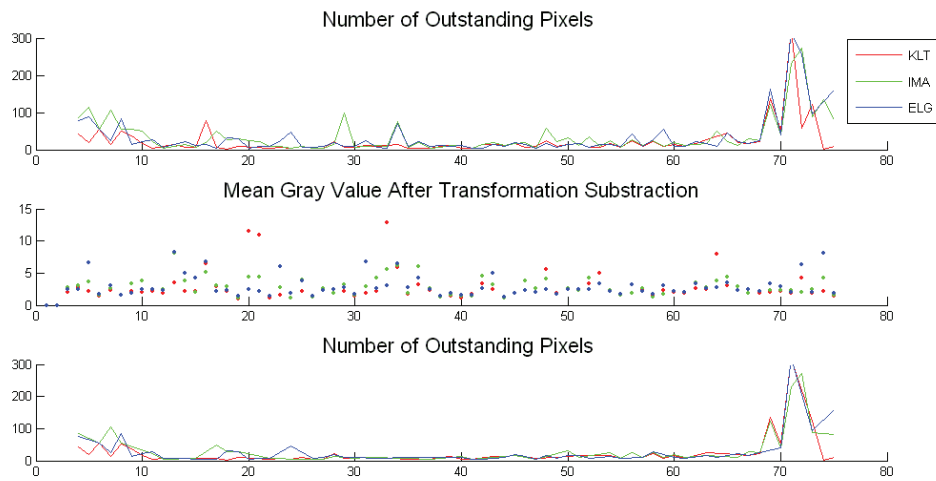
Figure 3. The AlignMap is analysed for all algorithms while processing a 75 frame field video. A car is moving on the ground, getting closer, then leaving the view of the camera.. On the diagrams values are presented for each time instant. In the first chart number of pixels with large error values are displayed. On the second mean value is displayed. Registration can be considered successful if mean value is less than 3.0 (heuristic value). The third chart shows the number of outstanding pixels after filtering for good registration.
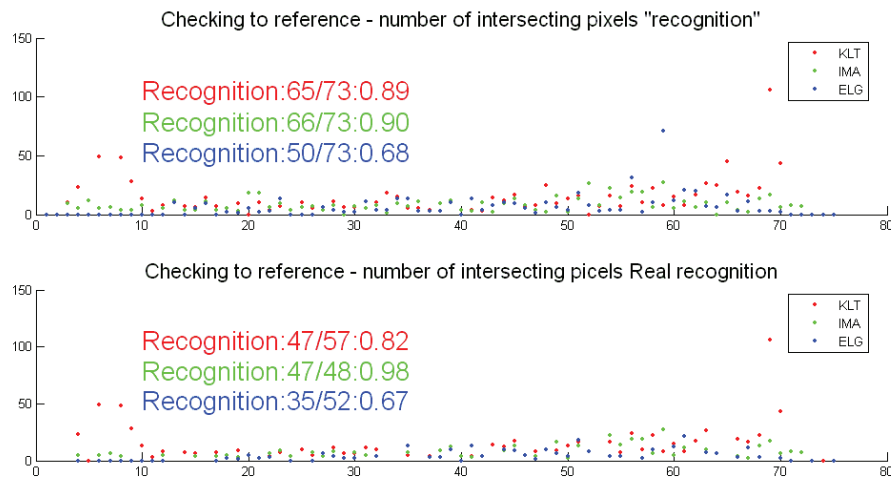
Figure 4. Count of intersecting pixels on DetectionMask and Reference. Object is detected if at least on pixel is overlapping. In the top chart before filtering, on the bottom after registration filtering. Recognition rate is given as frames with detection over all frame number.

[7] K. Kaaniche, B. Champion, C. Pegard, and P. Vasseur, "A vision algorithm for dynamic detection of moving vehicles with a uav," in *Proceedings IEEE International Conference on Robotics and Automation, ICRA 2005.*, pp. 1878–1883, 2005.

[8] H. Sawhney, Y. Guo, and R. Kumar, "Independent motion detection in 3d scenes," *IEEE Transactions on Pattern Analysis and Machine Intelligence*, vol. 22, pp. 1191–1199, 2000.

[9] J. Shi and C. Tomasi, "Good features to track," in *Proceedings of the Computer Vision and Pattern Recognition, CVPR '94.*, pp. 593–600, 1994.

[10] R. Hartley and A. Zisserman, *Multiple view geometry in computer vision.* Cambridge University Press, 2000.

[11] B. Zitova and J. Flusser, "Image registration methods: a survey," *Image and Vision Computing*, vol. 21, pp. 977–1000, Oct. 2003.

[12] B. D. Lucas and T. Kanade, "An iterative image registration technique with an application to stereo vision," in *Proceedings of the DARPA Image Understanding Workshop*, pp. 674–679, 1981.

[13] C. Harris and M. Stephens, "A combined corner and edge detector," in *Proceedings of the Fourth Alvey Vision Conference*, (Manchester, UK), pp. 147–151, 1988.

[14] C. Rekeczky, I. Szatmari, D. Balya, G. Timar, and A. Zarandy, "Cellular multiadaptive analogic architecture: a computational framework for uav applications," *IEEE Transactions on Circuits and Systems I: Fundamental Theory and Applications*, vol. 51, pp. 864–884, 2004.

[15] B. Soos and C. Rekeczky, "Elastic grid based analysis of motion field for object-motion detection in airborne video flows," in *Proceedings of the IEEE International Symposium on Circuits and Systems, ISCAS 2007.*, pp. 617–620, 2007.

Simple Reaction Kinetic Model of Rapid (G Protein Dependent) and Slow (β-arrestin Dependent) Transmission

Dávid Csercsik

(Supervisor: Dr. Katalin Hangos)

csercsik@scl.sztaki.hu

Abstract—In this paper the qualitative dynamic behavior of reaction kinetic models of G protein signaling is examined. A G protein coupled signaling structure is defined, which is extended to be able to take the effect of slow transmission, RGS mediated feedback regulation and ERK-phosphatase mediated feedback regulation into account.

The resulting model gives rise to an acceptable qualitative approximation of the G protein dependent and independent ERK activation dynamics that is in good agreement with the experimentally observed behavior.

Index Terms—Reaction kinetic systems, G protein signaling, MAPK/ERK, Regulators of G protein signaling, Slow transmission

I. INTRODUCTION

Diverse signaling molecules, including neurotransmitters, hormones, phospholipids, photons, odorants, taste ligands and mitogens, bind to their specific G protein-coupled receptors (**GPCR**s), also known as seven-transmembrane receptors (7TMRs), in the membrane of the target cells, which subsequently interact with their respective G proteins to induce a cascade of downstream i.e. intracellular signaling.

The G proteins are heterotrimeric signaling molecules composed of three subunits, α, β and γ, which dissociate upon receptor-induced exchange of GDP for GTP on the α subunit (Gα) to form a free Gα and a dimer of G$\beta\gamma$ subunits [1]. Many isoforms of these subunits have been cloned in the past years and have been classified into four groups according to the subtype of their α subunit: Gαs, Gαi, Gαq and Gα12. All these Gα subunits, as well as the dissociated $\beta\gamma$ subunits, and other receptor-interacting proteins are capable of initiating diverse downstream signaling pathways via second messenger molecules, such as cyclic AMP, inositol triphosphate, diacylglycerol, and calcium.

Activation of the signal induced by the GPCR depends on the rate at which ligand-bound receptor catalyzes exchange of GDP for GTP on the Gα subunit. Following exchange, GTP-bound Gα dissociates, at least partially, from both the receptor and G$\beta\gamma$ coplex. The length of time that GαGTP and G$\beta\gamma$ can interact with effectors is determined by the rate at which Gα hydrolyzes GTP to GDP. Following hydrolysis, inactive GαGDP binds G$\beta\gamma$ with high affinity, and terminates

Process Control Research Group, Systems and Control Laboratory Computer and Automation Research Institute, Hungarian Academy of Sciences H-1518, P.O. Box 63, Budapest, Hungary csercsik@scl.sztaki.hu

G$\beta\gamma$ signaling. GTPase-activating proteins (GAPs) speed up the hydrolysis of GTP by Gα [2]. In this article G$\beta\gamma$ signaling events are not examined.

The most accepted classic paradigm of signaling until nowadays has been that the significantly important elements which contribute to information transfer into the internal system of the cell are the α and $\beta\gamma$ subunits of G proteins (see the review [3]). One of the most important main targets of the intracellular pathways affected by G protein related signaling is the family of MAPK/ERK cascades [4]. Proteins called G protein-coupled receptor kinases (GRKs) are able to rapidly terminate this signaling response via phosphorylating the receptor, typically on its cytoplasmic tail [5]. Following phosphorylation, β-Arrestins bind the receptor, which blocks further G protein-initiated signaling.

In recent years it has been shown that β-Arrestins not only take part in receptor desensitization [6], but form an endocyctic protein complex, which initiates a G protein independent activation of ERK [7], [8], [9].

Another important mechanism contributing to the dynamics of signaling is the feedback regulation, about which there are only a few models available in the literature [10], [11]. At the same time, efforts to take into account the β-Arrestin dependent slow transmission as a second pathway convergent to G protein signaling is not prevalent either in literature.

Much effort has been made nowadays to find plausible mathematical models for the description of G protein related signaling dynamics [12], [13], [14], [15], in order to analyze signaling dynamics and ligand efficacy.

To join the above mentioned efforts, the aim of our paper is to propose a simple (in a sense minimal) reaction kinetic model and the implied equations for G protein signaling, based on biochemical and physiological observations collected about cell signaling pathways corresponding to a simplified model of fast-, and slow-transmission as well as the regulation of G protein signaling that is able to reproduce the downstream activation pattern (like ERK or Akt) recently described in [16] qualitatively.

We aim at constructing a model in strict reaction kinetic form, in order to stay in a model class for which the deficiency-based multistability-related results of Feinberg et al. [17], [18] can be applied in the future. These results provide very strong theorems about qualitative behavior of reaction kinetic systems, based only on the structure of the reaction

network, independent of its parameters. Furthermore, these and other [19] multistability-related results offer the possibility to explain interesting physiological phenomena related to typical dynamic, pulsatile intercellular signals.

II. MATERIALS AND METHODS

A. Slow transmission

Following GPCR activation, the ligand-bind receptor can be phosphorylated by GPCR kinases (GRKs). As described in [20] in the case of dopamine, β-Arrestins bind to the receptors after phosphorylation to uncouple them from G proteins and participate in the recruitment of the endocytic protein complex, thus leading to an attenuation of GPCR signaling.

On the other hand, the signaling complex composed of the ligand, the receptor, β-Arrestin2, and PP2A can dephosphorylate the protein Akt on the site Thr308, and initiate a G protein independent second messenger cascade. Furthermore, an another signaling complex binding to the phosphorylated receptor composed of β-Arrestin, ERK1/2, Raf-1 and MEK can initiate ERK activation [16].

B. Regulation of signaling

As described in [16], β-Arrestins that bind the receptor after phosphorylation, can serve as scaffolding molecules that facilitate cell signaling to ERK and other subgroups of MAPK proteins through MEK and Raf, as described in [4]. The activation of MAPK cascades can be furthermore initiated by a small GTP-binding protein (smGP; RAS-family protein), which transmits the signal either directly or through a mediator kinase to the MAPK kinase (MAP3K or MAPK^3) level of the MAPK cascades. As DeWire describes in [16], with si-RNA methods and the application of mutant receptors, it can be shown, that the resulting ERK phosphorylation (activation) is composed as a result of the activation induced by G proteins and the activation originated from β-Arrestin mediated slow transmission.

Experimental investigations show that the G protein-mediated ERK activity is maximal at 2 min after stimulation, and the β-arrestin2 mediated ERK activity is minimal until 10 min post-stimulation, but is responsible for nearly 100% of ERK signaling at times beyond 30 min [16].

It has also been shown [21], [22] that the regulators of G protein signaling (RGS) are basically the guanosine triphosphatase (GTPase)-accelerating proteins that specifically interact with G protein α subunits. RGS proteins enhance the intrinsic rate at which certain heterotrimeric G protein α-subunits hydrolyze GTP to GDP, thereby limiting the duration that α-subunits activate downstream effectors. This activity defines them as GTPase activating proteins (GAPs).

These regulator proteins display remarkable selectivity and specificity in their regulation of receptors, ion channels, and other G protein-mediated physiological events [23]. Recent findings show that RGS proteins selectively regulate signaling by certain G protein-coupled receptors (GPCRs) in cells, irrespective of the coupled G protein [24].

Furthermore, RGS proteins can change the nature of the start and end of a signaling event, while leaving the intensity of the signal unchanged [2].

There are multiple RGS subfamilies consisting of over 20 different RGS proteins. RGS2 blocks $Gq\alpha$-mediated signaling, a finding consistent with its potent $Gq\alpha$ GAP activity. It can be assumed that RGS proteins (RGS2 and RGS3) are up-regulated via the phosphorylation of mitogen-activated protein kinases (MAPK or ERK). These are feed-back regulated through map kinase phosphatases (MAPKP), which are able to dephosphorylate MAPK-s [25], [10].

C. Model development

The basic conceptin model development is to define a model with the reactions describing the MAPK activation, and to take into account the RGS-mediated G protein feedback regulation, and MAPKP (ERKP) mediated ERK auto-regulation.

We assume that β-Arrestin, PP2A and Akt is in great excess, and they bind rapidly to the receptor forming the signaling complex, which immediately activates the second messenger cascade leading to the induction of ERK signaling. Furthermore, the ERK signaling cascade (MAP3K, MAPKK, MAPK) is neglected in the case of G protein based signaling. We also suppose that RGS proteins are activated by the active form of ERK [10].
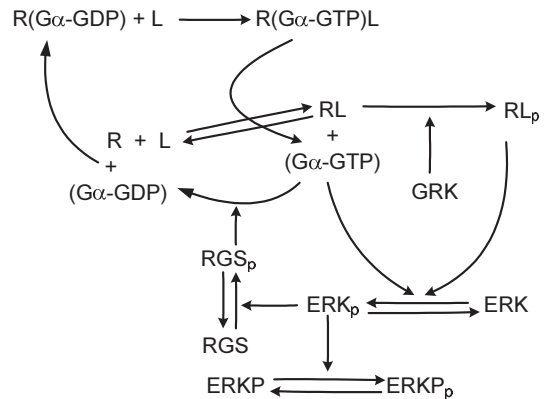

Fig. 1. The reaction scheme of G protein signaling, ERK activation and regulation of signaling

Where an arrow points to a specie, it means transformation, and when it points to an other arrow, it refers to enzymatic catalysis.

The resulting reaction scheme in Fig. 1 summarizes the structure of all the reactions, and the reaction graph can be derived from it. It is important to observe a large, RGS mediated and a small $ERKP$ feedback loop, which implies a cascade structure.

D. Simulation results

For the simulation, the parameters were obtained via parameter estimation with MATLAB using the Nelder-Mead simplex algorithm for the best fit of experimental data of DeWire et al. [16]. The right sub-figure of Figure 2 and both sub-figures of Figure 3 show averaged experimental values,

and their empirical variances denoted by circles. For a good fit we expect the model to provide trajectories which remain in the intervals defined by the experimental deviations.

Note that the spontaneous deactivation of RGS protein was neglected in these final simulation experiments. The time interval of the simulations was 60 minutes in this case. As before, the initial conditions were set to describe a fully deactivated cell with all signaling activations on the basal level.

It is important to note that if we wish to compare the resulting parameter values with the values found in the literature, we have to denormalize every concentration (which is hardly feasible due to imperfect information about intracellular protein concentrations), and modify the corresponding rate constants to achieve the same time patterns. This is because a simulation method with normalized concentrations has been used in our study to analyze only the qualitative features of the model structure.
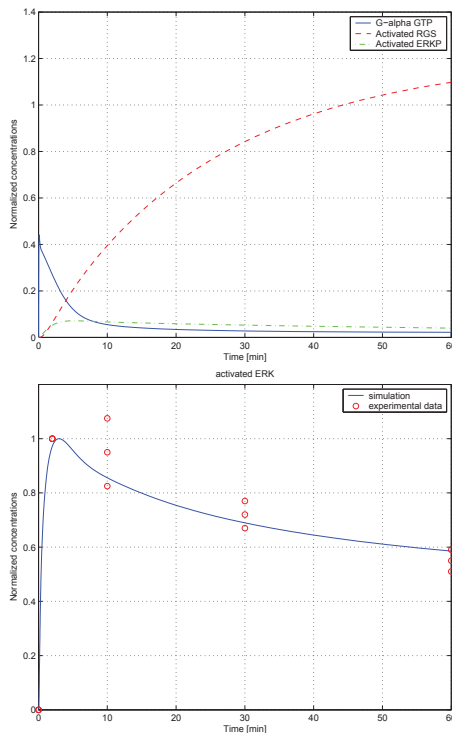
Fig. 2. $G\alpha - GTP$ activation and the activation pattern of ERK and the corresponding regulators. The circles on the second plot correspond to experimental results.

The results of the simulations, i.e. the system responses are depicted in Figs. 2 and 3. In the first sub-figure of Fig. 2 the simulated $G\alpha$, RGS and ERKP -activation pattern can bee seen. Here again, the total activated ERK concentration is taken into account, which includes also the complexes, where the activated ERK acts as an enzyme (ERKP and RGS activation). In the case of other components, the concentration of the free element is depicted. In the case of ERKP the total active concentration is depicted (the sum of the free active enzyme and the complex with ERK).

The $G\alpha$-activation pattern is strongly affected by receptor phosphorylation and ERK-induced activation of RGS-proteins,

which rapidly dephosphorylate the $G\alpha - GTP$ to $G\alpha - GDP$. The activation of GRK in the model is not related to ERK activation, so the RL_p concentration does not change significantly.
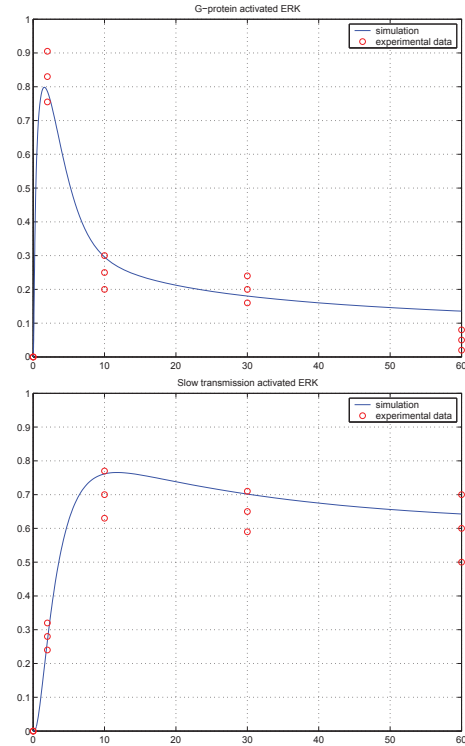

Fig. 3. G protein versus β-Arrestin mediated signaling. The circles correspond to experimental results

In Fig. 3 we can see the ERK, RGS and ERKP activation pattern corresponding to pure G protein dependent and G protein independent, RL_p (β-Arrestin) mediated signaling. The first sub-figure of Fig. 3 depicts the ERK, RGS and ERKP activation in the case, when no slow transmission is taken into account. In the right sub-figure the G protein independent signaling is illustrated.

E. Discussion

It can be seen in both Fig. 3 and 2 that the G protein activation and the G protein induced ERK activation has a pulsative maximum around 2 min, and is eliminated via the feedback of RGS activation. The G protein independent ERK activation, which can be related to the RL_p concentration, has a slower rising period, and remains more stable during the simulation period.

As it can be seen in the second plot of Figure 2, the resulting activation pattern inherits the qualitative features of both pathways: The rapid maxima of ERK activation at 2-3 minutes can be related to the G protein dependent pathway, and the remaining tonic activation originates from the slow transmission pathway. Both the theoretical considerations and simulation results show that the resulting activation pattern of the second plot of Figure 2 is not the simple sum of the activation patterns depicted in Figure 3, because of the feedback mechanisms and other effects.

We have to note again, because of the lack of information about intracellular protein concentrations and in vivo reaction rate constants, normalized concentrations were used. This implies that the identified parameters can not be directly compared to literature data related to measurements with known concentrations. But the model fulfills its main aim, and shows the required qualitative dynamic behavior and complexity for the description of the two-pathway regulated signaling system.

III. CONCLUSIONS AND FUTURE WORK

In this paper we have shown that if we take both ERK-mediated RGS and MAPKP feedback regulations into account, a qualitatively acceptable downstream behavior can be obtained in total ERK activation as well as in particular cases of G protein dependent and/or independent signaling.

Based on the simulation results presented here, we can conclude that modeling of slow transmission, RGS and MAPK-mediated regulation of signaling can be efficiently described using the framework of reaction kinetic systems, that may be essential when analyzing the dynamic behavior for physiological cell signaling. This type of model enables us to use the deficiency-based multistability-related results of Feinberg et al. [17], [18].

IV. ACKNOWLEDGEMENTS

REFERENCES

[1] J. S. Gutkind, "The pathways connecting G protein-coupled receptors to the nucleus through divergent mitogen-activated protein kinase cascades," *J. Biol. Chem.*, vol. 273, pp. 1839–1842, 1998.

[2] N. Zerangue and L. Y. Jan, "G-protein signaling: Fine-tuning signaling kinetics," *Curr. Biol.*, vol. 8, pp. 313–316, 1998.

[3] R. J. Lefkowitz, "Historical review: a brief history and personal reprospective of seven-transmembrane receptors," *Trends Pharmacol. Sci.*, vol. 25, pp. 413–422, 2004.

[4] W. Kolch, F. Calder, and D. Gilbert, "When kinases meet mathematics: the systems biology of MAPK signalling," *FEBS Lett.*, vol. 579, pp. 1891–1895, 2005.

[5] J. A. Pitcher, N. J. Freedman, and R. J. Lefkowitz, "G protein-coupled receptor kinases," *Annu. Rev. Biochem.*, vol. 67, pp. 653–692, 1998.

[6] N. J. Freedman and R. J. Lefkowitz, "Desensitization of G protein-coupled receptors," *Recent Prog. Horm. Res.*, vol. 51, pp. 319–351, 1996.

[7] K. A. DeFea, Z. D. Vaughn, E. M. O'Bryan, D. Nishijima, O. Dery, and N. W. Bunett, "The proliferative and antiapoptotic effects of substance P are facilitated by formation of a beta-arrestin-dependent scaffolding complex," *P. Natl. Acad. Sci. USA*, vol. 98, pp. 11 086–91, 2000.

[8] L. M. Luttrell, F. L. Roudabush, E. W. Choy, W. E. Miller, and M. E. Field, "Activation and targeting of extracellular signal-regulated kinases by beta-arrestin scaffolds," *P. Natl. Acad. Sci. USA*, vol. 98, pp. 2449–2454, 2001.

[9] J. M. Beaulieu, T. D. Sotinkova, W. D. Yao, L. Kockeritz, J. R. Woodgett, R. Gainetdinov, and M. G. Caron, "Lithium antagonizes dopamine-dependent behaviors mediated by an AKT/glycogen synthase kinase 3 signaling cascade," *P. Natl. Acad. Sci. USA*, vol. 101, pp. 5099–5114, 2004.

[10] D. C. Krauker, K. M. Page, and S. Sealfon, "Module dynamics of the GnRH signal transduction network," *J. Theor. Biol.*, vol. 218, pp. 457–470, 2002.

[11] H. Zhong, S. Wade, P. Woolf, J. Linderman, M. Clark, J. Traynor, and R. Neubig, "A spatial focusing model for G protein signals: RGS protein-mediated kinetic scaffolding," *J. Biol. Chem.*, vol. 278, pp. 7278–7284, 2003.

[12] J. A. Adams, G. M. Omann, and J. J. Linderman, "A mathematical model for ligand/receptor/G-protein dynamics and acrin polimerization in human neutrophils," *J. Theor. Biol.*, vol. 193, pp. 543–560, 1998.

[13] G. M. O. T. A. Riccobene and J. J. Linderman, "Modeling activation and desensitization of G-protein coupled receptors provides insight into ligand efficacy," *J. Theor. Biol.*, vol. 200, pp. 207–222, 1999.

[14] P. J. Woolf and J. J. Linderman, "From the static to the dynamic: Three models of signal transduction in G-protein coupled receptors," in *Biomed. Appl. Comp. Mod.*, A. Christopoulos, Ed., 2000, pp. 87–108.

[15] T. L. Kinzer-Ursem and J. J. Linderman, "Both ligand- and cell-specific parameters control ligand agonism in a kinetic model of G protein coupled receptor signaling," *PLOS Comput. Biol.*, vol. in press, 2008.

[16] S. M. DeWire, S. Ahn, R. J. Lefkowitz, and S. K.Shenoy, "β-Arrestins and cell signaling," *Annu. Rev. Physiol*, vol. 69, pp. 483–510, 2007.

[17] M. Feinberg, "On chemical kinetics of a certain class," *Arc. Ration. Mech. An.*, vol. 46, pp. 1–41, 2004.

[18] G. Craciun and M. Feinberg, "Understanding bistability in complex enzyme-driven reaction networks," *P. Natl. Acad. Sci. USA*, vol. 103, pp. 8697–8702, 2006.

[19] J. Tyson, C. Chen, and B. Novák, "Network dynamics and cell physiology," *Nature Reviews Molecular Cell Biology*, vol. 2, pp. 908–916, 2001.

[20] J. M. Beaulieu, T. D. Sotinkova, S. Marion, R. J. Lefkowitz, R. R. Gainetdinov, and M. G. Caron, "An Akt/β-Arrestin 2/PP2A signaling complex mediates dopaminergic neurotransmission and behavior," *Cell*, vol. 122, pp. 261–273, 2005.

[21] J. H. Kehrl and S. Sinnarajah, "RGS2: a multifunctional regulator of G-protein signaling," *Int. J. Biochem. Cell B.*, vol. 32, pp. 432–438, 2001.

[22] M. R. Koelle, "A new family of G-protein regulators - the RGS proteins," *Curr. Biol.*, vol. 9, pp. 143–147, 1997.

[23] G. Xie and P. P. Palmer, "How regulators of G protein signaling achieve selective regulation," *J. Mol. Biol.*, vol. 366, pp. 349–365, 2007.

[24] K. L. Neitzel and J. R. Hepler, "Cellular mechanisms that determine selective RGS protein regulation of G-protein-coupled receptor signaling," *Semin. Cell Dev. Biol.*, vol. 17, pp. 383–389, 2006.

[25] U. S. Bhalla, P. T. Ram, and R. Iyengar, "MAP kinase phosphatase as a locus of flexibility in a mitogen-activated protein kinase signaling network," *Science*, vol. 297, pp. 1018–1023, 2002.

Dávid Csercsik obtained his first degree in Electric Engineering at the Budapest University of Technology and Economics in 2005. He obtained his second MSc. in Biomedical engineering in 2007. He is a member of the Process Control Research Group of the Systems and Control Laboratory in the Computer and Automation Research Institute of the Hungarian Academy of Sciences. Besides he is a Phd student at the Information Technology Faculty of the Pázmány Péter Catholic University.

His main interests include systems biology, theory of reaction kinetic networks, nonlinear systems and control theory, computational neuroscience, modeling and model simplification of biochemical processes, intracellular signaling pathway dynamics and the dynamics of the female hormonal cycle.

An Object Tracking Algorithm on Several Massively Parallel Architectures

Norbert Bérci

(Supervisors: Dr. Péter Szolgay, Dr. Tamás Roska)

berci.norbert@itk.ppke.hu

Abstract—**Novel human-machine interfaces are tend to be based on direct touch and available in two versions: either a touch screen or a touch pad. More recently even multi-touch has been introduced, but the basic way of working is the same: the user have to physically touch something. Our proposed system processes optically captured video flow, thus has no limitations of a fixed (both in space and in size) screen. We have developed an algorithm [1] for finger tracking but after some simplification it seems like general object tracking can be solved with it as well. In this paper we present the details of the implementation on two different platforms and also some measurements regarding processing speed.**

I. INTRODUCTION

A. Motivation

Graphical user interfaces become more and more complex to be able to express sophisticated user commands. There are application areas where the conventional human-machine interfaces like the keyboard and the mouse have some drawbacks. They can not fulfill some features amongst which are: unwired, contactless interface, distant monitoring and control, extraordinary working conditions.

In the field of computer aided design (CAD), engineering (CAE), manufacturing (CAM) and especially in virtual reality systems control via hand gestures is a natural choice. Unlike voice control – the other natural command mechanism – selectivity is as simple as setting the viewport of the camera or zooming in.

B. Goals

We aim to develop a gesture recognition system based on visual image flow and implemented on a platform which allows the processing to be real-time. We hope that speed and precision parameters could be set by choosing the underlying hardware. Today the only viable solution is to implement it on the CNN paradigm [2] [3] based cellular wave computers. In the following sections we will discuss the implementataion on two of them.

C. Cellular Wave Computers

We have choosen the CNN architecture for design and implementation platform, since it is extremely well suited to image processing tasks. It has processing elements arranged in a grid which allows one-to-one mapping of each to a pixel.

Due to its analog and locally connected nature, processing is very fast and it allows non-linear dynamics to appear. A more detailed description can be found in [4].

1) The Bi-i System: The first development platform is the Bi-i system [5] [6] which is a standalone smart camera. The main parts are a CNN type ACE16k [7] image sensor-processor analogic chip for the spatio-temporal image processing tasks, a Texas Instruments TMS320C6415 DSP for fixed point computations and an ETRAX 100 LX from Axis as a communicating processor.

The system is packaged into a 154 mm x 82 mm x 140 mm box, and has power consumption about 15-20 W.

2) The eye-RIS System: The eye-RIS system is a programmable vision system using Anafocus' Smart Image Sensor technology, and an Altera NIOS-II 32 bit RISC processor for the control and classical algorithmic computing tasks.

The system is packaged into a 80 mm x 80 mm x 70 mm box, and according to the specifications has about 1.5 W power consumption.

II. ALGORITHMIC DETAILS

In the following sections we present the two different versions of the algorithm implemented on the two platforms. Basically the algorithmic differences are due to the different comand set, but it also represents the advancement of the algorithm itself.

A. The Bi-i version of the algorithm

1) Brief Description: The algoritm itself is based on feature extraction and object tracking. We have to make a distinction between hand postures and gestures: as explained in [8], a posture is a static configuration of the hand which could be identified from a still picture, in contrast to the gesture, which is a dynamic movement of the fingers and the hand to form a sign. This latter is not or just partially recognizable from a still picture, because it might be possible that the dynamics started from the same position may end up in two or more different gestures (so it can only be distinguished at one of the last frames) or the gesture itself depends on timing: information is distributed among the phases of the gesture.

We have been dealing with gestures only, static images were not considered. It is worth to note that posture recognition is
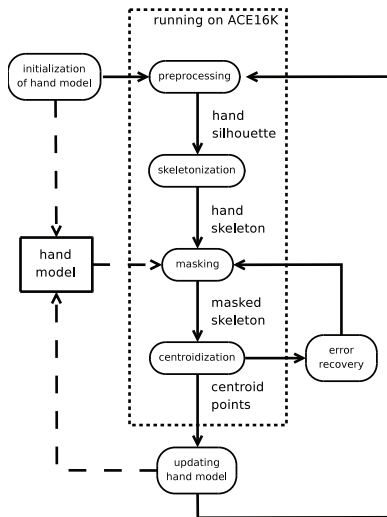
Fig. 1. The flowchart of the implemented algorithm. Blocks inside the dashed line run on the ACE16K visual processor, all the others have been implemented on the DSP.

Fig. 2. Measurements of frame processing times broken up into smaller algorithmic parts of the flowchart.

also possible with the presented system, but just as a part of a longer, dynamic movement.

To decide what kind of features should be tracked, we had to take into consideration the anatomy of the hand for feature candidates common on an average hand, and the abilities of the architecture used. Furthermore, tracked features should be easily mapped to the underlying hand model, which serves for supporting and guiding the recognition process.

2) Finger Tracking on the Bi-i System: The Bi-i implementation derives the skeleton of the hand and uses a wireframe model which is sufficient for our needs and aims. Other features have been regarded to a supporting role: when the image quality decreases, detection and usage of other features may be needed at the price of framedropping.

This version of the algorithm can be seen on figure 1. The two main parts of the algorithm are the pixel processing part which runs on the ACE16k processor and contains the preprocessing, skeletonization, masking and centroidization parts and the hand model part which runs on the DSP and its role is to support and aid the recognition task. It is utilized for error recovery also.

3) The Importance of Initialization: Recognition seems more difficult for dynamic image flows, but if we initialize the parameters of the hand model in the start position, we are able to collect lots of valuable information which can be utilized later. Such information include: length of the fingers, aspect ratio of the palm, grayscale level of the skin, the specific parameters of the separating edge to name a few.

What is more important, the initialization makes it possible to transform the recognition process to a tracking task: we do not want to find the hand in every frame independently of each other, but be able to follow it while moving. This makes it also possible to have a convenient starting position to find the hand, and later only partial or defective information is
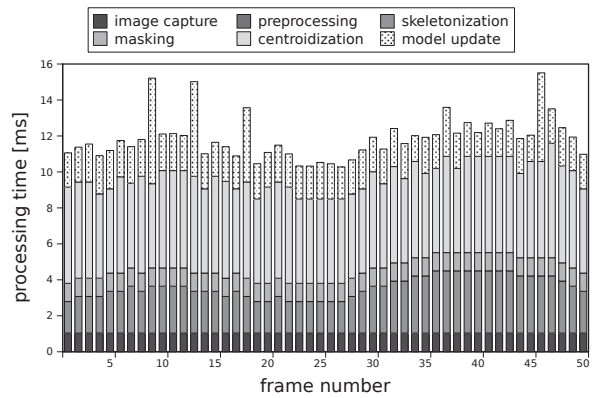
enough to follow it, since we know the initial parameters and deformation is not possible just bending of the fingers' joints and the wrist.

4) The Hand Model: With the masked skeleton and the centroid at hand, we are able to calculate the current direction of the fingers which will be also stored in the hand model. The computation is done in the following way: the masked centroid should have a skeleton touching the edge of the mask, since the skeleton should drive into the palm. Otherwise we have found something which is not the intended fingertip, so an error recovery method should be applied. From the centroid and the point where the skeleton touches the edge of the mask, the finger direction can be easily derived.

5) Preprocessing: The algorithm presented only deals with finger tracking. Its input is a segmented image: background removed, only the object should be present. Despite segmentation in general is a difficult task, in our case it can be solved by several different means: in the case of finger tracking it can be based on skin color discrimination, otherwise object motion based or high contrast based segmentation can be utilized. We have used the latter, since high illumination is also needed for high frame rate image acquisition.

6) Measurements: As can be seen on figure 2 the average processing time is about 12 ms, but the actual time is a bit unsteady, mainly due to the hand model and the input dependent processing algorithm parts (error recovery, skeletonization).

B. Object Tracking on the eye-RIS System

Compared to the previous version, several algorithm components have been removed. We gained faster processing, but the resulting system is not so robust (input should be higher quality than the first version). All parts of the algorithm run on the Q-eye chip, the conventional RISC processor in the system has not been used for computation. We have removed the hand model, so it is now considered a general object tracking system.

Since the two algorithms share lot of parts, we only emphasize the differences here. All other information can be found
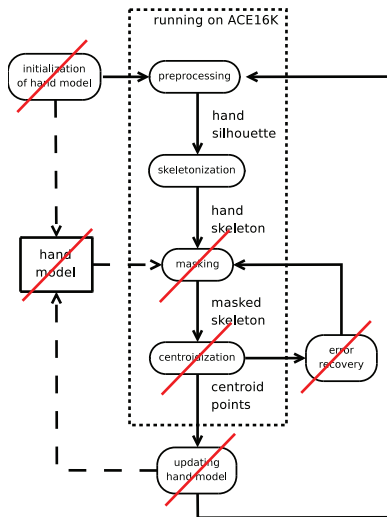
Fig. 3. The flowchart of the implemented algorithm. Some algorithm parts were dropped out, so it is completely executed on the Q-Eye visual processor

in the Bi-i version of the algorithm.

1) Skeletonization in a Central Role and Its Consequences: One of the characteristics of the skeletonization is that a single cell noise can easily disturb the process and multiple branches appears where should not, so uniformity of the silhouette is very useful. This was also taken into consideration during the design of the preprocessing step which produce the silhouette of the hand.

We must emphasize that the vital part of the algorithm is the skeletonization. We have used the native implementation of this algorithm on both systems, but it turned out that the robustness and precision could be greatly improved by another skeletonization process. The main problem is the relative unstability of the skeleton which means that under special circumstances, little (in extreme cases only one pixel) difference in the input image makes a huge difference in the computed skeleton. Different skeletonization algorithms are under investigation [9].

2) Preprocessing of the input image: In order for the skeletonization to work properly, a preprocessing step is necessary after which a well separated silhouette of the hand should be available. This preprocessing is currently composed of a static image correction to remove the uniformity artifacts of the cells of the chip caused by the manufacturing process, then we explicitly set the optics to defocus the image a bit, which makes the contour smooth for a better skeletonization and last a threshold function to convert the image to binary.

3) Robustness: If the fingers are thick, the environment surrounding the skeleton is uniformly black, and make lots of space available for the masks. The ability to follow high speed motions depends on the framerate the optical input and the thickness of the fingers. If we have to follow only one finger (replacing a mouse), the input can be zoomed, so there will be plenty of space in the input image for the masks and that way recognition of faster movements becomes available.
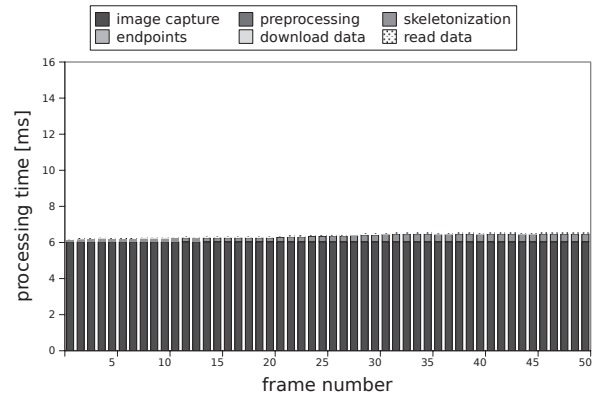

Fig. 4. The flowchart of the implemented algorithm. Blocks inside the dashed line run on the ACE16K visual processor, all the others have been implemented on the DSP.

subtask	avg. ratio of frame time	avg. time spent
image capture	94.42%	6,0399
preprocessing	0.05%	0,0034
skeletonization	4.72%	0,3038
endpoint detection	0.55%	0,0353
points download	0.08%	0,0054
read data	0.17%	0,0111

TABLE I
RATIO BETWEEN THE DIFFERENT COMPUTATION SUBTASKS WHEN COMPUTING ONE FRAME.

The skeletonization process does not connect previously unconnected objects, so the skeleton of the hand is virtually independent of the background which can be easily discarded this way.

4) Measurements: The measurements of the modified algorithm running on the Eye-RIS system is presented in figure 4. The processing time has been remarkably decreased mostly due to the removed algorithm components. What it the main advantage of the new algorithm is that despite its simplicity, it solves the same problem. The frame processing time of approximately 6.4 ms enables very high frame rate computation. It is also worth to note that the major part of the time spent on image grabbing. Table I summarizes the average ratio between each computation task. The computation itself takes only a fraction of a milisecond, and its major part is the skeletonization.

III. CONCLUSIONS

The presented system has the following enhancements: it uses a skeleton based approach which makes the system independent of the tiny shape differences in the hands and most notably slight differences in the edge. This is also benefical for the masking and tracing.

- instantly available (no worn parts, not even markers)
- hand size neutral implementation
- execution up to 100-150 FPS under ordinary (office) lightning conditions

- the second version of the algorithm meets the even stricter requirements of real-time systems, since deviances in computation time are minimal, the computation time varies only in the skeletonization part, which itself depends on the tracked object size and shape
- processing time only verly slightly depends on the number of object tracked
- the algorithm is able to track multiple objects and under ordinary (office) conditions, tracking time very slightly depends on the number of the tracked objects

IV. ACKNOWLEDGMENTS

We wish to express our gratitude for our institute, the Péter Pázmány Catholic University, Faculty of Information Technology. We also wish to thank to all of the collegaues who we have discussed the topics with and for their comments.

A. Further Research

1) The hand model should be intensively analyzed, and a proper model developed for tracking all the fingertips, joints, wrist.
2) The characteristics of the commonly used gestures should be analyzed, the widely used Deaf sign languages can hopefully be recognized paving the way for computer translation between the Deaf and hearing people.
3) Although the algorithm and implementation described herein is a frame based approach, lots of the preprocessing and feature extraction can be done on a paralell hardware, especially on a multilayer chip.
4) Further studies have been planned to revise the system to achieve truly grayscale operation, especially the skeletionization process on the Bi-i hardware. That might abolish the tiny branches and also might help to more precisely separate the fingers, which is one of the main issues here.

COMMENTS

A paper focused on the measurements of the algorithms has been accepted for the International Symposium on Nonlinear Theory and its Applications 2008 as an invited paper (paper id 2183), and it will be published in the proceedings of the conference.

REFERENCES

[1] N. Bérci and P. Szolgay, "Vision based human-machine interface via hand gestures," in *Proc. Eur. Conf. on Circ. Theory and Design (ECCTD)*, Seville, Spain, Aug. 26–30, 2007, pp. 496–499.
[2] L. O. Chua and L. Yang, "Cellular neural networks: Theory," *IEEE Trans. Circuits Syst.*, vol. 35, pp. 1257–1272, Oct. 1998.
[3] ——, "Cellular neural networks: Applications," *IEEE Trans. Circuits Syst.*, vol. 35, pp. 1273–1290, Oct. 1998.
[4] L. O. Chua and T. Roska, *Cellular Neural Networks and Visual Computing*. Cambridge, UK: Cambridge University Pess, 2002.
[5] Á. Zarándy and C. Rekeczky, "Bi-i: a standalone cellular vision system, Part I. Architecture and ultra high frame rate processing examples," in *Proc. 8th Int. Workshop on CNNs and their Appl. (CNNA)*, Budapest, Hungary, Jul. 22–24, 2004, pp. 4–9.
[6] ——, "Bi-i: a standalone cellular vision system, Part II. Topographic and non-topographic algorithms and related applications," in *Proc. Int. Workshop on CNNs and their Appl. (CNNA)*, Budapest, Hungary, Jul. 22–24, 2004, pp. 10–15.
[7] G. Liñán, R. Domínguez-Castro, S. Espejo, and Á. Rodríguez-Vázquez, "ACE16k: A programmable focal plane vision processor with 128x128 resolution," in *Proc. Eur. Conf. on Circ. Theory and Design (ECCTD)*, Espoo, Finland, Aug. 28–31, 2001, pp. 345–348.
[8] J. J. LaViola, "A survey of hand posture and gesture recognition tehniques and technology," Department of Computer Science, Brown University, Providence, Rhode Island, USA, Tech. Rep. CS-99-11, 1999.
[9] H. Blum., "A transformation for extracting new descriptors of shape," in *Models of the perception of Speech and Visual Form*. Cambridge, MA: MIT Press, 1967, pp. 362–380.

Accelerating Ocean Current Simulations by Using Cell Broadband Engine

András Kiss

(Supervisor: Péter Szolgay)

Abstract—**IBM has recently introduced the Cell Broadband Engine (Cell BE) Architecture, which contains 8 identical vector processors in an array structure. More Cell Processors are attached on the IBM Blade Center QS21 rack for enormous computing power. In this paper the implementation of a Navier-Stokes equation solver on the Cell BE is described. The kernel is optimized according to the special requirements of the Cell BE and may implement on a set of QS21 racks. In addition, the 2-D Princeton Ocean Model is implemented on the Cell BE. Our solutions performance is measured and the speed, power, area parameters are compared with different hardware implementations.**

I. INTRODUCTION

A. Cell Broadband Engine

The Cell Broadband Engine Architecture (CBEA) is developed by the alliance of Sony Computer Entertainment, Toshiba, and IBM. The first implementation of the CBEA, designed for the Sony PlayStation 3 game console, is the Cell Broadband Engine, known as Cell Processor. It is designed to get high computational performance with low power and small area usage. The Cell processor can be split into four components:

- the Power Processor Element (PPE),
- the Synergistic Processor Elements (SPEs),
- the Element Interconnect Bus (EIB),
- the external input, output structures.

The PPE is a conventional dual-threaded 64bit PowerPC processor for control the operation of the eight SPEs. It contains a 32 KB instruction and 32KB data L1 cache and a 512KB L2 cache. Each PPU can complete two double precision operations per clock cycle (using multiply-add instructions), or eight single precision operations per clock cycle. The PPE can run existing operating systems and manages the communication between the SPEs.

The SPE (1) is a RISC processor with 128-bit SIMD (Single Instruction Multiple Data) organization, therefore it can not run operating systems. It is designed to handle streaming data. In order to take full advantage of the SPEs, the programs running will need to be vectorised. Each SPE contains a 256 KB embedded SRAM, called Local Storage. An SPE can operate on 16 8-bit integers, 8 16-bit integers, or 4 single precision floating point numbers in a single clock cycle. The SPU can access the system memory through DMA transfers, but not directly.

The EIB is a communication ring bus with 4 rings. Two rings goes clockwise and two goes counterclockwise. They
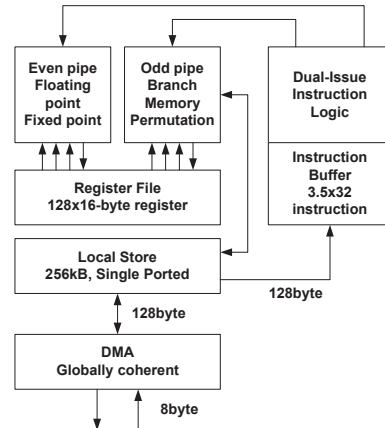

Fig. 1. Block diagram of the SPE co-processor

connect the PPE, the eight SPEs, the memory controller and two off-chip I/O interfaces. It contains an arbitration unit for controlling the traffic on the EIB.

I/O devices can be accessed via two Rambus FlexIO interfaces where one of them (the Broadband Interface (BIF)) is coherent and makes it possible to connect two Cell processors directly.

B. The QS21 Cell Blade

The IBM BladeCenter QS21 (2) is a second generation blade system based on Cell Broadband Engine processors. The QS21 contains two high-performance Cell BE processors (interconnected with a broadband interface) with 2 GB standard processor memory. Consequently a single-wide blade contains two Power Processing Unit and 16 Synergistic Processor Elements and provides more than 400GFLOPS computing power. Several QS21 Cell Blade may be interconnected via high speed interfaces in a Blade Center house. A single chassis can handle 14 single-wide blade racks up to 6.4 TFLOPS computing power.

II. OCEAN MODEL

Several studies proved the effectiveness of the CNN-UM solution of different PDEs [1], [2]. But the results cannot be used in real life implementations because of the limitations of the analog CNN-UM chips such as low precision, temperature sensitivity or the application of non-linear templates. Some previous results show that emulated digital architectures can be
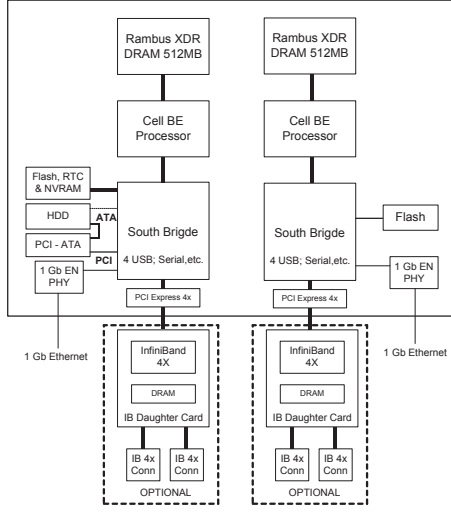
Fig. 2.   Block diagram of the IBM QS21 BladeCenter

very efficiently used in the computation of the CNN dynamics [3], [4] and in the solution of PDEs [5], [6], [7]. Using the CNN simulation kernel described in [4] helped to solve Navier-Stokes PDE on the Cell architecture. The details will be presented here.

Simulation of compressible and incompressible fluids is one of the most exciting areas of the solution of PDEs because these equations appear in many important applications in aerodynamics, meteorology, and oceanography. Modeling ocean currents plays a very important role both in mediumterm weather forecasting and global climate simulations. In general, ocean models describe the response of the variable density ocean to atmospheric momentum and heat forcing. The Princeton Ocean Model (POM) [8] use several horizontal layers to describe the motion in the deeper regions of the ocean. It is a sigma coordinate model in which the vertical coordinate is scaled on the water column depth.

$$\frac{\partial DU}{\partial x} + \frac{\partial DV}{\partial y} + \frac{\partial \omega}{\partial \sigma} + \frac{\partial \eta}{\partial t} = 0 \qquad (1)$$

$$\frac{\partial UD}{\partial t} + \frac{\partial U^2 D}{\partial x} + \frac{\partial UVD}{\partial y} + \frac{\partial U\omega}{\partial \sigma} - fVD+$$

$$+gD\frac{\partial \eta}{\partial x} + \frac{gD^2}{\rho_0} \int_{\sigma}^{0} \left[\frac{\partial \rho'}{\partial x} - \frac{\sigma'}{D}\frac{\partial D}{\partial x}\frac{\partial \rho'}{\partial \sigma'} \right] d\sigma' = \qquad (2)$$

$$= \frac{\partial}{\partial \sigma}\left[\frac{K_M}{D}\frac{\partial U}{\partial \sigma} \right] + F_x$$

$$\frac{\partial VD}{\partial t} + \frac{\partial UVD}{\partial x} + \frac{\partial V^2 D}{\partial y} + \frac{\partial V\omega}{\partial \sigma} - fUD+$$

$$+gD\frac{\partial \eta}{\partial y} + \frac{gD^2}{\rho_0} \int_{\sigma}^{0} \left[\frac{\partial \rho'}{\partial y} - \frac{\sigma'}{D}\frac{\partial D}{\partial y}\frac{\partial \rho'}{\partial \sigma'} \right] d\sigma' = \qquad (3)$$

$$= \frac{\partial}{\partial \sigma}\left[\frac{K_M}{D}\frac{\partial V}{\partial \sigma} \right] + F_y$$

where x,y are the conventional 2-D Cartesian coordinates;

$\sigma = \frac{z-\eta}{H+\eta}$, $D \equiv H + \eta$, where H(x,y) is the bottom topography and $\eta(x,y,t)$ is the surface elevation. The U and V terms are the horizontal and vertical velocities . The ω denotes the transformed vertical velocity according to the σ coordinates. The solution of equations (1)-(3) is based on the freely available Fortran source code of the POM [8]. The discretization in space is done according to the Arakawa-C differencing scheme where the variables are located on a staggered mesh. The mass transports U and V are located at the center of the box boundaries facing the x and y directions, respectively. All other parameters are located at the center of mesh boxes. The horizontal grid uses curvilinear orthogonal coordinates.

The equations, governing the dynamics of coastal circulation, contain fast moving external gravity waves and slow moving internal gravity waves. It is desirable in terms of computer economy to separate the vertically integrated equations (external mode) from the vertical structure equations (internal mode). This technique, known as mode splitting permits the calculation of the free surface elevation with little sacrifice in computational time by solving the velocity transport separately from the three-dimensional calculation of the velocity and the thermodynamic properties.

The external mode calculation is responsible for computing surface elevation and the vertically averaged velocities. The internal mode computes horizontal and vertical velocities (U, V), temperature (T) and salinity (S). During the calculation the former uses short time step, whereas the latter uses longer time step. Using this method many external steps are evaluated for every long internal time step. These results are used for the internal mode computation.

The velocity external mode equations are obtained by integrating the internal mode equations over the depth, thereby eliminating all vertical structure. Thus, by integrating Equations (1)-(3) from $\sigma = -1$ to $\sigma = 0$ the following equations can be obtained:

$$\frac{\partial \eta}{\partial t} + \frac{\partial \overline{U}D}{\partial x} + \frac{\partial \overline{V}D}{\partial y} = 0 \qquad (4a)$$

$$\frac{\partial \overline{U}D}{\partial t} + \frac{\partial \overline{U}^2 D}{\partial x} + \frac{\partial \overline{UV}D}{\partial y} - f\overline{V}D + gD\frac{\partial \eta}{\partial x} =$$

$$= - <wu(0)> + <wu(-1)> -$$

$$- \frac{gD}{\rho_0} \int_{-1}^{0}\int_{\sigma}^{0} \left[D\frac{\partial \rho'}{\partial x} - \frac{\partial D}{\partial x}\sigma'\frac{\partial \rho'}{\partial \sigma} \right] d\sigma'd\sigma \qquad (4b)$$

$$\frac{\partial \overline{V}D}{\partial t} + \frac{\partial \overline{UV}D}{\partial x} + \frac{\partial \overline{V}^2 D}{\partial y} + f\overline{U}D + gD\frac{\partial \eta}{\partial y} =$$

$$= - <wv(0)> + <wv(-1)> -$$

$$- \frac{gD}{\rho_0} \int_{-1}^{0}\int_{\sigma}^{0} \left[D\frac{\partial \rho'}{\partial y} - \frac{\partial D}{\partial y}\sigma'\frac{\partial \rho'}{\partial \sigma} \right] d\sigma'd\sigma \qquad (4c)$$

The overbars denote vertically integrated velocities such as $\overline{U} \equiv \int_{-1}^{0} U d\sigma$. The wind stress components are $-<wu(0)>$
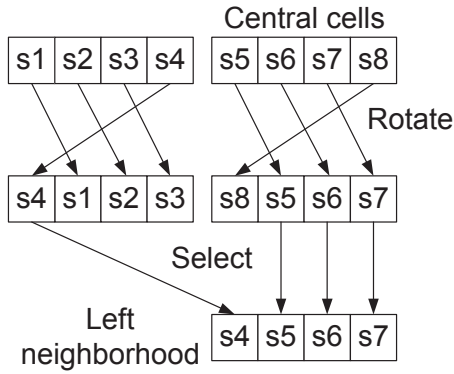
Fig. 3.   Generation of the left neighborhood

Fig. 4.   Rearrangement of the state values

and $-< wv(0) >$, and the bottom stress components are $-< wu(-1) >$ and $-< wv(-1) >$. U, V are the horizontal velocities, f is the Coriolis parameter, g is gravitational acceleration, ρ_0 and ρ' are the reference and in situ density, respectively.

III. IMPLEMENTATION

The large (128-entry) register file of the SPE makes it possible to store the neighborhood of the currently processed cell during the solution of the governing equations. The number of load instructions can be decreased significantly.

Since the SPEs cannot address the global memory directly, the users application running on the SPE is responsible to carry out data transfer between the local memory of the SPE and the global memory via DMA transactions. Since the relatively small local memory of the SPEs does not allow to store all the required data, an efficient buffering method is required. In our solution a belt of 5 rows is stored in the local memory from the array: 3 rows are required to form the local neighborhood of the currently processed row, one line is required for data synchronization, and one line is required to allow overlap of the computation and communication. Depending on the size of the users code the 256Kbyte local memory of the SPE can approximately store data for a 128 cell wide array.

The SPEs in the Cell architecture are SIMD-only units hence the state values of the cells should be grouped into vectors. The size of the registers is 128bit and 32bit floating point numbers are used during the computation. Accordingly, our vectors contain 4 elements. Let's denote the state value of the ith cell by si.

It seems obvious to pack 4 neighboring cells into one vector $\{s5, s6, s7, s8\}$. However, constructing the vector which contains the left $\{s4, s5, s6, s7\}$ and right $\{s6, s7, s8, s9\}$ neighbors of the cells is somewhat complicated because 2 "rotate" and 1 "select" instructions are needed to generate the required vector (see Figure 3). This limits the utilization of the floating-point pipeline because 3 integer instructions (rotate and select) must be carried out to generate the left and right neighborhood of the cell, before a floating point instruction can be issued.

This limitation can be removed by slicing the CNN cell array into 4 vertical stripes and rearranging the cell values.
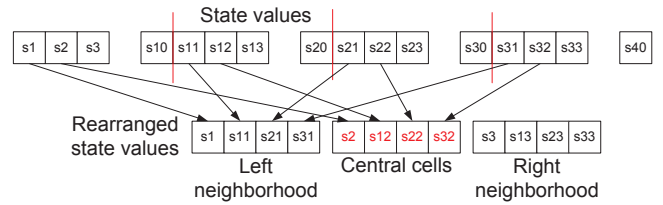
In the above case, the 4-element vector contains data from the 4 different slices as shown in Figure 4. This makes it possible to eliminate the shift and shuffle operations to create the neighborhood of the cells in the vector. The rearrangement should be carried out only once, at the beginning of the computation and can be carried out by the PPE. Though, this solution improves the performance of the simulation data, data dependency between the floating-point instructions may still cause pipeline stalls. In order to eliminate this dependency the inner loop of the computation must be rolled out. Instead of waiting for the result of the first floating-point instruction, the computation of the next group of cells is started. The level of unrolling is limited by the size of the register file.

To achieve even faster computation multiple SPEs can be used. The data can be partitioned between the SPEs by horizontally striping the cell array. The communication of the state values is required between the adjacent SPEs when the first or last line of the stripe is computed. Due to the row-wise arrangement of the state values, this communication between the adjacent SPEs can be carried out by a single DMA operation. Additionally, the ring structure of the EIB is well suited for the communication between neighboring SPEs.

IV. PERFORMANCE AND CONCLUSIONS

For testing and performance evaluation purposes a simple initial setup was used which is included in the Fortran source code of the POM (5). This solves the problem of the flow through a channel which includes an island or a seamount at the center of the domain. The size of the modeled ocean is 1024km, the north and south boundaries are closed, the east and west boundaries are open, the grid size is $128 \times 128 \times 32$ and the horizontal grid resolution is 8km. The simulation was ran using 6s internal timestep and 180s external timestep, the simulated time interval was 72 hours. Experimental results of the average iteration time are summarized in Table I.

The achievable performance of the Cell using different number of SPEs is compared to the performance of the Intel Core 2 Duo T7200 2GHz scalar processor. Comparison of the required computation time of one iteration in external (2D) and internal (3D) mode show that the external mode computations can be carried out 126 times faster. The result is significant saving on computation time. Performance of the six-SPE solution is compared to the performance of a high performance microprocessor. The external mode calculations on the 4 Cell processor on the QS21 system are 278-time faster than on the Core 2 Duo microprocessor, while in the internal mode 362-time speedup can be achived. During a 72 hours simulation using both internal and external mode calculations
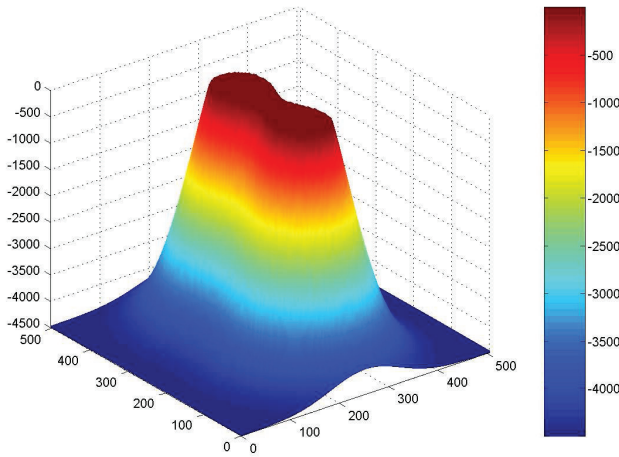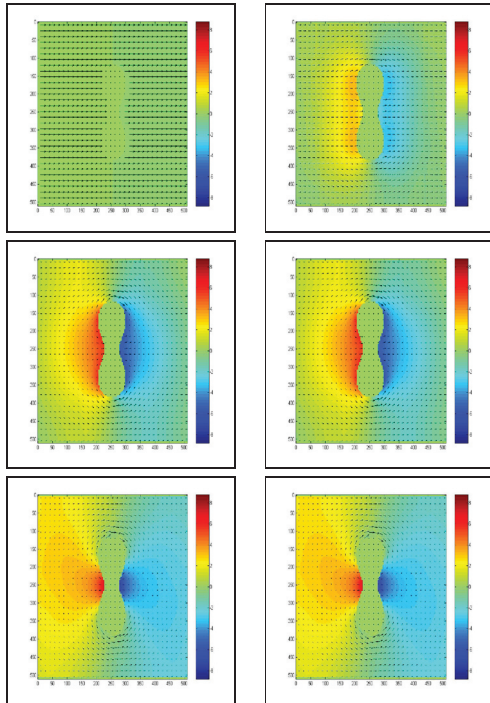
Fig. 5.   Ocean surface example

Fig. 6.   Results after some given iteration steps of the black and white skeletonization

85-time speedup was measured on the PS3 system and 296-time speedup on the QS21 system.

Complex spatio-temporal dynamical problems are analyzed by a topographic array processor. The Cellular Nonlinear Circuits were successfully used to solve the 3-D Princeton Ocean Model and significant performance improvement was achieved. Our solution was optimized according to the special requirements of the Cell architecture. Performance comparison showed that about 17-time speedup can be achieved with respect to a high performance microprocessor in the single SPE solution, while the speedup is 279-time higher when all the 32 SPEs are utilized on the QS21 system.

Parameters	Implementation		
	Core2Duo	CELL (6 SPEs)	2×QS21* (4×8 SPEs)
Iteration time in 2D (ms)	8.2	0.103	0.0294
Iteration time in 3D (ms)	1117	12.98	3.0785
Computation time of a 72 hour simulation (s)	1962.7	23.16	6.617
Power (W)	65	85	340
Area (mm^2)	143	253	1012

(cell array size: $128 \times 128 \times 32$; *The results of the 3D ocean model on the QS21 Blade Center are estimated results.)

A. Further Research

Next step will be the implementation on the QS21 system. At this time the QS21 is under installation in our institute.

COMMENTS

The extended version of this paper has been accepted for the 11th International Workshop on Cellular Neural Networks and their Applications, CNNA 2008.

REFERENCES

[1] P. Szolgay, G. Vörös, and Gy. Erőss. On the Applications of the Cellular Neural Network Paradigm in Mechanical Vibrating System. *IEEE. Trans. Circuits and Systems-I, Fundamental Theory and Applications*, 40(3):222–227, 1993.
[2] Z. Nagy and P. Szolgay. Numerical solution of a class of PDEs by using emulated digital CNN-UM on FPGAs. *Proc. Of 16th European Conf. On Circuits Theory and Design*, II:181–184, September 2003.
[3] Z. Nagy and P. Szolgay. Configurable Multi-layer CNN-UM Emulator on FPGA. *IEEE Transaction on Circuit and Systems I: Fundamental Theory and Applications*, 50:774–778, 2003.
[4] Z. Nagy, Z. Kincses, L. Kék, and P. Szolgay. CNN Model on Cell Multiprocessor Array. *Proceedings of the European Conference on Circuit Theory and Design (ECCTD'2007)*, pages 276–279, 2007.
[5] Z. Nagy and P. Szolgay. Solving Partial Differential Equations on Emulated Digital CNN-UM Architectures. *Functional Differential Equations*, 13:61–87, 2006.
[6] P. Kozma, P. Sonkoly, , and P. Szolgay. Seismic Wave Modeling on CNN-UM Architecture. *Functional Differential Equations*, 13(1):43–60, 2006.
[7] Z. Nagy, Zs. Vörösházi, and P. Szolgay. Emulated Digital CNN-UM Solution of Partial Differential Equations. *Int. J. CTA*, 34(4):445–470, 2006.
[8] The Princeton Ocean Model (POM). [Online] http://www.aos.princeton.edu/aos.

New Methods for Reliable Packet Transfer and Energy Balancing in Wireless Sensor Networks

András Bojárszky

(Supervisor: Dr. János Levendovszky)
bojarszky.andras@itk.ppke.hu

Abstract— **In this paper some novel unicast protocols are developed for wireless sensor networks (WSNs) in order to ensure reliable packet transmission and maximize the lifespan at the same time. The optimal transmission energies and the optimal numbers for repeated packet transfers are derived which guarantee that the packets are received by the Base Station (BS) with a given probability, subject to achieving the longest possible lifespan. These protocols can be applied in biomedical applications where energy consumption and longevity are of crucial importance. The optimization has been carried out for the chain protocol (when nodes are forwarding the packets toward the BS via the neighbouring nodes) and for the shortcut type of protocols (when packet is handed down to neighbours in the chain until on certain node it gets transmitted directly to the BS). The reliability of information transfer is enhanced by repeated low-energy packet transmissions. The new results have been tested by extensive simulations which also demonstrated that the lifespan of WSN can significantly be increased by the new unicast protocols.**

Keywords— **Communication systems, Communication system routing, Network reliability, Protocols**

I. INTRODUCTION

In most of the applications the WSN must convey the collected data to a single Base Station. In this set-up we assume that each node generates packets randomly and these packets are then transferred to the BS by multihop transmissions as indicated by Figure 1.
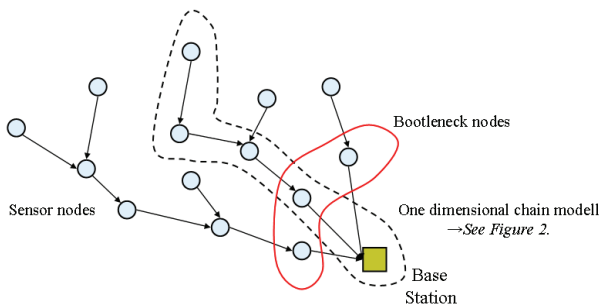

Figure 1. Spanning tree for the unicast flat routing

In this case the nodes being closer to the BS can get quickly overloaded as they have to retransmit almost all the packets sent to the BS. This results in very short longevity. In order to circumvent this, we propose novel unicast energy aware protocols which maximize the lifespan of the network. These novel methods assume that the distances between the nodes are known. Based on this information minimal energy consumption is achieved together with a guaranteed level of reliability (the probability of each packet reaching the BS properly is beyond a given a given threshold).

There are four energy balancing methods proposed by Haenggi [11]: (i) distance variation, (ii) balanced data compression, (iii) shortcut routing, and (iv) equalization end-to-end reliability. The latter satisfies reliability constraints by using uniform transmission energies and no packet transmission repetition. In our proposed methods reliability constraints are met by using lower transmission energies.

The paper addresses reliable packet transmission in WSN when packets are to be received on the Base Station (BS) with a given reliability in terms of keeping the error probability under a given threshold [1]. Since the success of every individual packet transmission depends on the distance and the energy of transmission, the probability of correct reception will diminish exponentially with respect to the number hops, in the case of multi-hop packet transfers [2]. This effect can be compensated by repeated packet transmissions. In this way, low-energy packet transmissions can still result in reliable information transfer by choosing an appropriate number of repetition. Furthermore, the overall energy consumption needed for repeated transfer may still be lower than a single high energy transmission needed to achieve a given level of reliability.

We investigate this scheme in the case of two different protocols:

- *Chain protocol* when packet transfer takes place over a 1D chain of nodes (created some routing algorithm running prior to the packet transfer), and the nodes send each packet to their neighbours on the nearside of the BS. Each node in the chain repeats the transmission according to a given number optimized prior to the transmission,

- *Shortcut protocol* when the packet travels in the chain down to a certain node l which then sends the packet directly to the BS (shortcut). In this protocol the nodes participating in the packet transfer also repeat the packet transmission a number of times and this number is optimized prior to the communication.

Our concern is to derive the appropriate transmission energies and the appropriate number for repeated transfer needed to achieve a given reliability and to minimize the overall energy consumption at the same time. This problem leads to a constrained optimization which finally yields two optimal vectors characterizing the packet transfer from a source node i to the BS as follows:

- the optimal transmission energy vector $\mathbf{g}_{opt}^{(i)} = \left(g_{1,opt}^{(i)}, g_{2,opt}^{(i)}, ..., g_{i,opt}^{(i)}, 0, ..., 0 \right)$ where component $g_{j,opt}$ describes the energy needed to transmit the packet form node j to node j-1; and

- the optimal number of repeated transmissions $\mathbf{a}_{\text{opt}}^{(i)} = \left(a_{1,\text{opt}}^{(i)}, a_{2,\text{opt}}^{(i)}, ..., a_{i,\text{opt}}^{(i)}, 0, ..., 0 \right)$ to achieve a reliable packet transfer to the BS, where $a_{j,\text{opt}}^{(i)}$ represents the number of re-transmission by node j.

In the case of the shortcut protocol (a packet originating from node i handed down to neighbours in the chain till node l_i from where it is directly sent to the BS) the optimal energy vector is described as $\mathbf{g}_{\text{opt}}^{(i)} = \left(0, ..., 0, G_{l_i,\text{opt}}^{(i)}, g_{l_i+1,\text{opt}}^{(i)}, ..., g_{i,\text{opt}}^{(i)}, 0, ..., 0 \right)$, where $G_{l_i,\text{opt}}$ denotes the shortcut energy to BS from node l_i and $\mathbf{a}_{\text{opt}}^{(i)} = \left(0, ..., 0, a_{l_i,\text{opt}}^{(i)}, a_{l_i+1,\text{opt}}^{(i)}, ..., a_{i,\text{opt}}^{(i)}, 0, ..., 0 \right)$ contains the optimal repetitions. In the latter case the optimization also involves to find the appropriate l_i.

In this paper we will optimize the variables described above and compare the achieved lifespan to the longevities of repetition-free protocols.

II. THE MODEL

After the routing protocol has found the path to the base station, the subsequent nodes participating in the packet transfer can be regarded as a one dimensional chain labeled by $i = 1, ..., N$ and depicted by the Fig. 1.
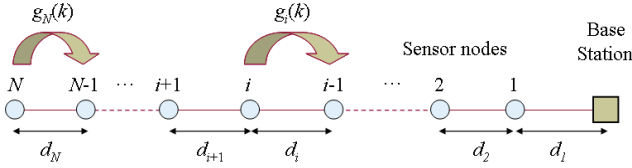

Figure 2. One dimensional chain model for WSN

The system is characterized as follows:

The topology is uniquely defined by a distance vector $\mathbf{d} = \left(d_1, ..., d_N \right)$, where $d_i, i = 1, ..., N$ denotes the distance between node i and i-1, respectively, whereas the energy needed to transmit packet over distance d is given as $g = \dfrac{d^\alpha \Theta \sigma_Z^2}{-\ln P} + g_0$ dictated by the Rayleigh model [11] (where d is the distance, α depends on the propagation type, P is the reliability of correct reception, Θ is the threshold, σ_Z^2 is the noise energy, while g_0 represents the consumption of the electronics during transmitting and receiving). For simplicity, this expression connecting the reliability parameter P of the transmission with the transmission energy g is denoted by $P = \Psi(g)$. The initial battery power on each node is the same and denoted by C and the energy state of the nodes at the kth time instant is expressed by vector $\mathbf{c}(k) = \left(c_1(k), ..., c_N(k) \right)$;

As a result, a WSN is fully characterized by vectors $\mathbf{g}$, $\mathbf{p}$, and $\mathbf{c}$ respectively.

III. RELIABLE PACKET TRANSFER

In the case of the chain protocol, the end-to-end probability of correct packet reception at the BS is

$P_{\text{EE}} = \displaystyle\prod_{j=1}^{i} P_j$, and the associated energies are $g_j = \dfrac{d_j^\alpha \Theta \sigma_Z^2}{-\ln P_j} + g_0$, $j = 1, ..., i$. As a result, a given P_{EE} can be achieved by several choices of P_j-s (i.e. several factorizations) yielding different energy consumptions.

A. Reliable packet transfer by packet repetition

The packet transmissions can be made repeatedly to increase reliability in such a way that the packet generated by node i is retransmitted a_i-times. As a result, in the case of the chain protocol the reliability constraint is fulfilled if

$$\prod_{j=1}^{i} \left(\sum_{n=1}^{a_j} \binom{a_j}{n} P_j^n \left(1 - P_j \right)^{a_i - n} \right) \geq 1 - \varepsilon, \tag{1}$$

where $P_j = \Psi(g_j)$ The goal is to maximize the minimum remaining energy on the bottleneck node according to the following objective function:

$$\mathbf{a}_{\text{opt}}^{(i)}, \mathbf{g}_{\text{opt}}^{(i)} : \max_{a, \mathbf{g}} \ \min_{j:1 \leq j \leq i} c_j(k+1). \tag{2}$$

where $c_j(k+1) = c_j(k) - a_i g_j$; $1 \leq j \leq i$, subject to the reliability constraint (1). In this case the optimization will return $\mathbf{g}_{\text{opt}}^{(i)} = \left(g_{1,\text{opt}}^{(i)}, ..., g_{i,\text{opt}}^{(i)}, 0...0 \right)$ and $\mathbf{a}_{\text{opt}}^{(i)} = \left(a_{1,\text{opt}}^{(i)}, a_{2,\text{opt}}^{(i)}, ..., a_{i,\text{opt}}^{(i)}, 0, ..., 0 \right)$.

The problem can be similarly posed for the shortcut protocol. The reliability constraint is

$$\prod_{j=l}^{i} \left(\sum_{n=1}^{a_j} \binom{a_j}{n} P_j^n \left(1 - P_j \right)^{a_i - n} \right) \geq 1 - \varepsilon, . \tag{3}$$

where $P_j := \Psi(g_j)$. Again the minimum remaining energy is to be maximized according to the objective function

$$a_{i,\text{opt}}, \mathbf{g}_{\text{opt}}^{(i)} : \max_{a, \mathbf{g}} \ \min_{j:l_i \leq j \leq i} c_j(k+1). \tag{4}$$

where $c_j(k+1) = c_j(k) - a_j g_j$ for $j = l_i+1, ..., i$ and $c_{l_i}(k+1) = c_{l_i}(k) - a_{l_i} G_{l_i}$ The optimization will return the vectors $\mathbf{g}_{\text{opt}}^{(i)} = \left(0, ..., 0, G_{l_i,\text{opt}}^{(i)}, g_{l_i+1,\text{opt}}^{(i)}, ..., g_{i,\text{opt}}^{(i)}, 0, ..., 0 \right)$ and $\mathbf{a}_{\text{opt}}^{(i)} = \left(0, ..., 0, a_{l_i,\text{opt}}^{(i)}, a_{l_i+1,\text{opt}}^{(i)}, ..., a_{i,\text{opt}}^{(i)}, 0, ..., 0 \right)$.

B. The optimization algorithm

The optimization problems posed in (2) can be solved by special combinatorial optimization technique (i.e. "constrained walk in the state space"), providing the optimal solutions. Since this optimization can be carried out off-line priori to the deploying the WSN any optimization algorithm will suffice to find the optimal parameters. The solution can then be downloaded to the nodes in the form of tables indicating that if a packet arrives to node j originating from node i then the corresponding transmission energy is $g_{j,\text{opt}}^{(i)}$

and the repetition factor is $a_{i,\text{opt}}$, respectively. The optimization is carried out for all possible source nodes $i = 1,...,N$. The algorithm is represented by the following block diagram:
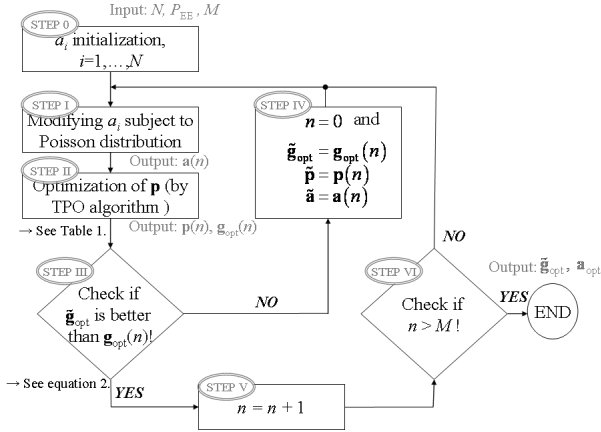

Figure 3. The flow diagram of the general optimization algorithm

The input of the optimization algorithm are (i) the number of nodes N; (ii) a control parameter M which influences the running time of the algorithm; (iii) the transmission probability P_{EE}; and (iv) the distances d_i. The transmission probability $\mathbf{p}$ vector is initially set uniformly. In the case of multiplication after rearranging (3) one can obtain the following polynom of order a_i:

$$P_{\text{EE}} = \sum_{j=1}^{a_i} \sum_{k=0}^{a_i - j} \binom{a_i}{j} \binom{a_i - j}{k} P_i^{j+k} \cdot (-1)^k \qquad (5)$$

Selecting the proper roots of the polynom the value of P_i can be obtained.

Since (2) is defined over a discrete set the optimum is sought by stochastic search akin to the Mathias algorithm. The transmission probability optimization (TPO) algorithm is described in Table 1.

TABLE I.   THE STEPS OF THE TPO ALGORITHM

Steps	Action
step 0.	we set the initial $\mathbf{p}$ vector according to (4)
step 1.	by matrix $\mathbf{P}_{\text{mod}}$, we modify vector $\mathbf{p}$ subject to the condition that the product of the components remains the same: $P_j = P_j \cdot P_{\text{mod}\,j,k}$ and $P_k = P_k / P_{\text{mod}\,j,k}$ $\forall j,k$
step 2.	we calculate the transmission energy vector $\mathbf{g}(m)$;
step 3.	we evaluate the objective function (2) and check whether the newly obtained solution $\mathbf{g}(m)$ is better the previously stored $\mathbf{g}_{\text{opt}}$;
step 4.	if yes then $\mathbf{g}(m)$ gets stored and we set $m=0$;
step 5.	if not then $\mathbf{g}(m)$ is discarded and $\mathbf{g}_{\text{opt}}$ remains unchanged while $m = m + 1$
step 6.	if m equals the simulation parameter M then the algorithm ends

IV. NUMERICAL RESULTS

In this section the performance of the protocols described above are investigated by extensive simulations.

The lifespan was defined as the number of steps until which each node has the energy to transmit packets complying with the given reliability parameter. As soon as, a node (the bottleneck node) goes flat (being not able to participate in the reliable packet transfer, because of falling short of the required energy), then network is considered dead. Fig. 4 depicts the lifespan achieved by the chain protocol (eg. PEDAP) and shortcut protocol (eg. LEACH) compared with the energy balanced chain and shortcut with and without repetition. The investigated WSN contained 8 nodes the locations of which were subject to Gaussian and the required reliability P_{EE} was set 0.91. The figure exhibits the number of sent packets.
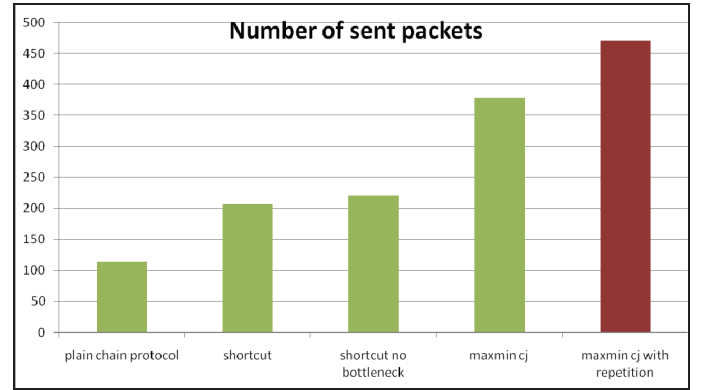

Figure 4. Number of sent packets

One can see the protoco with packet repetition achieve better longevity than the unbalanced chain and shortcut protocols (the gain is approximately 30%).

The next figure shows the examination of optimal repetition factor $a_{i,\text{opt}}$ for one node-to-node link as a function of reliability parameter and node distance.
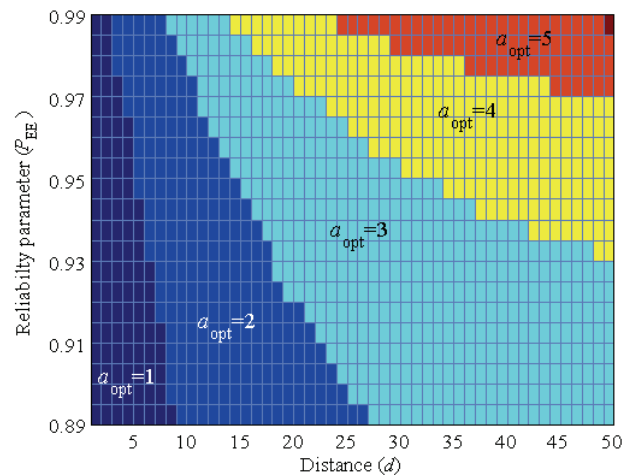

Figure 5. The optimal repetition factor for a node-to-node link as function of distance and reliability parameter

From Fig. 5 one can see that with increasing distance and reliability the number of repetition also increases (e.g. in the case of reliability $P_{\text{EE}} = 0.96$ and d=30m $a_{\text{opt}} = 3$ whereas in

the case of the same distance but with $P_{EE} = 0.98$ a_{opt} increases to 4).
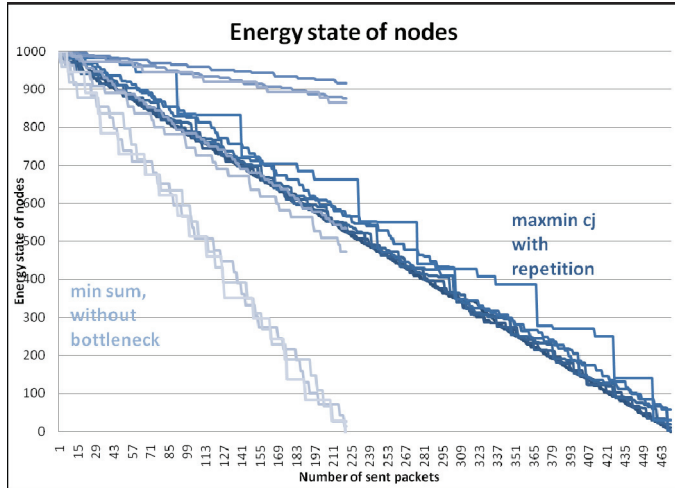

Figure 6. Energy state of the nodes as function of number of packets

It is easy to see from the Figure 6. that the bottleneck node will go flat after sending 221 packets without energy balancing, while other nodes have energy in abundance. When applying the new energy balancing protocol each node will go flat approximately at the same time after sending 470 packets. (the gain is roughly 210%) which is a great improvement in longevity.

V. CONCLUSION

In this paper, novel energy balancing packet forwarding methods have been developed to maximize the lifespan of WSNs and to ensure reliable packet transfer at the same time.

We have optimized the transmission energies of the nodes as well as the necessary number of repeated packet transfer in order to minimize the energy consumption of the bottleneck node (the node with the lowest available energy) subject to satisfying a given the reliability constraint. Two scenarios have been studied: (i) the chain protocol (nodes are passing the incoming packet to their neighbours closer to the BS); (ii) the shortcut protocol (the packet travels along the chain hop-by-hop and then on a certain node it gets sent directly to the BS).

The underlying protocol optimization was reduced to a constrained optimization problem which has been solved by a stochastic search algorithm.

It has been demonstrated that the novel optimization can significantly increase the lifespan of WSN and enhance its

ability to carry data to BS. This enhancement in lifespan is crucial in biomedical applications [12,13].

One possible extension of the method is to let each node participating in the transfer of packet i repeat the packet in a number of times set individually. This repeat numbers are denoted by $a_j^{(i)}$ $j = 1, 2, ..., i$. Furthermore, the method discussed here can easily be extended to multicast transfers, as well.

REFERENCES

[1] J. Levendovszky, A. Olah, A. Bojarszky, B. Karlocai, "Energy balancing by combinatorial optimization for wireless sensor networks," IWDN07 Conference, pp. 1–6., September 2007.

[2] A. Goldsmith and S. Wicker. August, "Design challenges for energy-constrained ad hoc wireless networks," IEEE Wireless Communications Magazine, Vol. 9, pp. 8–27., 2002.

[3] C. Intanagonwiwat, R. Govindan, D. Estrin, "Directed Diffusion: a scalable and robust communication paradigm for sensor networks," Proc. 6th Annual Int. Conf. Mobile Computing and Networking, Boston, August 2000.

[4] D. Bragonsky, D. Estrin, "Rumour routing algorithm for sensor networks," First ACM Int. Workshop on WSN and Applications, pp. 22-31., Atlanta, September 2002.

[5] F. Ye, G. Zhong, S. Lu, L. Zhang, "GRAdient broadcast: a robust data delivery protocol for larga scale sensor netwokrs," ACM Wireless Netwroks Journal, Vol. 11, pp. 285–298., 2005.

[6] J. Kulik, W. Heinzelman, H. Balakrishnan, "Negotiation-based protocolls for disseminetting information in wireless sensor networks," ACM Wireless Networks Journal, Vol. 8, pp. 169–185., 2002.

[7] C. Karlof, Y. Li, J. Polastre, "ARRIVE: algorithm for robust routing in volatile environments," Technical Report, UCB/CSD-03-1233, 2002.

[8] Y. Yun, R. Govindan, D. Estrin, " Geographical and energy aware routing: a recursive data dissemination protocol for wireless sensor networks," Technical Report, UCLA/CSD-TR-01-0023, 2001.

[9] W. Heinzelman, A. Chandrakasan, H. Balakrishnan. "Energy-Efficient Communication Protocols for Wireless Microsensor Networks," Proc. 33rd Hawaii Int. Conf. on Systems Sciences, pp. 223–234, Hawaii, January 2000.

[10] H. Ozgur, Tan, I. Korpeoglu, "Power Efficient Data Gathering and Aggregation in Wireless Sensor Networks," ACM SIGMOD Record, Vol. 32, Issue 4, pp- 66–71., 2003.

[11] M. Haenggi, "On Routing in Random Rayleigh Fading Networks," IEEE Transactions on Wireless Communications, vol. 4, pp. 1553–1562., 2005.

[12] C.Y. Chong and S.P. Kumar, "Sensor networks: evolution, opportinties and challenges," IEEE Proceedings, Vol. 91, No. 8, pp. 1247–1254., 2003.

[13] D. Puccinelli, M. Haenggi, "Wireless sensor networks – applications and challenges of ubiquitous sensing," IEEE Circuits and Systems Magazine, Vol. 5, pp. 19–31., 2005.

Extending the lifetime of medical implants through cooperative communications

Barnabás Hegyi
(Supervisor: Dr. János Levendovszky)
hegyi.barnabas@itk.ppke.hu

Abstract—The power consumption of battery-operated medical implants – such as pacemakers or cardioverter-defibrillators – is of crucial importance in telemedicine and telecare applications. One way to decrease power consumption is to mitigate the effect of fading that the in-body to off-body communication channel is subject to. In this paper, we reveal and assess the potential of cooperative communications to combat fading – and hence to extend the lifetime of battery-operated implants – in medical implant communication systems. In order to carry out our analysis, we set up a statistical channel model for the in-body to off-body communication channel based on the findings in the literature on radio wave propagation from medical implants. We also include a realistic power consumption model along with the typical figures for the state-of-the-art low-power transceivers in our model. In the particular cooperative communication scenario we consider, multiple cooperating receiver units are installed across the room accommodating the patient with a medical implant inside his/her body. Our investigations have shown that – compared to the traditional, non-cooperative communication approach – the lifetime of battery-operated medical implants can significantly be extended by means of the proposed cooperative communications scheme.

I. INTRODUCTION

With the ever-growing development of information and communication technologies, novel types of services such as telemedicine and telecare have become feasible. One important technological component of these remotely delivered services is obviously wireless communications – and primarily radio communications.

Wireless (radio) devices in telemedicine and telecare systems may be located off, on and inside the human body. The latter devices – called implants – can communicate to the outside ones in various ways. In the case of the solution, in which the carrier frequency falls into a relatively higher domain – typically into the ultra high frequency (UHF) band – the propagating radio waves enable higher bit rates and longer ranges measurable in meters. This alternative offers more comfort – and e.g. continuous monitoring – to the patient but, in turn, implies greater challenges for the system and device designers as implants with this particular communication technique are generally powered by non-rechargeable batteries.

In 2002, the European Telecommunications Standards

Institute (ETSI) standardized the Medical Implants Communications System (MICS) [2], which is specified to be used by active medical implants communicating to each other or to an external controller in the UHF band. The unlicensed frequency band allocated to the system is from 402 to 405 MHz. (Note that a similar standard was issued for the United States by the Federal Communication Commission (FCC) in 1999 [3].)

A good example of a telemedicine system operating in the MICS band is the Biotronik Home Monitoring system [4]. In this particular system, the data (trend, event, etc.) transmitted by the (battery-operated) implanted pacemaker or cardioverter-defibrillator is received by an exterior device, which then automatically forwards it to Biotronik's Service Centre via the cellular telephone system (GSM). Afterwards, the centre analyzes the data and edits a report, which can be viewed online by the attending physician or – upon request – sent to him/her by fax, e-mail or text message (SMS).

The communication between a body-implanted device and an off-body transceiver is treated by only a relatively few papers in the literature on a link level. One such treatment is provided [5], where the performance of a traditional (non-cooperative) radio link between a medical implant and a single base station – both located in the same hospital appointment room – is considered. However – to the best of our knowledge – no effort to date in the literature has been made to unveil or to assess the potential of cooperative communications to combat fading – and hence to extend the lifetime of battery-operated implants – in medical implant communication systems.

Radio channels are generally subject to some kind of fading in most propagation environments. In a large number of the practical scenarios, the small dimensions of wireless network nodes prevent the use of multiple antennas on a single node for combating fading. However, by taking advantage of the broadcast nature of the wireless media, the effect of fading can be mitigated through node collaboration usually termed as cooperative diversity [6].

In our particular cooperative communication scenario, we consider a single room accommodating a patient with a medical implant inside his/her body (Figure 1). The implant intends to communicate its sensed data to the outside world at regular intervals. In the case of the traditional, non-cooperative communication approach, the data is received by the only receiver unit in the room, which is placed in the immediate proximity of the patient. Contrary to that, for the cooperative communication scenario, the packet transmitted by the implant is received by multiple battery-operated,

wireless cooperating receiver units (CRUs) installed across the room (Figure 1). After that, a couple of the CRUs are selected for cooperation. Finally, these CRUs relay their packet to the gateway CRU (G-CRU) in the room, which then makes the final decision on the implant packet and forwards it to the service centre through – as an example – the internet or the 3G network.

The advantage of the cooperative approach over the non-cooperative one arises from the fact that the radio channel towards the single receiver unit located in the proximity of the implant might be more adversely affected by fading than

Fig. 1. The room accommodating the patient. The CRUs and the G-CRU installed across the room are highlighted by the thin circles and the thick circle, respectively. The packet transmitted by the implant is received by multiple CRUs, which then cooperatively make the decision on the implant packet. (The illustration was prepared by Dávid Tisza.)

the channels towards other locations of the room. Under these circumstances, the reception of the implant packet may be more reliable in these locations even if they are farther off from the implant. Thus, by applying multiple receiver units in different locations of the room, the required transmission power of the implant can be reduced under a given reliability constraint. This reduction in transmission power can be converted into lifetime gain, which stands in the main focus of attention in this paper.

II. TOPOLOGY AND ENERGY CONSUMPTION MODEL

A. Topology model

Since our purpose is to evaluate the potential of cooperative communications to prolong the lifespan of medical implants in general, we do not consider a specific spatial arrangement of the CRUs in the room. Instead, the positions of the CRUs are regarded as random variables; in particular, they are assumed to be distributed according to a 2D homogeneous Poisson distribution with parameter ρ.

In order to take the mobility of the patient into account, we consider also the location ($\mathbf{r}$) and orientation ($\mathbf{r}_0$) of the implant/patient as random variables. We assume that $\mathbf{r}$ follows a uniform distribution over the area of the room, while $\mathbf{r}_0$ is assumed to be uniformly distributed over the unit circle.

B. Energy consumption model

We apply the power consumption model used in [7], which takes into account both circuit power consumption and the losses of the RF power amplifier. The power consumed at transmission (P_t) and at reception (P_r) is expressed as

$$P_t(P_{tr}) = \eta_{PA}^{-1} P_{tr} + P_{circ,t} , \qquad (1)$$

and

$$P_r = P_{circ,r} , \qquad (2)$$

respectively. Here η_{PA} is the efficiency of the RF PA of the transceiver, P_{tr} is the transmission power, while $P_{circ,t}$ and $P_{circ,r}$ is the circuit power consumption at transmission and at reception, respectively.

Several low-power UHF transceiver designs – for biomedical applications – have recently been reported in the literature. In order to make the analysis as realistic as possible, we are going to assume typical (e.g. [8][9]) $P_{circ,t}$ and η_{PA} values for the implanted device in our simulations.

III. RADIO PROPAGATION MODEL

In this section – based on the achievements in the literature on radio wave propagation from medical implants – we provide a plausible statistical model of the propagation channel between the implant and the CRUs (and that between the CRUs). The establishment of such statistical model is essential when assessing the potential of cooperative diversity to extend the lifetime of medical implants.

A. Multipath fading

The radio waves emitted by the transmitter are reflected, scattered or diffracted by the objects surrounding the receiver. The components created in this way may sum up either constructively or destructively at the receiver giving rise to the phenomenon of multipath fading.

Johansson et al. measured the path loss for the MICS band (at the mid-band frequency of 403.5 MHz) in an indoor environment [5]. The observed variations of the path loss around its mean were attributed to multipath fading. The measured path loss was compared to free space loss and its large-scale mean was found to be in a good agreement with that. The excess loss that needs to be added to free space loss in order to cover a given percentage of the measured area was also calculated.

In order to incorporate multipath fading into our model, we assume Rice-fading [10] in the room as it is presumable that there is always a line-of-sight (LOS) multipath component (MPC) among the MPCs propagating between the implant and the CRUs. Based on the excess loss values presented in [5], we estimated the K_r parameter of the fading (called Rice-factor) to have a value of around 0 dB.

B. Polarization mismatch

A possible mismatch between the polarization of the incoming radiation and that of the receiver antenna may lead to additional losses in the radio communication link [5].

Johansson calculated the transversal radiation pattern of an implant placed in a homogeneous numerical human phantom [5]. The phantom was filled with a muscle-simulating (virtual) liquid [1]. The calculations were carried out using the finite-difference time-domain (FDTD) method for optimum (matched) polarization as well as for the polarization that is perpendicular to the transversal plane. The ratio of the calculated patterns and hence the polarization was found to show significant variations over the different directions of the plane.

Nevertheless, none of the related studies in the literature – such as [5] and [11] – has given an analytical or even a statistical description of these variations. For this reasons, we propose the following simple probabilistic model for the (far-field) polarization of the wave transmitted towards CRU_i:

$$p_{\vartheta,i}^{t} = \cos\beta_i, \tag{3}$$

$$p_{\varphi,i}^{t} = \sin\beta_i \cdot e^{j\gamma_i}, \tag{4}$$

where β_i and γ_i ($i = 1,...,N$) are random variables that are uniformly distributed over the interval $[0,2\pi]$, while $p_{\vartheta,i}^{t}$ and $p_{\varphi,i}^{t}$ are the components of the polarization in the spherical polar coordinate system centered at the implant with coordinates ϑ and φ, $\vartheta = 0$ lying in the vertical direction. (Variable N denotes the number of CRUs in the room.)

C. Radiation efficiency and radiation pattern

When assessing the performance of a wireless communication link, the antenna characteristics such as the radiation efficiency and the radiation pattern also need to be taken into account for both the transmitter and the receiver antenna.

For an implanted antenna, the implant itself and the body are located in the near-field of the antenna and, as a result, they have a fundamental effect on the radiation characteristics [1]. Therefore, for implanted antennas, the antenna characteristics are regarded as that of the complex made up of the implanted antenna, the implant and the body.

Johansson estimated the radiation efficiency (η) of a wireless implant in the MICS band using the FDTD method [1][5]. The radiation efficiency was found to be around -30dB depending on the body (i.e. homogeneous numerical phantom) shape and the depth of the implant in the phantom.

Johansson simulated also the radiation pattern of a wireless implant under the assumption of optimum polarization matching [5]. The results revealed considerable variations in the radiation pattern and the margin that has to be added to the maximum directivity to get a given percentage of coverage over all the possible angles was estimated.

Changes in body posture cause significant alterations in the radiation pattern of the implant [5]. This effect can be interpreted as a kind of shadow fading [1]. Johansson et al. calculated the radiation pattern of a wireless implant placed into a numerical phantom for 8 different arm positions [5]. The excess loss that needs to be added to the mean of the 8

directivity patterns in order to cover a given percentage of the entire spatial angle was determined.

Nonetheless, no analytical or detailed statistical description of either the radiation pattern or that of the impact of body posture has been provided by any of the related studies in the literature ([5][11]). Variations due to shadowing effects show a log-normal distribution in most of the practical cases [10]. Moreover, when measuring the path loss from a physical numerical phantom filled with animal organs, the variations of the path loss around its mean was also attributed to shadowing effects by Alomainy et al [12]. The measured path loss samples showed a log-normal distribution. As a consequence of these findings, we propose to approximate the variations in the radiation pattern and those due to the changes in body posture by an axially symmetric 2D directivity pattern ($D(\phi)$) which has the property that if we consider a random direction that follows a uniform distribution, then the corresponding directivity pattern value is distributed according to a truncated log-normal distribution. The actual values of the different parameters of the distribution can be estimated based on the numerical and measurement results presented in [5] and [11], respectively.

D. The resulting propagation model

Now the only thing that remains is to piece together our propagation model in the following two equations, which concern the implant-to-CRU_i and the CRU_i-to-CRU_j channels gains (h_{I,CRU_i} and h_{CRU_i,CRU_j}), respectively ($i, j = 1,...,N$).

$$\left|h_{I,CRU_i}\right|^2 = \\ = \left(\frac{4\pi\lambda}{d_{I,CRU_i}}\right)^2 \left|a_{\vartheta,i}^{R} p_{\vartheta,i}^{t} p_{\vartheta,i}^{r} + a_{\varphi,i}^{R} p_{\varphi,i}^{t} p_{\varphi,i}^{r}\right|^2 \eta D(\phi_i), \tag{5}$$

$$\left|h_{CRU_i,CRU_j}\right|^2 = \\ = \left(\frac{4\pi\lambda}{d_{CRU_i,CRU_j}}\right)^2 \left|a_{\vartheta,ij}^{R} p_{\vartheta,i}^{r} p_{\vartheta,j}^{r} + a_{\vartheta,ij}^{R} p_{\varphi,i}^{r} p_{\varphi,j}^{r}\right|^2, \tag{6}$$

where the first factor in the equations is the expression of free space loss with λ being the wavelength in air. Variables $p_{\vartheta,i}^{r}$ and $p_{\varphi,i}^{r}$ are the ϑ- and φ-components of the unit vector describing the polarization of the antenna of CRU_i, respectively. Furthermore, variables d_{I,CRU_i} and d_{CRU_i,CRU_j} denote the distance between the implant and CRU_i and that between CRU_i and CRU, respectively, whereas ϕ_i is the orientation of CRU_i relative to the implant.

Finally, $a_{\vartheta,i}^{R}$ ($a_{\varphi,i}^{R}$) and $a_{\vartheta,ij}^{R}$ ($a_{\varphi,ij}^{R}$) represent the Rice-fading coefficients for the ϑ- (φ)-component of the radiated wave in the case of the implant-to-CRU_i and CRU_i-to-CRU_j channels, respectively.

The propagation model set up in this section is obviously just an approximation. This – among other things – is due to the fact that it has been put together based on the results of

some studies that treated the different aspects of the propagation channel separately. We had to rely on this solution since – to the best of our knowledge – no paper to date investigates the properties of the in-body to off-body propagation channel in an indoor environment directly and as a whole. However, the establishment of a more accurate statistical channel model – either by FDTD simulations or by measurements – requires a considerable amount of time and effort, and therefore it is out of the scope of this paper.

IV. COOPERATIVE COMMUNICATION SCHEME

A. Relaying stage

There are a number of relaying schemes treated in the literature of cooperative communications. In our investigations, we apply the relaying method termed as amplify-and-forward (e.g. [13]), while in terms of medium access, we choose to employ the so called repetition based relaying (e.g. [13]).

The different versions of the implant packet are optimally combined at the G-CRU according to maximum ratio combining [10]. It is easy to see that, for the hypothetic case when the total transmission power of the relaying CRUs (P_{CRU}) converges to infinity (CRUs with unlimited transmission power), the resultant signal-to-noise ratio (SNR) of the combined relay packet is given by

$$\lim_{P_{CRU} \to \infty} SNR_{max} = \sum_{i=1}^{n} \frac{P_I}{\sigma_n^2} \left| h_{I,CRU_i} \right|^2 . \tag{7}$$

The expression behind the summation sign in (26) is the SNR of the implant-to-CRU$_i$ channel (SNR_{I,CRU_i}) and will henceforth be referred to as the received SNR of CRU$_i$. (Variable n denotes the number of selected relays, P_I is the transmission power of the implant, while σ_n^2 is the variance of receiver noise.)

The combined relay packet and the packet that is received directly are optimally combined by the G-CRU according to MRC. Thus the resultant SNR of the packet to be decoded by the G-CRU is expressed as

$$SNR_{res} = \frac{P_I}{\sigma_n^2} \left| h_{I,G\text{-}CRU} \right|^2 + SNR_{max} . \tag{8}$$

B. Relay selection stage

Due to the relatively low number of CRUs, i.e. potential relays in the room, we apply the following simple, centralized relay selection procedure. At the beginning of the procedure, the CRUs (except for the G-CRU) send their received SNR to the G-CRU one after the other. The G-CRU then selects a number of n CRUs based on a given selection criterion and finally it broadcasts the outcome of the selection procedure to the CRUs. Concerning the relay selection criterion, we investigate the case when the G-CRU simply selects the CRUs with the highest received SNR. Based on (7), one can immediately find that the criterion just mentioned is the optimal relay selection criterion when $P_{CRU} \to \infty$.

C. Lifetime gain

As already mentioned in the introduction, in the case of the traditional, non-cooperative communication approach, only a single receiver unit is used in the immediate vicinity of the patient. We are going to model the location of this unit ($\mathbf{r}_{SRU}$) as if it were identical to that of the CRU that is found the closest to the implant in the statistical topology model introduced in Section II. In this way, both the relative proximity and the uncertain placement of the single receiver unit (SRU) are taken into account in our model.

According to the reliability constraint we place on the communication link from the implant to the outside world, the transmission power of the implant shall be high enough in order for the outage event of an unacceptably low resultant SNR (SNR_{res}) to have a sufficiently low probability.

Finally, we define the lifetime gain as the relative difference in lifetime between the cooperative and non-cooperative approaches. Lifetime is assumed to be directly proportional to the reciprocal of the power consumed at transmission (P_t) and, hence, the lifetime gain takes the form of

$$G_{lifetime} = \frac{P_t \left(P_I^{non\text{-}coop} \right)}{P_t \left(P_I^{coop} \right)} - 1 . \tag{9}$$

Here $P_I^{non\text{-}coop}$ and P_I^{coop} denotes the minimum transmission power level of the implant that satisfies the above reliability constraint for the non-cooperative and cooperative communication scheme, respectively.

V. PERFORMANCE ANALYSIS

The performance analysis is carried out numerically using Monte Carlo simulations.

Figure 2 describes the minimum implant transmission power (P_I^{coop}) as a function of the number of relaying CRUs (n) under the assumption of infinite total relay power ($P_{CRU} = \infty$). The diagram shows that the transmission power of the implant can considerably be reduced by employing the proposed cooperative strategy. Figure 3 describes the lifetime gain ($G_{lifetime}$) as a function of the number of relaying CRUs (n) for $P_{CRU} = \infty$ and for circularly polarized CRU antennas. It should be noted that the lifetime of the implant can significantly be prolonged by applying the cooperative communication approach described above.

Please note that – for the case of CRUs with limited transmission power ($P_{CRU} < \infty$) – we also investigated the effect of various power allocation strategies and relay selection criteria. We found that even if P_{CRU} was orders of magnitude lower than $P_{circ,t}$, uniform power allocation combined with the simple relay selection criterion described in Section IV.A did not (practically) perform worse than optimal power allocation combined with a more complex selection criterion that takes into account the channel gain of both the implant-to-CRU$_i$ and the CRU$_i$-to-G-CRU
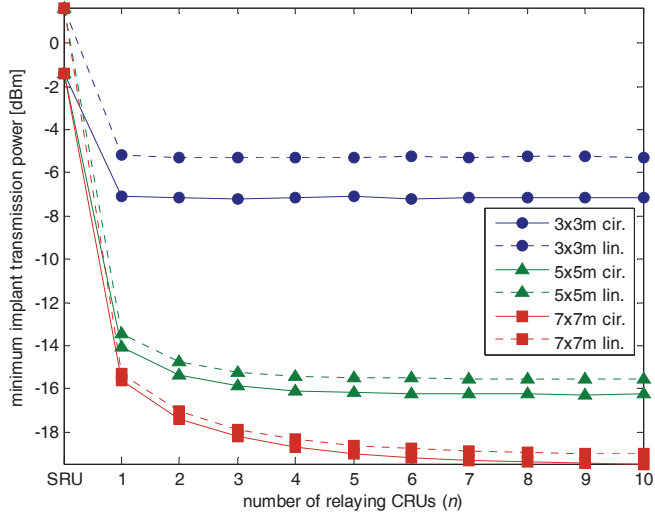
channels.

Fig. 2. Minimum implant transmission power vs. number of relaying CRUs (n) ($P_{CRU} = \infty$). The case of the traditional, non-cooperative approach is also plotted and referred to as 'SRU'. The different curves belong to different room sizes and CRU antenna polarizations (circular or linear).
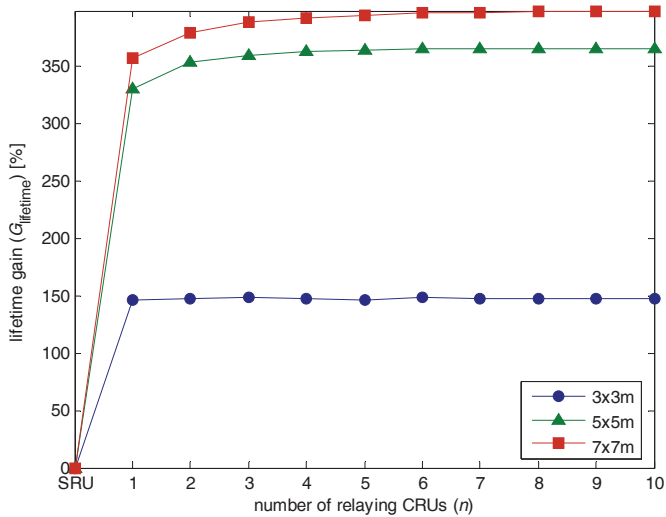

Fig. 3. Lifetime gain ($G_{lifetime}$) vs. number of relaying CRUs (n) ($P_{CRU} = \infty$, circular CRU antenna polarization). The case of the traditional, non-cooperative approach is also plotted and referred to as 'SRU'. The different curves belong to different room sizes.

VI. Conclusions

We have demonstrated in our investigations that the power consumption of the implant – stemming primarily from the data communication towards the outside world – can significantly be reduced by means of the proposed cooperative communication scheme. Since it is a plausible assumption that the presence of the patient is limited to only a couple of rooms (home, work place, etc.) during the day, this reduction in power consumption may also result in an actual and considerable lifetime gain for the implant in practice. In addition to extending the lifetime of the implant, the suggested collaborative procedure offers the alternative benefit of a more frequent and more intensive data communication between the implant and the outside world. Finally, the proposed method provides more comfort to the patient as the SRU does not need to be worn on his/her belt all the time or carried with him/her upon changing his/her location in the room.

References

[1] P. S. Hall, Y. Hao, *Antennas and Propagation for Body-Centric Wireless Communications*. Boston – London: Artech House, 2006, ch. 8–9.

[2] *Electromagnetic compatibility and radio spectrum matters (ERM); Short range devices (SRD); Ultra low power active medical implants (ULP-AMI) and peripherals (ULP-AMI-P) operating in the frequency range 402 MHz to 405 MHz; Part 1: Technical characteristics and test methods*, ETSI Standard EN 301 839-1 V1.2.1, 2007.

[3] FCC Standard 47 CFR 95.601-95.673 Subpart E, 1999.

[4] Biotronik Home Monitoring, http://www.biotronik.de.

[5] A. J. Johansson, "Wireless communication with medical implants: antennas and propagation," Ph.D. dissertation, Department of Electroscience, Faculty of Engineering, Lund University, Lund, Sweden, 2004.

[6] J. N. Laneman; G. W. Wornell, "Distributed space-time-coded protocols for exploiting cooperative diversity in wireless networks," *IEEE Transactions on Information Theory*, vol. 49, pp. 2415–2425, October 2003.

[7] L. Song, D. Hatzinakos, "Cooperative transmission in poisson distributed wireless sensor networks: protocol and outage probability," *IEEE Transactions on Wireless Communications*, vol. 5, pp. 2834–2843, October 2006.

[8] A. Tekin, M. R. Yuce, J. Shabani, L. Wentai, "A low-power FSK modulator/demodulator for an MICS band transceiver", in *Proc. 2006 IEEE Radio and Wireless Symposium*, San Diego, CA, USA, 2006, pp. 159–162.

[9] M. .M. El-Desouki, M. J. Deen, Y. M. Haddara, "A low-power CMOS class-E power amplifier for biotelemetry applications," in *Proc. 35th European Microwave Conference*, Paris, France, 2005, vol. 1, 4 pp.

[10] A. F. Molisch, *Wireless Communications*. Chichester: John Wiley & Sons, 2005, ch. 5, 7, 13.

[11] W. G. Scanlon, J. B. Burns, N. E. Evans, "Radiowave propagation from a tissue-implanted source at 418 MHz and 916.5 MHz," *IEEE Transactions on Biomedical Engineering*, vol. 47, pp.527–534, April 2000.

[12] A. Alomainy, Y. Hao, Y. Yuan, Y. Liu, "Modelling and characterisation of radio propagation from wireless implants at different frequencies," in. *Proc. 9th European Conference on Wireless Technology*, Manchester, UK, 2006, pp. 119-122.

[13] J. N. Laneman, D. N. C. Tse, G. W. Wornell, "Cooperative diversity in wireless networks: Efficient protocols and outage behavior," *IEEE Transactions on Information Theory*, vol. 50, pp. 3062–3080, December 2004.

Neural network based multiuser detection

Dávid Tisza, János Levendovszky

Pázmány Péter Catholic University, Budapest

Abstract—In this paper a new neural network based detection algorithm has been developed for multiuser detection (MUD). After providing a general discretized model of Code Division Multiple Access/Direct Sequence system a neural algorithm is used to minimize the underlying quadratic form which implements the minimum error probability (Bayesian) decision. Novel solutions have been introduced to make the algorithm capable of global minimization to secure the lowest possible error probability. Besides the algorithmic description, an extensive performance analysis has been carried out by implementing a software package modeling all the aspects of multi access systems. The underlying numerical analysis has also proven the superiority of the new method over the the traditional (RAKE, MMSE and decorrelation based) receiver algorithms.

I. Introduction

In the latest communication technologies multiple access has become all-pervading method for sharing the limited resources efficiently. It provides an optimal reuse of resources and a pre-defined quality of service as well. One of the most frequently used multi access techniques is the CDMA protocol which is applied in third generation mobile communications. [1] In CDMA-DS (code division multiple access direct sequence) every user has a pseudo random codeword or code sequence and this is transmitted with a much more higher clock rate (small chip time) than the original data rate instead of modulating each data symbol. This gives rise to the phenomenon of spreading. The originally narrow band process spreads out to a much wider band and gets similar to a background noise process and gains less vulnerability to narrow band jamming interferences. These properties motivated the first applications of this technique in military applications, where it was used for secure and disguised communications. Beside the mobile telephone systems this can be used in wireless networking techniques among PCs, or the emerging wireless sensorial environments where event driven information is transported along the network, and energy efficiency is important. While a broad range of efficient source and channel coding, modulation [2], [3], and multiple access methods [4], [5] are proposed, the bottleneck of the problem is to find low complexity and good performance algorithms for the detection phases. Therefore the paper delves into the analysis of novel multiuser detection algorithms based on neural architectures.

II. The model

In general a block representation radio communication system using code spreading can be the following:

For describing the detection problem mathematically, we need a discrete-time model of the "analogue" parts. Focusing on the detection and decision phase of the process, we are not
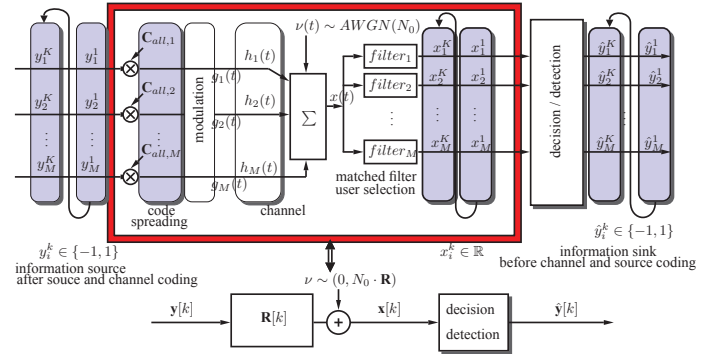

Figure 1. Block representation of the communication model

dealing with the source and channel coding and the modulation in detail. So we make the following assumptions :

- The bit flow from the users at the output of the channel coder follows a Bernoulli distribution such that: $y_i(k) \in \{-1; +1\}$, $P(y_i(k) = +1) = P(y_i(k) = -1) = 0.5, \forall i, k$. This can be achieved with proper source coding for almost any information source.
- We do not use interleaving or scrambling techniques.
- The baseband modulation is assumed to be BPSK, so the the symbols also can take only two values like $y_i(k)$. The symbols length will be denoted by T_s.
- We assume that the communication channel can have distinct distortion for any user but the users communicate synchronously.
- At the receiver antenna side, the background and any other noise is modeled with an additive white Gaussian noise with spectral density N_0.
- Matched filters are used for the user separation at the receiver side.

The following notation will be used:

- M the number of users,
- y_i^k or $y_i[k]$ is the ith user's bit at time instant k,
- $g_i(t)$ is the transmitted wave of user i,
- $\nu(t)$ the noise on the receiver,
- h the impulse response of channel distortion. $h_i(t)$ the time continuous, $h_i[k]$ the time discretized of user i,
- N length of a spreading codeword,
- $\mathbf{C}$ the code matrix, containing the codewords in its columns. $type(\mathbf{C}) = N \times M$, $\mathbf{C}_{j,i}$ is the jth component $(j = 0 \dots N - 1)$ of the ith user's codeword.
- $s_i(t)$ is the so called signature waveform of user i. It is the modulated form of the codeword belonging to user i,
- T_s is the total length of the signature signal,
- N is the length of the codeword,

- $T_c = \frac{T_s}{N}$ is the "chip time"
- $e(t)$ is the chip waveform element.
- $\mathbf{R}$ the discrete channel matrix containing the Inter Symbol interferences and the Multiple Access Interferences as well.

The "analogue" parts of the communication model are fully derivated in [6]. Due to the limited size of this paper, we only focus on the most important features of the model demonstrated by the following example. In figure II the following used: $e(t) = \sqrt{\frac{2}{N}}\sin(Tc \cdot \pi \cdot t)$ so that $\int_0^{T_s}(s_i(t))^2 dt = 1, \forall i$ and $h_i(t) = 1\delta(t) + 0.6\delta(t - 1Tc) + 0.4\delta(t - 2Tc) + 0.2\delta(t - 3Tc) + 0.2\delta(t - 7Tc), \forall i$.
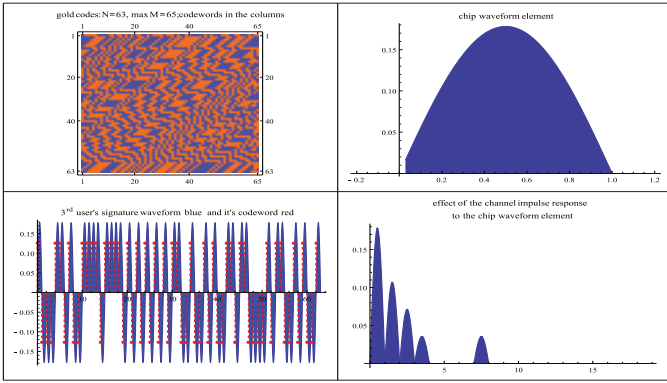
Figure 2. examples - top left:$\mathbf{C}$, top right:$e(t)$, bottom left:$s_3(t)$-blue and $\mathbf{C}_{all,3}$-red, bottom right:$e(t) * h_3(t)$

And an the 3rd user's signature waveform without and with distortion under the channel mentioned before.
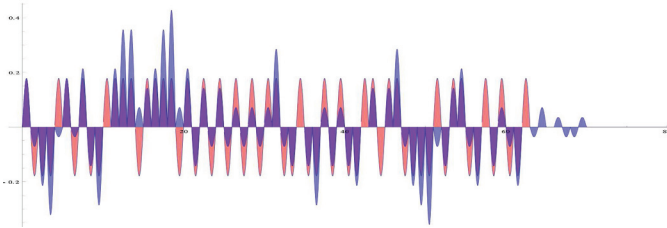
Figure 3. 3rd user's signature waveform without(red) and with distortion(blue), overlaps are purple

The received signal at the antenna can be described as:

$$x(t) = \sum_{n=0}^{N-1}\sum_{k=0}^{K-1} y_n[k]s_n(t - kT_s - \tau_n) * h_n(t) + \nu(t), \quad (1)$$

where τ_n is the assynchronousness of user n from the main synchron symbol time. This signal then passes through a matched filter bank for separating the users.

Under the assumptions, the encirculated part on figure II can be reduced to a linear distortion on the input bit vector

along multiple blocks.

$$\mathbf{x}_j[k] = filter_j(kT_s) =$$

$$\sum_{i=0}^{N-1}\sum_{k=0}^{K-1} y_i[k]\underbrace{\langle v_i(t), v_j^*(t - kT_s)\rangle}_{\mathbf{R}_{i,j}[k]} + \underbrace{\langle \nu(t), v_j^*(t - kT_s)\rangle}_{\nu_j}(2)$$

$$\mathbf{x}[k] = \sum_{k=0}^{K}\mathbf{R}[k]\cdot\mathbf{y}[k] + \nu, \quad \nu \sim \mathcal{N}(0, N_0 \cdot \mathbf{R}) \quad (3)$$

So if we assume that $\tau_i = 0, \forall i$ then $\mathbf{R}_{i,j}[k]$ can be expressed as follows:

$$\mathbf{R}_{i,j}[k] = \sum_{m=0}^{N-1}\sum_{n=0}^{N-1}\mathbf{C}_{n,i}\cdot\mathbf{C}_{m,j}\cdot$$

$$\sum_{p=0}^{N_s-1}\sum_{q=0}^{N_s-1} h_i[p]\cdot h_j[q]\cdot\hat{e}(n,m,p,q,k) \quad (4)$$

where $h_i[k]$ is the discretized version of the $h_i(t)$ for T_c periods. N_s is the length of $h_i[k]$. $N_s \cdot T_c$ = support of $h_i(t)$ and $\hat{e}(n,m,p,q,k)$ represents the cross correlation measures between each chips at different time values. This function should be extended in an asynchronous case.

$$\hat{e}(n,m,p,q,k) = \begin{cases} 1, \text{if} & (n+p) = (m+q+k\cdot N) \\ 0, & otherwise \end{cases}$$

As a result $\mathbf{R}$ will hold the inter symbol interferences and the multiuser interferences as well, so it will be a block toeplitz type matrix. For example it can be the following if $N = 63$ long Gold codes are used with $M = 62$ users and with $h_i = [1, 0.6, 0.4, 0.2, 0, 0, 0, 0.2], \forall i$
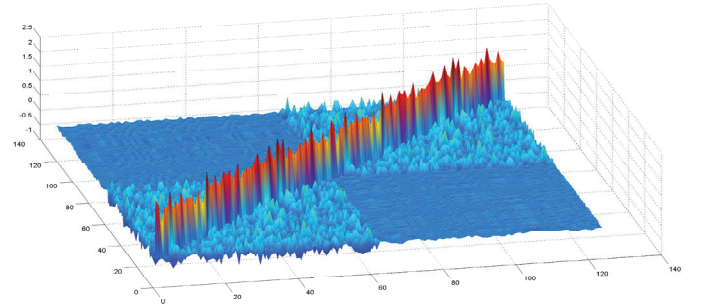

Figure 4. example for a channel matrix

The noise is also transformed due to the use of the matched filters. The noise was defined as: $\nu_i = \langle \nu(t), v_j^*(t - kT_s)\rangle$, so it is still weakly stationer and independent. As a result the covariance matrix will be the following:

$$\mathbf{\Sigma}_{i,j}[k] = \mathbb{E}(\nu_i \cdot \nu_j) = N_0 \cdot \mathbf{R}_{i,j}[k] \quad (5)$$

III. DECISION ALGORITHMS

The minimum error probability (Bayesian) decision boils down to a minimization of a quadratic form as indicated by the following formula [7]:

$$\mathbf{y}_{opt} := \underset{\mathbf{y}\in\{-1,1\}^M}{\arg\max} P(\mathbf{y}|\mathbf{x}) = \underset{\mathbf{y}\in\{-1,1\}^M}{\arg\max} \frac{P(\mathbf{x}|\mathbf{y})\cdot P(\mathbf{y})}{P(\mathbf{x})} =$$

$$\underset{\mathbf{y}\in\{-1,1\}^M}{\arg\max} P(\mathbf{x}|\mathbf{y})\cdot P(\mathbf{y}) = \underset{\mathbf{y}\in\{-1,1\}^M}{\arg\max} P(\mathbf{x}|\mathbf{y}) \quad (6)$$

$$\mathbf{y}_{opt} = \operatorname*{argmax}_{\mathbf{y} \in \{-1,1\}^{M \cdot K}} \frac{1}{(2\pi)^{\frac{M \cdot K}{2}} \cdot |\mathbf{\Sigma}^{-1}|^{1/2}} \cdot$$

$$\cdot \exp \left\{ -\frac{1}{2} (\mathbf{x} - \mathbf{R}\mathbf{y})^T \mathbf{\Sigma}^{-1} (\mathbf{x} - \mathbf{R}\mathbf{y}) \right\}$$

$$\mathbf{y}_{opt} = \operatorname*{argmin}_{\mathbf{y} \in \{-1,1\}^{M \cdot K}} (\mathbf{x} - \mathbf{R}\mathbf{y})^T \mathbf{\Sigma}^{-1} (\mathbf{x} - \mathbf{R}\mathbf{y}) \quad (7)$$

$$\mathbf{y}_{opt} = \operatorname*{argmin}_{\mathbf{y} \in \{-1,1\}^{M \cdot K}} \mathbf{y}\mathbf{W}\mathbf{y}^T - 2\mathbf{b}^T \mathbf{y} \quad (8)$$

where $\mathbf{W} = \mathbf{R}^T \cdot \mathbf{\Sigma}^{-1} \cdot \mathbf{R}$ and $\mathbf{b} = \mathbf{R}^T \cdot \mathbf{\Sigma}^{-1} \cdot \mathbf{x}$, because but due to synchronity and (5) it reduces to $\mathbf{W} = \mathbf{R}$ and $\mathbf{b} = \mathbf{x}$.

There are several well known decision strategies such as:

- threshold detection: $sgn(\mathbf{x}) = sgn(\mathbf{R}\mathbf{y} + \nu)$, $\nu \sim \mathcal{N}(\mathbf{0}, N_0\mathbf{R})$
  $sgn(\mathbf{x}) = sgn(\mathbf{R}\mathbf{y} + \nu) = sgn(\mathbf{R}\mathbf{y} + \sqrt{N_0}\sqrt{\mathbf{R}} \cdot \vartheta)$, $\vartheta \sim \mathcal{N}(\mathbf{0}, \mathbf{1})$

- decorrelating detection: $sgn(\mathbf{m}) = sgn(\mathbf{R}^{-1} \cdot \mathbf{x}) = sgn\left(\mathbf{R}^{-1} \cdot (\mathbf{R} \cdot \mathbf{y} + \nu)\right)$ Using the linear transformation of a multidimensional Gaussian random variable the noise term will be: $sgn(\mathbf{m}) = sgn(\mathbf{y} + \eta)$, $\eta \sim \mathcal{N}(\mathbf{0}, N_0\mathbf{R}^{-1})$

- MMSE detection: $sgn(\mathbf{m}) = sgn\left((\mathbf{R} + \sqrt{N_0}\mathbf{I})^{-1} \cdot \mathbf{x}\right)$, which aims to minimize the overall square error introduced by the noise and by the interferences.

However all of these traditional algorithm have fallen sort of providing low bit error rate (yielding a tolerated level of quality of service).

IV. NEURAL BASED MULTIUSER DETECTION ALGORITHMS

In the paper we use the Hopfield Neural Network for the sake of minimizing the underlying quadratic form and, as a result, carrying out the optimal detection. However if there are several local minima over the search space than the traditional Hopfield Neural Network can stuck into one of them. [8] As a result we need to modify the original Hopfield algorithm in order to obtain the global optimum. [9]
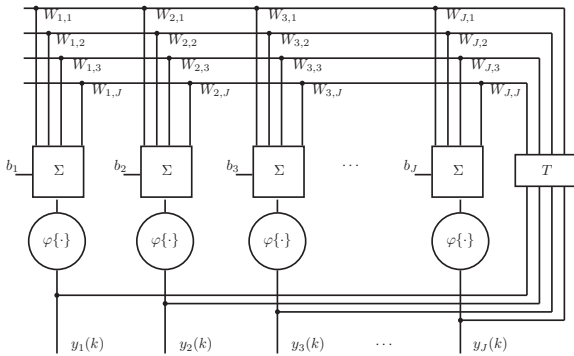

Figure 5.   Block representation of a general Hopfield net

This structure can be extended if we put a state dependent function like a hysteresis type nonlinearity in place of the sgn function $\varphi(y(k)) = sght_h(y(k))$.

$$sght_h(y(k)) = \begin{cases} sgn(y(k) - h) & \text{if } y(k-1) = -1 \\ sgn(y(k) + h) & \text{if } y(k-1) = +1 \end{cases}$$

The convergence properties of this network can be analyzed using the Lyapunov theory. With the hysteric type Hopfield net, it can be proven that [9]

Theorem 1: If

1) $\mathbf{W}$ is a symmetric matrix which is eye-opened with parameter D and has positive diagonal elements, and
2) there exists an $\mathbf{m}$ such that $\mathbf{W}\mathbf{m} = \mathbf{b}$ and $\mathbf{m} \in dC$ where

$$dC := \{\mathbf{u} : \varepsilon \leq |\mathbf{u}_i| \leq 2 - \varepsilon\}$$

$$\varepsilon = \frac{3 + \frac{\kappa}{\min_i \sum_{j,j \neq i} \mathbf{W}_{i,j}}}{1 + D}, \text{ and}$$

3) the hysteric parameter is defined h_i as

$$h_i = \mathbf{W}_{i,i} + \kappa, \quad \kappa > 0$$

then

1) (uniqueness); the algorithm has one and only one steady state corresponding to the global minimum of the quadratic form $\mathbf{y}^T\mathbf{W}\mathbf{y} - 2\mathbf{b}^T\mathbf{y}$ over the set of N-dimensional binary vectors;
2) (stability); the algorithm is stable;
3) (bound on the transient time); the necessary number of steps needed to achieve the steady state (transient time) can be upper bounded by the following expression:

$$TR \leq \frac{N^2 \|\mathbf{W}\| + 2\sqrt{N^3} \|\mathbf{y}\| + N \|\mathbf{W}^{-1}\| \|\mathbf{b}\|^2}{4\kappa}$$

Based on the theorem this modified Hopfield Neural Network can approximate the Bayesian decision. Thus we have implemented it for multiuser detection and it's performance is treated in the next section.

V. PERFORMANCE ANALYSIS AND NUMERICAL RESULTS

The proposed detection algorithm was tested under the following conditions:

- Two type of spreading code families were used: Gold codes [10] and the Hadamard codes, one of the orthogonal code family.
- The chip number is not equal at the two codes (for the Gold, 63 long is used, for the Hadamard 64 is used), but almost fully loaded channels were inspected: $M = 62$
- Every user had the same channel distortion function, and it was assumed that they communicate synchronously. This model can represent a CDMA downlink communication.
- Empirical Bit Error Probabilities were computed on different SNR levels.

A sub case of the simulation where $h_i[0] = 1$, $h_i[k] = 0, k \neq 0 \quad \forall i$ means no channel distortion, but we still have the interferences from the user's spreading codes. This case is only to show that the model is really extending this simple case: It can be seen that the detectors of orthogonal code family (black, solid) perform at the same bit error rate due to the fact that it has no MUI at all and with this circumstances the rake detection is the optimal. When the Gold codes are used to the same transmission and the same noise, it introduces interference among the users so the single user detector, the
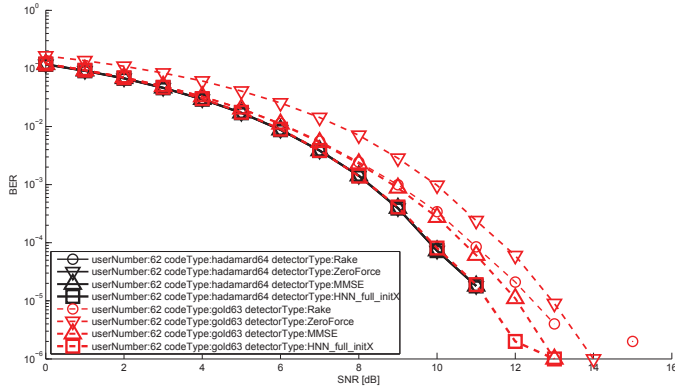
Figure 6.   transmission in ideal channel, but with MUI

zero forcing and the MMSE performs differently. Among them the MMSE performs the best but the Hopfield net can achieve better bit error rates, very closely to the optimal detection computed at the orthogonal code family. The Gold codes themselves has the advantage that their synchronity can be easily adjusted due to the cross correlation property of the codes [10].

We have investigated the case when a fast two-path distortion is introduced, where the $h_i[k] = h_j[k], \forall i, j$ and $h_i = [1, 0.6]$. In this case the difference between the MMSE
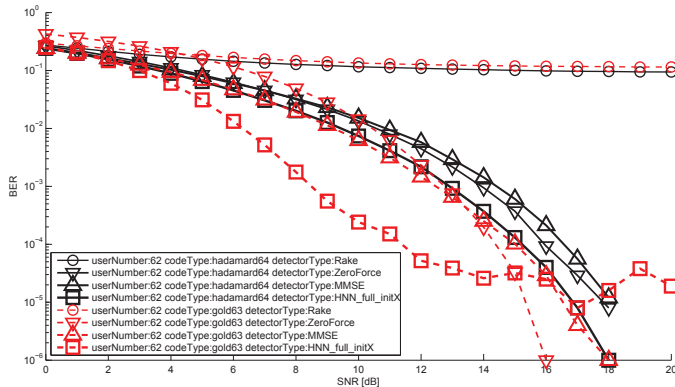
Figure 7.   transmission in fast two path channel

and the ZeroForcing strategy is also clearly exhibited. Due to the good and nearly time invariant cross correlation values of the Gold codes it performs better than the orthogonal code family. The Hopfield net also outperforms the other detection algorithms.

VI. CONCLUSION

Based on the numerical results the proposed neural network based detection algorithm for multiuser detection (MUD) can perform better than the traditional (RAKE, MMSE and decorrelation based) receiver algorithms, while it has polynomial complexity running time, thus it helps real-time communication.

VII. FUTURE WORK

The testing of the proposed detection algorithms will be extended for asynchronous cases as well, and this way they can be appropriate in a massively multiple system where many communication nodes share the same medium (like wireless sensorial networks - WSN). In WSN event driven information sources are typical so collision detection or avoidance can be a factor. The next step of this project is to adopt and test these methods in WSN environment, where we expect to avoid collisions and as a result the longevity of the network can be considerably increased. In general further investigation will be persued into the applicability and effectivity of these algorithms due to special conditions shuch as the small computing capacity and the battery based mode of the operation.

REFERENCES

[1] M. S. M. R. Karim, *W-CDMA and cdma2000 for 3G Mobile Networks*. McGraw-Hill, 2002.
[2] S. Haykin, *Digital Communications*.   Toronto, Canada: John Wiley & Sons LTD, 1988.
[3] J. G. Proakis, *Digital Communications*.   Singapore: McGraw Hill, 1995.
[4] S. V. R.Lupas, "Linear multiuser detectors for synchronous code-division multiple-access channels," in *IEEE Trans. Information Theory*, no. 1, 1989, pp. 123–136.
[5] S. V. H.V.Poor, "Single-user detectors for multiuser channels," in *IEEE Trans. Comm.*, no. 1, 1988, pp. 50–60.
[6] S. Verdú, *Multiuser Detection*.   New York: Cambridge University Press, 1998.
[7] A. F. Molisch, *Wireless Communications*, 1st ed.   John Wiley & Sons LTD, 2006.
[8] F. Raúl, Rojas Jerome, *Neural Networks - A Systematic Introduction*. Springer, 1996.
[9] M. W. Levendovszky, J. and van der Meulen, "Hysteretic neural networks for global optimization of quadratic forms," in *Neural Network World*, no. 5, 1992, pp. 475–496.
[10] R. Gold, "Optimal binary sequences for spread spectrum multiplexing," in *IEEE Transactions on Information Technology*, vol. 13, no. 4, 1967, pp. 629–621.

Improving Energy Efficiency in WSN by Sleeping Strategies

Gergely Treplán
(Supervisor: Dr. János Levendovszky)
trege@digitus.itk.ppke.hu

Abstract—**The paper introduces novel deterministic and stochastic data link layer protocols for expanding the life span of wireless sensor networks. This improvement has been achieved by introducing the well known sleeping mode and optimizing the sleeping/awake ratio in order to avoid too much packet repetition. The novel method is based on acknowledgements which can then be combined by any upper-layer protocols.**

Keywords—**Communication systems, sleeping protocols, WOR, WSN, QoS**

I. INTRODUCTION

Due to the recent developments in communication technologies and microelectronics Wireless Sensor Networks (WSNs) are capable of conveying high resolution information processes to a Base Station (BS) [1, 2]. One of the most important problems of WSNs stems from the limited energy storage capacity which severe limits the longevity [3, 4]. The major energy consumption of a sensor node results from the active state of its radio component (Mica2: CC1000, TI: CC2500) [5]. Thus sleeping entails the switch of the radio module. However, if the receiving node is sleeping too much then the transmission node must listen to the channel and send the packet several times which incurs higher energy consumption on its side. Thus, the energy need of packet transmission strongly depends on the probability of sleeping, the packet length and the quality of the radio link. As a result, the networks frequently rely on multihop communication schemes to the BS which poses new challenges to the channel access method as well. On of the most used energy saving methods in the introduction of sleeping mode, which implies that nodes are awakened to switch higher energy consumption Tx/Rx mode based on a certain strategy which specifies the timing and duration of awakening. The paper is concerned with developing an optimal strategy by which longevity is maximized.

II. ASSUMPTIONS AND RELATED WORK

There are many packet forwarding algorithms in wireless networks [6, 7]. The article makes the following main assumptions of the network:

- The traffic is random, information packets can be generated anywhere and anytime.
- The energies of the nodes are limited.
- Measured information is collected by a BS with infinite energy, which can plot the state of the network to a graphical interface.
- Not every node can 'see' the BS.

Singlehop communication is a simple solution, where the node sends packets directly to the BS. The disadvantage of this is that the nodes with large distances from the BS run out of energy too fast until they are not able to communicate directly to the BS. In order to avoid this shortcoming, there is a simple multihop solution, where the nodes self organize into a chain structure along which the information is transmitted. The drawback of this solution however is that the nodes close to BS will get overloaded by forwarding to the traffic of the nodes being further away from the BS. Many elegant protocols was devised to find a balance between this two simple communication schemes, e.g. LEACH [8] suggests a clustering routing protocol, where the cluster heads are selected randomly based on an optimized distribution. The problem is the extra energy consumption of the communication for creating this hierarchy. Pegasis [9] uses an optimized chain structure, but efficiency is largely depends on the topology. The new packet forwarding methods enable us to reach longer life span of the network regardless of routing protocols being used.

The main problem with these optimized protocols that they assume that energy consumption is independent from the data link protocol. However, channel access model can significantly influence the life span of the network.

The most widely used channel access protocols in WSNs are B-MAC [10] and S-MAC [11]. The B-MAC provides an asynchronous channel access method, where duty cycling can be optimized for a given platform. The S-MAC is a method using loose synchronization which is a reliable adaptive protocol; however there is no analytical proof of the protocol performance and it has only been validated by measurements [12]. We will introduce an asynchronous channel access model that reveals the analytical relation between the preamble length and the probability of a router node waking and the life span of the network. The extension of the model allows us the optimization of the data link protocol in a given networking policy, which significantly increases the longevity of a network.

III. LINK MODEL

The life span of a wireless networks is defined by how often the electricity consuming parts are turned on, and typically the active state of the radio chip generates most of this consumption. Therefore our primary objective is to have the radio interface in sleep mode as many times and as long durations as possible. On the other hand, if a receiver node sleeps too much, then the sender node must retransmit the messages more often. The average cost of a packet depends on the probability, that the receiver station is awake, the length of the digital packet, and the quality of the link. Our goal is to minimize the energy consumption of the bottleneck node; hence the loss of a node can destroy the connectivity of the network. Let T_C be the chip time of the radio module, which is need to process one byte of information.

A. The protocol

Let us suppose, that a sender station generates information with the probability p in time period T_C, and it wants to transmit it as soon as possible. Let L be the length of the preamble which is proportional with the probability of receiving the packet, when the receiver station sleeps most of the time. This value has to be greater than the time between the wake states in B-MAC protocol, so the packet has not to be retransmitted because of sleep. Let s be the probability that, a receiver node wakes in time period T_C, and checks whether the channel is busy (CCA) [10]. If a receiver detects the Signal to Noise Ratio (SNR) above a given threshold, then it wakes and switches to Rx mode, to be able to process the packet.

B. Energy used by the sender node

It is easy to see that the probability of a successful delivery in case of a single transmission is:

$$P = 1 - (1 - s)^L .$$

Let ζ be a random variable denoting the number of transmissions, which clearly defines the sender's consumption. The probability of sending a packet n times is the following:

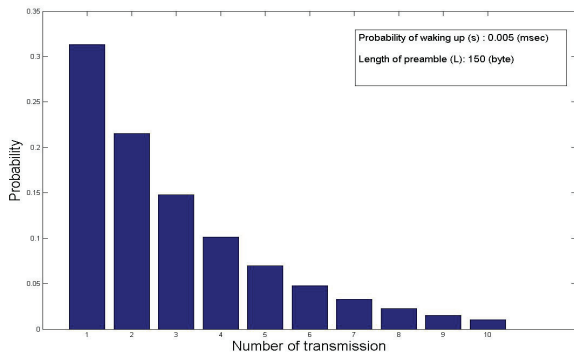$$P(\zeta = n) = (1 - s)^{L(n-1)} (1 - (1 - s)^L) . \qquad (1)$$

It is clear, that (1) is a geometrical distribution (Figure 1.), and so the expected value is:

$$E\{\zeta\} = \frac{1}{1 - (1 - s)^L} .$$

Therefore the average consumption of the sender is the following:

$$E_{tx} = \frac{p \times c_{tx} \times (L + L_{packet})}{1 - (1 - s)^L} . \qquad (2)$$

C. Energy use of the receiver node

First, the receiver is wasting energy, if he wakes up, and there is no transmission. The consumption of the so called idle listening is

$$E_{idle} = s \times c_{cca} \times t_{cca} . \qquad (3)$$

Because of the asynchronous channel the energy used in the case of a successful transmission is:

$$E_{rx} = p \times c_{rx} \times \left(\frac{L}{2} + L_{packet} \right). \qquad (4)$$

We want the energy distribution of the nodes as close to uniform distribution as possible (i.e. the nodes are running out of energy simultaneously, because of the bottleneck measure). So far, the problem can be perceived as the following optimization task:

$$\left[s_{opt}, L_{opt} \right] = \arg\min_{s,L} \left\{ \max\left[E_{tx}, E_{rx} + E_{idle} \right] \right\} .$$
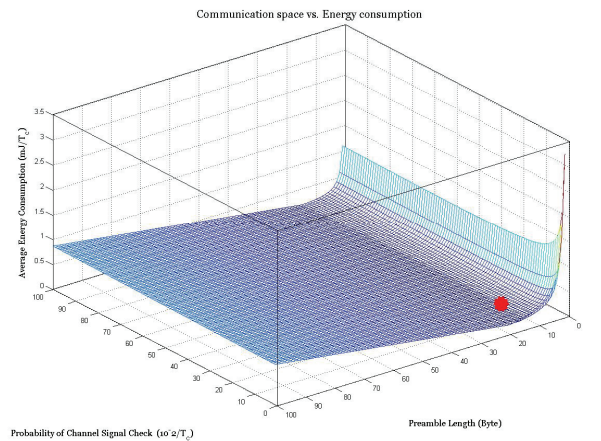

Figure 2: Relation between the free parameter space and the average energy consumption of the bottleneck node. Global optimum can be found by any gradient based algorithm in polynomial time.

Figure 1: Distribution of transmission number in the given configuration.

Figure 2 shows that it is worth developing a solution to the problem. In the next chapter, we will have a look at a multiple node environments and we will make a model, where the same optimization can be solved numerically.

IV. MODEL OF CHAIN PROTOCOL

In a multihop network we have to extend the model with the possibility, that some of nodes receive and transmit different amount of information, hence they will be in active mode more than the others. It is important to note, that a radio station can not decide from the synchronization preamble, whether the packet was addressed to it. Because of this phenomena called overhearing receivers sometimes turn on the Rx mode for a packet that was no sent to it. In B-MAC it wastes a lot of extra energy, since the preamble is quite long. We will also investigate the effects of the channel noise and packet interference, might lead to loss of packets. Let L_i, s_i, p_i be the length of the preamble, the waking up and packet generation probability of node i.

A. Overhearing

We would like to determine the waste of energy used because of the overhearing. Let the number of packets overheard by node i ξ_i. Suppose, that node i is in the range of node j. In a chain protocol node j sends packets to node j-1 (Figure 3.). The probability, that a packet is overheard m times by node i, if the sender node j transmits the packet n times is:

$$P(\xi_{ij} = m \mid \zeta_j = n) = \binom{n}{m}\left(1-s_i\right)^{L_j(n-m)}\left(1-\left(1-s_i\right)^{L_j m}\right)$$

Therefore the conditional expected value can be written as

$$\mathrm{E}\left\{\xi_{ij} \mid \zeta_j = n\right\} = n \times \left(1-\left(1-s_i\right)^{L_j}\right).$$

Finally we can calculate the expected number of overheard packets if the source is node j:

$$\mathrm{E}\left\{\xi_{ij}\right\} = \left(1-\left(1-s_i\right)^{L_j}\right)\sum_{n=1}^{\infty} n \times \left(1-s_{j-1}\right)^{L_j(n-1)}\left(1-\left(1-s_{j-1}\right)^{L_j}\right) =$$
$$= \frac{1-\left(1-s_i\right)^{L_j}}{1-\left(1-s_{j-1}\right)^{L_j}}$$

The total wasted energy then is

$$E^{(i)}_{\text{overhearing}} = \sum_j p_j \times c_{rxb} \frac{1-\left(1-s_i\right)^{L_j}}{1-\left(1-s_{j-1}\right)^{L_j}}\left(\frac{L_j}{2}+2\right), \qquad (5)$$

where $j \neq i$ and the node i can see that packets originated from node j. Instead of the length of the packet we calculate with 2 bytes, since in a case of an RF communication, we typically use the first 2 bytes to address the packet, which allows the receiver to realize, that it is unnecessary to process the payload.
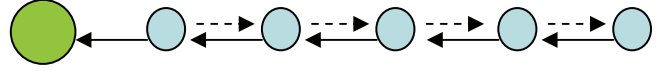

Figure 3: Possible overhearing events in chain protocol. One can see that the node behind the sender can overhear the packet. Collision phenomena are also a negative factor of the efficiency.

B. Noisy radio channel

Another problem is that the radio channel is noisy, so even if the receiver is awake and there is no interference, packets might still be lost [13]. This is dependent of the topology, which has been modeled many ways to predict the probability of a successful repetition. In this work we suppose relative packet indicator, which gives the probability of making a connection. Let us call it visibility and denote with $\mathbf{V}$, where $V_{i,j}$ means the rate of successful transmission from node i to node j. Therefore the expected number of transmission has to be recalculated as

$$\mathrm{E}\left\{\zeta_j\right\} = \frac{1}{1-\left(1-s_{j-1}\right)^{L_j}} \cdot \frac{1}{V_{j,j-1}}.$$

C. Optimization

It has to be noted that the traffic generation probabilities have to be summed across the route:

$$\overline{p_i} = \sum_{j \geq i} p_i.$$

We have developed all the cases influences the energy consumption, hence free parameters can be chosen optimally:

$$\left[\mathbf{s}_{\text{opt}}, \mathbf{L}_{\text{opt}}\right] = \underset{\mathbf{s},\mathbf{L}}{\arg\min}\left\{\max_i\left[E_{\text{tx}} + E_{\text{rx}} + E_{\text{idle}} + E_{\text{overhearing}}\right]\right\}.$$

V. SLEEPING MODE COMBINED WITH MINHOP ROUTING

In this chapter we will extend our multihop chain to a 2 dimensional spanning tree. We used the well known MinHop [12] routing method to estimate the energy consumption in a given sleeping configuration. MinHop was chosen because of the fact, that the receiver node consumes at least energy that much the sender node does. That is the reason for aiming to avoid a lot of router, which have to periodically check, whether a packet is in the air. After the routing protocol, we can do the same optimization method as we had shown in the last chapter.

We have to deal with the multi children, because there are nodes routes packets arrived from different senders. We have to estimate the average preamble length of packets, and it is the following:

$$\overline{L}^{(i)}_{rx} = \frac{1}{|\mathbf{C}_i|}\sum_{j \in \mathbf{C}_i} L_j,$$

where $\mathbf{C}_i$ is the set of nodes forward their packets to node i. This reformulates equation (4) as follows:

$$E_{rx}^{(i)} = p \times c_{rx} \times \left(\frac{\overline{L}_{rx}^{(i)}}{2} + L_{\text{packet}} \right).$$

VI. NUMERICAL RESULTS AND PERFORMANCE ANALYSIS

With the help of a Matlab simulation pack we compared the different communication strategies analyzed in this article. The obtained results are depicted by Figure 4. The T_c, t_{cca}, c_{cca}, c_{rx}, c_{tx} are platform dependent constant variables, which were chosen based on the specification of Crossbow Mica2 motes. The traffic model of the test network was $p_i = 60 \times 5 \times 10^{-4}$, $\forall i$, so average in every five minutes one packet was generated per node. It was a five nodes network, where not all the elements could 'see' each other. The significant improvement was achieved, because of overhearing time and retransmission number reduction. One can see the longevity can be increase by a factor 2-3 in comparison with traditional protocols.

VII. CONCLUSION AND FUTURE WORK

In the research reported here, I managed to develop a general model for the energy consumption of WSN in the case of different communication scenarios. Based on this model the sleeping period can be numerically optimized by using any traditional optimization methods.

In the future work, first I am going to complete this work and optimize jointly the routing and the link protocol. Secondly, I am going to develop some deterministic sleeping strategies, where the underlying delay can also be expressed analytically. These future developments will be implemented on the so called EZ-430 motes, designed by Texas Instruments.
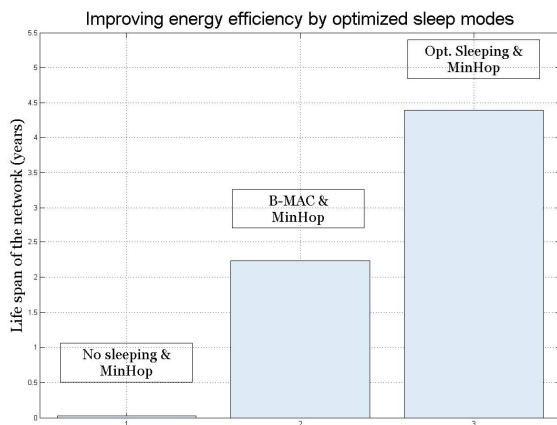
REFERENCES

[1] C.Y. Chong and S.P. Kumar. August, 2003. Sensor networks: Evolution, opportunities, and challenges. *IEEE Proceedings*: 1247–1254.

[2] A. Mainwaring, J. Polastre, R. Szewczyk, D. Culler, and J. Anderson. September, 2002. Wireless sensor networks for habitat monitoring. *First ACM Workshop on Wireless Sensor Networks and Applications*, Georgia: Atlanta.

[3] R. Jurdak. Wireless Ad Hoc and Sensor Networks: A Cross-Layer Design Perspective. Springer-Verlag. ISBN: 978-0-387-39022-2, 2007.

[4] September, 2002. Wireless sensor networks for habitat monitoring. *First ACM Workshop on Wireless Sensor Networks and Applications*, Georgia: Atlanta.

[5] D. Puccinelli and M. Haenggi. August, 2005. Wireless Sensor Networks-Applications and Challenges of Ubiquitous Sensing. *IEEE Circuits and Systems Magazine* 5: 19-29.

[6] Wendi Heinzelman, Anantha Chandrakasan, and Hari Balakrishnan. January, 2000. Energy-Efficient Communication Protocols for Wireless Microsensor Networks. *Proc. Hawaaian Int'l Conf. on Systems Science*.

[7] W. Heinzelman, A. Sinha, A. Wang, A. Chandrakasan. June, 2000. Energy-scalable algorithms and protocols for wireless microsensor networks. *Proc. International Conference on Acoustics, Speech, and Signal Processing (ICASSP '00)*.

[8] W. Heinzelman, A. Chandrakasan, and H. Balakrishnan. Energy-efficient communication protocol for wireless microsensor networks. In Proceedings of the Hawaii International Conference on System Sciences, Maui, Hawaii, Jan 2000.12.

[9] S. Lindsey and C. S. Raghavendra. Pegasis: Power-efficient gathering in sensor information systems. In IEEE Aerospace Conference, March 2002.

[10] Polastre, J., Hill, J., Culler.: Versatile low power media access for wireless sensor networks. In: Proc. of the 2nd ACM Conf. on Embedded Networked Sensor. Systems (SenSys 2004), Baltimore, MD (2004) 95–107.

[11] Wei Ye, John Heidemann, Deborah Estrin, "Medium Access Control with Coordinated, Adaptive Sleeping for Wireless Sensor Networks", Technical Report ISI-TR-567, USC/Information Sciences Institute, January 2003.

[12] U. Malesci, S. Madden, "A Measurement-based Analysis of the Intercation between Network Layers in TinyOS", Proc. European Workshop on Sensor Networks (EWSN 2006), LNCS 3868, pp. 292-309, 2006.

[13] T. S. Rappaport: *Wireless Communications: Principles and Practice*, 2nd edition, Prentice Hall PTR., December 2001.

Figure 4: Performance analysis of the different protocols. Life span might be increased by the novel optimized protocol.

Quality of Service traffic controlling in communication networks

Peter Vizi

peter.vizi@itk.ppke.hu

(Supervisor: Prof. Janos Levendovszky)

Abstract—In this paper novel algorithms for Quality of Service communication are presented. Two fields of packet exchange are concerned: in the first part a new method for finding multicast tree is shown, based on stochastic measure; in the second part an energy constrained technique for providing reliable communication is introduced. After giving the description of these algorithms, extensive simulations results are presented. Numerical results show that the multicast tree based on new stochastic measure provide better Quality of Service, and the proposed method can prolong the lifetime of energy constrained network units.

I. INTRODUCTION

OPTIMIZATION of communication protocols both in wired and wireless networks is an intensive field of development. The first part of this paper is concerned with multicast routing in packet switched network, after that a wireless packet forwarding technique is evaluated, based on cooperative communication.

One of the major challenges in IP networking is to ensure Quality of Service (QoS) routing, which selects paths or a tree to fulfil end-to-end delay requirements [1]–[3] as opposed to traditional shortest path routing, e.g. Open Shortest Path First (OSPF). Because of the manifold optimization criteria, QoS routing can prove to be a very complicated task [4]. Furthermore, QoS-aware routing protocols often reduce the representation of link state information by topology aggregation (e.g.: (Q)OSPF, PNNI) in order to minimize the amount of synchronized data among routers [5]. Thus link delays are periodically advertised when the delay surpasses a given threshold (e.g. in PNNI and QOSPF standards, see [5]). These thresholds are defined in advance. This prompts us to take delays into account as random variables characterized by their probability distribution functions over the interval between two reported thresholds [6], [7]. The least-cost routing (finding a tree with minimum delay to each destination) is analogous with the Steiner tree problem. In this paper novel link measure is used, that exploits some statistical assumptions. Extensive simulation is carried out to test the performance of our method, which prove to be able to guarantee better Quality of Service with incomplete information.

Wireless Sensorial Networks provide solution for data acquisition where the area to be observed is large or hazardous, or we can not damage the surroundings with the deployment of wired devices [8]. What is one of the advantage of these networks - namely battery powered devices - can be the largest drawback during operation. The limitation of battery power affects all aspects of the application of these networks, thus if one would like to provide QoS communication between these devices, she has to consider this factor as well. QoS communication may be required in a WSN, when important data - for example medical information - is handled. This leads us to two criteria which we have to take into account when seeking for novel algorithms: provide predefined packet arrival probability, while consume as few energy as possible. In this paper the technique of cooperation between nodes is used to provide reliable communication [9], [10], while the Decode-and-Forward strategy [11], and the Rayleigh fading link model is used [12]. Numerical simulations prove, that if we use relay nodes, instead directly sending packets to the destination, considerable amount of energy may be spared, providing the same packet arrival probability.

II. MULTICAST ROUTING

Incomplete information means that either due to link state fluctuation or aggregation, at a given time there are no concrete information about the state of the communication network. This environment does not fit to the use of traditional routing algorithms.

Because of this uncertainty we have to model link states with random variables, which gives us opportunity to create novel algorithms.

A. The Model

The communication network at hand is modeled as a graph $G(V, E)$, where $u \in V$ are the nodes, $(u, v) \in E$ are the edges. Link state corresponding to $(u, v) \in E$ is denoted by $\delta_{(u,v)}$, which is a delay-type measure. This delay is subject to the probability distribution $F_{(u,v)}(x) = P\left(\delta_{(u,v)} > x\right)$.

In this network we are searching for a tree T, which most probably fulfills the Quality-of-Service criterion:

$$\tilde{T} : \max_{T \in \mathcal{T}} P \left(\max_{R \in \mathcal{R}_{s,d_i}} \sum_{(u,v) \in R} \delta_{(u,v)} < \beta \right), \qquad (1)$$

where $\mathcal{T}$ is the set of all the possible trees, originating from s with leafs $d_i, i = 1, \ldots, N$, $\mathcal{R}_{s,d_i}$ is the set of all the paths from s to d_i. Equation (1) expresses the tree, where even the worst path fulfills the Quality-of-Service criterion. Besides this requirement we could search for a tree, where for example the overall cost of is under a given parameter, but this case is not analyzed here.

Link delay is advertised only when it surpasses a certain threshold (see [5], [13]), which can be one of the sources of uncertainty. This type of advertisement advertisement can be justified with the fact that in the IP network signalling data and the valuable information uses the same channel. There is a conflict between the performance of the routing algorithm and the data rate of the network: if we want to provide accurate information for the routing, we have to send routing information frequently, which means that signalling consumes large amount of bandwidth. Advertisement thresholds are defined by the Link Advertisement Scheme, which can be equidistant or non-equidistant.

B. Gauss Approximation of Link Descriptors

Between two advertisements the concrete value of the link delay is not known, the link state is described by the random variable $\delta_{(u,v)} \in (t_i, t_{i+1})$. We assume that the distribution of this random variable is Gaussian $\mathcal{N}(m_{(u,v)}, \sigma_{(u,v)})$ over (t_i, t_{i+1}), with the parameter $m_{(u,v)} = \frac{t_i + t_{i+1}}{2}$, and we assume that $\sigma_{(u,v)} = \sqrt{m_{(u,v)}}$. It can be shown that with these assumptions we can over-perform the classical Open Shortest Path First algorithm in case of Quality-of-Service routing problem, if we chose a new measure

$$\kappa_{(u,v)} = m_{(u,v)} \tag{2}$$

for the Bellman-Ford algorithm.

In this paper however this new measure is used for providing solution the QoS multicast routing problem. Two particular algorithms are analyzed:

- Kou-Markowsky heuristic algorithm for finding a Steiner-tree [14];
- the second algorithm is based on the unicast routing algorithm, which merges paths from the source to the destinations.

Each algorithm is run with two types of link measure: first using the hop-count then wit h(2) as measure.

C. Performance Analysis

In each simulation a number of random network is generated, and the performance of four routing method was evaluated. The actual delay parameter on each link is generated according to Normal distribution. In each network a set of destination nodes were selected. After this the four tree was constructed, then for each route from the source to the destinations its quality calculated as

$$\eta_{R_{s,d_i}} = P\left(\sum_{(u,v) \in R_{s,d_i}} \delta_{(u,v)} > \beta \right), \tag{3}$$

for each Quality-of-Service parameter β. The worst value for all the four methods is chosen for a given β and that is plotted on Figure 3.
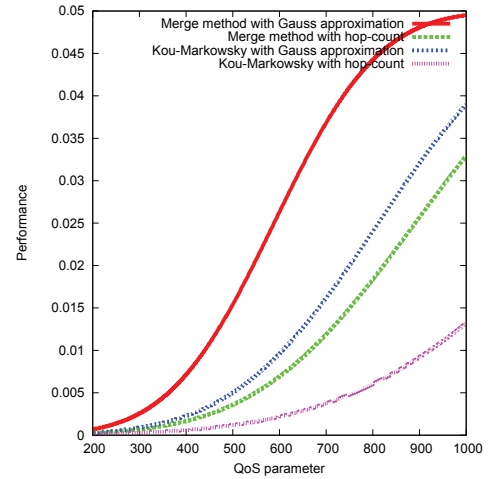

Fig. 1. The probability of fulfilling the QoS requirement (β) for all the four methods: Merging paths with Gaussian approximation (red), Merging paths with hop-count as measure (green), Kou-Markowsky algorithm with Gaussian approximation (blue), Kou-Markowsky algorithm with hop-count as measure (purple).

D. Conclusion

Novel methods for finding delay-constrained multicast trees were presented. The idea behind is to exploit the properties of the link descriptors which are modeled as random variables. Assuming Gaussian approximation over the advertised delay value we can introduce a new link measure (2). This measure proved to enhance the performance of both the Kou-Markowsky algorithm and the intuitive path merging algorithm.

Future work should concern the optimization of the Link State Advertisement scheme, as this is a key matter to provide reliable communication with the least signalling.

III. COOPERATIVE COMMUNICATION

The main advantage of cooperative communication in wireless networks stems from the nature of fading radio channel. Because of this property transmitted radio signals may be received with different quality by geographically diverse receivers. These receivers may be used as relay nodes, which can amplify and forward or decode and forward the packets, and these transmission may enhance the reception on the destination node. This way higher spectral efficiency may be achieved [15], but in our case this can be used to reduce the overall energy consumption, while providing the same packet arriving probability.

A. The Model

The communication setup is depicted in Figure 2. There is information to be transmitted from the Source to the Destination, this is carried out by not directly sending radio signals to the Destination but via intermediate, relay nodes. According to the Rayleigh fading radio model [12], [16] the distance of communicating nodes and the energy used for reliable communication can be included in the following formula

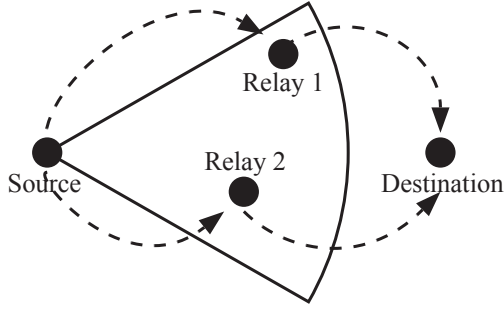$$g = \frac{d^\alpha \cdot \Theta \cdot N}{-\ln P}, \tag{4}$$

Fig. 2. Cooperative communication model: a set of relay nodes are selected which are in a given radius between the Source and the Destination.

where g is the transmit power, d is the distance between the communicating nodes, α is the path loss exponent, Θ is the Signal to Interference and Noise Ratio of successful reception, N represents the noise power and P the reception probability. The analytical connection between the reception probability, the distance and transmit energy can be transformed into

$$P = \exp\left(-\frac{\Theta \cdot N}{g \cdot d^{-\alpha}}\right) = \Psi\left(g, d\right). \quad (5)$$

Using Equation (5) we can express the reception probability between the Source and the ith relay node can be expressed as

$$P_{S,i} = \Psi\left(g_0, d_i\right), \quad \forall i = 1, \ldots, K, \quad (6)$$

where g_0 is the transmit energy of the Source, d_i is the distance between the Source and the ith relay node and there are K number or relays.

Similarly the reception probability between the ith relay and the Destination can be formulated:

$$P_{i,D} = \Psi\left(g_i, D_i\right), \quad \forall i = 1, \ldots, K, \quad (7)$$

note that g_i is the sending energy of the ith relay and D_i is the distance between the relay node and the Destination.

After these considerations we can express the probability of successful reception between the Source and the Destination as the inverse of failure:

$$P_{S,D} = 1 - \prod_{i=1}^{K} \left(1 - P_{S,i} \cdot P_{i,D}\right). \quad (8)$$

Taking into account the constraint of QoS communication, we have to ensure a margin of error of ε

$$P_{S,D} \geq 1 - \varepsilon. \quad (9)$$

One can formulate a set of constraints in connection with the life-span of the network. One possibility is to minimize the maximal spent energy

$$\bar{g}_{opt} = \min_{(g_0, g_1, \ldots, g_K)} \max_{i=0,1,\ldots,K} \left(g_i\right), \quad (10)$$

or taking into account the current energy level c of each node, one can search for the maximum of the remaining energy levels

$$\bar{g}_{opt} = \max_{(g_0, g_1, \ldots, g_K)} \min_{i=0,1,\ldots,K} \left(c_i - g_i\right). \quad (11)$$

In this paper the later is used, because the network is considered operational until the first node runs out of battery power. This criterion provides us with a $K + 1$ dimensional space, where we have to carry out a conditional optimization of (11) with respect to (9). Solving this problem with exhaustive search is unfeasible, because of the low computational capacity of the devices.

B. Optimizing the Residual Energy

We assume that the sending energy of the Source (g_0) is already optimal, and our goal is to find the optimal energy for the relay nodes ($g_1, g_2, \ldots, g_K$). In this case the optimal energies for the relays are that guarantee equal residual energy after sending their packages. To prove this statement first we have to consider (9), from which it is obvious that the network consumes the least energy if the inequality becomes equality, which is equivalent with

$$\sum_{i=1}^{K} -\ln\left(1 - P_{S,i} \cdot P_{i,D}\right) = -\ln(\varepsilon). \quad (12)$$

It can be seen, that if g_0 is given the above equation defines a K dimensional continuous surface. Our optimization criterion (11) can be reformulated as: we are searching for the maximal value of A for which

$$c_i - g_i \geq A, \quad \forall i = 1, \ldots, K. \quad (13)$$

We can define S_A as a set of points in the K dimensional space as

$$S_A = \{(g_1, g_2, \ldots, g_K) \, , c_i - g_i \geq A, \quad \forall i = 1, \ldots, K\} \quad (14)$$

which is convex, bordered by hyper-planes, and the ith plane has a constant value of $c_i - A$ at the ith coordinate, and there is a point P_A for which each coordinate is $c_i - A$.

Taking into account these considerations, we are searching for those points which satisfy (12) and maximize (13) in terms of A, and these points belong to the intersection of S_A and the K dimensional surface of (12). If we consider $\min_i (c_i - g_i) = A$, the solutions are in the border of S_A, and the solutions for (13) are the points on the intersection of S_A and the surface defined by (12). It can be proven that A is maximal only when the above mentioned intersection contains only one point, which is P_A. This means that

$$g_i = c_i - A \quad \forall i = 1, \ldots, K, \quad (15)$$

which results in the residual energy on each node to be A.

The fact that we have to provide equal energy on each node results in the following criterion

$$\prod_{i=1}^{K} \left(1 - P_{S,i} \cdot P_{i,D}\right) = \prod_{i=1}^{K} \left(1 - P_{S,i} \cdot \Psi\left(c_i - A, D_i\right)\right) = \varepsilon, \quad (16)$$

which has only one unknown variable A. Additionally it can be seen that this function is monotonously increasing, and optimal value which satisfies (16) can be easily found.

Furthermore if we take into account the sending energy of the Source node, it can be proven that under the reliability
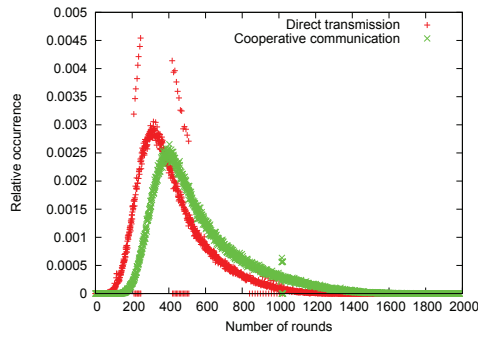
Fig. 3. The number of rounds (life-span) is plotted against relative occurrence. The cooperative communication (green) provides longer operation time than direct communication (red).

parameter $1 - \varepsilon$ the maximal residual energy of the communicating nodes is achieved if the remaining energy on all nodes are the same. This results in the following equation to be solved

$$\prod_{i=1}^{K} (1 - \Psi(c_0 - A, d_i) \cdot \Psi(c_i - A, D_i)) = \varepsilon, \qquad (17)$$

which can be solved using the Brent method.

C. Performance Analysis

In this section the performance of this new method is evaluated. In each simulation the position of nodes were random, and the communication was round-based: round by round one Source was chosen, which generated one packet. As the ε parameter 0.1 was used, which ensured 0.9 packet arrival probability. The cooperative method was compared to the case when the packet is sent directly to the Destination, with the same ε. The network was considered inoperable when the first node run out of battery power, and the life-span was defined as the number of turns run.

With these constraints a number of networks were generated consecutively, the life-span was recorded and summarized in a histogram on Figure 3. As the results show using cooperative communication can expand the life-span of the network.

D. Conclusion and Future Work

According to the simulation results the longevity of Wireless Sensorial Networks can be prolonged if we exploit the possibilities of cooperative communication. Large amount of energy can be saved if we do not send directly to the destination node, while maintaining the same quality of packet arrival.

Further investigation is required in the selection of relay nodes. An optimal set of nodes should be chosen as relays, which can provide the required quality, while consuming the least energy.

REFERENCES

[1] D. H. Lorenz and A. Orda, "QoS routing in networks with uncertain parameters," *IEEE/ACM Transactions on Networking*, vol. 6, no. 6, pp. 768–778, 1998. [Online]. Available: citeseer.ist.psu.edu/lorenz98qos.html

[2] S. Chen and K. Nahrstedt, "On finding multi-constrained paths," in *ICC'98*. IEEE, 1998, pp. 874 –879. [Online]. Available: citeseer.ist.psu.edu/chen98finding.html

[3] ——, "An overview of quality-of-service routing for the next generation high-speed networks: Problems and solutions," *Networks*, vol. 12, no. 6, pp. 64–79, 1998.

[4] J. Jaffe, "Algorithms for finding path with multiple constraints," *Networks*, vol. 14, pp. 95–116, 1984.

[5] ATM Forum, "Private network-network interface specification version," 1996. [Online]. Available: citeseer.ist.psu.edu/article/forum96private.html

[6] R. Guerin and A. Orda, "Qos routing in networks with inaccurate information: theory and algorithms," *Networking, IEEE/ACM Transactions on*, vol. 7, no. 3, pp. 350–364, Jun 1999.

[7] A. Shaikh, J. Rexford, and K. S. Shin, "Dynamics of quality-of-service routing with inaccurate link-state informaiton," Tech. Rep. CSE-TR-350-97, 17 1997. [Online]. Available: citeseer.ist.psu.edu/shaikh97dynamics.html

[8] C.-Y. Chong and S. Kumar, "Sensor networks: evolution, opportunities, and challenges," *Proceedings of the IEEE*, vol. 91, no. 8, pp. 1247–1256, Aug. 2003.

[9] A. Sendonaris, E. Erkip, and B. Aazhang, "User cooperation diversity. part i. system description," *Communications, IEEE Transactions on*, vol. 51, no. 11, pp. 1927–1938, Nov. 2003.

[10] L. Song and D. Hatzinakos, "Cooperative transmission in poisson distributed wireless sensor networks: protocol and outage probability," *Wireless Communications, IEEE Transactions on*, vol. 5, no. 10, pp. 2834–2843, Oct. 2006.

[11] J. Laneman, D. Tse, and G. Wornell, "Cooperative diversity in wireless networks: Efficient protocols and outage behavior," *Information Theory, IEEE Transactions on*, vol. 50, no. 12, pp. 3062–3080, Dec. 2004.

[12] M. Haenggi, "Energy-balancing strategies for wireless sensor networks," *Circuits and Systems, 2003. ISCAS '03. Proceedings of the 2003 International Symposium on*, vol. 4, pp. IV–828–IV–831 vol.4, May 2003.

[13] G. Apostolopoulos, S. Kama, D. Williams, R. Guerin, A. Orda, and T. Przygienda, "QoS Routing Mechanisms and OSPF Extensions," RFC 2676 (Experimental), Aug. 1999. [Online]. Available: http://www.ietf.org/rfc/rfc2676.txt

[14] L. Kou, G. Markowsky, and L. Berman, "A fast algorithm for steiner trees," *Acta Informatica (Historical Archive)*, vol. 15, no. 2, pp. 141–145, June 1981. [Online]. Available: http://www.metapress.com/link.asp?id=V7W86M72174K7267

[15] J. Laneman and G. Wornell, "Distributed space-time-coded protocols for exploiting cooperative diversity in wireless networks," *Information Theory, IEEE Transactions on*, vol. 49, no. 10, pp. 2415–2425, Oct. 2003.

[16] M. Haenggi, "On routing in random rayleigh fading networks," *Wireless Communications, IEEE Transactions on*, vol. 4, no. 4, pp. 1553–1562, July 2005.

Research and Assessment of Novel Acute and Chronic Brain Multielectrodes

László Grand

(Supervisors: Dr. György Karmos, Dr. István Ulbert)

grand@cogpsyphy.hu

Abstract— **Present cutting edge acute and chronic extracellular recording multielectrodes make us possible to investigate how different brain structures work. The quality of recorded signal depends much on the electrode properties and also on unclear immunological processes arises right after each implantation.**

We investigated in-vivo and in-vitro properties of a novel, chronically implantable cortical laminar epoxy shaft fine wire multielectrode. Besides, performance of one-, two- and three-dimensional silicon multielectrodes fabricated by Neuroprobes consortium were assessed regarding to their Unit, Multiunit (MUA) and Field Potential (FP) recording capabilities. In addition we have made the first steps towards the realization of a novel, more robust acute silicon laminar multielectrode that can penetrate dura mater without bending or breaking while inserted into the tissue.

At the end of this paper a two dimensional finite element model (Comsol Multiphysics) is proposed as a useful tool for comparing theoretical and in vitro measured signals.

I. INTRODUCTION

Neural electrodes with multiple contacts give us the possibility to learn more about cortical or deeper brain structures and their functions via recording signals from extracellular space. Unit, Multiunit activity (MUA) and Field Potentials (FP) can be acquired with the same electrode if the implantation technique as well as the electrode properties are adequate. Long-term recorded Unit, MUA and FPs could tell us more than the specific role of a distinct brain region in a complex information processing network. They are reliable indicators of electrode efficiency and help us to distinguish between useful and less effective electrode geometries and materials. Beside in-vivo performance analysis, in-vitro measured impedance values can predict the short and long-term success of a given electrode.

Present-day cutting edge neural multielectrodes may be categorized into two basic groups. The first is the wire array approach, the second group is the silicon carrier based multielectrodes. Many paper concluded that wire laminar arrays have better long-term performance but silicon technology provides smaller electrodes, theoretical better resolution and less tissue damage [6,14,16]. The fabrication process is, however, difficult.

L. Grand is with the Faculty of Information Technology, Péter Pázmány Catholic University, Budapest, Hungary (phone: +36-1-886-4700; fax: +36-1-886-4725; e-mail: grand@cogpsyphy.hu).

Immunological response followed right after the implantation influences the performance of each electrode to a great extent. Signal degradation takes place on every implanted electrode. However, there is a significant difference in point of scale and the time of degradation begins between the different electrodes.

In this year our aim was to investigate a novel, laminar epoxy shaft fine wire multielectrode that makes us possible to record Unit, MUA and FPs from rat cortical areas chronically. We also had the possibility to characterize acute performance of novel one-, two- and three-dimensional silicon electrodes on ketamine-xylazine anesthetized rats fabricated by Neuroprobes European consortium. Besides, we have started to piece together the technology required for fabrication of a more robust but still small in size silicon laminar multielectrode. Our experiments ended up proving that a sharp tip silicon electrode with straight lateral walls can be fabricated by applying various etching and photolithography processes.

A Finite Element Model for virtual performance analysis of different electrodes is proposed as a useful tool for designing more efficient neural probes.

This paper summarizes our results on the above mentioned topics as well as my future plans.

II. EPOXY SHAFT FINE WIRE MULTIELECTRODE FOR LONG-TERM RAT CORTEX STUDIES

Our question was whether it was possible to use a specially designed laminar array electrode for chronic recordings on rats. For realizing that goal, we used a similar technology that was published by this group earlier [13]. The cut ends of 18 insulated Pt-Ir (90%-10%) wires provide the 18 Pt-Ir sites. Each contact is 25μm in diameter, arranged under each other with 100μm intercontact spacing. Wires are embedded into a tapering epoxy shape that is 250 μm in diameter at its thickest part (Figure 1). Thanks to the small size of the electrode it causes relatively small damage in the brain tissue during implantation. It has a sharp tip but incising dura mater is necessary for implantation. Output leads are embedded into silicone elastomer that makes them flexible and they are connected to a Precidip connector.

Our aim was to implant the primary auditory cortex (A1) of rats with the above mentioned multielectrode. In order to be able to assess the exact position of A1, we had to build a surface mapping multielectrode. Our novel mapping electrode consists of 23 stainless steel sites (d=230 μm). The size of the bottom of the epoxy shape where the Pt-Ir

contacts are is about 2.5*2.5 mm. The intercontact spacing is 200 μm (Figure 2). After placing the mapping electrode gently on the dura, sound stimuli were given (1/s) via a high quality loudspeaker (Kenwood, KFC-T201). Auditory evoked potentials (AEP) were recorded from every site. Selection of A1 based on AEP amplitude and timing.
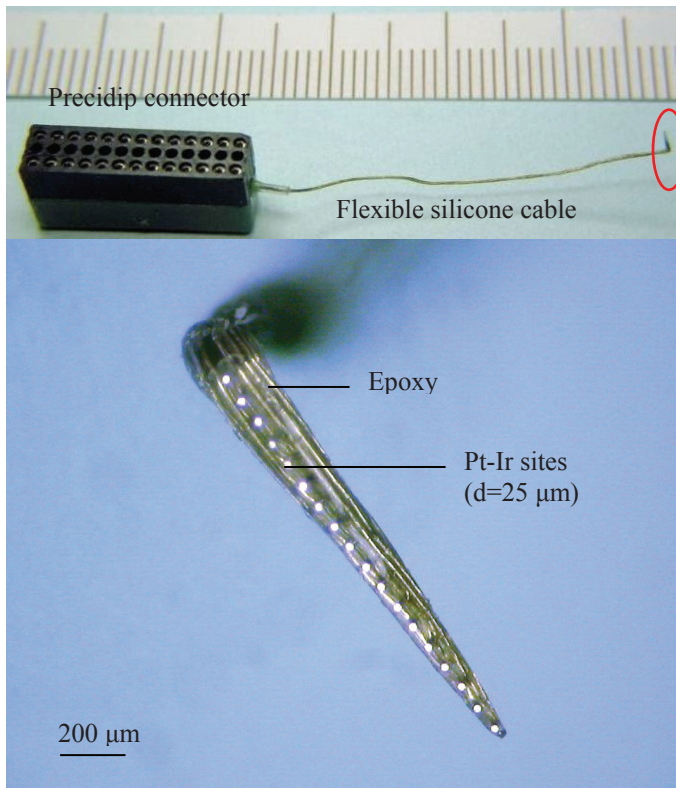

Fig 1. The chronically implantable laminar wire electrode array.

This implanted multielectrode array makes us possible to record rat cortical bioelectric signals chronically during the natural sleep-wake cycle. Impedance of the contacts was measured before implantation with a single channel Electrochemical Activation and Sensing Instrument (EASI, Bak Inc.). The average impedance value of the implanted electrode at 1kHz was 674.16 kΩ. SD was 108.71. The average impedance value of the mapping electrode at 1 kHz was 41.6 kΩ since its larger site size. SD was 27.55.

LFP (band pass: 0.1Hz-500Hz, 24dB/oct) and MUA (band pass: 300Hz-5000Hz, 24dB/oct) referenced to the frontal bone were recorded with the 18 channel laminar multielectrode. LFPs were sampled at 2kHz/channel rate with 16bit precision, while multiple units were sampled at 20kHz/channel rate with 12bit precision (LabView, National Instruments, Austin, TX), and stored on hard drive for off-line analysis. Acoustic stimuli were generated by Tucker-Davis Technologies (TDT, Gainesville, FL) System III hardware and software. Click stimuli (1/s, 3/s) were presented via the above mentioned loudspeaker and was recorded on the 24th channel.
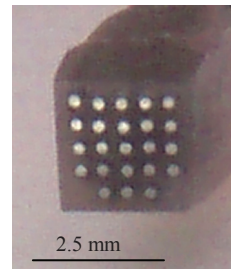
Fig 2. The surface mapping multielectrode.

We have no long-term data yet, however good quality FPs and MUA was recorded a month after the implantation.

III. CHARACTERIZATION OF 1D, 2D AND 3D NEUROPROBES SILICON ELECTRODES

Within the frame of this study we investigated the in-vitro and in-vivo recording capabilities of one-, two- and even three-dimensional silicon electrode arrays designed and fabricated by Neuroprobes consortium. There are nine contacts on the 1D probe, the intercontact spacing is 650 μm (Figure 3A). Since this relatively high value, it gives us a useful tool for recording MUA as well as FPs from different structures of the brain. The 2D fork shape probe has 36 contacts, 9 on each electrode shaft (Figure 3B). The 3D array included 4*4 electrode shaft with 4 contacts on each (Figure 3C) [1].
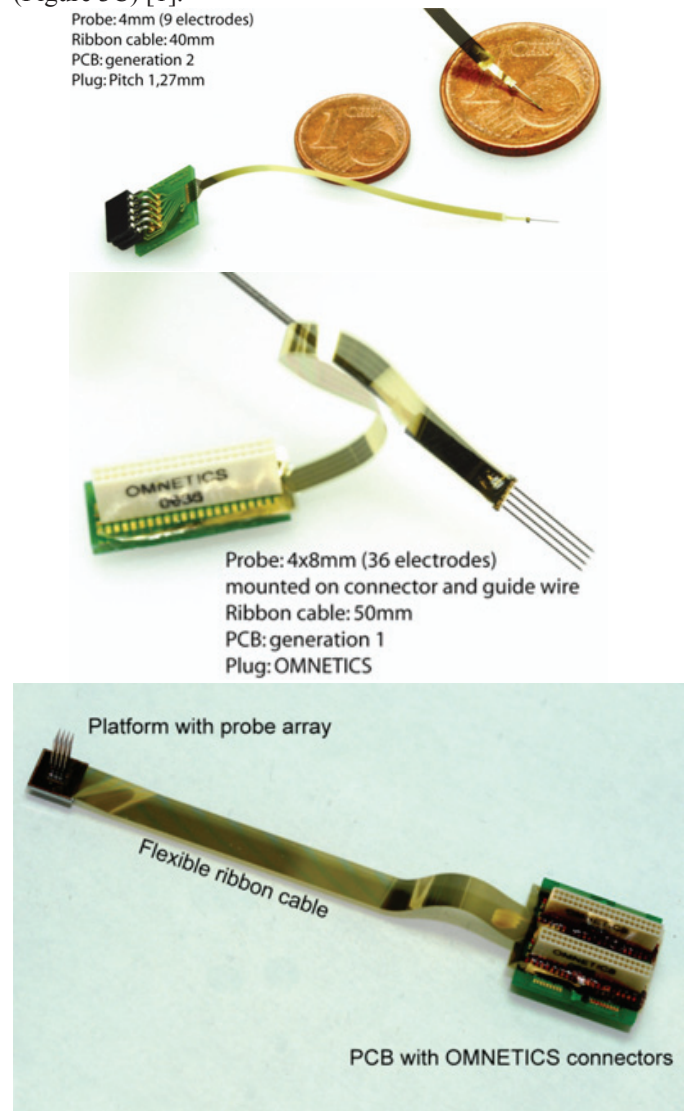
Fig 3. 1D (A), 2D (B) and 3D (C) Neuroprobes silicon probes [9].

The rat was anesthetized with ketamine-xylazine. Duration of the experiment was about eight hours long. Since our primary goal was to assess the MUA recording ability of these electrodes we decided to implant the somatosensory area because of the relatively large cell somas there. Commercially available stereotaxic frame (David Kopf Instruments) was used to set the appropriate coordinates (Anterior-posterior: -3 to -6 from bregma, medial-lateral: 1 to 5). After we had removed the skin a window shape craniotomy was made. The dura remained intact, no serious bleeding was apparent. Impedance on each site before and after the acute implantation was measured. Contacts with impedance higher than 2MΩ were considered bad (20%). The average impedance of good contacts on the 1D probes were 794.5 kΩ before (SD=354.3) and 799.28 after (SD=323.37) implantation. That was 973.41 kΩ on 2D probes (SD=123.68) before surgery.

Ketamine-Xylazine induced slow oscillations were evident not just in signals recorded from cortex (CX) but also in signals acquired from hippocampus (HC) and thalamus (TH). Good quality, high amplitude FPs were observed from almost all of the available electrodes. High impedance sites gave not useful signals but flat lines in FP.

However MUA was not seen in cortical layers, we were able to acquire that from thalamus. High and low amplitude MUA was seen on different channels of the multielectrode. MUA and corresponding FPs recorded from a 1D probe are represented (Figure 4). In order to investigate properties of bursting activity on channel with the highest MUA amplitude we filtered the signal with a bandpass filter (300-5000 Hz, 24 dB, IIR). Thresholding was used to retrieve exact timing of different burst onsets. Five different sweeps and the grand average of every sweep are shown on Figure 5.
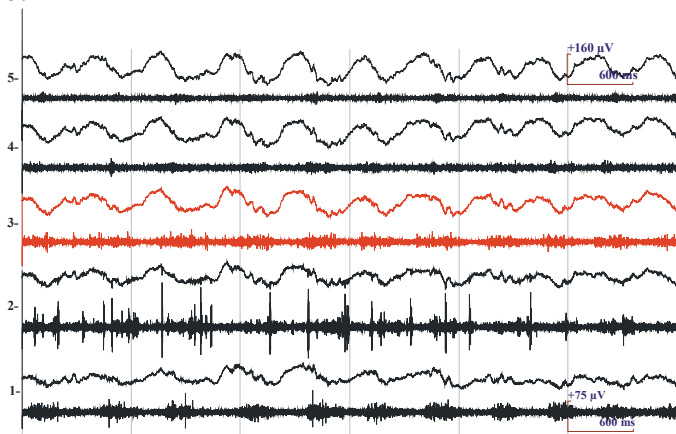
Fig 4: FPs and MUA recorded from thalamus with a 1D probe. Site number 1 is located the deepest.
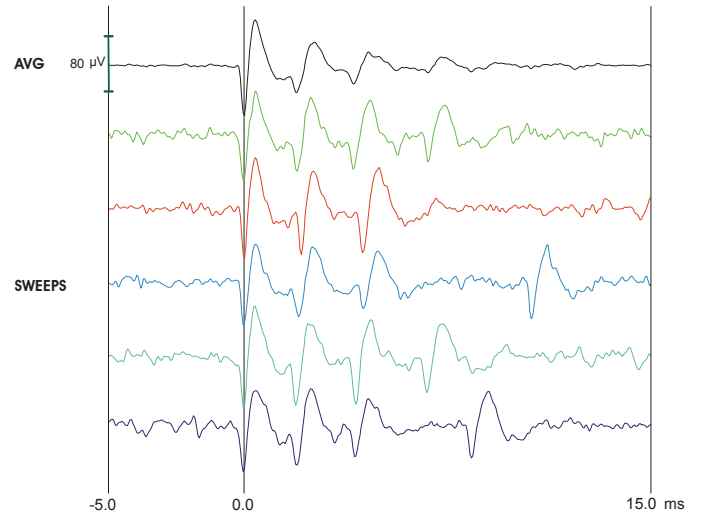
Fig 5: Single sweeps and grand average (AVG) of multi unit bursts. The signal was recorded by the site with the highest MUA amplitude on a 1D silicon electrode.

We found that manual and slow mechanical insertion through dura with 1D and 2D probes was satisfactory. 3D probe insertion through dura caused 1-2 mm dimpling but it could brake in. Recording FPs and MUA was possible with all the electrodes. We found impedance values relatively high and that might be the answer to the question why mechanical and electrical artifacts took place several times during the recording sessions.

IV. TOWARDS A MORE ROBUST LAMINAR SILICON MULTIELECTRODE

The aim of this project is to build the first Hungarian silicon laminar multielectrode in cooperation with the Research Institute for Technical Physics and Materials Science of the Hungarian Academy of Sciences (MTA-MFA).

Since we started from scratch the first step was to investigate the feasibility of a sharp tip and lateral walls electrode fabrication with different etching processes. A two sided etching process was chosen in order to provide a multielectrode with sharp sailboat bow shaped tip and rounded bottom. The width of the silicon shank is 256 μm, its length is 7mm and its thickness is 100 μm (Figure 6). There is a $SiO_2/Si_3N_4/SiO_2$ sandwich structure lays on the pure silicon that includes gold leads belonging to different contacts along the silicon shaft. The upper SiO_2 layer is exposed at the contact and platinum is deposited on a thin titanium adhesive layer.
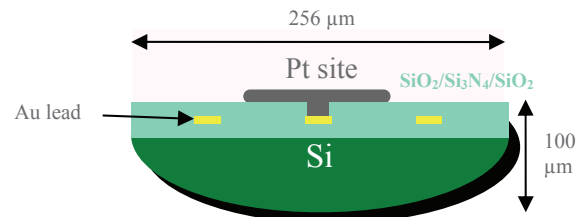

Fig 6. Cross section of the Hungarian silicon electrode.

We have proven that the shape of the multielectrode can be fabricated with repeated etching processes and need to step towards the metallization. Gold leads will be protected

from extracellular fluid with the $SiO_2/Si_3N_4/SiO_2$ structure. First platinum then platinum-iridium will be the contact material. The first acute laminar silicon probe will have 24 contacts.

The silicon probe will be glued and wire bonded to a specially designed Printed Circuit Board (Figure 7).

This electrode will be stiff and robust enough to penetrate both the dura and pia mater but remain small in size. Our future plan is to fabricate it that long that is suitable for deep brain recordings. Chemical sensor integration for local chemical sensing is also our future goal together with the Institute of Biomedical Engineering of the Imperial College London.

Fig 7. The PCB of the Hungarian acute silicon probe. The white arrow indicates the place to where the back of the silicon electrode will be glued and wire bonded.

V. FINITE ELEMENT MODELING OF MULTI ELECTRODES

Finite Element Modeling (FEM) gives us a powerful tool for electrode performance analysis [2]. After building up the virtual in vitro setup together with the electrode which performance we need to know more about, we can compare the theoretically calculated values with those we acquired during the 'real world' performance analysis. We used Comsol Multiphysics 3.4 for our FEM study.

Our goal is to build up a realistic model of the in vitro setup we use for electrode testing. First we created a realistic model of the laminar wire multielectrode array that has been used for long in our laboratory [13]. Only the very tip of the electrode was modeled because of the computational cost. The model included 6 platinum wires (d=20.32 μm, σ=9.435x10^5 Sm^{-1}, εr=1) with polyimide insulation layer (2*2.54 μm). Intercontact spacing was 100 μm. The cut ends of the wires gave the contacts. Those extended 2 μm outward the epoxy shape (σ=9.435*10^5, εr=1) that included the wires. The epoxy shape was attached to the stainless steel (SS304) tubing. A monopolar AC source was placed into the model with different distances (30, 75, 150, 225 μm) from the electrode. AC with various amplitudes (50Hz, 0.1- 0.5-1V) was applied with the monopolar voltage source (d=10μm). The electrode as well as the AC source was dipped into saline (σ=1 Sm-1, εr=80). The model is shown on Figure 8.
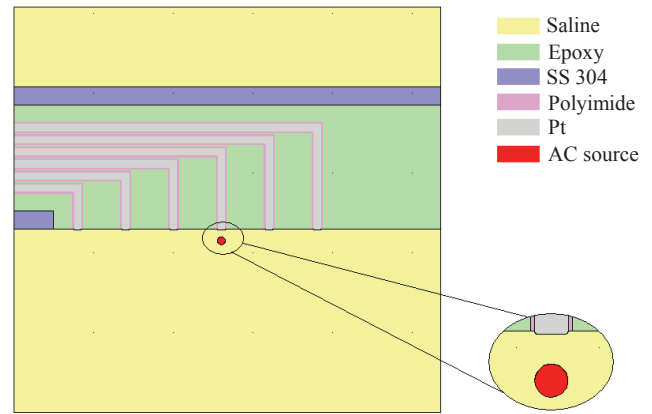

Fig 8. The 2D FEM environment with the laminar wire multielectrode.

Calculated values on the closest electrode contact to the AC source as a function of distance and applied voltage are shown on Figure 9.

VI. FUTURE PLANS

My primary goal in the near future is to collect more data from rats implanted with the epoxy shaft fine wire multielectrode. Further in-vitro and in-vivo studies, together with histological analysis is needed to prove the efficacy and life time of the suggested method.

Metallization is the next step for the Hungarian silicon electrode project. Once we have the first working multielectrode fabricated we will start to improve its performance with permanent testing. The long-term future goal is to fabricate chronically implantable and deep brain multielectrodes with ChemFETs in cooperation with the Institute of Biomedical Engineering of the Imperial College London.
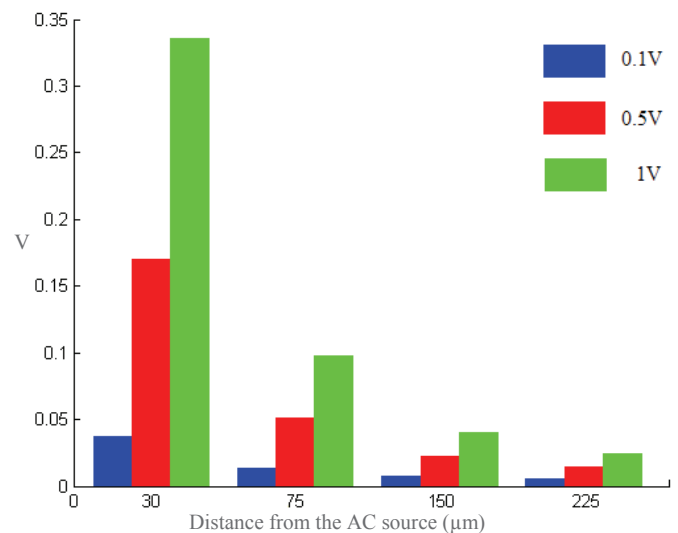

Fig 9. Teoretical signal amplitude as a function of the source-electrode contact distance and applied voltage.

The Helmholtz double layer is a crucial element of the FEM that is not included in our model yet. Since approaching the realistic model is only possible with the built in double layer the next step of the near future is to include that in our model. Investigating how the recorded signal depends on the distance, amplitude and even the

frequency of the AC source and comparing those with the real world data we obtain by using the in-vitro setup can help us designing more reliable and better multielectrodes. Since our AC source is monopolar we will change it to bipolar. Building up and modeling silicon electrodes and comparing their efficacy with fine wire arrays will take place in the future.

During this academic year I was a co-author of one published paper [5]. Another paper in which I am a co-author was reviewed and will be published soon [1]. Three posters [3,4,7] are also the result of this year.

However my previous work about a cortical gating mechanism of cats was not included in this paper, my future plan is to publish the results in this year.

REFERENCES

[1] A. A. A. Aarts, H. P. Neves, I. Ulbert, L. Wittner, L. Grand, M. B. A. Fontes, S. Herwik, S. Kisban, O. Paul, P. Ruther, R. P. Puers, C. Van Hoof, A 3D slim-base probe array for In vivo recorded neuron activity", Conference publication EMBC, 2008.

[2] D. R. Cantrell, S. Inayat, A. Taflove, R. S. Ruoff, J. B. Troy, "Incorporation of the electrode-electrolyte interface into finite-element models of metal microelectrodes", *J Neural Eng*, vol. 5,pp. 54-67, 2008.

[3] R. Csercsa, A. Magony, D. Fabó, L. Entz, L. Wittner, B. Dombovári, L. Grand, L. Erőss, I. Ulbert, "Laminar properties and sparse cell firing in sleep slow oscillation in humans", *Poster at the 6th FENS Forum of European Neuroscience*, Geneva, 2008.

[4] B. Dombóvári, L. Grand, L. Wittner, G. Karmos, I. Ulbert, , "Comparison of auditory information processing in sleep and anesthesia, IBRO poster, Debrecen, 2007.

[5] D. Fabó, Z. Maglóczky, L. Wittner, A. Pék, L. Eross, S. Czirják, J. Vajda, A. Sólyom, G. Rásonyi, A. Szucs, A. Kelemen, V. Juhos, L. Grand, B. Dombovári, P. Halász, T. F. Freund, E. Halgren, G. Karmos, I. Ulbert, "Properties of in vivo interictal spike generation int he human subiculum", Brain, vol. 131(2),pp. 485-499, 2007.

[6] D.R. Kipke., R. J. Vetter, J. C. Williams, J. F. Hetke, "Silicon-substrate intracortical microelectrode arrays for long-term recording of neuronal spike activity in cerebral cortex", *IEEE Trans Neural Syst Rehabil Eng*, vol. 11(2),pp. 151-155, 2003.

[7] N. B. Langhals, L. Grand, R. J. Vetter, D. R. Kipke, "Characterization of Noise and Capacitive Losses of Microelectrodes through Recordings and Modeling", *BMES*, Los Angeles, 2007.

[8] K. A. Ludwig,, J. D. Uram, J. Yang, D. C. Martin, D. R. Kipke, " Chronic neural recordings using silicon microelectrode arrays electrochemically deposited with a poly(3,4-ethylenedioxythiophene) (PEDOT) film", *J Neural Eng*, vol. 3(1),pp. 59-70, 2006.

[9] Neuroprobes silicon multielectrodes, http://www.neuroprobes.com

[10] R. A. Normann, E. M. Maynard, P. J. Rousche, D. J. Warren, "A neural interface for a cortical vision prosthesis", *Vision Res*, vol. 39(15),pp. 2577-87, 1999.

[11] P. J. Rousche, D. Pellinen, D. P. Pivin Jr., J. C. Williams, R. J. Vetter, D. R. Kipke, "Flexible Polyimide-based intracortical electrode arrays with bioactive capability", *IEEE Trans. on Biomedical Engineering*, vol. 48(3),pp. 361-371, 2001.

[12] A. Starr, K. D. Wise, J. Csongradi, "An evaluation of photoengraved microelectrodes for extracellular single-unit recording", *IEEE Trans Biomed Eng*, vol. 20(4),pp. 291-293, 1973.

[13] I. Ulbert, E. Halgren, G. Heit, G. Karmos, "Multiple microelectrode-recording system for human intracortical applications", *J Neurosci Methods*, vol. 106(1),pp. 69-79, 2001.

[14] R. J. Vetter, J. C. Williams, J. F. Hetke, E. A. Nunamaker, D. R. Kipke, "Chronic neural recording using silicon-substrate microelectrode arrays implanted in cerebral cortex", *IEEE Trans Biomed Eng*,vol. 51(6),pp. 896-904, 2004.

[15] J. C. Williams, R. L. Rennaker, D. R. Kipke, "Stability of chronic multichannel neural recordings: Implications for a long-term neural interface", *Neurocomputing*, vol. 26-27,pp. 1069-1076, 1999.

[16] K. D. Wise, D. J. Anderson, J. F. Hetke, D. R. Kipke, K. Najafi, "High-density electronic interfaces to the nervous system", *Proceedings of the IEEE*, vol. 92(1),pp. 76-97, 2004.

[17] K. D. Wise, J. B. Angell, A. Starr, "An integrated-circuit approach to extracellular microelectrodes", *IEEE Trans Biomed Eng*, vol. 17(3),pp. 238-47, 1970.

State Detection of Cortical Slow Sleep Oscillation

Andor Magony

(Supervisors: Dr. György Karmos and Dr. István Ulbert)

magan@digitus.itk.ppke.hu

Abstract—**Sleep seems to be one of the last complex integrated behaviors for which the adaptive advantage remains unknown. There is, however, no shortage of theories explaining the functions of sleep: energy conservation and protection against energetic exhaustion, restoration of tissular integrity, neuronal plasticity, processing of memory traces. A distinguished stage of sleep, deep sleep or slow sleep, has a very special oscillatory feature, fluctuating between the so-called 'up-states' and 'down-states', practically the on-and-off states of the cortex. According to recent findings this phenomenon might play role in memory processes, but probably also in the epileptogenesis and seizure generation. The detection of this oscillation, however, is not trivial at all, and there is an emerging need for new approaches supported by information technology.**

I. INTRODUCTION

Sleep is a process during which deep physiological changes can be observed in animals and humans affecting both the peripheral and the central nervous system. Also, sleep seems to be one of the last complex integrated behaviors for which the adaptive advantage remains unknown. There is, however, no shortage of theories explaining the functions of sleep: energy conservation and protection against energetic exhaustion, restoration of tissular integrity, neuronal plasticity, processing of memory traces. The situation becomes more complicated because of the presence of two special types of sleep (slow wave sleep, SWS, and rapid eye movement, REM), which may have different and independent functions. Theories to explain sleep often rely on EEG patterns recorded during sleep sessions. Historically five major types of continuous rhythmic sinusoidal EEG activity are recognized (delta, theta, alpha, beta and gamma). There is however no precise agreement on the frequency ranges for each type. Rhythmic slow activity in wakefulness is common in young children, but is abnormal in adults. In addition to the above types of rhythmic activity, individual transient waveforms such as sharp waves, spikes, spike-and-wave complexes occur in epilepsy, and other types of transients occur during sleep. The sleeping cycle is constituted of recurring stages, through which the depth of the sleep shows a non-uniform pattern. Presently, scientists determine sleep categories of two general types: REM (Rapid Eye Movement) and NREM (non-REM). Statistically speaking the NREM accounts for 75-80 per cent of total sleep time, and can be further categorized as follows:

- Stage 1, characterized by near-disappearance of the alpha waves seen occipitally in awake states, and by the first appearance of theta waves. This stage is often referred to as 'drowsy sleep'. It shows at the beginning of sleep (for mostly being a transition state into Stage 2) and is related with sudden twitches or jerks many people experience when falling asleep. Throughout this period, people lose muscle tone, as well as conscious awareness of the external environment: stage 1 can be thought of as a gateway state between wake and sleep.

- Stage 2 is characterized by 'sleep spindles' (12-16 Hz) and 'K-complexes'. Electromyographic recordings show lowering power, while conscious awareness of the external environment evaporates. This stage occupies 45-55 per cent of total sleep.

- Stage 3, with delta waves, also called delta rhythms (1-4 Hz), is thought to be part of slow-wave sleep (SWS) and acts principally as a transition into stage four. In general it occupies 3-8 per cent of total sleep time.

- Stage 4 is the deep sleep, where slow sleep oscillations (SO, 0.1-1Hz) appear. It governs the first third of the night and accounts for 10-15 per cetn of total sleep time. This stage is usually depicted as the deepest stage of sleep, for it is exceptionally difficult to wake someone in this state. Also, this is considered to be the stage in which night terror and sleepwalking occur. I have paid special attention to the analysis of this stage in animals and epileptic humans with laminar multielectrodes.
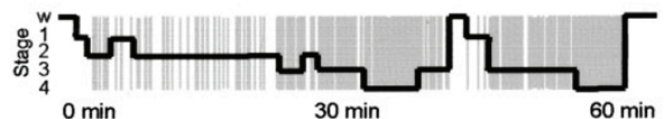

Figure 1. Stages in a sleep cycle

II. THE SLOW OSCILLATION

In 1993 Mircea Steriade and his colleagues described a slow (below 1 Hz) oscillation of intracellularly recorded neocortical and thalamic neurons and proposed that this oscillation observed in anesthetized and naturally sleeping cats is the emergent activity of a synchronized network. The concepts of synchrony and of an antinomy between synchronized and desynchronized electroencephalographic (EEG) patterns were widely used over the past six decades to distinguish the high-amplitude slow waves during sleep from the low-amplitude fast waves during wakefulness. However, when inferring the process of synchrony among neurons, one has to rely on simultaneous recordings from multiple sites. Steriade and his colleagues showed with intracellular

recordings that in the sleeping cat during the slow oscillation both in ketamine-xylazine anesthesia and natural sleep the cortical neurons produce rhytmic hyperpolarization and depolarization periods. In the hyperpolarization period the neurons are inactive for a few hundred milliseconds, while in the depolarization period the membrane potential can exceed firing threshold and neurons generate action potentials. The slow oscillation can be generated and sustained by the cerebral cortex alone, it is resistant to thalamic lesion, but disrupted by the sectioning of intracortical pathways, though restored a few hours later. This is supported by the observation that up-state as well as down-state appears in the cortex earlier than in the thalamus. There is a critical mass of cortical tissue which is needed to exhibit this type of activity, however under certain circumstances, in vitro cortical slices can also show similar pattern. During up-state a window is opened so that thalamic input is able to reach the cortex, while during down-state this window is closed. This refers to a subtle strategy of stimulus processing that enables the incoming auditory, tactile or olfactory stimuli from the outer world to reach the cortical level even during slow wave sleep. This strategy needs to fit the physiological circumstances of slow wave sleep, that are the phases of the slow oscillation. Furthermore, it needs to ensure the sufficient amount of sleep (sleep protecting effect), on the other hand the stimulus processing requirements for awakening should be met (awakening effect). As mentioned earlier, the cortex oscillates between active (up-state) and inactive (down-state) states during deep sleep. Hyperpolarization during down-state does not provide adequate conditions for stimulus processing, since neurons are in a less excitable state. The opposite applies for up-state. In active state (that is similar to the awake state) there is stimulus processing, this state is responsible for the awakening effect. The inactive state (in which stimulus processing is reduced) is responsible for the sleep protecting effect. For example when a zebra is sleeping and hears a faint noise of a lion footstep, it remains asleep, but when the noise is accompanied by a roar, the smell of the lion, or further footsteps, the window opens for the thalamic input, the cortex reacts and the zebra wakes up. Emerging evidences suggest that non-REM period, especially SO sleep plays an important role in declarative memory consolidation in animal models as well as in humans. The basic substrate of these processes are identified as theta/gamma interactions, spindle and numerous other, including gamma frequency band oscillations linked to the up-state of the slow oscillation. Recent findings of coalescing neuronal rhythms orchestrated by the cortical slow oscillation also strengthen the role of sleep in memory consolidation. It is also well known, that sleep modulates epileptic activity. Human studies show, that slow wave sleep (SWS) enhances paroxysmal activity and nocturnal seizures are often observed in patients with frontal lobe epilepsy. In animal models, extensive intra- and extracellular observations revealed, that seizures also often develop from the cortical slow oscillation (SO). In these models, the epileptiform activity and seizures consist of several well defined electrical patterns of intracortical events, such as spike-wave, polyspike-wave complexes and fast runs.

Similar building blocks were found in the human disease too with scalp and intracranial field potential recordings.
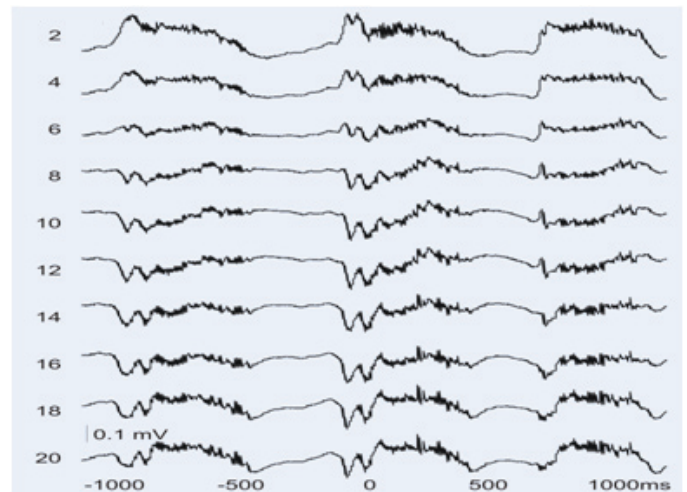

Figure 2.   Slow oscillation on field potential

III. METHODS AND MATERIALS

In the laboratories of the Comparative Psychophysiological Group of the Institute for Psychology, Hungarian Academy of Sciences, we employ the products of Neuroscan, the world leading developer of software and hardware for neuroscience applications. Primarily, we use Neuroscan Edit, a software which is appropriate for most offline data analysis methods. We have gained experiences in other software products as well, such as DataView (by Dr. W. J. Heitler, University of St Andrews, Scotland) for event clustering (spike sorting) with 3D visualisation of principal components, wavelets and other parameters, EEGLab (by Arnaud Delorme, Scott Makeig, University of California San Diego) an open source Matlab toolbox for electrophysiological research. For data acquisition we use AcqUnit and AcqMUA, LabView-based customized systems created by Dr. István Ulbert. After having evaluated the above-mentioned products we concluded that we need to develop a brand new software, given the name SpikeSolution, in order to execute some specific functions we need for our research. These customized functions include PSTH analysis, Hilbert transform, CSD maps, coherence maps, different types of spike sorting (based on PCA, CEM, k-means). To make its use easier we applied some other functions as well. For example different types of data display, raster plots, applications of the Fast Fourier Transform, etc. A very important part of SpikeSolution is the state detection. This feature is essential for the analysis of slow wave sleep and cannot be found in any other programs. We applied different state detection methods, those previously published and those developed by us also.

IV. STATE DETECTION

After all it seems obvious that the role of the slow sleep oscillation is quite extensive. Still, even with the ever-growing
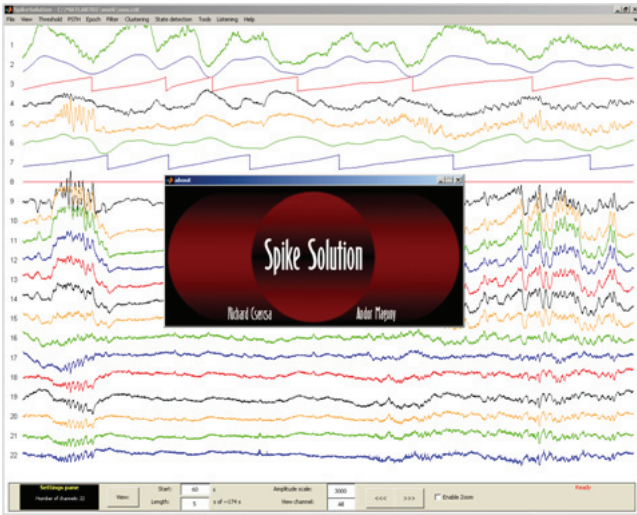
Figure 3. Main screen of SpikeSolution

Figure 4. A: original signal B: filtered signal C: Hilbert transform

capacity and computational power of modern computers the analysis of this phenomenon is immensely difficult necessitating the use of special approaches. To begin with, the detection and differentiation of the two states of slow oscillation is not trivial at all. Primarily, the enormous amount of internal and external noise, and the dynamics of the brain itself are undesired confusing factors. Often, even for the experienced eye it is really hard to observe the phenomenon, not regarding the fact that the majority of the experiments can only be carried out in animals, while human recordings - due to ethical and other issues - are very hard to obtain. Fortunately, I have been lucky enough to be supplied with both animal and human recordings in the Institute for Psychology, Hungarian Academy of Sciences.

The theoretical detection of slow oscillations led us to three approaches which will be discussed in the following sections.

A. Detection with Hilbert transform

Hilbert transform is a mathematical transformation employed to obtain the phase of the original signal. The definition of the Hilbert transform is as follows:

$$\hat{s}(t) = \mathcal{H}\{s\} = (h * s)(t) = \int_{-\infty}^{\infty} s(\tau)h(t-\tau)d\tau = \frac{1}{\pi}\int_{-\infty}^{\infty} \frac{s(\tau)}{t-\tau}\,d\tau.$$

where $h(t) = \frac{1}{\pi t}$.

In biological usage it is recommended to use a filter before the transformation in order to remove the irrelevant components (e.g. frequencies out of the 4-7 Hz range in case of examination of theta activity in the hippocampus). During down-state detection we first filter the signal recorded with the desired electrode in the frequency range of the slow oscillation (0.5 - 3 Hz). Thus we get a sinus-like signal on which we can apply the Hilbert transform that specifies the phase in every sample point. We defined the valley of the sinus signal as the down-state and the peak as the up-state of the slow oscillation.
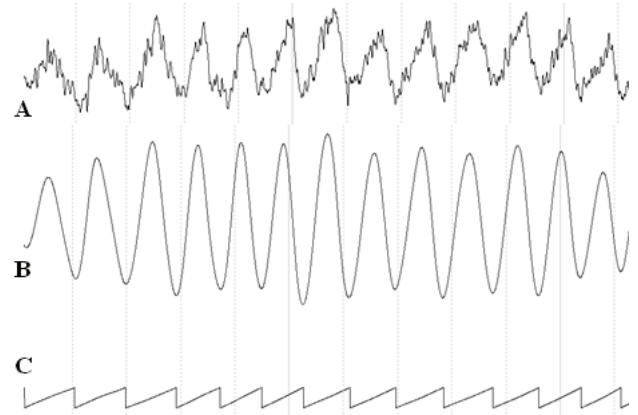
B. Detection with Gamma oscillation

It is known, that we can observe an activity in the gamma frequency range in the course of the active 'up-states'. Thus, if we can filter the selected channel(s) in the range of 20-100 Hz, we have the pure gamma activity of the signal. The steps of the algorithm are:

1) Filtering the signal in the frequency range of 20 - 100 Hz (preferably multiplying the Fast Fourier Transform (FFT) of the signal with one in the region between 20 and 100 Hz and with zero elsewhere, then transforming back to time domain using inverse FFT) in order to emphasize the gamma oscillation that appears in up-states.
2) Calculating the root mean square (RMS) with a 50 ms moving window to determine the power of the gamma oscillation.
3) Displaying the histogram of the sampled values with the extreme values (by a user-specified percentage) cut off, which is ideally expected to be bimodal.
4) Setting a threshold level at the trough between the two heaps of the histogram. It can be determined either automatically or manually, by a user-given value, percentile, or a mouse click.
5) Considering values above the threshold level as up-states and below that as down-states with the criteria that no up-state or down-state can be shorter than 50 ms.
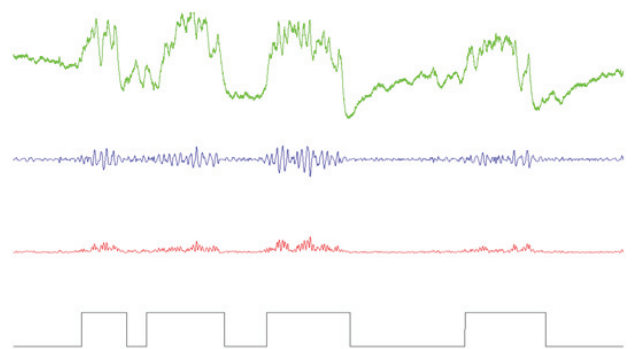

Figure 5. Green: original signal, blue: filtered signal, red: root mean square, black: detected states

C. Detection from MUA

If we still cannot derive appropriate results from the FP, we need to apply the third approach based on multi-unit activity (MUA) analysis, in which case we have a high-frequency-range signal depicting fast action potentials. Given a threshold value, this function determines up- and down-states from MUA recordings during slow wave sleep with certain criteria. Levels above threshold are considered as up-states, while levels below threshold as down-states. The user may specify the minimum duration of up- and down-states. In case the detected states do not last long enough, they are classified as the opposite state.
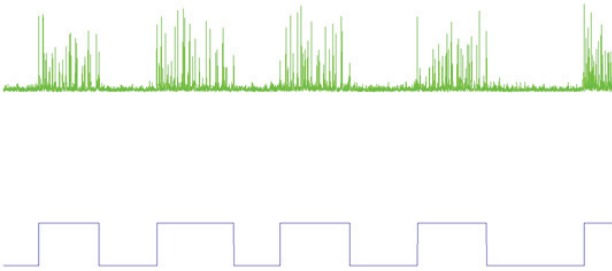
Figure 6.   Green: original signal, blue: detected states

V.   RESULTS AND DISCUSSION

We have employed the three different approaches with different efficacy. Comparing the three state detection methods, we have found the Hilbert transformation as the most robust one. It was the most stable method if compared with human expert state detection outcome. MUA method was sometimes unusable, because of the lack of large action potentials. The gamma band power method was also ambiguous sometimes, if the signal contained contaminations from movement and muscle activity. All in all, we can conclude that the appropriate detection algorithms have been carried out, and it depends only on the piece of data which particular algorithm will fit the needs most. It is worth to apply all the possible detection algorithm and then make a comparison of the results, it is even appropriate as a first level verification.

VI.   FURTHER PLANS

It is worth to note that by using these detection algorithms the transitions between the two states can easily be determined. This is important if we take into consideration, that according to some findings it is these transition points that may produce special conditions and circumstances enabling an epileptic seizure to start. This may be because of the interconnections now said to be found between these transitions and partly hippocampal high frequency oscillations (HFO), as well as sleep spindles. On my roadmap these things are set as milestones and I would really like to examine the possible relations among these phenomena.

REFERENCES

[1] M. S. R. C. Dossi, A. Nunez, "Electrophysiology of a slow (0.5-4 hz) intrinsic oscillation of cat thalamocortical neurones in vivo," *J Physiology*, vol. 447, pp. 215–234, 1992.

[2] I. T. M. S. D. A. Nita, Y. Cisse, "Waking-sleep modulation of paroxysmal activities induced by partial cortical deafferentation," *Cerebral Cortex*, pp. 149–156, 2006.

[3] M. M. I. T. M. Volgushev, S. Chauvette, "Precise long-range synchronization of activity and silence in neocortical neurons during slow-wave sleep," *J Neuroscience*, vol. 26, pp. 5665–5672, 2006.

Heuristic Method for Heartbeat Detection in Fetal Phonocardiographic Signals

Endre Kósa
(Supervisor: Dr. Ferenc Kovács)
kosen@digitus.itk.ppke.hu

Abstract—**This paper presents a heuristics-based, successive approximation method for heartbeat detection in fetal phonocardiographic signals, which takes advantage on some a priori biological knowledge. The algorithm reaches above 90% in terms of accuracy of heart rate identification. It is computationally effective and easily parallelizable. A method for signal qualification is also presented.**

Keywords**: fetal phonocardiography, cardiotocography, fetal heart rate**

I. INTRODUCTION

Different methods of fetal phonocardiography (PCG) have been proposed in the last 20 years. The most important diagnostic information PCG can provide is the fetal heart rate (FHR) function, which can be calculated from the beat to beat time (Tbb, consult Fig. 1.), by the following way:

$$FHR = 60 \cdot \frac{1}{T_{bb}[\text{sec}]} \qquad (1)$$
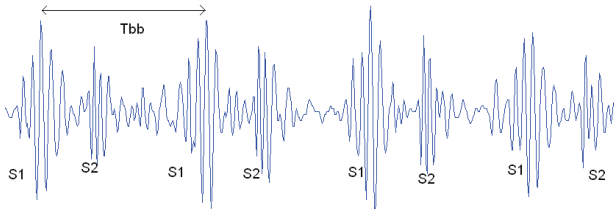
Fig. 1. Good quality fetal PCG signal

It has been shown that standard tools of signal processing may be sufficient for heartbeat detection in standard (adult) phonocardiography [5], [6], [9], but in case of fetal PCG, extreme noise levels might be present. Therefore, standard methods provide results with limited accuracy. Using multiple sensors (properly calibrated microphones) widens the possibilities: different denoising methods might be used ([10]), however in this paper we focus on one acoustic sensor scenario as it was proposed in [2]. The approach we present takes some physiologic features of small variations into consideration: since average fetal FHR value is fixed within a pre-defined range (100-200) the average length of a fetal cardiac cycle, including the length of the systolic and diastolic period can be formulated as well.

In the 2nd section we present this method and construct an algorithm utilizing it. In the 3rd section we compare its efficiency with the current standard method, finally, in section 4 we draw the conclusions.
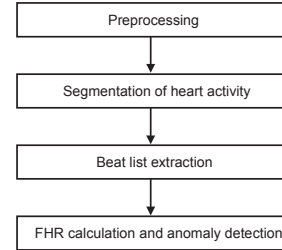

Fig. 2. General scheme of a PCG-processing algorithm

II. METHOD

The main steps of the algorithm can be seen in Fig. 2. First, we remove irrelevant sections (signal level is below a certain limit) and apply optional filters. Then we segment the signal in several iterations, by first distinguishing respiratory from physiologically active sections, than further segmenting active sections to S1 and S2 sections, corresponding to the systolic and diastolic activity of the fetal heart. In the last iteration, we look for further information – mostly anomaly detection – within, and between S1-S2 sounds.

A. Concept of phonocardiogram segmentation

The most general feature of the acoustic signal of a fetal heart is the most obvious: it has higher frequency and intensity than its surrounding. However, due to very high noise levels and different analog or digital filters, the measure and variation of these features widely disperse. Since in one acoustic sensor scenario separation of statistically independent noise is not always possible, and because of disturbances due to fetal movement, standard wavelet tools, including continuous, discrete, or non-linear wavelets, and methods emphasizing signal autocorrelation have their limitations. The presented heuristic approach only relies on the most general features of the signal.

First we take the short term differentials of a signal, sum it up over a short window, and take the difference of the neighboring windows. This enhances the robustness in noisy signal.

$$E[x] = \sum_{i=x}^{x+\alpha} \big(s[i+1]-s[1]\big) - \sum_{j=x-\alpha}^{x} \big(s[j+1]-s[j]\big) \qquad (2)$$

After – the same way as creating the differentials in the Haar-transform – we simply subtract the result from the original signal, however, once again, we take these differences in a window (having bigger size than in (2)), and the output will be the difference of two neighboring windows.

$$D[x] = \sum_{i=x}^{x+A}\big(s[i]-E[i]\big) - \sum_{j=x-A}^{x}\big(s[j]-E[j]\big) \qquad (3)$$

Finally, we take the differences in the same way, and in the last step, cut off the negative parts. As a result, we get small "waves" covering either a full cardiac cycle, or a given S1 or S2 sound, depending on α and A . Refer to Fig. 5.

$$F_1[x] = \begin{cases} \displaystyle\sum_{i=x}^{x+A}\big(D[i+1]-D[i]\big) - \sum_{j=x-A}^{x}\big(D[j+1]-D[j]\big) & if\ >0 \\[4pt] 0 & otherwise \end{cases} \qquad (4)$$

Fig. 3.1. presents the original signal, Fig. 3.2. is the output of (2), Fig. 3.3. is the output of the differences in small window, Fig. 3.4. is the output of differences in large window (3), Fig. 3.5. is the output of the terms in (4), and Fig. 3.6. is the output of (4). Sample length is 2 seconds.
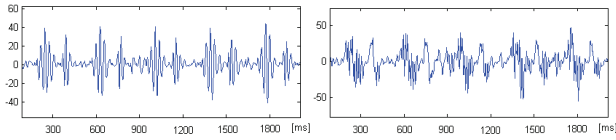
Fig. 3.1.

Fig. 3.2.
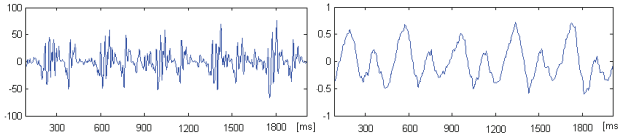
Fig. 3.3.

Fig. 3.4.
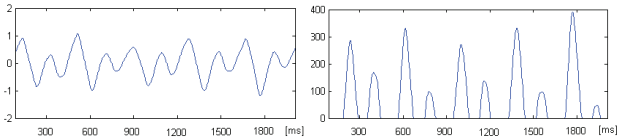
Fig. 3.5.

Fig. 3.6.

B. Weighted frequency generation

Another important need is to build-up a spectrum-like function of the heart activity frequency. Above a certain level of noise, Fourier spectrum may bear only a limited amount of useful information, but having the cardiac cycle candidates, we are able to construct a heuristic frequency function as follows:

$$f[x] = \sum_{i=1}^{L}\sum_{\substack{j=i\\j\neq i}}^{L} \big(|t[i]|+|t[j]|\big)\cdot\frac{\min\big(|t[i]|,|t[j]|\big)}{\max\big(|t[i]|,|t[j]|\big)}\ where\,|i-j|=x \qquad (5)$$

The output of (5) is a function, where at each point we get a weighted occurrence frequency of the given distance between two peaks. The weighing is based upon the assumption that peaks of similar magnitude contain more relevant information about the dominant distance (~frequency) of a given sample. This function takes its input from (4), therefore the peaks are either the S1-S2 sounds, or cardiac cycles as a whole, see Fig. 5.

$$d[x] = F_1[x+1] - F_1[x] \qquad (6)$$

$$t[x] = \begin{cases} F_1[x] & where\ d[x]\le 0,\ d[x]>0 \\[4pt] 0 & otherwise \end{cases}$$

The output of this function contains relevant information about the quality of the signal (autocorrelation factor of the first harmonics), as well as nominal Tbb and nominal distances of S1 and S2 sounds (first three significant peaks), see Fig. 4.
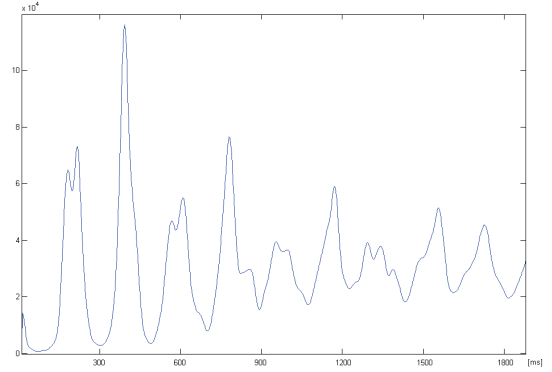

Fig. 4. Example of a spectrum

C. Successive approximation of heartbeats

The methods presented in A. and B. will be used for the successive approximation of the beats. As it can be seen, we have 2 free parameters, which we will adjust in different iterations, and which are related to physiological parameters. Refer to Fig. 5. In 1st step we calculate the output over 360 ms (average length of a fetal cardiac cycle), and by using small window size of 40 ms. This means filtering out the respiratory sections, so we get the location of each cardiac cycle, therefore we are able to calculate FHR curve.

We take this as an input for the first frequency calculation. Refer to Fig. 4. As it can be seen, the most significant peak is the nominal FHR of the given sample. If this function meets a certain quality criterion, we continue to iterate with smaller time windows. Now we use window sizes of 180 ms and 20 ms, which will reveal the positions of S1 and S2 sounds, see Fig. 5.
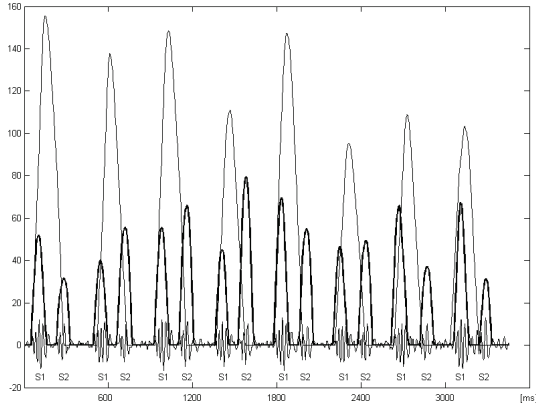
Fig. 5. Output of the first two iterations

The 2nd frequency function will give us information on nominal FHR, nominal S1-S2, and nominal S2-S1 distances, represented by the 3rd, 2nd, 1st significant peaks respectively. If this once again meets certain conditions, further iteration might reveal information corresponding to morphologic anomalies, which will be covered in E.

D. S1-S2 distinction strategies

Once we have the 2nd iteration, in theory, we have selected all S1 and S2 sounds, but we still have to decide for every filtered signal section, whether it is an S1, an S2, extrasystole, or noise. This is based on three approaches: on the rhythmicity of fetal heart activity (1), information content of the given short term signal (2), and finally, the correlation factor with previous beats (3). Regarding (1), it depends on the noise and the physiologic character of the given fetus, if this information is descriptive or not. The 2nd iteration of frequency generation will let us know, if the distance between the 2nd and 3rd significant peaks meets a minimum distance criterion or not. If so, we will rely upon this information, otherwise not. It is also possible to distinguish by the "weight center" of each short term signals. The first iteration reveals the cardiac cycle as a whole, while the second filters out the particular S1 and S2 sounds, therefore, normally S1 can be found on the left of cardiac cycle's centre point, and S2 to the right. Due to noise and physiologic factors, one of the heart sounds may be much more intensive than the other, in this case, this does not hold. Regarding (2), the information content of a short term signal is tightly coupled to the output of Eq. 4., however, this is not a common sense transform method, therefore the mapping from signal to this curve is not unambiguous. Still, if we have two significant groups as a result, we will use the assumption that this holds, otherwise not. (3) might be used on both the raw signal, or on the output of (4).

It is important to note, that most of the algorithms generate the list of beats as a requisition of FHR calculation. In our case, however, FHR estimation is possible from the 1st iteration, therefore the generation of S1 and S2 lists will provide additional information, but is not a necessity.

E. Anomaly detection

The three important anomalies, which can be revealed by using PCG are a variety of splits [7-8] and murmures [1],

and extrasystole [1]. The 2nd iteration of the algorithm may reveal extrasystoles, but for proper murmur and split detection, we introduce the 3rd iteration, further enhancing the resolution by using time window of 50-80ms. Unfortunately, a significant part of the samples doesn't have high enough quality to perform this step. On the other hand, in some cases FHR variability alone provides enough information about fetal well being [3].

Introducing the above methods, we review the algorithm in Fig. 6.
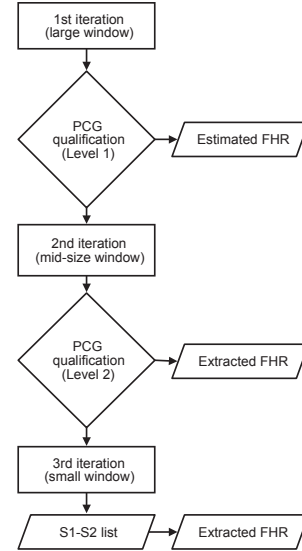

Fig. 6. Scheme of the algorithm

This algorithm was created primarily for offline processing. The only reason we need real time FHR values is to provide user feedback on the fetal PCG monitoring instrument, therefore methods with limited reliability might be sufficient. However, an online version of this algorithm can be constructed by pre-defining the latency limit of the display, and calculating momentary FHR from the given amount of previous time interval. Given amount means that we must make the compromise in between good temporal resolution (shorter time window) and high robustness (longer), which might depend on recording quality of the given instrument, as well as on the age of the fetus.

III. RESULTS

For comparison, we had two scenarios: first, we examined a group of five reference records. These samples were taken simultaneously with clinical standard ultrasound cardiotocography and a PCG device. The autocorrelation method was calculated the same way as it was presented in [2]. Second, we randomly selected small fragments of varying quality signals, and selected all the cardiac cycles manually.

Other signal processing methods for the same problem can be found in the literature, like linear continuous wavelet transform [1], matching pursuit method [4] and autocorrelation-based method [2], but the latter provided the best results, therefore it is, what we compare our results with.

A. Comparison with reference records

TABLE I

COMPARISON WITH REFERENCE RECORDS

SAMPLE	AVERAGE ABSOLUTE ERROR AND STANDARD DEVIATION (AUTOCORRELATION METHOD)		AVERAGE ABSOLUTE ERROR AND STANDARD DEVIATION (PRESENTED METHOD)	
#1.	95.45	54.31	24.30	38.40
#2.	29.13	41.30	14.11	21.62
#3.	25.61	46.03	12.93	24.21
#4.	81.38	54.91	12.38	22.59
#5.	26.43	44.92	13.05	21.61

In Table I. we summarize our results. The numeric results show significant difference. However, it is important to note, that in some cases the autocorrelation method fails to reveal any cardiac information. On the other hand, in some cases, autocorrelation method and the presented method provide FHR information, while the reference record does not.

Fig. 7. presents an example of about 1.5 minutes, where the autocorrelation method fails to provide any useful information (FHR vs. time). The first function represents the reference record, in the middle the output of autocorrelation method can be seen, and the third is the output of the presented method. It is important to note, that the dual measurement scenario reduces the quality of the PCG recording, hence the accuracy of both the algorithms is below the usual.
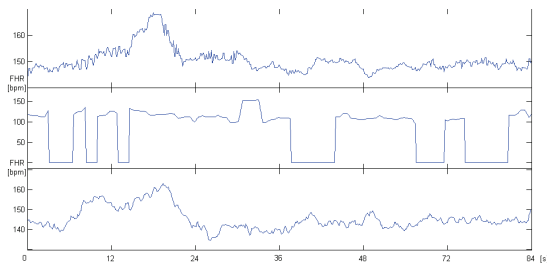

Fig. 7. Example of the failure of autocorrelation method

B. Beat decetcion

In this section we discuss the comparison results with samples of manually selected cardiac cycles. Refer to Table II for numeric results. As can be seen, the presented method has significant advantage over autocorrelation. For a particular example, see Fig. 8, where the gray function is the reference, the solid black is the result of autocorrelation method and the boxed is the result of the presented method.

IV. CONCLUSION

In this paper we presented a method to enhance beat detection accuracy in low quality fetal PCG signals. Since most diagnostic information about a fetus is based on her heart rate variability, it is crucial to have a method with sufficient reliability revealing FHR rates even in the noisiest conditions.

TABLE II

COMPARISON WITH AUTOCORRELATION METHOD

NO.	NO. OF BEATS	MATCH	RATIO CORRECT	AUTO-CORR MATCH	AUTO-CORR RATIO
#1	144	135	93,75%	118	81,94%
#2	127	119	93,70%	101	79,53%
#3	138	114	82,61%	90	65,22%
#4	147	132	89,80%	134	91,16%
#5	153	130	84,97%	128	83,66%
#6	136	131	96,32%	129	94,85%
#7	146	141	96,58%	138	94,52%
#8	150	147	98,00%	113	75,33%

REFERENCES

[1] F. Kovács, M. Török, I. Hábermajer, "An Improved Phonocardiographic Method for Long-Term Fetal Heart Rate Monitoring", *IEEE Trans. Biomet. Eng.* Vol.47, No.1, pp. 225-230, Jan. 2000

[2] F. Kovács, Cs. Horváth, M. Török, G. Hosszú: "Long-Term Phonocardiographic Fetal Home Monitoring for Telemedicine Systems", *Proc. 27th. Ann. Intern. Conf. IEEE Eng. Med. Biol. Soc., EMBC '05,* Shanghai, 1-4. Sept. 2005, p.313.

[3] M. Signorini et al., "Linear and nonlinear parameters for the analysis of fetal heat rate from cardiotocographic recordings", *IEEE Trans. Biomed. Eng.* Vol. 50., No.3, pp. 365-374, March 2003.

[4] Cs. Horváth, B. Üveges, F. Kovács, Ph.D., G. Hosszú, Ph.D. Application of the Matching Pursuit method in Fetal Phonocardiographic Telemedicine System, EMDC 07 Int. Biomed. Eng. Conf. Lyon, pp. 222-226.

[5] M.S. Obaidat, Phonocardiogram signal analysis: techniques and performance comparison, J. Med. Eng. Technol. 17 (6) (1993) 221–227.

[6] W.J. Williams, in: M. Akay (Ed.), Time–frequency and Wavelets in Biomedical Signal Processing, IEEE Press Series in BME, 1997, pp. 3–8.

[7] A. Harris, G. Sutton, M. Towers, Physiological and Clinical Aspects of Cardiac Auscultation, Medicine Ltd., London, UK, 1976.

[8] J.A. Shaver, R. Salerni, P.S. Reddy, Normal and abnormal heart sound in cardiac diagnosis, Part I: systolic sounds, Curr. Probl. Cardiol. 10 (3) (1995).

[9] S.M. Debbal, F. Bereksi-Reguig, Analysis of the second heart sound using continuous wavelet transform, J. Med. Eng. Technol. 28 (4) (2004)151–156.

[10] A.K. Mitra et al. System simulation and comparative analysis of foetal heart sound de-noising techniques for advanced phonocardiography, *Int. J. Biomedical Engineering and Technology, Vol. 1, No. 1, 2007, p.73.*

Hyperalgesia and Allodynia Model in Healthy Volunteers as well as an fMRI Biomarker for Reliable Measurement of Pain Intensity

István Kóbor
(Supervisor: Dr. Zoltán Vidnyánszky)
ikobor@gmail.com

Abstract— **The primary goal of this project is to develop a hyperalgesia and allodynia model in healthy volunteers as well as to elaborate an fMRI biomarker for reliable measurement of pain intensity. In order to achieve this, we developed experimental set-ups for mechanical noxious stimulation, subjective pain rating protocols and fMRI protocols for measuring pain-related brain activations. Three psychophysics methods were developed and compared to measure hyperalgesia induced by capsaicin treatment. The central sensitization method results in hyperalgesia, that can be demonstrated with both the scaling and the categorization tests. The sensitization index demonstrates that significant hyperalgesia arises primarily with stimulation of large intensity. Surprisingly when we measured in separate sessions with the peripheral sensitization method, hyperalgesia was not observed. However, in the case when we measured simultaneously the peripheral sensitization effect we found robust hyperalgesia. The sensitization index demonstrates that significant hyperalgesia arises primarily from stimulation of large intensity.**

Index Terms—**hyperalgesia, allodynia, psychophysics, functional magnetic resonance imaging**

I. INTRODUCTION

Pain is a highly subjective, multifactorial and complex experience: *''an unpleasant sensory and emotional experience associated with actual or potential tissue damage, or described in terms of such damage.'' (Merksey and Bogduk, 1994).* The perception of pain is a rather complex neuronal process. Many parts of the brain are active during pain perception (anterior cingulate cortex, insular cortex, somatosensory cortex, amygdala, thalamus etc.). While the management and treatment of acute pain is reasonably good, the needs of chronic pain sufferers are largely unmet, creating an enormous emotional and financial burden to sufferers, carers, and society. Relatively few investigations focused on the neural correlates of

I. Kóbor is with the MR Research Center – Szentágothai Knowledge Center – Semmelweis University, Budapest, H-1083, Hungary (email: ikobor@gmail.com)

Z. Vidnyánszky is with Neurobionics Research Group, Hungarian Academy of Sciences –Pázmány Péter Catholic University – Semmelweis University, Budapest, H-1094, Hungary (email: vidnyanszky@digitus.itk.ppke.hu).

neuropathic pain. The findings concerning the balance between peripheral versus central influences are contraversial. Our goal in this project is to develop a hyperalgesia and allodynia model in healthy volunteers as well as an fMRI biomarker for reliable measurement of pain intensity. In order to achieve this, we developed experimental set-ups for mechanical noxious stimulation, elaborated subjective pain rating protocols, designed fMRI protocols for measuring pain-related brain activations, and determined the balance between peripheral versus central influences with the help of attentional modulation.

II. STIMULI AND METHODS

24 healthy subjects participated in this experiment. In the psychophysics experiments, we used manual TOUCH TEST^{TM} von-Frey sensory filaments (forces: 8g, 10g, 15g, 26g, 60g, 100g, 180g, 300g). For the MR experiments, we developed a PC-MR-compatible mechanical stimulus presentation equipment (forces: min. 100mN to max. 1,1 N), (Fig. 1). In order to create hyperalgesia in healthy people, we used heat /capsaicin sensitization model (Petersen and Rowbotham, 1999), heated a square area 9 cm2 (3*3) on the left or right legs (musculus gastrocnemius caput). Then topically applied capsaicin (0,075%) cream (Zostrix, Rodlen Laboratories, Inc., Vernon Hills, IL) on the medial side of the leg on a particular area.


Fig.1. MR-compatible mechanical stimulus presentation equipment

We measured subjective pain perception in two ways. In one case with scaling method, where subjects answered with the movement of a pc-mouse which tuned a scroll bar between the two end points (not painful - very painful) of subjective pain intensity. In the other case, we used the categorization method, where subjects answered with the

aid of left (not painful) and right (painful) pc-mouse button. Naturally, the stimulations were randomized. We used Matlab 7.1. (MathWorks, Inc., Sherborn, MA) for both the stimulus presentation and the statistical analyses. We calculated grand average, standard error and sensitization index (R capsaicin treatment - R control)/(R capsaicin treatment + R control). In the capsaicin model, two kinds of sensitization exists (Fig. 2). The peripheral sensitization refers to sensitization at the peripheral level (i.e. peripheral nervous system) while central sensitization refers to sensitization at the central level, (i.e. spine, back horn and supraspinal levels). In the case of the peripheral sensitization, we stimulated the skin area treated with capsaicin A, while, in the case central sensitization, we stimulated the skin area right outside the treated area B.
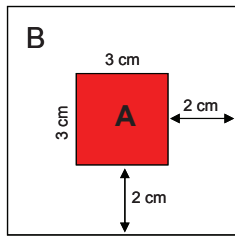
Condition s	Treatment	Area of treatment	Area of stimulations	Type of sensitisation
1	hyperalgesia	A	A	**Peripheral sensitization**
2	control	-	A	control
3	hyperalgesia	A	B	**Central sensitization**
4	control	-	B	control

Fig.2. Peripheral and central sensitization

III. RESULTS

In the first experiment we measured in separate sessions the peripheral sensitization on the right leg (Fig. 3 A,B). Stimulation of the treated area did not result in a stronger perception of pain as compared to the stimulation of untreated area (control condition). In the central sensitization model (Fig. 4 A,B) stimulation right outside the treated area resulted in a significantly stronger perception of pain (hyperalgesia) as compared to the stimulation of the same surface without treatment (control condition). The effect of central sensitization was bigger in the scaling task rather than in categorization task. In the third psychophysics experiment we measured simultaneously the peripheral sensitization on the left and right legs (Fig. 5 A,B). Simultaneous stimulation of the treated area on one leg and the same area on the other untreated leg resulted in a significantly stronger perception of pain (hyperalgesia) as compared to the control condition.
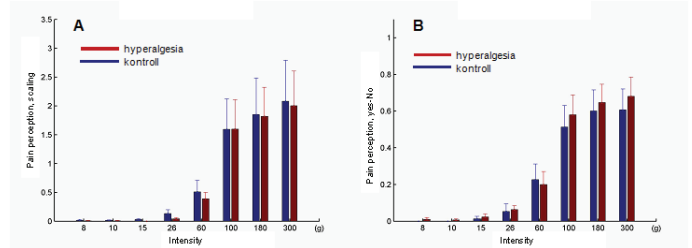

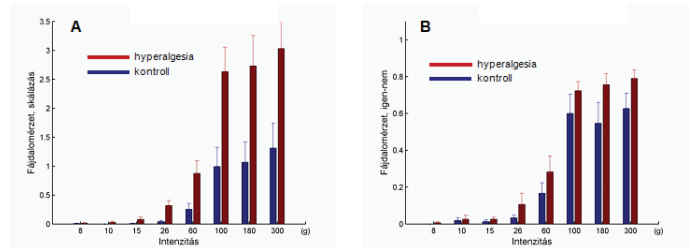Fig.3 A,B Peripheral sensitization on the right leg

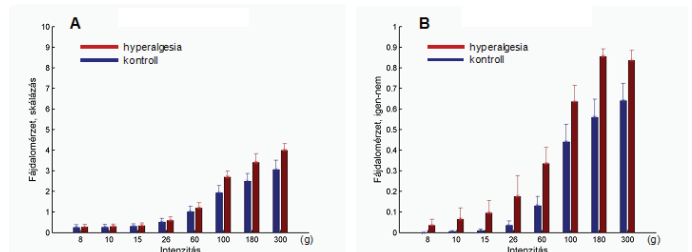Fig.4 A,B Central sensitization on the right leg

Fig.5 A,B Peripheral sensitization on the both legs

Our findings were significant with stimulation of large intensity in both tasks (scaling and categorization) in the case of central sensitization method on the right leg (Fig. 6 A,B) and also in case of the peripheral sensitization method when simultaneously stimulating both legs (Fig. 7 A,B).
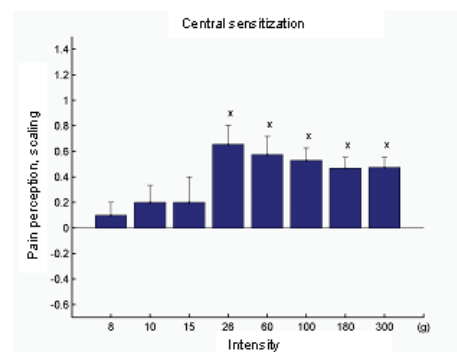

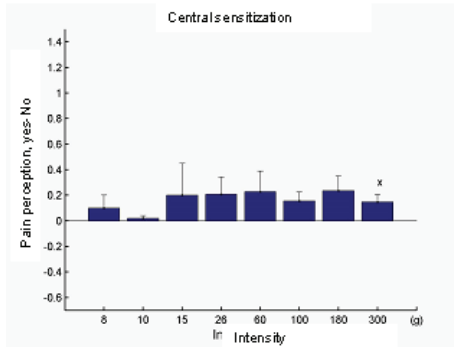Fig.6 A Central sensitization - sensitization index, scaling method

Fig.6 B Central sensitization - sensitization index, pain-categorization method
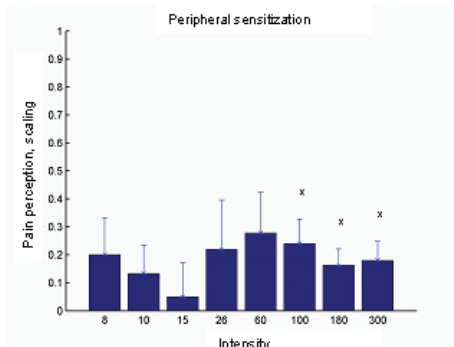

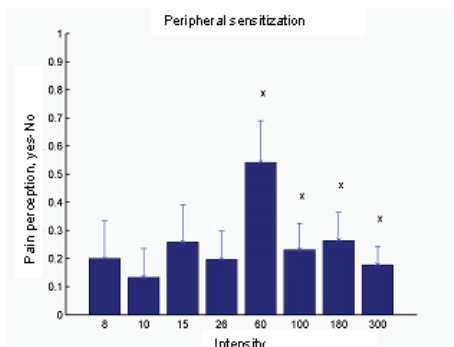Fig.7 A Peripheral sensitization - sensitization index, scaling method

Fig.7 B Peripheral sensitization - sensitization index, pain-categorization method

IV. CONCLUSION

Three psychophysics methods were developed and compared to measure hyperalgesia induced by capsaicin treatment. The central sensitization method results in hyperalgesia that can be demonstrated with both the scaling and the categorization tests. The sensitization index demonstrates that significant hyperalgesia arises primarily with stimulation of large intensity. Surprisingly when we measured in separate sessions with the peripheral sensitization method, hyperalgesia was not observed. However in the case when we measured simultaneously the peripheral sensitization effect we found robust hyperalgesia. The sensitization index demonstrates that significant hyperalgesia arises primarily from stimulation of large intensity.

REFERENCES

[1] I.Tracey, "Nociceptive processing in the human brain," *Curr. Opin Neurobiol*, vol. 15, pp. 478-487, 2005.
[2] R. Rolke et. al., "Quantitative sensory testing in the German Research Network on Neuropathic pain (DFNS): standardized protocol and reference values," *Pain,* vol. 123, pp. 231-43, 2006.
[3] K. Wiech, et al., "Modulation of pain processing in hyperalgesia by cognitive demand," *Neuroimage*, vol. 27, pp. 59-69, 2005.
[4] L. Zambreanu et al., "A role for the brainstem in central sensitization in humans. Evidence from functional magnetic resonance imaging." *Pain.*, vol. 114, pp. 397–407, 2005.
[5] K.L Petersen at al., "Effect of remifentanil on pain and secondary hyperalgesia associated with the heat-capsaicin sensitization model in healthy volunteers. ," *Anesthesiology.*, vol. 94, pp. 15-20, 2001.

Analysis of the Aggregation of the Trp-cage Miniprotein Using a Simplified Protein Model

Gergely Gyimesi
(Supervisors: Dr. András Szilágyi and Dr. Péter Závodszky)
ggyimesi@enzim.hu

Abstract—**Discrete (or discontinuous) molecular dynamics (DMD) is an old but significantly underutilized method to simulate macromolecular systems. DMD uses a step potential with discrete energy values. Combining this method with coarse-grained protein models yields a speedup of several orders of magnitude relative to conventional molecular dynamics. A coarse-grained protein model and force field is implemented based on literature and corrected. The folding transition of the Trp-cage miniprotein is reproduced in a replica exchange molecular dynamics (REMD) simulation framework. The dimerization of the Trp-cage protein is studied using REMD and a stable, symmetric homodimer structure is identified.**

Index Terms—**discrete, molecular dynamics, Trp-cage, protein, dimer**

I. INTRODUCTION

The traditional approach to computational biophysics studies of molecular systems is brute force molecular dynamics simulations of these systems under conditions of interest. With such an approach, the protein models – geometries and interaction parameters – that underlie computer simulations are developed separately from studies of the actual biophysical systems. The aim of these "high-resolution" models is to include as much detail as is known about the physical geometry and interactions in real proteins, to develop an "ideal" protein model that can be applied to any biophysical system. The advantages of this approach are its rigor and cross-system transferability; the disadvantages are that the time- and length scales that are accessible to computer simulations do not, in many cases, reach biologically relevant scales. Traditional molecular dynamics simulations have been widely used in studying protein dynamics, however, an intrinsic limitation of these methods lies in their inability to span time scales from femtoseconds (10^{-15} s) to seconds. Sampling time scales in the μs to s range is often necessary to arrive at reliable conclusions about the dynamics of proteins and protein complexes.

An alternative approach is hypothesis-driven and based on tailoring simplified protein models to the systems of

interest. The aim of these intuitive models is to capture the most important details and driving forces that govern the dynamics of the studied system. Although such models are usually not transferable across different systems and rely on experimental verification, they often provide a good balance between complexity and computational cost. Using such simplified protein models with rapid simulation methodology allows us to study the dynamics of complex protein systems on biologically relevant length and time scales [1].

II. DISCRETE MOLECULAR DYNAMICS

Discrete molecular dynamics (DMD) incorporates a radically different philosophy of molecular dynamics simulations than has been used previously in the field of molecular modeling. Traditional methods employ continuous potentials such as the Lennard-Jones potential and an iterative numerical solution of the Newtonian equations of motion. In contrast, DMD methods define discrete interaction potentials between atom pairs. The use of such step-potentials decomposes the trajectory of the simulated system to instantaneous collision events separated by ballistic runs where no forces are exerted on the individual atoms. This model can be simulated in an event-driven framework, where the time of the next collision event is calculated, and the system is advanced to that collision by the exact solution of ballistic equations. Such simplifications make DMD simulations sufficiently rapid to access the dynamics of large molecular complexes on a biologically relevant time scale [2].

III. TRP-CAGE

The Trp-cage miniprotein is the smallest known independently folding protein fragment, consisting of only 20 amino acids. It exhibits cooperative folding with a melting point of 3 °C and a folding time of approx. 4 μs, which makes it one of the fastest folding proteins known [3]. A point mutant variant of the Trp-cage has been shown to form amyloid-like fibrils when exposed to heat treatment (J. Kardos, personal communication). These structures show high β-sheet content but their exact atomic structure and mechanism of formation remains unknown. In order to study the molecular mechanism of association and propose an atomic-level structure of the fibrils we applied the methodology of discrete molecular dynamics together with a suitable coarse-grained model adopted from literature.

IV. Coarse-grained Model

The coarse-grained protein model we chose to implement was specifically designed to describe the folding of the Trp-cage miniprotein [4]. There are 4 united atoms—N, C, O, C_α—mimicking the protein backbone. Most protein side-chains are represented by C_β and C_γ beads; for β-branched amino acids (Thr, Ile, Leu) a second γ-bead ($C_{\gamma 2}$) is introduced. For bulky amino acids (Arg, Lys, Trp), an additional C_δ bead is included (Fig. 2).

A. Bonded interactions

To represent bonded interactions between atoms, the model uses distance constraints. Here, distance constraints are infinitely high square-well potentials centered around an ideal value, allowing a ±2% fluctuation in the distance between two atoms. Such constraints are introduced between 1-2 atom pairs (covalent bonds), 1-3 pairs (bond angles) and the 1-4 atoms of the ω peptide dihedral angle (Fig. 2).

B. Non-bonded interactions

Non-bonded interactions in the peptide backbone (atoms N, C, O, C_α and C_β) are treated as hard-core repulsions when the atoms come closer than the sum of their atomic radii. To account for weaker excluded-volume effects acting between local (e.g. 1-4) atom pairs, we assigned smaller atomic radii for these pairs.

Side-chain interactions include the hydrophobic interaction, aromatic interaction between aromatic amino acids, aromatic-proline interaction between aromatic and proline side-chains, and salt-bridge interaction between oppositely charged side-chains.

Here, hydrophobic, salt-bridge, and aromatic interactions act solely between β-, γ-, and δ-beads of different side-chains. To assign various types of interactions to all pairs of beads, all side-chain beads are categorized into the following six types: hydrophobic (H), amphipathic (A), aromatic (AR), neutral polar (P), positively charged (PC), and negatively charged (NC). A bead can belong to more than one category, for example, the γ-bead of phenylalanine is both hydrophobic and aromatic.

Only pairwise interactions between side-chain beads are considered in this model, and the potential functions are stepwise:

$$E_{ij} = \begin{cases} +\infty, & d < HC_i + HC_j \\ -2\varepsilon_{ij}/3, & HC_i + HC_j \leq d < IR_i + IR_j \\ -\varepsilon_{ij}/3, & IR_i + IR_j \leq d < IR_i + IR_j + IR_{ext} \\ 0, & IR_i + IR_j + IR_{ext} \leq d \end{cases} \quad (1)$$

where i and j indicate different side-chain beads, HC is the hardcore radius of each bead, and IR is the radius of interaction range for each bead. The parameter IR_{ext} is introduced to allow a small attraction before the two beads come to their interaction ranges. In our study, we set IR_{ext} to 0.75 Å.

Hydrophobic interactions are assigned between two hydrophobic beads and between a hydrophobic and an amphipathic bead if both beads are not aromatic and not proline. The interaction strengths are ε_{HH} and ε_{HA}, respectively. Aromatic interactions are assigned between

two aromatic beads—namely C_γ of Phe and Tyr and C_δ of Trp—with a strength of ε_{AR}. The aromatic-proline interaction is assigned between the γ bead of proline and the aromatic bead; the interaction strength is $\varepsilon_{AR\text{-}PRO}$. Salt-bridge interactions are assigned between positively charged and negatively charged beads; the salt-bridge strength is ε_{SB}. Two beads of the same charge experience hard-core repulsion.

C. Hydrogen bonds

Hydrogen bond interactions are introduced between the backbone beads and between the backbone and polar side-chain beads. The hydrogen bond interaction is between the backbone nitrogen N_i as donor, and the carbonyl oxygen O_j as acceptor. To mimic the angular dependence of the backbone hydrogen bond, maximum and minimum distances are defined for the auxiliary pairs N_i–C_j, $C_{\alpha i}$–O_j, C_{i-1}–O_j, and for the hydrogen bonding pair N_i–O_j (Fig. 2). When any one of the four pairs comes to their corresponding maximum or minimum distances, we verify that the distances of the other three pairs are within their ranges. If so, a hydrogen bond is formed and the potential energy is decreased by ε_{HB}^{MM}. Once the bond is formed, its atoms cannot form any other hydrogen bonds unless the existing hydrogen bond breaks. The mechanism for the dissociation of the hydrogen bond is similar. Once any one of the four pairs comes to their maximum or minimum distance and the kinetic energy is enough to overcome the loss of the potential energy ε_{HB}^{MM}, the hydrogen bond breaks. Hydrogen bonds between the backbone and certain side-chains are also defined, with the γ beads of Asn, Asp, Gln, Glu, Ser, and Thr acting as acceptors and Ser, Thr, Asn, and Gln as donors. In the case of sidechain-mainchain hydrogen bonds, the bond energy is ε_{HB}^{SM} and distance criteria are introduced between neighboring atoms similar to backbone hydrogen bonds.

V. Geometric Parameters

One of the serious problems we faced during the implementation of the protein model is that many of the parameters were missing from the original paper or erroneously defined. These include the hard-core radii of certain atoms, distance constraints defining the geometry, and the treatment of 1-4 pairs in the backbone. We introduced the concept of local (1-4) and non-local hard-core interactions as described earlier and used the same radii for the C_α and carbonyl C atoms, leading to eight different hard-core parameters to be determined. These parameters were set in such a way that sterically allowed conformations in Ramachandran space match the experimentally determined allowed regions. This was performed by running short simulations on an (Ala)$_3$ test system and adjusting the parameters on a trial-and-error basis. The hard-core parameters were fine-tuned by running longer simulations on polyalanine peptides and observing α-helix formation during the course of the simulation. The parameters were further adjusted to facilitate α-helix formation in the model protein.

The remaining geometrical parameters (e.g. distance

constraints defining the geometry) were recalculated using experimentally determined structures from the Protein Data Bank (PDB). For a given united atom pair, all distances in structures having a resolution higher than 1.5 Å were calculated and the median of values was taken as the ideal distance.

VI. Folding Simulations

In order to perform successful folding simulations, the energetic parameters of the original published model also needed adjustment. This was done using a trial-and-error method by running longer folding and unfolding simulations at various temperatures and adjusting the parameters based on feedback from the simulations. The resulting parameter set was $\varepsilon_{HH} = 3.15\varepsilon$, $\varepsilon_{HA} = 1.80\varepsilon$, $\varepsilon_{AR} = 5.40\varepsilon$, $\varepsilon_{AR-PRO} = 4.50\varepsilon$, $\varepsilon_{SB} = 8.10\varepsilon$, $\varepsilon_{HB}^{MM} = 5.5\varepsilon$, $\varepsilon_{HB}^{SM} = 2.5\varepsilon$, with the energy unit $\varepsilon = 1\,kcal/mol$.

Using the adjusted parameter set, we were able to perform folding simulations on the Trp-cage system where the protein consistently reaches a stable state within 2 Å C_α-RMSD of the native conformation.

VII. Replica Exchange Method

One of the main advantages of coarse-grained DMD simulations is their ability to sample conformational space effectively. To further enhance sampling and get an overall view of the free energy surface of the Trp-cage system, we applied a method known as *replica exchange molecular dynamics* (REMD) [5], also known as *parallel tempering*. In the REMD method, multiple non-interacting copies (*replicas*) of the system are simulated in the canonical ensemble at different temperatures T_m. These replicas are arranged so that there is always exactly one replica at each temperature, and there is a one-to-one correspondence between temperatures and replicas. From time to time two replicas are exchanged by exchanging the coordinates and momenta of their atoms. This process is essentially equivalent to exchanging the two temperatures of the corresponding replicas. In order for this exchange process to converge towards an equilibrium distribution, it is sufficient to impose the detailed balance condition on the transition probabilities $w(i \rightarrow j)$, which leads to

$$\frac{w(i \rightarrow j)}{w(j \rightarrow i)} = e^{-(\beta_j - \beta_i)(E_i - E_j)} = e^{-\Delta}, \qquad (2)$$

where E_i is the potential energy of system i [5].

This can be easily satisfied by using a Metropolis criterion

$$w(i \rightarrow j) = \begin{cases} 1, & \Delta \leq 0 \\ e^{-\Delta}, & \Delta > 0 \end{cases}. \qquad (3)$$

The replica exchange method is effective because the high temperature replicas sample a wide range of configurations, and sufficiently low energy structures are transferred to lower temperature simulations for refinement. This avoids getting trapped in local minima and facilitates the thorough sampling of the free energy surface of the system.

In our simulations we used eight replicas at temperatures 700, 585, 489, 409, 342, 286, 239, and 200 K [5]. The exchange of replicas was attempted every 10 ps and only pairs corresponding to neighboring temperatures were exchanged.

VIII. Trp-cage

The replica exchange method was applied to get an overall view of the low-energy conformations of the Trp-cage system using our coarse-grained protein model. A simulation of 500 ns with eight replicas was carried out using the protocol described above.

The acceptance ratio of replica exchanges is shown on Table I. We can see that the acceptance ratios were large enough (> 10%) but are not quite uniform and tend to get larger towards lower and higher temperatures.

TABLE I
ACCEPTANCE RATIOS IN SINGLE-CHAIN SIMULATIONS

Transition	Ratio
200 ↔ 239 K	0.2558
239 ↔ 286 K	0.2075
286 ↔ 342 K	0.1756
342 ↔ 409 K	0.1532
409 ↔ 489 K	0.1098
489 ↔ 585 K	0.2617
585 ↔ 700 K	0.4520

In order to verify the adequate sampling of energy levels, we calculated a histogram of energy values (Fig. 1.). The distributions show a Gaussian-like shape with substantial overlap between neighboring temperatures, indicating that a sufficient number of replica exchanges have taken place. The overlap is higher towards lower and higher temperatures, suggesting an absolute minimum and maximum energy for the system as discretization generates discrete and finite energy levels with a well-defined minimum and maximum.
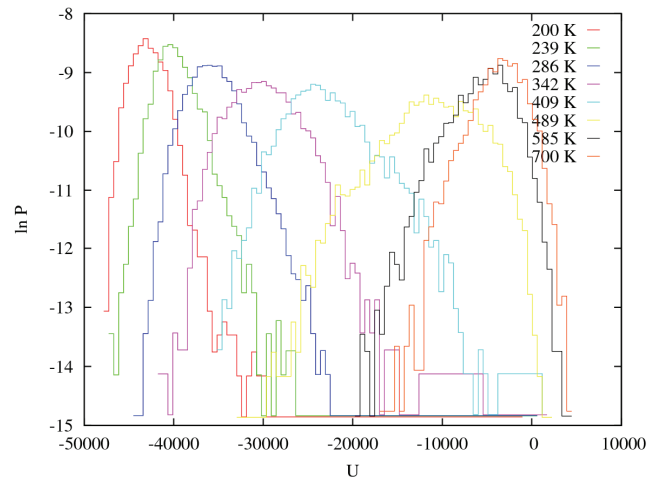

Fig. 1. Log-histogram of energy states of different replicas in the single-chain REMD simulation.

A plot of C_α-RMSD from the native structure vs. potential energy of structures taken from the trajectories of replicas (Fig. 2.) shows the funnel-like shape of the energy function. Replicas at high temperatures sample a wide range of configurations, and with the decrease of temperature the sampling converges towards the native state of the protein. The figure also indicates that the tip of the energy funnel is

not too sharp as there are many non-native structures with energies comparable to the native state.
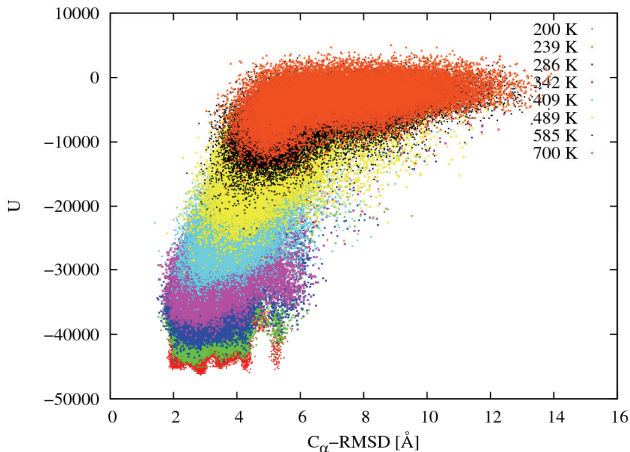

Fig. 2. Potential energies and RMSD from the native state of structures visited by replicas in the single-chain REMD simulation. The figure shows multiple non-native energy minima of similar values.

IX. TRP-CAGE DIMER FORMATION

To study the oligomerization properties of the Trp-cage protein, we performed REMD simulation containing two identical protein chains in a single simulation box. The parameters of the simulation were the same as in the previous section. A maximum distance constraint of 50 Å was imposed on the Gly10 C_α atoms in the two chains to avoid large separations.

The acceptance ratios in the double-chain simulation were significantly lower than those in the single-chain simulation (Table II). This could indicate that temperature spacing is too large, it has been shown that doubling the system size or number of particles N doubles the average energy spacing between adjacent temperatures, but only increases the energy fluctuations at a given temperature by $N^{1/2}$.

TABLE II
ACCEPTANCE RATIOS IN DOUBLE-CHAIN SIMULATIONS

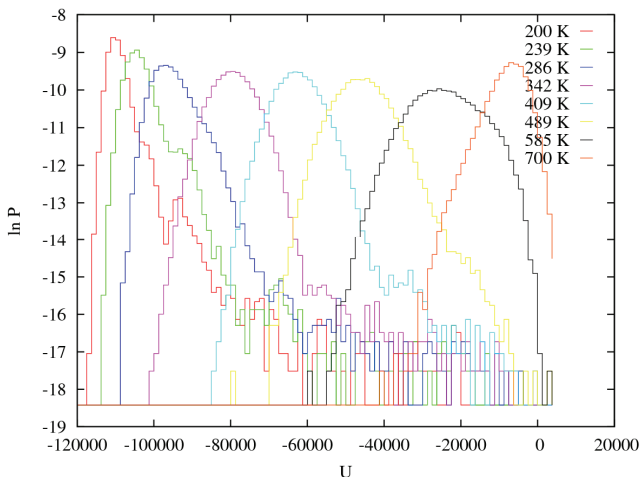| Transition	Ratio
200 ↔ 239 K	0.0936
239 ↔ 286 K	0.0750
286 ↔ 342 K	0.0145
342 ↔ 409 K	0.0265
409 ↔ 489 K	0.0462
489 ↔ 585 K	0.0393
585 ↔ 700 K	0.0993

Fig. 3. Log-histogram of energy states of different replicas in the double-chain REMD simulation.

The histogram of energy states (Fig. 3.) shows Gaussian distribution in middle temperatures that distorts towards extreme temperatures. This might be due to the finite energy levels present in the system, as discussed in the previous section.

To extract the most stable structures we randomly selected 500 structures from the trajectory of each replica and clustered them using the SPICKER algorithm [6]. The cluster analysis showed a single most populated cluster in which the two chains form a remarkably symmetric dimer.
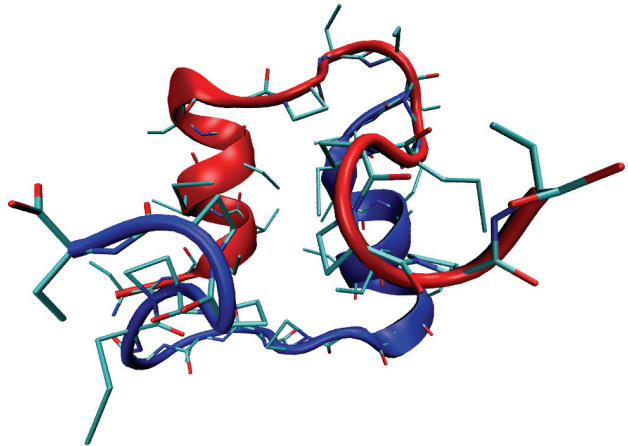

Fig. 4. Trp-cage coarse-grained dimer structure showing a native-like symmetric conformation. The chain backbones are colored red and blue.

X. CONCLUSION

We have implemented a DMD/REMD framework suitable to study the folding and association of small proteins. A corrected coarse-grained model has been used to fold Trp-cage to its native state. Double-chain simulations uncovered a stable, putative symmetric dimer structure, however, no β-sheet structures characteristic to amyloid-like fibers were found.

REFERENCES

[1] F. Ding, N. V. Dokholyan, "Simple but predictive protein models," *Trends in Biotechnology* 2005 Sep;23(9):450-5

[2] D. C. Rapaport, "The Art of Molecular Dynamics Simulations," 2nd Edition, Cambridge University Press, 2004

[3] L. Qiu, S. A. Pabit, A. E. Roitberg, S. J. Hagen, "Smaller and faster: the 20-residue Trp-cage protein folds in 4 micros," *J Am Chem Soc* 2002 Nov 6;124(44):12952-3

[4] F. Ding, S. V. Buldyrev, N. V. Dokholyan, "Folding Trp-cage to NMR resolution native structure using a coarse-grained protein model," *Biophys J.* 2005 Jan;88(1):147-55

[5] Y. Sugita, Y. Okamoto, "Replica-exchange molecular dynamics method for protein folding," *Chem Phys Lett* 1999 314:141-151.

[6] Y. Zhang, J. Skolnick, "SPICKER: a clustering approach to identify near-native protein folds," *J Comput Chem* 2004 Apr 30; 25(6):865-71.